MODELLING, ANALYSIS AND IDENTIFICATION OF MISALIGNMENT IN ROTOR SYSTEMS INTEGRATED WITH ACTIVE MAGNETIC BEARINGS

A Thesis Submitted in Partial fulfilment of the Requirements

for the Degree of

DOCTOR OF PHILOSOPHY

by

R. SIVA SRINIVAS

(Roll no. 156103043)

DEPARTMENT OF MECHANICAL ENGINEERING

INDIAN INSTITUTE OF TECHNOLOGY GUWAHATI

GUWAHATI -781039 INDIA

February 2021

Department of Mechanical Engineering
Indian Institute of Technology Guwahati
Guwahati-781039, India

CERTIFICATE

It is certified that the work contained in this Thesis titled "**Modelling, Analysis and Identification of Misalignment in Rotor Systems Integrated with Active Magnetic Bearings**" submitted by **Mr. R. Siva Srinivas** (Roll no. 156103043) to the Indian Institute of Technology Guwahati for the award of the degree of Doctor of Philosophy has been carried out under my supervision in the Department of Mechanical Engineering, Indian Institute of Technology Guwahati. This work has not been submitted elsewhere for the award of any other degree or diploma.

February 2021

Dr. Rajiv Tiwari
Professor
Department of Mechanical Engineering
Indian Institute of Technology Guwahati
Guwahati – 781039, India

To my Immortal friend

UG Krishnamurthi

Acknowledgements

I would like to thank my supervisor Prof. Rajiv Tiwari for his expert guidance and continuous support all through the duration of my research work. I am truly grateful to have gotten the opportunity to go through the whole journey of Ph.D. under his guidance. I cherish all the meetings and technical discussions we have had in his office and via telephone.

I would like to thank Dr. Kannababu, Aero engine research and design center, HAL, Bangalore for accepting to be my internal guide. I would like to thank my doctoral committee members Dr. S. K. Kakoty, Dr. H. B. Nemade, Dr. Atanu Banerjee and Dr. Karuna Kalita for giving their valuable suggestions during the annual progress seminars. I thank Dr. D. Bordoloi for the support he extended in Advanced Vibrations laboratory, IIT Guwahati. I am really thankful to all my lab mates for giving their valuable time to me. They have been very helpful in doing in-absentia course registration at the beginning of every semester for me. I cherish the time I spent with them during my visits to IITG. I wish them all success in their future endeavors. I thank Hostel Affairs Board for providing me accommodation in hostels during my temporary stays at IITG.

I am thankful to Dr. V. Sridhar, General Manager (Retd.), AERDC, HAL for encouraging me to carry out research by issuing the no objection certificate. His supportive gesture was the first stepping stone to carry out research work. I thank Mr. Chandrasekhar, Bharathi Engineering, Bangalore and his staff for helping me in building the rotor test rig. I thank Mr. Jayaramireddy, Mars Electricals, Bangalore for fabricating magnetic actuators.

I thank my parents, my brothers, my relatives and UG's friends for their encouragement during the past five years. I thank my in-laws for their continuous support and for coming over to Bangalore to stay with my family during my absence at home. I thank my wife Phani, my daughter Manogna and my son Ruthwik for always keeping me in high spirits.

When I look back, I will fondly remember the journeys I have made from Bangalore to Guwahati over the past five years. My stays at the various hostels of institute, mess food

and the walks on campus during the various seasons of year are deeply etched in my memory. I have understood that getting Ph.D. is as much about the journey as it is about the destination.

I again thank Prof. Rajiv Tiwari for making all this possible. I hope to work with him in the area of Machine Learning in the near future.

Finally and importantly I thank my friend and my mentor U.G. Krishnamurthi who is ever present everywhere. I thank Him for setting before me the goal of seeking ultimate reality like He did in His lifetime.

February 2021 R Siva Srinivas

Guwahati

Abstract

Condition monitoring in rotating machinery deals with diagnostics and rectification of various faults that are found in rotors and interconnecting components. Misalignment is one of the commonly encountered faults in industry which can lead to vibration in rotors, coupling, noise in bearings and sometimes eventual failures. There have been various vibration-based methods of monitoring misalignment, like orbits with loops, high axial vibration, and higher second harmonic of vibration. Some of the methods to tackle misalignment are placing shims below bearing housings and employing flexible couplings to transmit power between adjacent rotors.

In this work model-based identification of misalignment in coupled rotors integrated with active magnetic bearings has been studied. Active magnetic bearings function as auxiliary or main supports for the rotor system and attenuate the vibration produced due to misalignment. The stiffness of the coupling is modelled as the sum of static stiffness and time-varying additive stiffness. The additive coupling stiffness model is developed based on weight dominance criteria and a suitable steering function. The steering function is used to mimic the multi-harmonic nature of misalignment forces as noticed in various experiments.

The first model of the coupling considers the angular misalignment and is suitable for simple rotors connected by flexible coupling. It is based on the translational displacements at disc locations. The second model considers both parallel and angular misalignment and is suitable for rotors with multiple discs connected by either rigid or flexible coupling. It is based on translational and rotational displacements at coupling ends. The third and final model considers angular misalignment and is suitable for spline joints found in gas turbine rotors. It is based on translational and rotational displacements at spline joint ends.

The model of the coupling is integrated with the global equations of motion of the coupled rotor. The vibration responses at various rotor locations and current responses in AMBs are obtained by solving the equations of motion. The responses are passed through full spectrum algorithm to estimate the amplitude and phase of the integer harmonics of rotor vibration and AMB current. An identification algorithm has been

developed by rearranging the frequency domain equations of the coupled rotor system. By inputting the real and imaginary parts of the vibration and current to this algorithm the unknown parameters of the rotor-coupling-AMB system have been estimated.

The static and additive stiffness of coupling, displacement and current stiffness of AMBs, unbalance and phase of the discs, stiffness of bearings are the unknown parameters, which have been estimated from the linear least-squares problem. The identification algorithm has been tested against various levels of measurement noise and modelling bias and found to be robust.

Table of Contents

List of Figures

List of Tables

List of Symbols

A	Regression matrix
a_1, a_2	Constants
b	Regressand
b_1, b_2	Constants
c	Equivalent viscous damping
C	Damping Matrix
e	Disc eccentricity
E	Young's modulus of elasticity
f	Force Vector
G	Gyroscopic matrix
i	Current
$i = -n,\ldots,0,1,\ldots,+n$	Harmonic index
I	Area moment of inertia
I_i	ith harmonic of current
Im	Imaginary part
$j = \sqrt{-1}$	Imaginary number
k_{ij}	Direct and coupled shaft stiffness terms
k_s	AMB force displacement constant
k_i	AMB current displacement constant
K_P, K_I, K_D	Proportional, Integral and Derivative gains of PID controller
m	Disc mass
M	Mass matrix
n	Real number
p,q,r,s	Participation factors
Q	Generalized force
q	Displacement vector
R_i	i^{th} harmonic of complex displacement
T	Transformation matrix, Kinetic Energy
$s(t)$	Periodic time-varying steering function
t	Time

u	Vibration displacement vector
V	Potential energy, Complex Vibration response
X	Unknown vector
.	First order time derivative
..	Second order time derivative
×	Order of frequency
∞	Infinity

Subscripts

AMB	AMB
b	Bearing
c	Coupling
const	Constant
cu	Current
d	Disc
e	Element
fluc	Fluctuating
i	i^{th} coefficient
in	Inner
isb	Intershaft bearing
m	Master DOF
mis	Misalignment
ou	Outer
p_i,q_i,r_i,s_i	Participation factors
rad	Radial
s	Slave DOF
sh	Shaft
sp	Spline
st	Corresponding to static deflection
x	Along x coordinate axis
y	Along y coordinate axis
z	Along z coordinate axis

ξ	Along ξ coordinate axis
η	Along η coordinate axis

Superscripts

ACS	Additive coupling stiffness
d	Dynamic condensation
e	Element
h	Hybrid condensation
im	Imaginary
ROT	Rotational
re	Real
SCS	Static coupling stiffness
STAT	Stationary
T	Transpose

Greek

β	Phase angle of unbalance
δ	Corresponding to static deflection
φ	Angular displacement
λ	Constant
Ω_{in}	Angular speed of inner rotor
Ω_{ou}	Angular speed of outer ro
ω	Angular speed

Abbreviations

ACS	Additive coupling stiffness
AMB	Active magnetic bearing
CM	Condition monitoring
DOF	Degrees of freedom
FFT	Fast Fourier Transform
JB	Journal bearing

lbp	Load between pads
lop	Load on Pads
MMC	Metal matrix composite
PID	Proportional-Integral-Derivative
SCS	Static coupling stiffness
TPJB	Tilting pad journal bearing

CHAPTER 1

Introduction and Literature survey

1.1 Introduction

This chapter surveys the literature available on Active Magnetic Bearings (AMB) and their applications in rotating machinery. The first section presents an introduction to AMBs and its basic principles that will pave a way for understanding of the subsequent literature survey. The later sections that follow discuss the hardware required for implementation such as types of AMB actuators, DSP controllers, control laws, power amplifiers, sensors and touchdown bearings. The previous literature reviews on synchronous vibration suppression and condition monitoring are discussed next.

The later subsections elaborate on application of AMBs for (i) synchronous vibration suppression (ii) stability improvement iii) effect of control laws on AMB performance (iv) identification of cracked rotors (v) identification of bearing faults vi) identification of AMB forces and (vii) identification of AMB constants. The summary of the various applications of AMB in flexible rotordynamic systems is presented later. The last section presents the various possibilities of AMB applications in condition monitoring that have potential for further research.

1.2 Working Principle of AMBs

AMBs are typically used as bearings, and have the unique feature of no contact between the stationary housing called the stator and the rotating target called the rotor. A non-rotating rotor is first lifted into air by AMBs, i.e. it acts as pure bearing, and then the drive rotates it up to desired operating speed. During run-up AMBs act as a controller, suppressing unwanted high level of vibration, especially during resonances and instabilities. During transients and rundown, the rotor lands on touchdown bearings (Haberman and Brunet, 1984). AMBs can only produce attractive forces, therefore, a closed loop controller with additional hardware components are required to maintain stable operation. Primarily, AMBs offer advantages such as high attainable rotating speed, tuneable bearing rotordynamic parameters, no wear, no lubrication system, low losses, and wide operating temperature range, lower power consumption compared to fluid film bearings, rolling element bearing (Haberman and Liard, 1980; Maslen et al., 1996).

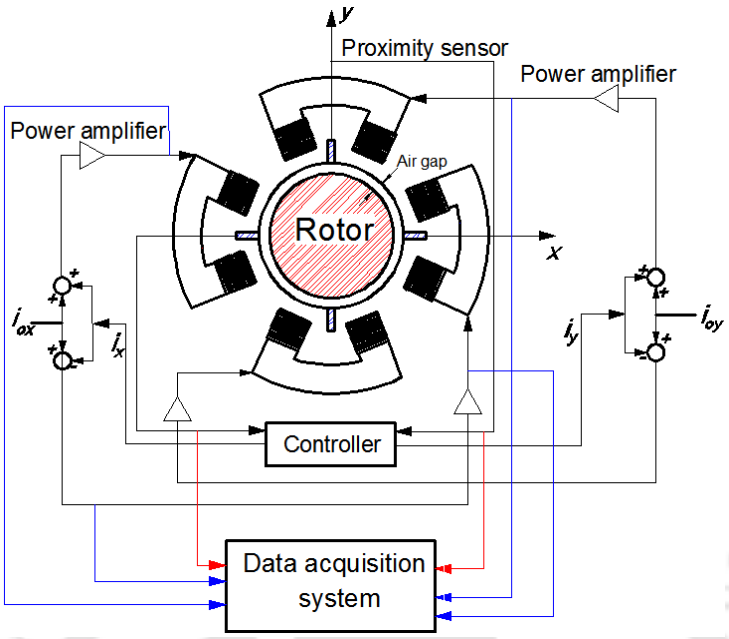

Figure 1-1Working principle of AMB–rotor system

The schematic representation of the components of AMBs and its working principle is shown in Figure 1-1. A magnetic bearing system consists of four basic components: magnetic actuator, controller, power amplifier, and shaft position (proximity) sensor. The non-contact proximity sensor sends measured signal to the controller when there is a change in rotor position. The controller sends correction signal to power amplifier, which then sends appropriate current correction to electromagnet coils. Electromagnets create magnetic flux to attract the rotor back to its equilibrium position. This process happens in real time thus levitating the rotor during its operation.

1.3 AMB Actuators

AMBs exert forces on the rotor without direct physical contact by generating attractive forces using electromagnets. The simplest AMB stator consists of two electric coils facing each other. At least three coils are necessary for a complete radial magnetic bearing in order to generate forces in two perpendicular directions. The most common design uses four independent coils (Larsonneur, 1990). Bornstein (1991) gave expressions for static and dynamic load capacities of magnetic bearings.

Radial AMBs are grouped into two primary structural configurations based on magnetic polarities of the stator relative to the rotor. If the stator poles in a given rotor transverse

plane have the same magnetic polarities, then it is termed as *homopolar*. The magnetic flux path in this configuration is as shown in Figure 1-2.

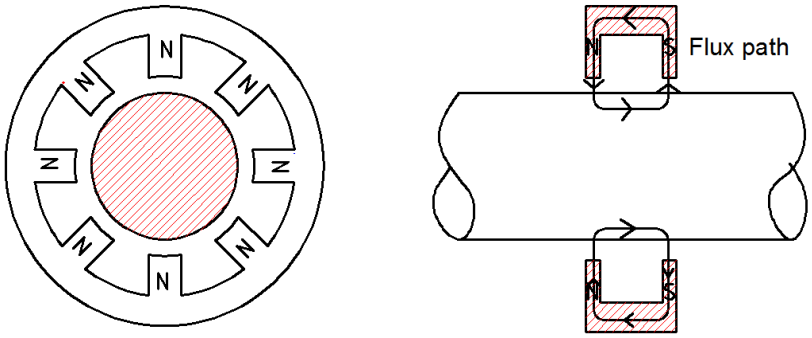

Figure 1-2 Homopolar radial magnetic bearing (HOMB)

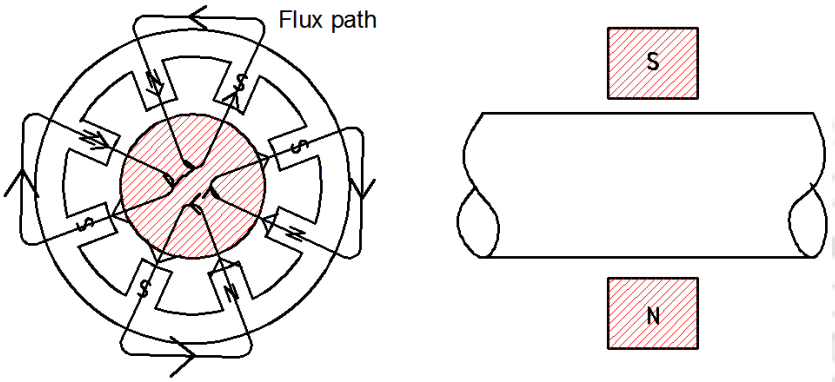

Figure 1-3 Heteropolar radial magnetic bearing (HEMB)

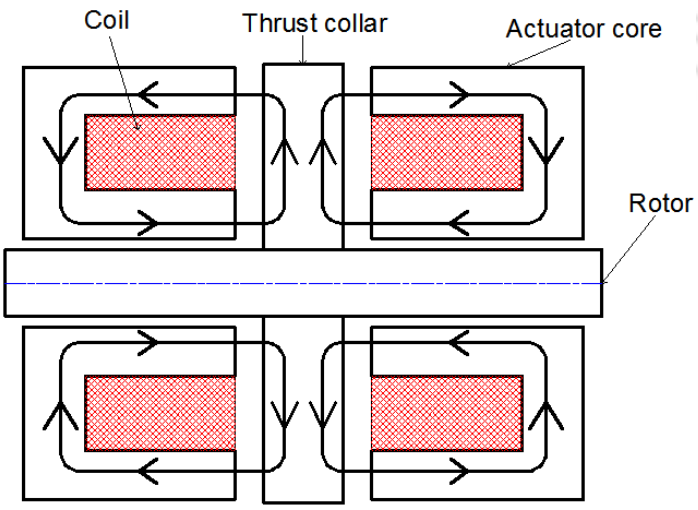

Figure 1-4 Double acting magnetic thrust bearing

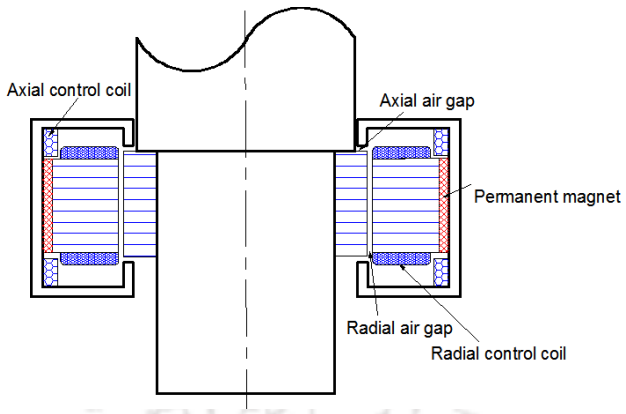

Figure 1-5 Radial - Axial magnetic bearing

With homopolar bearings, the rotor experiences lesser change in magnetic field around its circumference, and thus eddy currents are reduced significantly. This eliminates the need for a laminated collar on the shaft. If polarities of stator poles in a given rotor transverse plane vary, it is termed as *heteropolar* (Figure 1-3). The magnetic flux path is radial in this configuration. Its chief advantage lies in the simplicity of construction from laminations. However heteropolar bearings tend to induce substantially greater losses in the rotor, due to the high frequency changing magnetic field the rotor experiences, there by building up eddy currents. This issue is addressed by using them in conjunction with laminated ferromagnetic collar/sheets, called *core*, that are slid around the rotor to keep the eddy current losses as low as possible. This leads to less field variation around the circumference of the rotor and reduced eddy current losses (Kasarda et al., 1999; Schweitzer and Maslen, 2009). The *core* is generally made out of laminated electrical steel, which has high magnetic permeability, good saturation strength and reduced energy losses due to eddy current build up. Lusty et al. (2016) developed a core that was made out of Soft Magnetic Composite (SMC). Allaire et al. (1996) has given a comparison of power losses in HEMB and HOMB.

Figure 1-4 shows a double acting magnetic thrust bearing, which exerts axial force on the rotor in both directions. These are widely used in vertical centrifugal pumps. Combined radial-axial AMBs in addition to levitating the rotor also provide both radial and thrust (axial) control of the rotor (Figure 1-5). For more details on integrated magnetic bearing the reader can refer to McMullen et al. (2000) and Betchson (2000).

For more information on various design aspects of magnetic bearing actuators the reader can refer to Haberman and Brunet (1984), Chen (1988), Schweitzer and Maslen (2009), Rao and Tiwari (2009), Lijesh and Hirani (2015) and Barbaraci (2016).

1.4 Digital Signal Processing Unit

Digital signal processing unit, also called DSP controller, processes the rotor vibration signal according to a predefined control law and outputs control current, which is routed to power amplifiers. The position signal of rotor is digitized through an analog to digital converter before being sent to the plant controller, which is converted back to analog voltage signal through a digital to analog converter. The sample rate of the controller is generally two orders of magnitude higher than bandwidth of the tests performed. The low pass filter is used to attenuate high frequency electrical noise within the controller and to reduce the controller's high frequency gain above the bandwidth of hardware. To dampen out unwanted high frequency resonances existing above the frequency bandwidth of the system, notch filters are used. (Clements, 2000). The analog voltage signal is then sent to power amplifiers.

1.5 AMB Control Law

The magnetic bearing system is unstable in open loop and therefore feedback control is needed for the stable levitation of rotor. This function is commonly achieved by a controller, which controls rotor position based on the data transmitted from the position sensors. The controller supplies equal and opposite currents to poles to provide stabilizing force to rotor (Haberman and Brunet, 1984). The feedback control law plays a central role in AMB performance. So much so that a vast range of literature is available on the implementation of various control laws and their effect on the rotor dynamics of AMB supported systems. The PID control dominates the present AMB applications. However, these controllers do not always provide the desired performance and robustness, especially when the operating speed is above the system's critical speed and the gyroscopic effect is involved. This prevents their use in the more advanced applications of AMBs.

Over the years, a variety of controllers from simple SISO to complex multi-input and multi-output (MIMO) adoptive controllers have been used. A complete list of

controllers used in AMB systems is given in Schweitzer and Maslen (2009). For higher speeds, complex MIMO adoptive controllers, like the μ-synthesis and H_∞ controllers are being preferred over conventional and simpler SISO controllers as they have been found to improve the performance and robustness of a rotor–AMB system. Fittro and Knospe (2002), Maslen and Sawicki (2007), and Sawicki (2008) explained the motivation for the use of μ-synthesis controllers.

MIMO control methods usually rely on accurate analytical models and uncertainty characterizations. Due to geometrical and assembly features such as interference fits and abrupt changes in shaft diameters, bending stiffness of rotor changes, which in turn affects mode shapes, resonances and anti-resonances. As a regular exercise, *modal updating* (Friswell and Mottershead, 1995) is performed before implementation of these controllers, to improve the accuracy of finite element (FE) models of rotors. To obtain the final numerical model, which accurately describes the experimental model, the initial FE model of the flexible rotor needs to be fine-tuned based on the measured frequency response of the levitated rotor during run-ups. Various techniques developed by researchers for model updating are explained in works by Vazquez et al. (2001), Ahn et al. (2003), Sawicki and Maslen (2007), Wroblewski et al. (2012), Madden and Sawicki (2012), Sun et al. (2013), Stimac et al. (2013), Zhe et al. (2014) and Xu et al. (2015).

1.6 Power Amplifiers

Power amplifiers supply the electromagnets with the power for the magnetic field which generates the forces acting on the rotor. They act as a bridge between the control signals from the controller and applied current to the coils of electromagnetic actuator. In AMB applications, each bearing axis has a pair of power amplifies. The amplifiers are high voltage switches, which use transistors that are switched on/off at a high frequency to represent positive/negative voltage values, as commanded by the pulse-width modulation wave signal from the controller (Tiwari, 2011). Lately, switching power amplifies have come to replace analog power amplifiers. For more information, the reader can refer to Keith et al. (1990) and Jing (1995).

1.7 Sensors

Eddy current proximity probes are the most commonly used gap sensors in AMB applications. These are based on the fact that eddy currents are induced in a conductive material of the rotor as a result of the magnetic field of active electromagnet coil. The eddy current induces an opposing magnetic field, and hence reduces the inductance in the active electromagnet coil. As the distance between rotor and the transducer probe changes, impedance of the coil changes accordingly. Eddy current sensors have an excellent frequency response, almost linear characteristics and negligible phase shift, and are non-sensitive to external disturbances. They cover a displacement range of 2 mm. However, there are other types of non-contact displacement sensors/ transducers, e.g., the capacitive, inductive, magnetic, optical, combined displacement-velocity, photo-electric and laser types. (Schweitzer and Maslen, 2009; Tiwari, 2011).

Hall sensors are solid-state sensors that vary their output voltage proportional to magnetic field density. They are used for magnetic flux measurement in AMB applications by mounting them on the pole surfaces. Voigt and Santos (2012) embedded hall sensors in the pole instead of mounting on the pole and investigated the force estimation errors theoretically and experimentally.

1.8 Touch-down Bearings

For each AMB, rolling element bearings also called auxiliary or backup or retainer or touchdown bearings are mounted at one half the AMB air gap to protect the AMB components in the event of power failure or AMB load saturation. During normal operation they are not in contact with the rotor. According to ISO 14839, three typical orbit responses that can be detected in touchdown events are pendulum vibration, combined rub and bouncing, and full rub. Lyu et al. (2016) performed frequency response analysis on the orbits observed during touchdown. Lijesh and Hirani (2016) performed failure mode and effect analysis (FMEA) on AMBs to identify the various failure modes and the corresponding effects of those failures on performance. On a severity scale of 5, partial rub of rotor with AMB and touchdown events have been rated at 3 and 5 respectively. Halminen et al. (2017) developed two *elastic contact* mathematical models for back-up rolling element bearings with and without cage. Lyu et al. (2018) presented a rotor *relevitation* method after the instance of rotor coming in contact with touch down

bearings. A decentralized PID algorithm is used to identify rotor responses such as pendulum motion, combined rub and full annular rub to achieve relevitation of rotor. Saket et al. (2019) calibrated strain measurement data against AMB forces to experimentally investigate the flexible rotor-touchdown bearing contact conditions.

1.9 Synchronous Vibration Suppression: Earlier work

A rotor that operates well below its first bending critical speed is termed as rigid rotor. It can be balanced at low speeds and in any two arbitrary planes. Over the decades there has been vast amount of literature on various techniques of rigid rotor balancing. Vance (1988), Goodwin (1989), ISO 1940/1: 2003 and Muszynska (2005) can be refereed to know more on this topic.

A rotor that operates near or above the bending critical speed is termed as flexible rotor. Unlike a rigid rotor, the unbalance distribution changes along the length of rotor with speed. Hence, high speed balancing is to be done at individual critical speeds on different number of balancing planes. Since early 1950's there have been numerous books and papers on the vibration reduction in the flexible rotor by various traditional balancing methods, such as influence coefficient balancing, modal balancing and unified balancing. Bishop et al. (1959), Sharp (1980), Parkinson et al. (1980), Gnielka (1983), Gosiewski (1985, 1987), Darlow (1987, 1989) and Ehrich (1990), ISO 11342/1: 1998 are a few important technical papers that can be referred to for fundamental principles of the flexible rotor high-speed balancing. Zhou and Shi (2001) presented an article on active balancing and vibration control in rotating machinery.

1.10 Condition Monitoring of Rotor-Bearing Systems: Earlier work

Condition monitoring (CM) is the process of determining the condition of machinery while in operation by monitoring a parameter (or more) of machinery in order to identify significant changes, which are indicative of a developing fault. CM is a major component of predictive maintenance. It has unique benefit in that conditions that would shorten normal lifespan can be addressed before they develop into a major failure. There is vast amount of literature available on CM of mechanical systems by employing various techniques. It will be beyond the scope of this chapter to review the various techniques developed over the years. Davies (1998) has comprehensively treated the several CM

techniques that are in practice in industry. For the different signal processing techniques employed and transducers used in vibration based CM, the reader is advised to refer to Randall (2011) and Lee (2008).

Figure 1-6 gives pictorial abstract representation of various CM techniques employed in rotating machinery. Figure 1-6(a) is the traditional CM technique that has been in usage in industries for many decades. The output parameter of interest (vibration, acoustics, pressure, temperature, and oil debris) in rotating machinery is continuously monitored for increase/decrease in amplitude or appearance of new frequency components in spectrum. Based on previous experience the CM engineer attributes the abnormality noticed in the spectrum for possible faults generated within the system. There are several machine learning algorithms (artificial neural network and support vector machines (Alguindigue and Uhrig, 1991; Tsou and Shen, 1994; Meireles et al., 2003; Li et al., 2011) which exploit heuristic knowledge with measured data to develop expert system and that field is beyond the scope of the present chapter.

In Figure 1-6(b), a known external excitation is applied on the system and the generated output signal is processed for identification of suspected faults. This, however, requires accurate estimation (or measurement) of force that is input to the system. Estimation of frequency response function (FRF) from impact testing is one of the reliable and time tested ways of obtaining vibration signature, which can be used for fault diagnosis. Brown et al. (2015) gave guide lines to make good FRF measurements with impact testing. Chen et al. (2014) used this method and performed impulse response tests on gas turbine engine casing to diagnose the faults in main rotor ball bearings. The faults generated on the inner race, outer race and balls are significantly weakened as they transmit through the flexible housing to casing, thus rendering traditional spectrum monitoring ineffective. Wavelet envelope analysis was performed to effectively extract the signature corresponding to bearing faults. Tieu and Qiu (1997) identified the dynamic coefficients of journal bearings using the impulse responses from impact hammer tests.

Figure 1-6(c) shows a technique, wherein, the magnitude of unknown system faults is estimated from output signal produced by exciting these faults during operation. Lees and Edwards (1997) estimated the residual unbalance in flexible rotor system from run–up data. The data was later used for balancing the flexible rotor.

Figure 1-6(d) shows a technique wherein faults are deliberately introduced into the system and the system characteristics / magnitude of unknown system faults is estimated from output signal. Edwards et al. (2000) estimated the residual unbalance and shaft bend by exciting the rotor with trial masses during run-up. The technique has been used to estimate dynamic characteristics of supports. Tieu and Qiu (1994) identified the dynamic coefficients of journal bearings using experimental unbalance responses. Shravankumar and Tiwari (2012) used model-based method to estimate shaft viscous damping, unbalance eccentricity and crack stiffness of a Laval rotor.

In Figure 1-6(e), system diagnosis is performed with an AMB exciter/injector, which is used to amplify vibration signature that is characteristic of a particular fault. Faults in rolling element bearings, wear in journal bearings, presence of breathing crack have been detected using this method. This technique, however, compromises the structural integrity of component that contains the fault. A review of this technique is presented in Sections 2.5.3 and 2.5.6.

In Figure 1-6(f) AMB acts as auxiliary support, which suppresses the vibrations induced by faults. The vibration signal obtained from the system alone cannot be used for the fault diagnosis any more, as the AMB has now absorbed a proportion of vibration induced by the faults. However, the current and displacement signatures of AMB contain the characteristics of system faults. This fundamental difference between Figure 1-6(e) and Figure 1-6(f) is to be appreciated. Tiwari and Chougale (2014), and Tiwari and Viswanadh (2015) estimated the residual unbalance and bearing dynamic parameters of flexible and rigid rotor systems with AMB supports along the span of rotor, respectively. Singh and Tiwari (2015, 2016) used this technique to investigate the behaviour of simple rotors with a breathing crack.

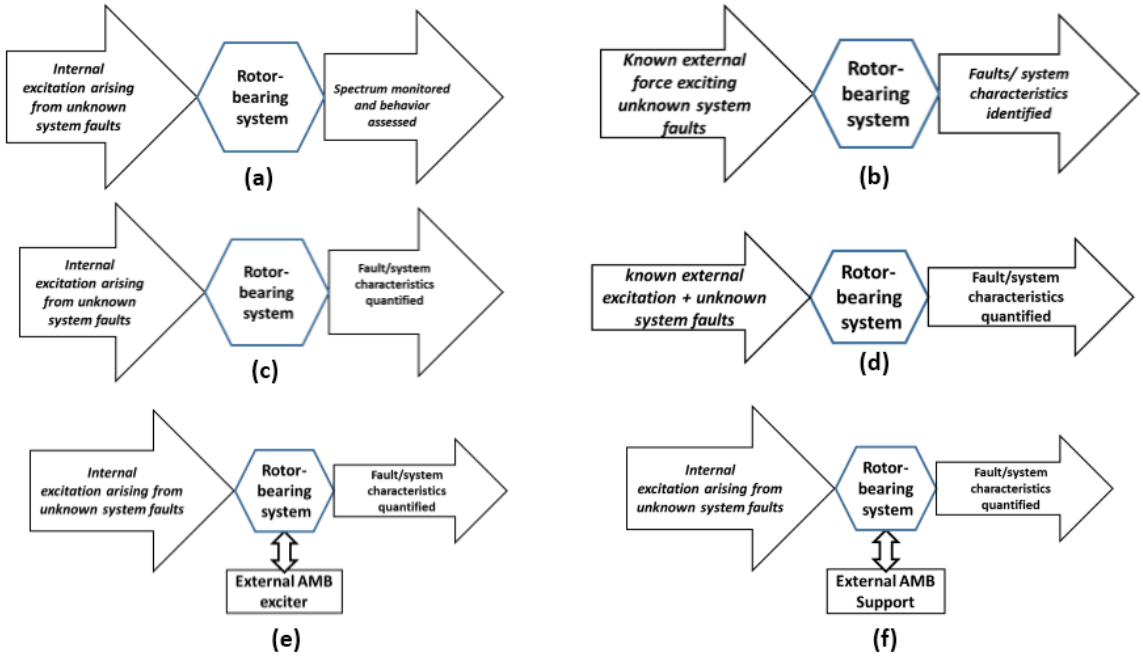

Figure 1-6 Different approaches in vibration based condition monitoring

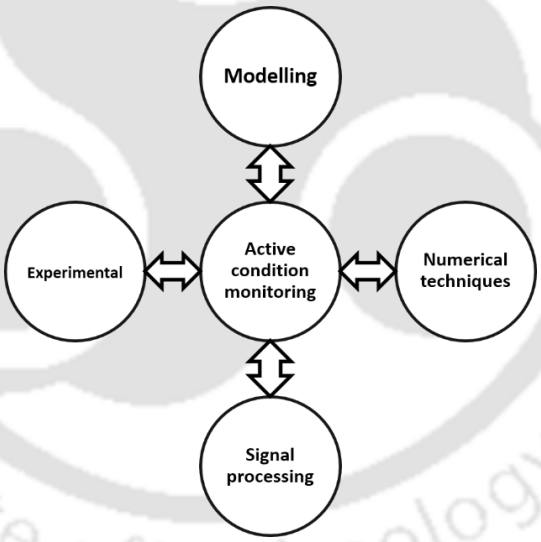

Figure 1-7 Active condition monitoring

In the traditional CM, the fault is diagnosed from signature and the machine is shut down to repair (replacement/ unbalance correction) the damaged component. Active condition monitoring (ACM) on the other hand is a real time monitoring technique, unlike the traditional CM, thus leading to significant reduction in downtime. ACM besides providing the spectral behaviour of various faults in real time like CM, also quantifies the magnitude of the fault. Figure 1-7 gives a pictorial summary of various aspects of an ACM. It begins with finite element modelling of the physical system, i.e. the rotor, stator

and bearings. Various faults, such as the unbalance, misalignment, crack forcing function etc. and various external excitations, such as the impulse load, magnetic forces etc. are introduced into the system equations of motion (numerical model). Experiments are then performed on the physical system in laboratory to measure the dynamic response, i.e. displacement, current along with their phases at predetermined locations along the rotor length. The experiments are repeated at various speeds and in different directions at the same speed (Tiwari, 2005). The response values in each case are fed into the regression equation, which is nothing but the equations of motion of dynamic system arranged in segregated matrix form for the convenience of quick generation of unknown system parameters. The accuracy of the estimated parameters depends primarily on the accuracy of numerical model and number of experimental readings. Moreover, the correctness of regression equation can be checked by performing numerical experiments before conducting the actual experiment and comparing the assumed and estimated values. Real time/ active estimation of dynamic parameters can be performed easily by positioning sensors at the appropriate locations on any rotor-bearing system that is amenable to be expressed in regression matrix form.

Smart condition monitoring (SCM), which is an advanced ACM technique is a concept that deals with monitoring and controlling a parameter (or more) in machinery in order to identify a significant change in not only system parameters but of controlling parameters, which are indicative of a developing fault. A smart machine can be defined as, “Machine that can detect, diagnose, reconfigure and adapt to the system faults in real time with its built-in capabilities” (Schweitzer and Maslen, 2009). Besides monitoring the conventional parameters, researchers can use AMB parameters, such as the control current and the air gap to their advantage to monitor the faults in rotor-bearing systems. Burrows et al. (1999), and Larsonneur and Richard (2008) discussed the central role AMBs have to play in smart machines.

Shravankumar and Tiwari (2012), Tiwari and Chougale (2014), Tiwari and Viswanadh (2015), Singh and Tiwari (2015, 2016), Roy and Tiwari (2018, 2019), Sarmah and Tiwari (2019, 2020), Prabhat and Tiwari (2019, 2020) have investigated various types of faults (e.g., crack, unbalance, bow, misalignment, etc.) in rotor systems with and without using AMBs using ACM technique.

Kasarda (2000) presented an overview of AMB technology and its applications. Schweitzer et al. (2009) in his book addressed the various topics related to AMB operation and applications. The topics discussed are hardware, AMB design criteria, AMB losses, AMB control laws, dynamics of rigid and flexible rotors supported on AMBs, touch down bearings and identification.

The next sub section deals with application of AMBs for vibration suppression in flexible rotor-bearing systems.

1.11 Synchronous Vibration Suppression in Flexible Rotors with AMBs

Allaire et al. (1983) studied vibration control of a single mass flexible rotor on damped flexible supports with active feedback control using proportional and derivative controls. The proportional control was found to move the critical speed and derivative control affected the amplitude of response, but not critical speeds. Increasing the derivative control ratio decreases the amplitude ratio. The two controls can be advantageously combined to move critical speeds and reduce peak amplitudes of vibration. Nonami (1988) explored the active vibration control of a one-meter long flexible rotor with five disks supported by magnetic bearings without considering gyroscopic effects. Two of the disks are used for magnetic bearings and two others are used for eddy current gap sensors - i.e., the bearings and sensors are not collocated. The shaft is connected to the driving motor by a flexible coupling. (Figure 1-8). The displacement signals from AMBs are the inputs for the analog controller. The controllability with and without collocation sensors and actuators located at the same distance along the rotor axis was discussed for higher order flexible modes. The author concluded that active control loops for higher flexible modes is necessary for the stabilization.

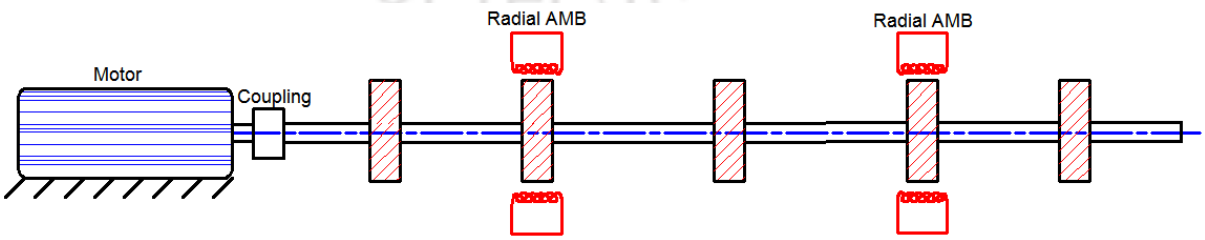

Figure 1-8 Test rig schematic: Nonami (1988)

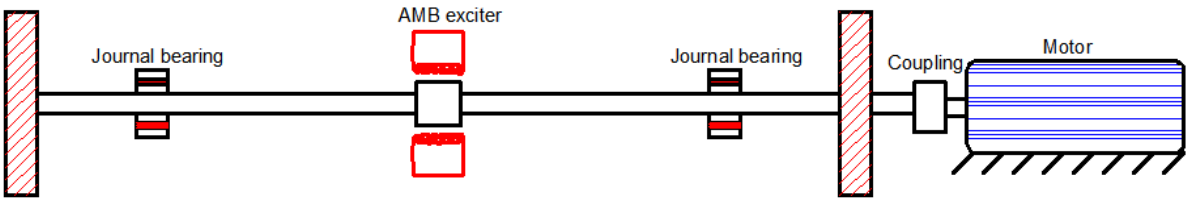

Figure 1-9 Test rig schematic: Burrows et al. (1989)

Burrows et al. (1988, 1989) studied the on-line parameter estimation and the vibration control of a flexible rotor supported on circumferential groove type oil-film bearings with the AMB as an exciter (Figure 1-9). The drive to rotor was provided by a 25 kW DC variable speed motor through a step-up flexible tooth belt and universal coupling. Eddy current probes were used to measure vibration at various positions along the rotor. The output of the transducers was sampled by a microprocessor attached to a mainframe computer. The actuator was designed to allow it to be positioned at various locations along the rotor length. It was experimentally demonstrated that single magnetic actuator can be used to estimate system characteristics and apply the optimum control force needed to minimize synchronous vibration. Subsequently, Kasarda et al. (1990) made experimental verification of damper effectiveness on three-disc rotor system supported on conventional bearings, to represent a multi-mass rotor. The magnetic damper was placed in various locations, i.e. mid-span, outboard and near one disc to observe the vibration reduction capabilities (Figure 1-10).

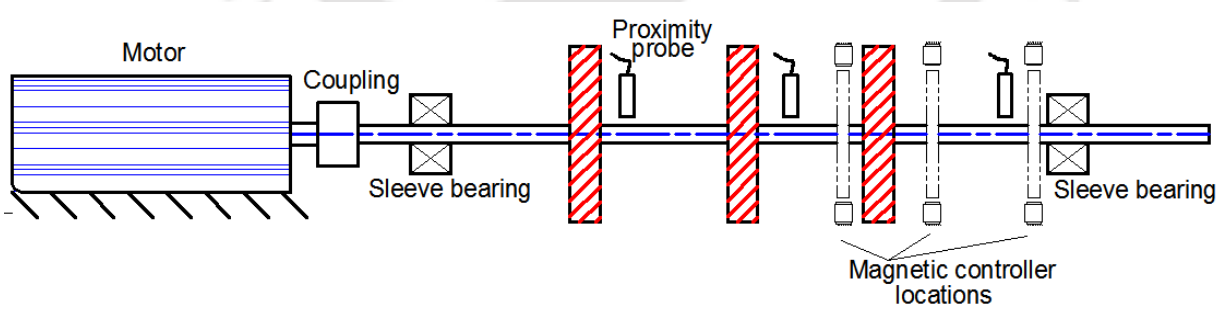

Figure 1-10 Test rig schematic: Kasarda et al. (1990)

Nonami and Ito (1996) evaluated the μ-synthesis design method for a flexible rotor-AMB system. An induction motor rotor is located in the middle of shaft and two radial AMBs are located on both sides of the motor rotor. A thrust AMB is located at left end of the shaft (Figure 1-11). The operating speed of this rotor is between the first bending mode and second bending mode. A reduced-order model was obtained in the

modal domain from the full-order system by truncating the flexible modes. By choosing appropriate weighting functions with respect to frequency, the µ-synthesis control system was designed using the Robust Control Toolbox in MATLAB™. The high stiffness provided by µ-synthesis control results in the stabilization of rotor. This controller provides greater stability, robustness and rejection of low frequency disturbances than H_∞ control.

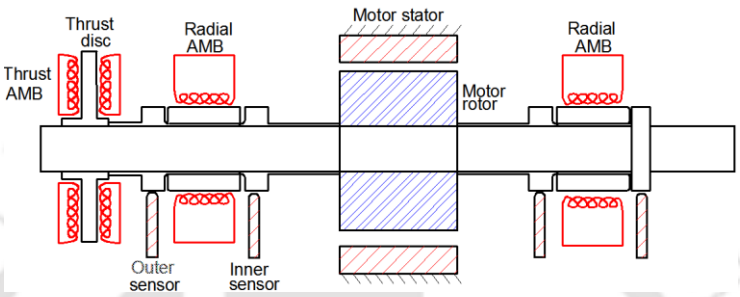

Figure 1-11 Test rig schematic: Nonami and Ito (1996)

Okada et al. (1999) developed a magnetic bearing to control the bending modes of a flexible rotor. The position control capability was used to support the rotor, while the inclination controls capability to increase the damping of bending modes. Mykhaylyshyn (2001) applied feed forward control approach to inject a force to counteract the rotor unbalance force in a flexible rotor. The rotor was supported by two bearings and an AMB was placed at bearings mid-span. The rotor was driven by an electrical motor through flexible aluminium coupling (Figure 1-12). By specific selection of frequency and phase as functions of the rotor running speed and rotor natural frequency, the proposed magnetic force injection waveform has been shown to be effective in reducing rotor vibrations. It was noticed that at a constant running speed, just below the first rotor critical speed, the rotor vibrations were reduced approximately by 90%. The method was implemented during the speed ramp test through the first critical speed.

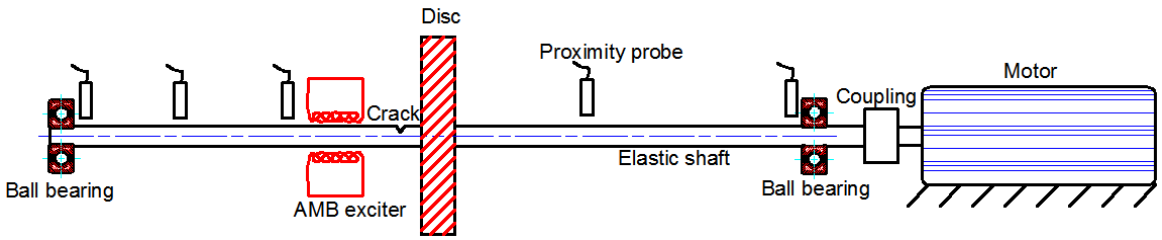

Figure 1-12 Test rig schematic: Mykhaylyshyn (2001)

Johnson et al. (2003) tested nine different sensor placement configurations along the length of high-speed test rotor. Different numbers and locations of sensors and actuators were used with different locations of disc with holes for the placement of unbalance weights and the impact of sensor and actuator location on the reduction of synchronous vibrations was studied (Figure 1-13). Filtered X-LMS algorithm, a time domain based adaptive feed forward approach has been used for reducing rotor vibration, as against the conventional frequency domain feed-forward approach. It was shown that using a larger number of error sensors than actuators result in better global reduction of vibration but decreased the local (at sensor locations) reduction. An attenuation as high as 48 dB was achieved using the filtered X-LMS algorithm.

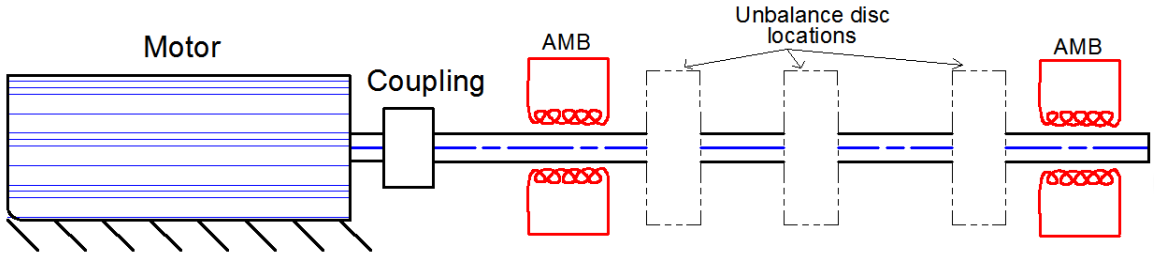

Figure 1-13 Test rig schematic: Johnson et al. (2003)

Ichihara et al. (2003) developed an extended physical model of a flexible rotor-AMB system that can pass through a critical speed of a flexible rotor by a controller that combined the PID for rigid modes, with linear quadratic (LQ) control for flexible modes.

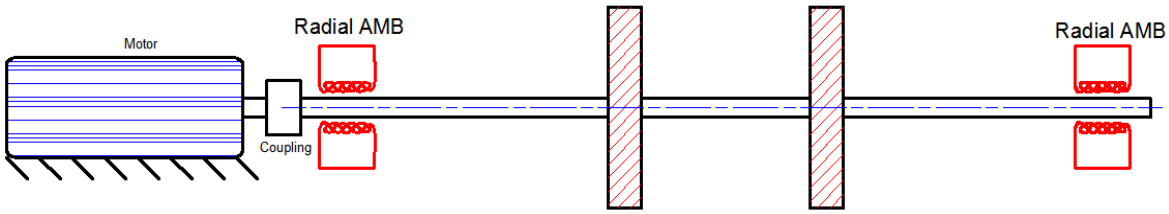

Figure 1-14 Test rig schematic: Mystkowski (2010)

Mystkowski (2010) investigated the rotordynamic stability and vibration control of flexible rotor with non-collocation of sensors and actuators, gyroscopic effects and modal uncertainty using a μ-synthesis controller. The rotor is supported by two radial AMBs. Each of the magnetic bearings has 8 electromagnets, each connected to two channels of power amplifiers (Figure 1-14). Since the μ -controller cannot levitate the rotor alone, a

PID control algorithm first brings the rotor into support after which the program switches to μ-synthesis control algorithm.

Das and Dutt (2010) employed active disturbance rejection control technique based on an extended state observer in conjunction with the PD law to control the transverse vibration of a flexible rotor-shaft system. The proposed control law was able to reduce the amplitude of rotor vibration in the presence of unbalance, destabilizing effect of the internal damping, and gyroscopic moment.

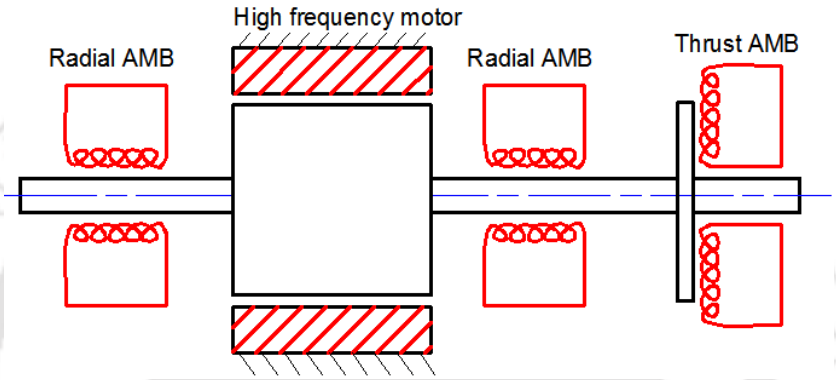

Figure 1-15 Test rig schematic: Basaran et al. (2011)

Basaran et al. (2011) designed and experimentally verified a H_∞ controller on a flexible rotor as it passed through the first critical speed. The flexible rotor is supported in radial directions by two sets of radial AMBs. A thrust AMB at the rotor end position limits the rotor axial displacements. A high frequency motor placed between the radial bearings levitates the rotor from touchdown position when control is applied to AMB system (Figure 1-15). Kozanecka et al. (2011) applied AMB as a vibration damper in the torque transmission system to a tail rotor of the conventional helicopter. A long flexible shaft supported on AMBs replaced the conventional shaft mounted on rolling element bearings (REB) resulting in the weight reduction. However, during start-up, the shaft had to pass through several critical speeds. The electromagnetic damper was optimized for the mass, geometry and material selection to achieve passage through three critical speeds and corresponding vibration amplitudes that were less than 50% of the bearing clearance. Zhong and Zhu (2013) tested a two degrees-of-freedom (DOFs) PID controller through the first critical speed of a flexible rotor in steady state response and acceleration response (Figure 1-16). The 2-DOFs PID controller showed higher damping of the closed-loop system and better robust stability than the 1-DOF PID controller.

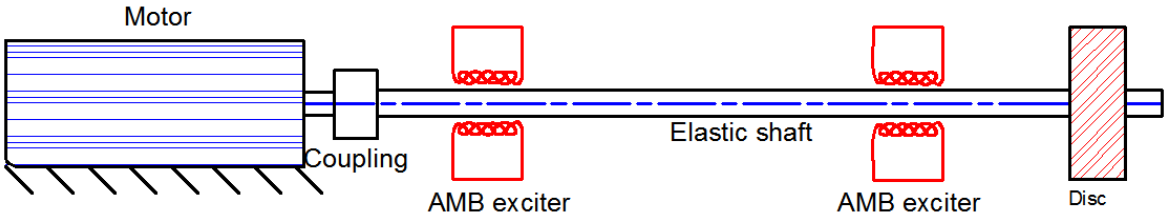

Figure 1-16 Test rig schematic: Zhong and Zhu (2013)

Defoy et al. (2014) made a comparative study of the performance of a simple PID, SISO fuzzy PID and polar fuzzy controllers on an academic flexible rotor test rig supported by AMBs (Figure 1-17). The rotor is driven by a 500W electric motor through a flexible coupling. The operating speed range includes three critical speeds (two rigid modes and one flexible mode). The polar fuzzy controller was found to exhibit better performance for the same level of robustness.

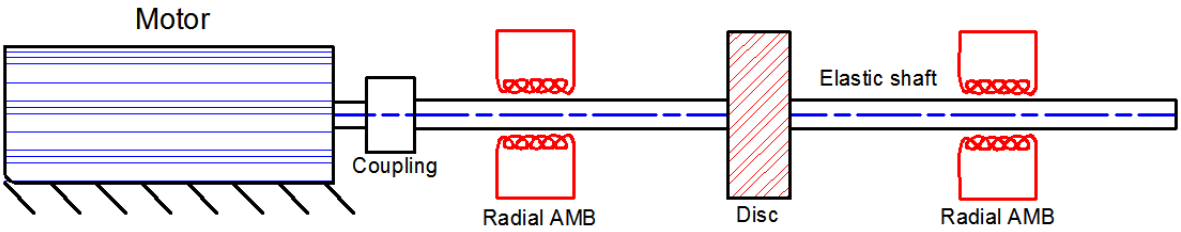

Figure 1-17 Test rig schematic: Defoy et al. (2014)

Wang et al. (2014) proposed a field balancing method for a magnetically levitated flexible rotor (MLFR) based on the virtual trial-weights (VTW) method below the critical speed. The VTW simulates the trial weights with the synchronous electromagnetic forces (SEF) supplied by AMBs. Using a synchronous notch filter in the AMB controller the rotor is supported freely, which improves the precision of rotor numerical model. Hence, the numerical model is sufficient for balancing the AMB rotor. Secondly, rigid mode vibrations in displacement output are eliminated, improving the bending mode vibrations. The above improvements permit a precise balancing below bending critical speed. Experimental results have shown that the proposed method can reduce the rotor imbalance significantly using only a single start-up.

Di and Lin (2014) implemented an all-coefficient adaptive control method to stabilize a flexible rotor AMB test rig shown in Figure 1-30. The simulation and experimental results demonstrated the performance of the controller at par with the results obtained with the benchmark synthesis controller. Zhao et al. (2015) investigated the

stability of a flexible rotor supported on AMBs, subject to the input and output constraints, using model predictive control (MPC) method. In addition to input constraints, i.e. geometrical limits of the actuators, the output constraints should also be addressed since rotor displacements have to be within the nominal air gap between the rotor and the stator of AMBs. The MPC was found to be effective in achieving stability and suppressing rotor vibrations. Fang et al. (2015) devised a damping control method, which minimized the rotor synchronous vibration amplitude near the critical speed with limited bearing force. The method was tested on a 315 kW magnetically suspended motor, which was operated between 1st and 2nd bending critical speeds. Figure 1-18 shows the motor weighing 325 kg driving a rotor of mass 72 kg supported on the radial and thrust AMBs. With the optimum phase compensator, the AMB system was able to provide maximum damping with smallest bearing force, and the corresponding resonance peak was smaller as compared to the response with the phase compensator. The rotor synchronous vibration magnitude at 1st critical speed was as low as 18 μm.

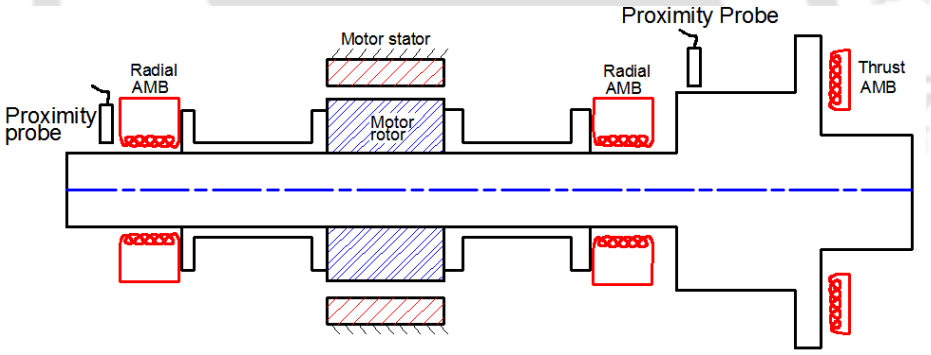

Figure 1-18 Test rig schematic: Fang et al. (2015)

Enemark and Santos (2016) identified the synchronous frequency displacement of magnetically suspended centrifugal compressors with an adaptive notch filter based on the coordinate transformation. The rotor system had two 2-DOF radial permanent-magnet-biased hybrid magnetic bearings (HMBs) and a single-DOF axial HMBs support the rotor system. Each magnetic bearing has 20 axially magnetised passive cylinder magnets placed in a circular pattern of a stationary ring. AMBs were driven by the *H*-bridge unipolar switching power amplifiers, independently. The simulation and experimental results showed significant reduction in the synchronous vibration force.

Zheng and Feng (2016) devised an adaptive notch filter to identify the synchronous frequency displacement of a magnetically suspended centrifugal compressor

as a compensation signal to eliminate the current stiffness force. Furthermore, a feed forward approach compensates displacement stiffness force and inhibits the imbalance vibration. The rotor system with two radial permanent-magnet-biased hybrid magnetic bearings and an axial HMBs are driven by the *H*-bridge unipolar switching power amplifiers, independently. A permanent magnet synchronous motor provides a rotational torque for the rotor. The rotor system is similar to the one shown in Figure 1-18. The AMB–rotor system is supported on two 2-DOF radial permanent-magnet-biased HMBs and a single-DOF axial HMB. The AMBs are driven by the *H*-bridge unipolar switching power amplifiers, independently. Rotational torque for the rotor is provided by a permanent magnet synchronous motor. The simulation and experimental results showed that the synchronous vibration force is significantly reduced at a speed of 30,000 rpm.

Lusty et al. (2014, 2016) developed a twin–shaft rotor consisting of a hollow tube primary rotor mounted on bearings and magnetically coupled to a secondary non-rotating shaft in a clamped configuration and located concentrically within the primary rotor (Figure 1-19). At rotor speeds, where vibration is not a problem, these inside-out AMBs are not activated, and thus there is no link between the two shafts. However, as critical speeds of primary shaft are approached, the AMBs are activated, thereby coupling the two shafts and changing the vibration behaviour of the rotor.

Roy et al. (2016) studied the influence of proportional and high-frequency band-limited derivative (PD_{hfbl}) control law on the dynamic behaviour of a rigid rotor-shaft system.

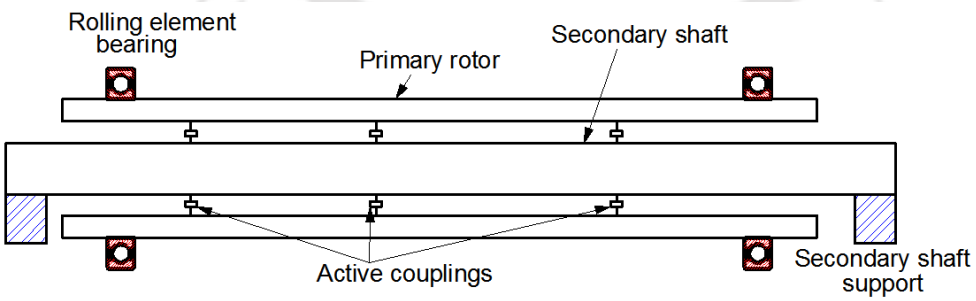

Figure 1-19 Test rig schematic: Lusty et al. (2016)

The PD_{hfbl} law proposed to generate viscoelastic semisolid-like behaviour of the AMB was found to be more efficient than the PID in positioning the rotor within closer tolerances and reducing the rotor unbalance response amplitude. Ranjan and Tiwari (2020)

used advanced influence coefficient method to balance flexible rotor supported on rolling element bearings below its first critical speed. The auxiliary AMB integrated with the rotor was used both as vibration suppressor and exciter to introduce virtual trial unbalances.

This section has presented some applications where AMBs have been used successfully for mitigating synchronous vibration of rotor systems, in general and flexible rotors in particular. Modal updating is vital in improving the dynamic characteristics of rotor-bearing system. Use of AMBs in estimating the residual unbalances for flexible rotor system is limited and development of such methods will save continuous controlling efforts required by AMBs.

1.12 AMB for Non-Synchronous Vibration Control of Rotors

Lang et al. (1996) carried out a numerical simulation in which AMBs are applied to control non-linear and non-synchronous vibrations of a rigid rotor excited by non-conservative cross-coupling mechanisms. Unknown cross-coupling parameters of a rotor are estimated on-line by a standard least-squares estimator along with a time-varying forgetting factor using an adaptive control algorithm of the AMB controller. Johnson et al. (1998) integrated a single heteropolar radial active magnetic bearing as a replacement to conventional ball bearing support into dynamic spin rig. The AMB was used to provide non-contact magnetic suspension and mechanical excitation of the rotor to induce turbo machinery blade vibrations. Spakovszky et al. (2000, 2001) demonstrated the use of AMBs as servo-actuators to achieve active tip-clearance control to stabilize rotating stall in a high speed single stage transonic axial compressor. Together with computational fluid dynamics (CFD) and experimental data, a 2-D compressor stability model was used in stochastic estimation and control analysis to determine the required AMB performance for compressor stall control.

Kasarda et al. (2004) achieved sub synchronous vibration control in single-disc flexible rotor mounted on journal bearings. One inboard AMB was used to induce synchronous excitations, while another AMB was used as Active Magnetic Damper (AMD) to control rotor vibrations (Figure 1-20). While AMD was able to successfully reduce the sub-synchronous vibrations by introducing additional stiffness and damping into the system, it was also found to alter the rotordynamic behaviour of the system,

which was reflected in the significant increase in synchronous vibrations, thus badly affecting the overall dynamic performance.

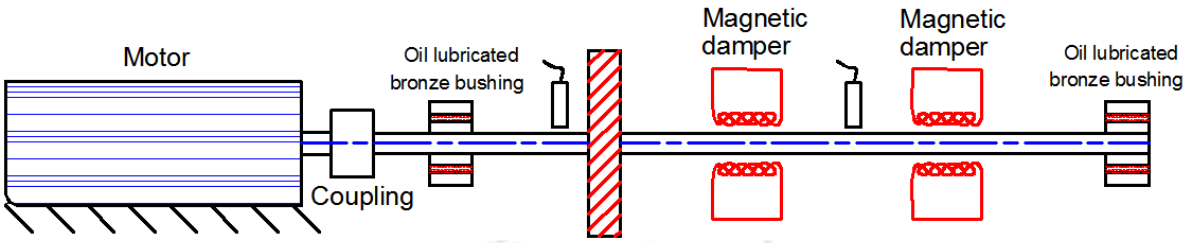

Figure 1-20 Test rig schematic: Kasarda et al. (2004)

Sahinkaya et al. (2002) investigated the attenuation of sub and super-harmonic vibration components resulting from the multi-frequency external excitation of the AMB supported rotor system by an electromagnetic shaker connected to the foundation. Speed-dependent multi-frequency influence coefficients were obtained using multiple frequency test signals applied through the magnetic bearings. Schroeder-phased harmonic sequence was used to select the relative phases of components so that the peak signal value is minimized. This prevents the possibility of the rotor displacement exceeding clearances or the bearing force saturation. The partial receptance matrix relating the measured output and the control input for all frequencies was used to develop the control algorithm.

Matsushita et al. (2002) excited the rotor on shaking table to simulate earthquake waves (Figure 1-21). A feed forward control method, which is proportional to the signal detected by accelerometers mounted on bearing housings, was designed to reduce the severity of response.

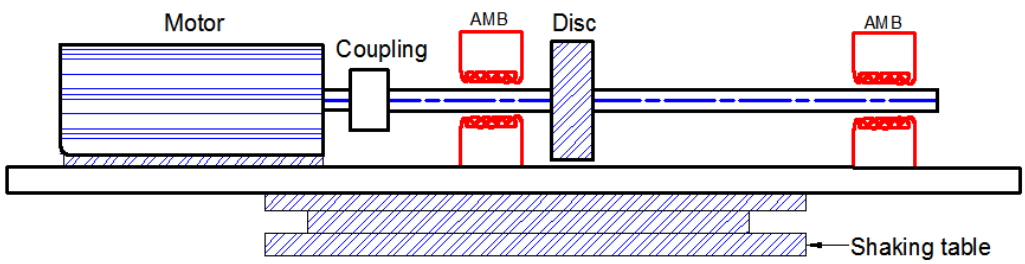

Figure 1-21 Test rig schematic: Matsushita et al. (2002)

The measured acceleration with a certain proportional gain is directly fed to the power amplifier to generate exciting force independently from PD main control. The

addition of commands from the main and feed forward loops generates a total magnetic force, which was found to reduce total rotor vibration to a low level.

Johnson and Kasarda (2002) experimentally investigated active control of acoustic gear noise and vibration using magnetic bearing actuators in a feed-forward active control scheme (Figure 1-22). A reference proximity sensor placed near the gear teeth was used to drive two AMBs through a time domain filtered X-Least Mean Square (X-LMS) control system to minimize outputs from both vibration and pressure error sensors.

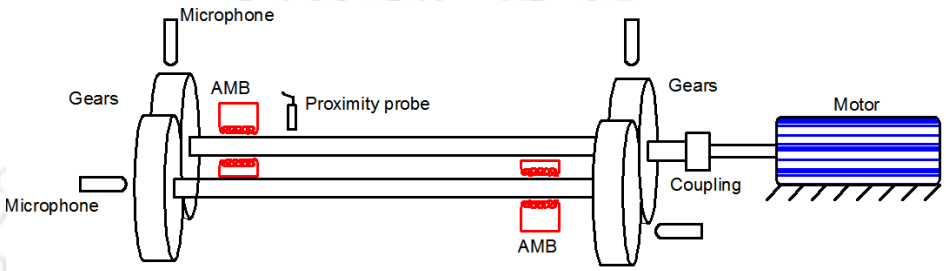

Figure 1-22 Test rig schematic: Johnson and Kasarda (2002)

Keogh et al. (2002a) incorporated transient dynamics into a harmonic controller, which is based on steady state vibration characteristics. Initially, the rotor was centralized in the bearings with PID control. To demonstrate transient vibration control, a mass-loss mechanism was arranged around the non-driven end disk, which was then detached using a solenoid activated blade mechanism. Transient vibration responses due to step changes in disturbance in each control axis were used in the design of controller. Keogh et al. (2002b) experimentally investigated dynamics and control of rotor vibration when contact with auxiliary bearings due to large unbalance induced in the presence of AMB supports (Figure 1-23). In the event of persistent contact the phase shift was found to be 180^0. The synchronous current controller based on the linear system causes the rotordynamic performance to deteriorate resulting in higher contact forces. A modified controller that was able to bring the rotor back from contacting to non-contacting state was developed.

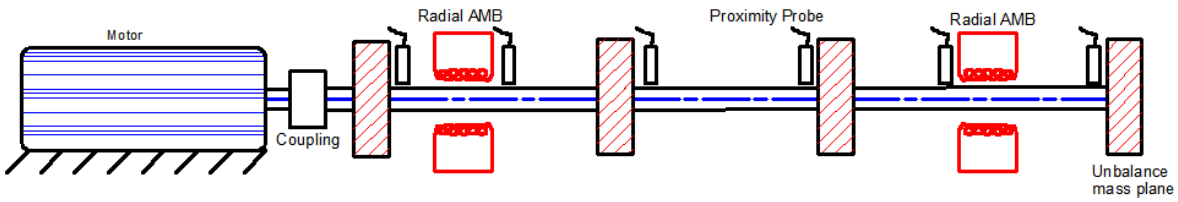

Figure 1-23 Test rig schematic: Keogh et al. (2002)

Lei and Palazzolo (2008) formulated a large-order, flexible shaft model for a flywheel supported with AMBs. The flywheel system supported by magnetic bearings has demonstrated the properties of robustness to standard sensor run out patterns, mass imbalances and inertial load impact. Keogh and Cole (2004, 2006) demonstrated the use of AMB in a flexible rotor test rig (Figure 1-23) by applying circular forces of a pre-set frequency at low running speeds to generate nonlinear orbits. The rotor was run at low speeds so as to be able to shut the system down to avoid impending failure. The orbits induced by AMBs showed good correlation with those generated by large unbalance and misalignment.

Marx and Nataraj (2007) presented a nonlinear model for the magnetic bearings to suppress the motion of AMB supported rotor systems that are exposed to the harmonic base excitation. The control method combined the PD feedback with feed-forward optimal control, where a known base motion was used to select a set of predetermined frequencies and their amplitudes for a control signal. Correction currents were computed based on sub and super harmonic responses of nonlinear systems.

Kasarda et al. (2005) experimentally investigated reduction of sub synchronous vibrations in a 3-mass test rig supported in fluid-film bushings by adding a single AMB, which functioned as a damper (Figure 1-24). It was found that increased tolerance to instability mechanism can be achieved by adding more damping in strategic locations on a rotor. Electromagnets were used to apply destabilizing sine wave perturbation signal to the rotor at or near the first rotor critical frequency.

Matras et al. (2006) tested an adaptive disturbance rejection control to suppress persistent excitations of known frequencies, such as mass unbalance and blade pass effects for large-scale space structures, whose amplitudes can vary over time (Figure 1-25).

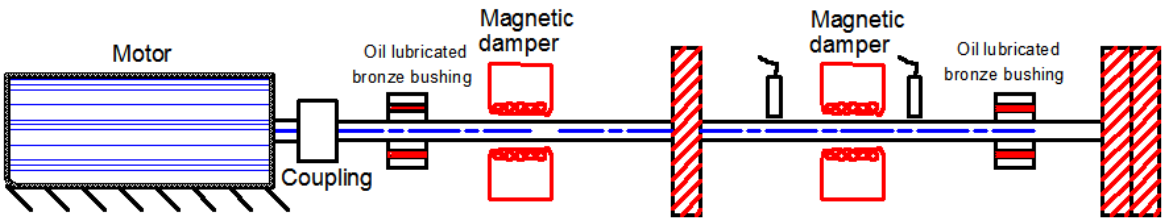

Figure 1-24 Test rig schematic: Kasarda et al. (2005)

Amer et al. (2006) and Eissa et al. (2008) investigated non-linear response of a rigid-disc rotor without gyroscopic effect subject to multi-excitation forces and suspended by AMBs. The method of multiple scales was applied to determine the parametric resonance condition and to study the system stability. The system was found to have a variety of phenomena, such as multi-valued solutions, jump and sensitivity to initial conditions.

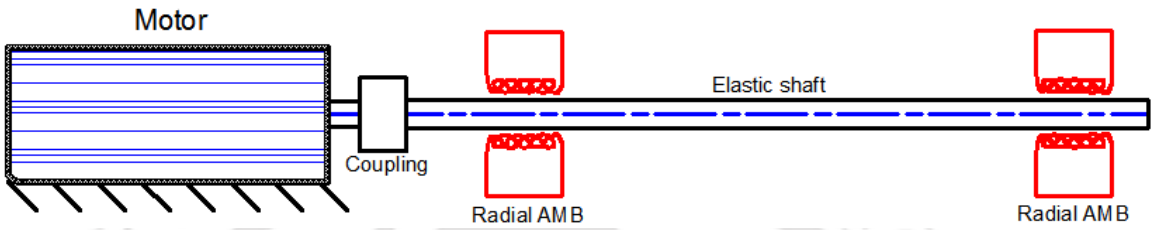

Figure 1-25 Test rig schematic: Matras et al. (2006)

Anegawa et al. (2008) experimentally investigated blade-shaft coupled resonance vibration using an AMB exciter. DeSmidt et al. (2004, 2008) developed an adaptive hybrid proportional –derivative multi-harmonic adaptive vibration control (PD-MHAVC) vibration control law for an AMB controlled driveline system to suppress multi-harmonic vibrations induced by the imbalance, misalignment and load-torque effects at multiple operating speeds. Das et al. (2008, 2009) observed that by incorporating the stiffness and damping effects, electromagnetic exciters help to reduce unbalance response amplitude and simultaneously raise stability limit speed of the rotor-shaft system. It was also found that there exist specific locations of the exciters along the shaft length that provide substantial reduction of response and increment of stability limit speed with relatively low value of control current. Greater number of turns of exciter coils, in particular, and higher pole-face area, in general, were found that provide higher stiffness and damping coefficient of the exciters and are beneficial to the reduction of response as well as the control current.

Hussain (2007, 2009, and 2010) numerically investigated the dynamics of a statically misaligned flexible rotor supported by AMBs. Nonlinearity arising from the magnetic actuator forces that are non-linear functions of coil current, air gap between rotor and stator, and geometrical coupling of magnetic actuators is incorporated into the mathematical model of rotor-bearing system. A variety of nonlinear phenomena were observed in the response. The occurrence of these phenomena, which included sub-

synchronous responses of period -2, -3, -4, -6, -8, -12, -14 and -16, quasi-periodicity and chaos, was found to be largely dependent on the magnitude of the geometric coupling parameter. For the geometric coupling parameter equal to zero, the response of the rotor was found to be synchronous irrespective of the magnitude of the static misalignment of rotor. For moderate values, non-synchronous response of rotor was observed for nonzero values of misalignment. For large values, non-synchronous vibration was found in the response of the rotor irrespective of misalignment amplitudes. The existence of multiple attractors was also observed within certain ranges of the speed. Sahinkaya et al. (2011) developed an adaptive multi-objective method to simultaneously address the conflicting requirements of control of rotor vibration and control of forces transmitted to the base in rotating machines using AMBs. An adaptive controller to achieve multi-objective optimization along with two-stage weighting structure was utilized.

Jiang and Zhu (2011) addressed the problem of vibration suppression in rotor-AMB system subjected to the multi-frequency periodic vibration with an adaptive FIR filter in time domain. Fast Block Least Mean Square (FBLMS) algorithm was adopted since the computational complexity would be invariable regardless of the number of frequency components in vibration disturbance resulting in lesser computational cost than that of the conventional FIR filter. Bouaziz et al. (2011) numerically investigated the dynamic response of a misaligned rotor, mounted on two identical AMBs. Angular misalignment was characterized by the presence of two dominant peaks: the first corresponded to 2X and the second to 4X. The magnitudes of the peaks were found to vary linearly with number of magnets. While the first harmonic was predominant, decrease of air gap strongly affected second harmonic. Moreover, it was found that increase in the number of magnets attenuates vibration due to misalignment defect.

Table 1-1 A chronological summary of papers on the control of vibration and instability

Authors (year)	Bearings	Type	Poles	RPM	Control	Sensors	Objective	Nature of work
Nikolajsen et al. (1979)	1 AMBR, 4 JB	-	-	6000	-	PP, TC,PDS	SVS	Exp.
Allaire et al. (1983)	1 AMBR, 2 BB	-	-	-	PD	-	SVS	Num.
Nonami (1988)	2 AMBR	HEMB	4	6000	-	PP	SVS	Exp.
Nonami et al. (1989)	2 AMBR, 1 AMBT	-	-	10000	-	PP	SVS	Exp.
Burrows et al. (1988, 1989)	1 AMBR, 2 JB	-	-	3700	-	PP	SVS & system parameters estimation	Num. & Exp.
Kasarda et al. (1990)	1 AMBR	HEMB	4	4000	-	PP	1st mode VS	Exp.
Knospe and Humphris (1992)	-	-	-	42300	FC, AOLC	-	VS	Exp.
Lee and Kim (1992)	1 AMBR, 2 BB	HOMB	4	5000	COFC	PP, Dynamo meter	SS & TR performances	Num & Exp.
Dhar and Barrett (1993)	2 AMBR	-	-	12000	-	-	Bearing parameters	Num.
Keogh et al. (1995)	1 AMB, 2 JB	-	-	3340	H_∞	PP	SS & TR VS	Num. & Exp.
Lang et al. (1996)	2 AMBR	-	-	20000	NAF	-	NSVS	Num.
Knospe et al. (1995)	2 AMBR	-	-	3000	NRC,RC, RCGS	PP	SVS	Exp.
Knospe et al. (1996)	2 AMBR	-	-	5000	AOLC	PP	SVS	Num. & Exp.
Nonami and Ito (1996)	2 AMBR, 1 AMBT	-	-	35000	H_∞,μ-synthesis, PID	PP	Stability and Performance	Num. & Exp.
Lum et al.(1996)	-	HEMB	8	1000	-	-	Adaptive auto centering	Num.
Knospe and Tamer (1997)	2 AMBR	-	-	4750	PID	PP	SVS	Exp.

Table 1-1 cont…

Authors (year)	Bearings	Type	Poles	RPM	Control	Sensors	Objective	Nature of work
Sheu et al. (1997)	1 AMBR, 3 BB	-	-	2000	-	-	VS	Num.
Shiau et al. (1997)	2 AMBR	HEMB	8	1000	H_∞, H_2	-	VS	Num.
Yang et al. (1997)	1 AMBR, 3 BB	-	-	2000	-	-	VS	Num.
Cole et al. (1998)	2 AMBs	-	-	6000	PID	PP	Base motion VS	Num. & Exp.
Cole et al. (1998)	2 AMBs	-	-	6000	PID	PP	Base motion VS	Num. & Exp.
Yu et al.(1998)	1 AMBR, 2 JB	-	-	-	-	PP	SVS	Num. & Exp.
Okada et al. (1999)	2 AMBR	HB	-	5000	PD	-	1st and 2nd mode SVS	Num.
Spakovszky et al.(2000, 2001)	2 JB, AMBR, AMBT	HEMB	16	8580	-	PT,	Stall control in AC	Exp.
Mykhaylyshyn (2001)	1 AMRB, 2 JB	-	8	2400	PID	ACC, PP	SVS	Num. & Exp.
Matsushita et al. (2002)	2 AMBR	-	-	6000	PD	ACC, PP	VS due to seismic waves	Num. & Exp.
Jeon et al, 2002	2 AMBR	-	-	10000	PID, LQG	PP	VS due to step response	Num. & Exp.
Johnson and Kasarda (2002)	2 AMBR, 2 BB	HEMB	8	51000	PID	PP, Microphone	Reduction of gear noise	Exp.
Keogh et al. (2002a, 2002b)	2 AMBR	HEMB	8	1740	PID, THO	PP	VS in mass-loss tests	Num. & Exp.
Sahinkaya et al. (2002)	2 AMBR	-	-	1440	PID	PP	MHVS	Exp.
Johnson et al. (2003)	2 AMBR	HEMB	8	3420	PID	PP	SVS	Num. & Exp.
Ichihara et al. (2003)	2 AMBR, 1 AMBT	HEMB	4	-	PID, LQ	PP	VS	Num. & Exp.
DeSmidt et al. (2004)	3 AMBR	HEMB	8	6000	MHAVC	PP, Torque sensor	MHVS	Num. & Exp.
Habib et al. (2004)	-	-	-	-	PD, FLC	PP	NSVS	Num.
Kasarda et al. (2004)	2 AMBR, 2 JB	HEMB	8	9000	PID	PP	SSVS	Exp.
Keogh and Cole (2004, 2006)	2 AMBR, 2 bushes	-	-	1800	PID	PP	Inducing nonlinear characteri	Exp.

Table 1-1 cont…

Authors (year)	Bearings	Type	Poles	RPM	Control	Sensors	Objective	Nature of work
Nakajima et al. (2005)	2 AMBR, 1AMBT	-	-	3000	PID, LQ	PP	VS	Num. & Exp.
Sanadgol and Maslen (2005)	2 AMBR, 1 AMBT	E-core	12	23000	-	-	SS in CC	Num.
Matras et al. (2006)	2 AMBR	-	-	7200	PD	PP	Adaptive disturbance rejection	Num. & Exp.
Amer et al. (2006)	2 AMBR	-	-		-	-	Parametrically excited rigid rotor	Num.
DeSmidt (2007)	-	-	-	15000	PD	-	Damage Idn. of bladed-disks	Num.
Marx and Nataraj (2007)	-	HEMB	8	30000	PDFB, OFF	-	Base excitation suppression	Num.
Anegawa et al. (2008)	1 AMBR, 1 BB	-	-	1800	-	DP, SG, SR	Blade-shaft coupled resonance	Exp.
Arredondo et al. (2008)	2 AMBR	HEMB	8	22000	2 SISO	PP, HS, LV	Stable levitation and control	Num. & Exp.
Hongwei et al. (2007)	2 AMBR	-	-	15000	-	-	Field DB	Num.
Das et al. (2008)	1 AMBR, 2 REB	HEMB	8	30000	PD	-	VS & IC	Num.
DeSmidt et al. (2008)	3 AMBRs	HEMB	8	4815	PD	PP	MHVS & IC	Num. & Exp.
Lei and Palazzolo (2008)	-	-		20000	-	-	Formulation of large order flexible rotors	Num.
Soulas and Kuzdzal (2009)	1 AMBR, 2 TPB	-	-	3600	OLC	PP	rotor dynamic response	Num. & Exp.
Tammi (2009)	1 AMBR, 2 JB	-	-	12000	PD with LPF	PP	VS	Num. & Exp.
Das et al. (2009)	1 AMB, 2 REB	HEMB	8	15000	PD	-	VS	Num.
Fan and Pan (2009, 2010a , 2010b	1 AMBR, 1 JB	HEMB	8	10500	PD	PP	Fluid-induced IC	Num. & Exp.
Das et al. (2011)	1 AMBR	HEMB	8	900	PD	-	CVC	Num.
Ding et al. (2010)	2 AMBR	HEMB	8	3000	PD, FLC, FPD & H∞	PP	Performance of controllers	Exp.

Table 1-1 cont…

Authors (year)	Bearings	Type	Poles	RPM	Control	Sensors	Objective	Nature of work
Hussain(2007, 2009, 2010)	2 AMBR	-	8	-	-	-	Dynamics of misaligned rotor	Num.
Mushi et al. (2010, 2012)	4 AMBR	HEMB	16	14200	μ-synthesis	PP, CT	Simulate aerodynamic loads	Num. & Exp.
Mystkowski (2010)	2 AMBR	HEMB	8	21000	PID, μ-synthesis	PP	VS	Exp.
Shafei and Dimitri (2010)	1 AMB, 2 JB	-	-	10000	-	-	Control of JB instability	Num.
De Moraes and Nicoletti (2010)	EMA in TPB, 1 BB	-	4	1200	PD	PP	VS	Exp.
Yoon et al. (2010, 2013)	2 AMBR, 1AMBT	-	-	23000	-	PT, TC	SS in CC	Exp.
Basaran et al. (2011)	2 AMBR, 1 AMBT	HEMB	8	11000	H_∞	PP	Passing 1st critical speed	Exp.
Bouaziz et al. (2011)	2 AMBR	HEMB	8, 12, 16	8000	-	-	VS due to misalignment	Num.
Jiang and Zhu (2011)	2 AMBR, 1 PMA	-	-	18000	FBLMS	PP	MHVS	Exp.
Sahinkaya et al. (2011)	2 AMBR	-	-	2400	PID, ROLAC, MO-ROLAC	PP	VS	Num.
Yang (2011)	2 PMB, 1 EMA	HEMB	4	1800	PID	Laser meter, HS	VS	
Kozanecka et al. (2011)	1 AMBR	HOMB, HEMB	4	5000	-	PP	VS of helicopter tail rotor TTS	Num. & Exp.
Arredondo and Jugo (2012)	2 AMBR	-	-	2100	PID, H∞, 2-dof	PP, HS	VS of spindle	Num. & Exp.
Cole et al. (2012)	2 BB, 1 AMBR	HEMB	-	6000	PD, FFB	PP, NCPES	Prevention of jump	Num. & Exp.
Funakoshi et al. (2012)	2 AMBR	HEMB	4	-	LQ, LJFC	-	Levitation and VS	Num. & Exp.
Hui et al. (2013)	2 AMBR, 1 AMBT	-	-	12000	PID, AILC	PP, CT	Vib. Disp. compensation	Num.
Bouaziz et al.	2 AMBR	HEMB	8, 12, 16	8000	PID	PP	Effect of misalignment	Num.
Riemann et al. (2013)	1 EMA, 2 JB	HB	4	3600	PID, μ-synthesis	PP, HS	Elimination of oil whip	Num. & Exp.

Table 1-1 cont…

Authors (year)	Bearings	Type	Poles	RPM	Control	Sensors	Objective	Nature of work
Stimac et al. (2013)	2 AMBR	HEMB	8	6000	PID	PP	SVS	Num. & Exp.
Zhong and Zhu (2013)	2 AMBR	HEMB	8	-	2-dof PID	PP	SS & TR VS	Num. & Exp.
Brusa (2014)	2 AMBR, 1 AMBT	-	-	10000	PID	PP	Contra-rotating damping	Num. & Exp.
Defoy et al. (2014)	2 AMBR	-	-	10000	PID, SISO	PP	Performance of controllers	Exp.
Koroishi et al. (2014)	1 EMA, 1 REB	HB	4	1850	LQR, FLC	PP, CT	SS & TR VS	Num. & Exp.
Viveros and Nicoletti (2014)	EMA in TPB, 1 BB	HB	4	1100	PD	PP, TS,	VS	Num. & Exp.
Wang et al. (2014)	2 AMBR, 1 AMBT	-	-	42000	SNF	PP	FRB with VTW	Num.
Bouaziz et al. (2015a, 2015b)	2 AMBR, 1 axial bearing	HEMB	8	20000	PD	PP, CT	AMB defects	Num.
Fang et al. (2015)	2 AMBR, 1 AMBT	-	-	12000	FF	PP	VS	Num. & Exp.
Huang et al. (2015)	2 AMBR	HEMB	4	8000	-	PP	Chatter suppression	Num.
Pesch and Sawicki (2015)	1 AMB, 1 JB	HEMB	4	4000	PD, μ-synthesis	PP	Stabilizing oil whip & oil whirl	Exp.
Tang et al. (2015)	2 AMBR, 1 AMBT	-	-	30000	PID with PLC, LQG	PP, CT	SVS	Num. & Exp.
Zhao et al. (2015)	4 AMBR	HEMB	16	14200	PID	-	Stability of a flexible rotor	Num.
Zhong and Palazzolo (2015)	1 AMBR	HOMB	8	3600, 7200, 9000	PD	PP	VS	Num.
Zheng et al. (2015)	2 AMBR, 1AMBT	HEMB	8	10000	PD + PSNF	PP, CT, HS	Active balancing	Exp.
Enemark and Santos (2016)	2 PAMB, 1 HMBT	Cylinder magnets	20	1080	FF with ANF	HS,ACC, PP	SVS	Num. & Exp.
Roy et al. (2016)	2 AMBR	HEMB	8	4000	PD, PD-hfbl	PP, HS	SVS	Num.
Lyu et al. (2016)	4 AMBR	HEMB	16	7600	μ-synthesis	PP	Emulate GE of flywheel	Exp.

Table 1-1 cont…

Authors (year)	Bearings	Type	Poles	RPM	Control	Sensors	Objective	Nature of work
Zheng and Feng. (2016)	2 AMBR,	HB	-	30000	PID	CT, ACC,	VS in CC	Num. & Exp.
Dimitri et al. (2016)	1 AMBR, 1 JB	Integrated	8	6000	FLC	PP	Elimination of oil whip	Num. & Exp.
Lusty et al. (2014, 2016)	1 AMB, 2 REB	HOMB	8	60000	PID	PP, Load cell	SVS	Num. & Exp.
Kumar et al. (2016)	1 AMB, 2 REB		12	-	-	-	-	Num.
Ranjan and Tiwari (2020)	1 AMB, 2 REB	HEMB	8	6680	PID	PP	Active balancing	Num. & Exp.

Abbreviations AC: Axial compressor; ACC: Accelerometer; AOLC: Adaptive open loop control; AILC: Adaptive iterative learning control; AMBR: Radial active magnetic bearing; AMBT: Thrust active magnetic bearing; ANF: Adaptive notch filter; BB: Ball bearing; BTS: Blade tip sensor; COFC: Constrained output feedback control; CT: Current sensor; CVC: Coupled vibration control; Disp. : Displacement; EMA: Electromagnetic actuator; Exp.: Experimental; FC: Feedback control; FF: Feed forward: FFB: Force feedback; FBLMS: Fast block least mean square algorithm; FLC: Fuzzy logic controller; FPD: Fuzzy PD; FRB: Flexible rotor balancing; GE: Gyroscopic effect HB: Hybrid bearing; HMB: Hybrid magnetic bearing; HS: Hall sensor; IC: Instability control; Idn. : Identification; JB: Journal bearing; LJFC: Local jerk feedback control; LPF: Low-pass filter; LQG: Linear-quadratic-Gaussian; MHAVC: Multi harmonic adaptive vibration control; LQR: Linear quadratic regulator; LV: Laser vibrometer; MHVS: Multiharmonic vibration control; MO-ROLAC: Multi objective recursive open loop adaptive control; NCPES: Noncontact photoelectric sensor; Num.: Numerical; NAF: Non-adaptive feedback; NRC: Non-recursive control; NSVS: Non synchronous vibration suppression; OFF: Optimal feed forward; OLC: Open-loop control; PAMB: passive magnetic bearing; PMB: Permanent magnetic bearing; PD: Proportional–derivative; PDFB: PD feedback; PDS: Photo diode sensor PID: Proportional-integral-derivative; $PD_{hfbl,}$: Proportional and high-frequency band-limited derivative; PLC: Phase lead compensator; PP: Proximity probe; PSNF: Phase shift notch filter; PT: Pressure transducer; RC: Recursive control; RCGS: Non-recursive control with gain scheduling; REB: Rolling element bearing; ROLAC: Recursive open loop adaptive control; SS: Steady state; SNF: Synchronous notch filter; SG: Strain gauge; SVS: Synchronous vibration suppression; SS: Surge suppression; SSVA: Sub synchronous vibration suppression SR: Slip ring; TC: Thermocouple; THO: Transient

harmonic oscillator; TPB: Tilting pad bearing; TR: Transient; TS: Temperature sensor; TTS: Torque transmission shaft; Vib: Vibration; VS: Vibration suppression; VTW: Virtual trial weights

Bouaziz et al. (2013) extended their earlier work to investigate dynamic behaviour of a coupled rotor bearing system with ball and socket flexible coupling in transient regime. It was reported that lateral and torsional natural frequencies were excited due to the presence of pure angular misalignment, which further caused the driven rotor centre to have orbits with two inner loops. Moraes and Nicoletti (2010), and Viveros and Nicoletti (2014) designed tilting-pad bearing with inbuilt 4-pole AMB actuator to derive the twin advantage of higher load-carrying capacity of tilting-pad bearing and actuation capacity of AMB (Figure 1-26). The hybrid bearing was deployed on the horizontal and vertical test rig configurations in conjunction with conventional ball bearings. A reduction in shaft-vibration amplitude at operating speed was achieved in both the cases.

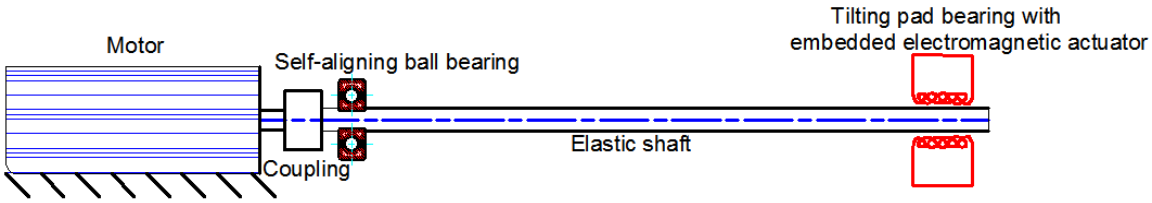

Figure 1-26 Test rig schematic: Viveros and Nicoletti et al. (2014)

Yang (2011) developed a compact electromagnetic actuator that can produce axial as well as radial forces on the rotor. Rotor levitation control is achieved by actuator axial force, while resonance-related oscillation suppression is realized by the radial force. Fang et al. (2015) devised an active vibration control method to simultaneously control the displacement, force and torque. Jun et al. (2016) mimicked rotordynamic characteristics of energy storage fly-wheels on a rotor AMB test rig. Two exciter AMBs were placed at mid and quarter spans of the shaft to generate forces that emulate stiffness and gyroscopic effects of flywheel systems. Emulated gyroscopic forces generated by exciter AMBs were similar to actual gyroscopic forces predicted by finite element analysis. Kumar et al. (2016) proposed a 12-pole radial AMB in which switching variation of AMB pole control currents generates a synchronous force rotating in the direction opposite to rotor unbalance. The change in direction of rotating force was achieved by the changing the phase of AC supply. Prabhat and Tiwari (2020) developed identification algorithm to estimate unbalance and misalignment between rotor and AMBs in levitated rigid rotor

systems. AMBs were used to lift the rotor system and to introduce *trial misalignments* as well.

AMBs have been used for control of vibrations due to the sub-synchronous, super-synchronous, seismic and multi-frequency harmonic excitations. They have been used to reduce the force transmitted to/from the base and active control of acoustic gear noise. Some authors have reported multi-objective optimization of simultaneous reduction of transmitted force and rotor vibrations. They have been used as simulators that mimicked the rotordynamic characteristics of flywheels. The dynamics and vibration suppression of rotors with driveline static misalignment have been studied. Circular forces at pre-set frequencies have been applied with AMBs to generate orbits that are representative of faults like unbalance and misalignment. The effect of the geometrical parameters of AMBs like the number of turns, pole face area, and number of poles on vibration suppression has been studied. A few authors have designed and developed hybrid AMBs that have higher load carrying capacity than traditional AMBs.

1.13 AMB for Stability Improvement

Nikolajsen et al. (1979) used an electromagnetic damper for the vibration control of supercritical transmission shaft with overhung turbine disc, which was supported on 4 journal bearings and a mid-span electromagnetic damper (Figure 1-27).

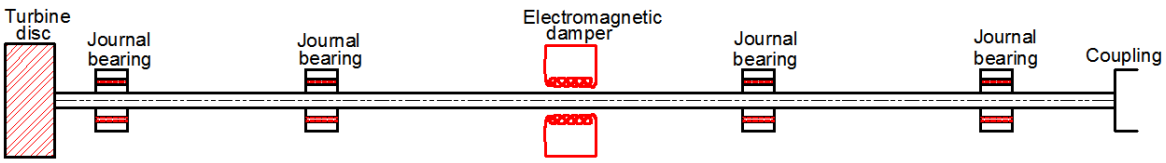

Figure 1-27 Test rig schematic: Nikolajsen et al. (1979)

Apart from controlling bending critical speed vibrations, the damper was found to suppress system instability associated with fluid-film bearings and second order vibrations associated with shaft stiffness asymmetry. The system response was numerically predicted by linearization of electromagnetic damping forces.

Lee and Kim (1992) performed output feedback control experiment when the rotor system is subject to external impulsive disturbance and imbalance to evaluate the transient and steady state performances of the controller. The flexible shaft assembled with four rigid discs is supported by two self-aligning type of radial ball bearings. The system is

driven by a 2 HP DC-servo motor through a flat belt and a flexible coupling in order to isolate the vibration originated from the motor (Figure 1-28). Before the controller was activated the computer-generated impulse disturbance was fed into the magnetic bearing. It was found to enable the rotor with initial residual system unbalance to run through first critical speed without excessive vibration while preserving stability against spill over effects.

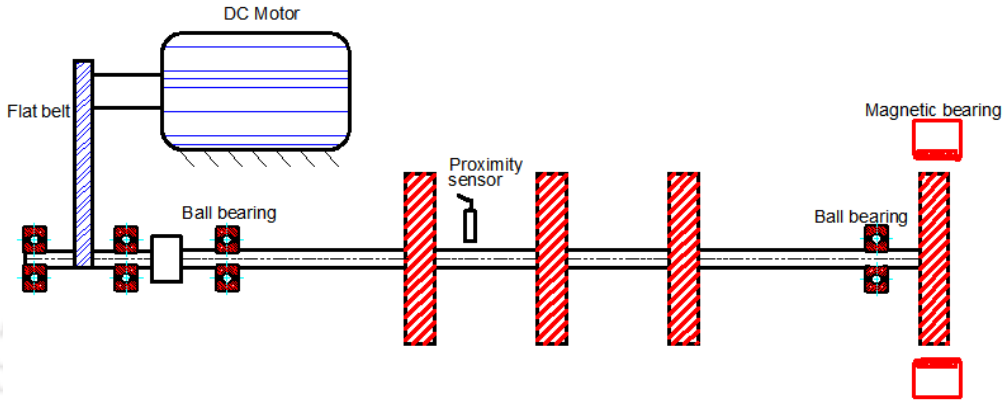

Figure 1-28 Test rig schematic: Lee and Kim (1992)

Dhar and Barrett (1993) developed a method for calculating the control forces, and bearing stiffness and damping coefficients in a multi-mass flexible rotor system mounted on magnetic bearings subjected to unbalance or harmonic excitation forces. Optimum control forces at magnetic bearing locations are evaluated based on minimization of modal response in a least-square sense, instead of minimization of physical responses at selected measurement locations. A significant reduction in rotor vibration amplitude was obtained at resonant frequencies by changing modal coordinates, thereby altering distribution of modal participations in response.

Fan and Pan (2009, 2010, and 2011) presented a method to raise instability threshold of a rotating machine supported on journal bearings by increasing the stiffness using an 8-pole AMB that functioned as electromagnetic exciter. The rotor was supported on an inboard oilite bronze bushing. Adjustable radial supporting springs were connected to rotor through a rolling element bearing in order to set the journal at any radial position inside outboard cylindrical fluid-lubricated bearing clearance (Figure 1-29). The sub-synchronous vibration components characteristic of oil-whirl and oil-whip instabilities

present in full spectrum, spectrum and orbit plots have been eliminated with an auxiliary electromagnetic actuator.

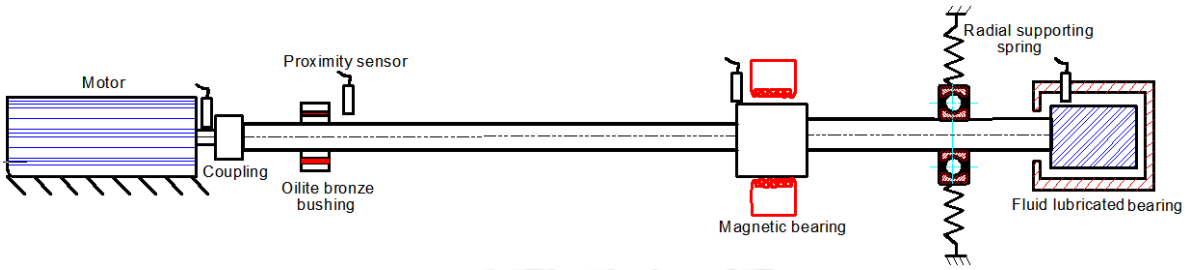

Figure 1-29 Test rig schematic: Fan and Pan (2009, 2010, and 2011)

Soulas and Kuzdzal (2009) used a magnetic bearing exciter (MBE) to determine logarithmic decrement of first forward whirling mode of large centrifugal compressor rotor system. The MBE driven by an open-loop control system was used to inject asynchronous forcing functions into the rotor supported by two tilt-pad oil-film journal bearings at various aerodynamic conditions, i.e. gas densities and power levels.

El-Shafei and Dimitri (2010) collocated a journal bearing with an AMB to control journal bearing instability and increase its range of operation. Journal bearings performed the function of load carrying machine element, while a smaller AMB was used as a controller machine element. Yoon et al. (2010, 2013) employed AMBs as servo actuators to suppress surge instability in a single-stage overhung centrifugal compressor. In an uncontrolled compressor, operating at the maximum pressure point is not possible due to its proximity to surge region and a small flow fluctuation would drive the system to instability region. It was found the right combination of controller and flow estimator method allows compressor to operate deep into former surge region. This allowed compressor to operate at the highest efficiency point on the characteristic map, while still retaining a very conservative surge margin.

Das et al. (2011) studied the influence of Electro Magnetic Actuator (EMA) to control coupled rotor vibrations due to combined bending and torsion of rotor-shaft supported on flexible bearings at both ends. The coupling behaviour of vibrations enabled simultaneous control of torsional and transverse vibrations by applying control force in transverse direction alone with a four-pole AMB. It was also found to increase stability limit speed. Mushi et al. (2010, 2012) designed a test rig to investigate rotordynamic instability arising from aerodynamic loads in the AMB supported turbo machinery. Two

exciter AMBs and two support AMBs in conjunction with a rotor were used in the study of rotordynamic instability of industrial machinery (Figure 1-30). The mid-span AMB was used to excite seal instability characteristic, while quarter-span AMB produced oil seal excitations.

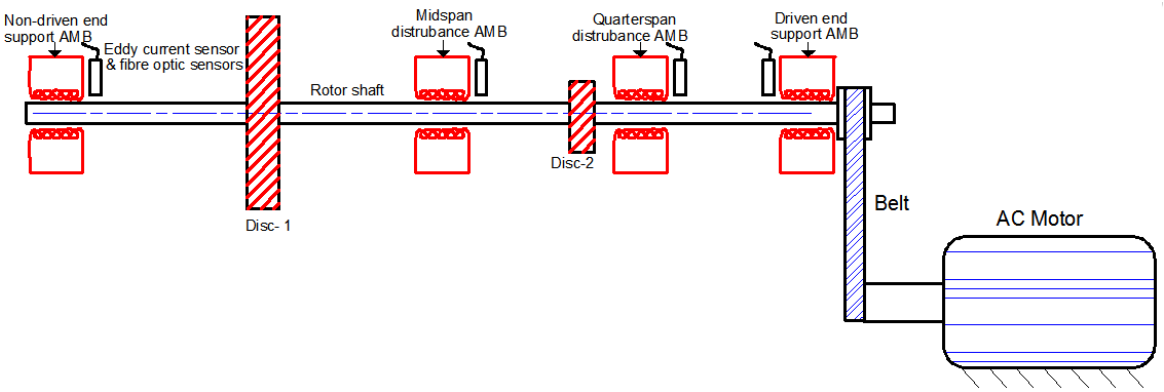

Figure 1-30 Test rig schematic: Mushi et al. (2010)

Cole et al. (2012) have performed experiments to successfully eliminate amplitude jump that arises from nonlinear rotor-stator contact in a small radial clearance with a single radial AMB. An active magnetic bearing (AMB) and a nonlinear stator interaction mechanism are positioned equidistantly along the shaft. The stator mechanism consists of a mass supported by four thin horizontal rods, the length of which can be varied in order to change stiffness (Figure 1-31). Arredondo and Jugo (2012) achieved precise positioning of a spindle levitated by AMBs with a 2-DOF controller. A controller achieved counteraction of vibrations generated by rotation by using 3 blocks, i.e. stabilization block, vibration minimization block and dynamics decoupler block.

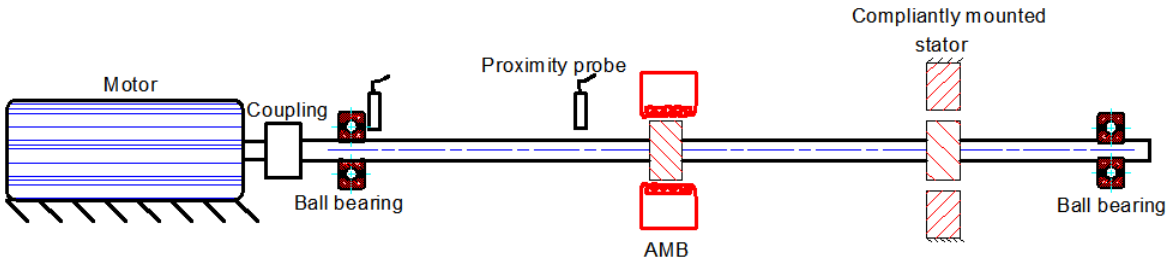

Figure 1-31 Test rig schematic: Cole et al. (2012)

Riemann et al. (2013) used μ-synthesis control technique to attenuate oil-whip instability effect of flexible hydro-dynamically supported rotors using electromagnetic actuators. The rotor, with lumped mass placed in the middle, is supported by two

hydrodynamic journal bearings, and a magnetic actuator is placed along the shaft (Figure 1-32). Two proximity sensors were used to obtain rotor orbits.

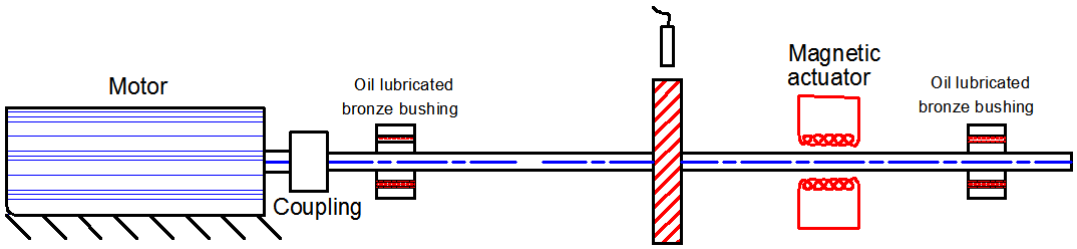

Figure 1-32 Test rig schematic: Riemann et al. (2013)

The controlled vibration levels with μ-synthesis are compared to the PID controller in vertical and horizontal directions. To facilitate implementation in industries two SISO controllers were used instead of a MIMO controller.

Brusa (2014) proposed an approach for dynamic stabilization of high-speed rotor by introducing damping action, whose direction of rotation is opposite to rotor angular speed, which seems contra-rotating in the fixed reference frame of rotor shaft. This method was meant to substitute the non-rotating damping provided by stator. The general arrangement of the rotor-bearing system is similar to the one shown in Figure 1-11 with a slight modification that thrust AMB is located inboard of the right AMB. In addition to the benefit derived from the absence of a fixed stator, it was also found that amount of damping required for a given stable operation of rotor is lower.

Huang et al. (2015) developed a controller to actively suppress chatter instability for higher achievable metal removal rate in milling process. An optimal controller with proper compensation for speed variation that eliminates vibration of an unloaded spindle rotor during acceleration/ deceleration was enhanced with an adaptive algorithm based on Fourier series analysis. Pesch and Sawicki (2015) stabilized oil-whip and the oil-whirl in a hydrodynamic bearing with an AMB. The rotor was supported by a hydrodynamic bearing on one side and a bushing on other side. Two discs are mounted near the bearing midspan and AMB is situated near the hydrodynamic bearing. The rotor is connected to an electric motor via a flexible coupling (Figure 1-33). The μ-synthesis controller was designed for the plant model, which included a hydrodynamic bearing model that allowed for application of parametric uncertainties. The method was demonstrated on a

hydrodynamic bearing test rig modified with an AMB by running the rotor above twice the first natural frequency.

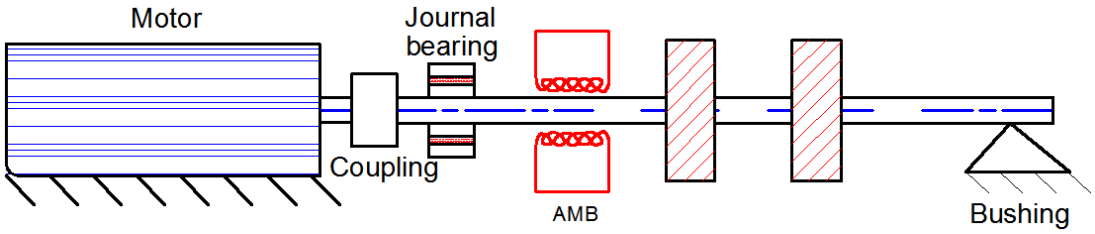

Figure 1-33 Test rig schematic: Pesch and Sawicki (2015)

Dimitri et al. (2016) designed and manufactured a prototype of an integrated journal bearing and AMB actuator. The integrated device, in conjunction with a fuzzy logic controller, was used to control sub-synchronous oil whip in a rotor test rig. The rotor designed to simulate industrial rotor behaviour was simply supported on two bearings: the designed integrated bearing at the drive end and a roller bearing at other end. Four disks are placed on the shaft which is driven by a 3 HP motor through a flexible coupling (Figure 1-34).

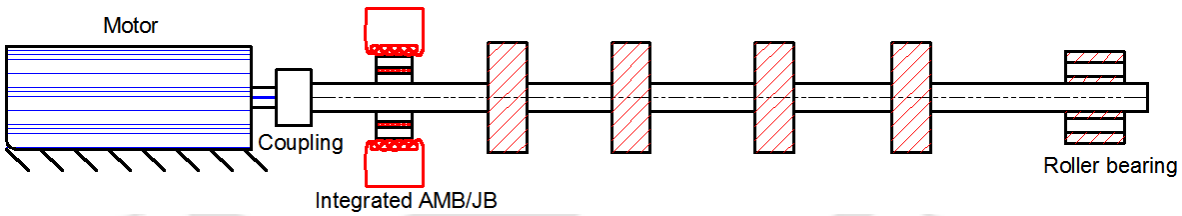

Figure 1-34 Test rig schematic: Dimitri et al. (2016)

AMBs have been used in rotors supported on hydrodynamic bearings to prevent instability problems otherwise encountered in such rotor systems. As electromagnetic exciters they inject additional stiffness and damping into the rotor- system thus resulting in increase of instability threshold, elimination of oil-whip and oil-whirl from operating range. They have been used as servo-actuators to stabilize rotating stall in axial compressors, suppress surge instability in centrifugal compressors. Conventional stators (non-rotating structure supporting the rotor) that introduces damping into system have been substituted by AMBs. They have been used to suppress chatter instability in milling spindles, simulate rotordynamic instability arising from aerodynamic loads due to presence of seals.

1.14 Control Algorithms-AMB Performance

To a control system designer, flexible systems pose a greater challenge than rigid rotors because of their wider mechanical bandwidth compared to rigid rotors. This means that mechanical response to high frequency forcing is much larger for a flexible rotor than it is for a rigid rotor. As a result, dynamic behaviour of feedback controller at high frequencies is much more important for flexible rotors than for rigid rotors (Maslen, 2009). Even though control system design is a fundamental design block of every rotor-AMB system, a few papers that have laid focus on comparative study of different controllers and their influence on the dynamic behaviour of rotor have been presented in this section.

Knospe and Humphris (1992) proposed two algorithms namely: feedback and adaptive open loop controls for attenuation of transmitted unbalance response of rotors supported on magnetic bearings. Open loop experimental results demonstrated over 20 dB reduction in synchronous vibration at a rotor critical speed. The notch filter technique, which is often referred to as an automatic balancing, was achieved by inserting notch filter in each feedback loop in series with a stabilizing phase lead controller that causes the effective stiffness and damping of bearings to be greatly reduced. This leads to bearings exerting little force upon the rotor and the rotor spins about its inertial axis. Keogh et al. (1995) experimentally implemented a controller to conduct the steady state and mass loss tests. Measurement error, caused by the shaft surface roughness was incorporated into the controller design.

Knospe et al. (1995), and Knospe and Tamer (1997) evaluated and compared performance of three algorithms in mitigating rotor vibration namely (1) non-recursive control law with simultaneous estimation, (2) recursive control law with simultaneous estimation, and (3) recursive control law with gain scheduling. It was found that all three algorithms provided synchronous vibration attenuation in steady state operation, however, differed greatly during transient tests and near critical speeds. Lum et al. (1996) implemented adaptive auto-centering that compensates for transmitted force due to imbalance in an AMB system. On-line identification of physical characteristics of rotor imbalance is performed and these identification results were used to tune a stabilizing controller. Adaptive auto-centering control unlike the adaptive feed-forward compensation is frequency independent and works under varying rotor speeds.

Shiau et al. (1997) achieved vibration control of a flexible rotor system with magnetic bearings using the hybrid method and H_∞ control theory. To reduce order of the system, a hybrid method that combines finite element method and generalized polynomial expansion method, was employed to model flexible rotor system. This method was found to suppress spill over effect and to be robust to parameter variation of a rotor system with magnetic bearings. Yang et al. (1997) developed a controller by combining experimental design in quality engineering and active damping control technique for vibration suppression of rotor systems. By using locations of sensor/actuator and feedback gains as design parameters, the controller design was shown to achieve a near optimal performance within two-sigma confidence limits among all possible parameter combinations.

Cole et al. (1998) integrated a high-order state-space controller (up to 50 states) in parallel with PID controller to be used for levitation. Experiments conducted on rig shown in Figure 1-23 showed that proposed controller can simultaneously cope with vibration resulting from direct rotor forcing as well as base motion that arises in transport and seismic events. The controller was found to be superior to PID controller in preventing contact between rotor and retainer bushes. Yu et al. (1998) developed a control algorithm using least-squares method for in situ tuning of electromagnetic actuator to reduce synchronous vibration of a rotor supported on oil-film bearings. To control vibration of a multimode rotor at operational speed, *D*-optimal statistical approach was used to determine the best location of actuator force. Ichihara et al. (2003) developed a controller that combined PID for rigid modes, with linear quadratic (LQ) control for flexible modes. This technique was used on a flexible rotor to pass through critical speeds and achieve high-speed rotation.

Habib et al. (2004) employed fuzzy logic control strategy for suppressing the non-synchronous response of a rigid rotor in AMB. It was shown numerically that non-synchronous behaviour in rotor response, such as period-doubling bifurcations, quasi-periodic and chaotic motions at certain range of operating parameters were successfully suppressed with the controller.

Sanadgol and Maslen (2005) applied back stepping method to design a controller capable of actively suppressing oscillations induced by compressor surge. A magnetic thrust bearing was used as a servo actuator to modulate tip clearance of unshrouded

centrifugal compressor thereby affecting compressor characteristic. The mass flow and pressure oscillations associated with compressor surge are very effectively suppressed and system trajectories remained on compressor characteristic map in the presence of disturbances downstream of compressor. Arredondo et al. (2008) presented modelling and control design for a laboratory AMB set-up. Symmetric properties of model allowed separation of translation and conical modes. This decoupled MIMO system into SISO subsystems, after which appropriate controllers for each SISO subsystem were designed to achieve stable levitation.

Tammi (2009) achieved rotor vibration attenuation with a supplementary electromagnetic actuator located outside rotor bearing span. The test rig consisted of a rotor supported by journal bearings and driven by an electrical motor. Rotor vibrations were attenuated with an electromagnetic actuator located outside of bearing span (Figure 1-35). An experimental comparison of active vibration control with an adaptive FIR filter with least-mean-squares algorithm and convergent control (CC) method with frequency domain adaptation algorithm was performed. The performance of the adaptive finite-duration impulse response (FIR) filter was found to be poorer than the performance of CC method in both steady-state and transient conditions.

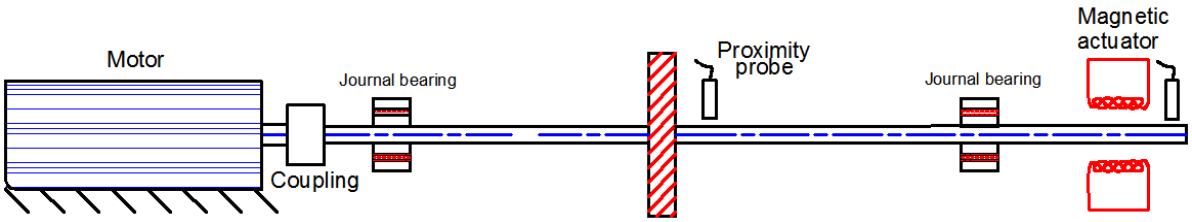

Figure 1-35 Test rig schematic: Tammi (2009)

Ding et al. (2010) experimentally investigated dynamic behaviour of rigid rotor supported on AMBs with four different control laws, viz. PD, Fuzzy PD, Fuzzy logic control and H_∞. Hui et al. (2013) developed a feed-forward compensation controller based the adaptive iterative learning control (ILC) algorithm and PID algorithm to restrain run-out. The simulation and experiments showed that compensation scheme resulted in minimum displacement of rotor system and improved the stability of control system.

Koroishi et al. (2014) studied the effectiveness of attenuating vibration of flexible rotor in steady-state and transient conditions with a hybrid electromagnetic actuator

(EMA). The EMA has 4 electromagnets, two for each control direction (Figure 1-36). Two different approaches for the active modal vibration control: linear quadratic regulator (LQR), fuzzy modal controller were implemented for control of rotor system. LQR controllers showed better results in unbalance response in steady state and transient conditions.

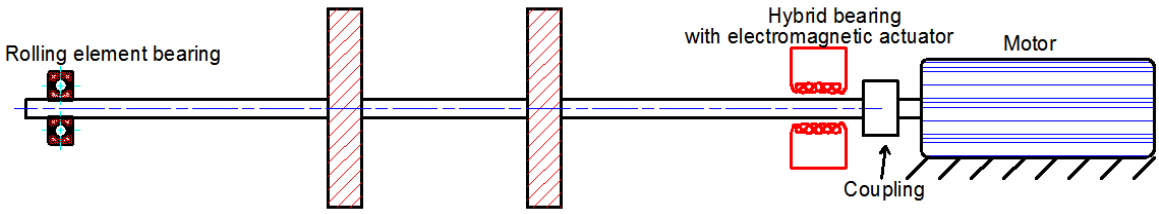

Figure 1-36 Test rig schematic: Koroishi et al. (2014)

Zheng et al. (2015) presented a phase shift notch filter connected with a controller in parallel-mode to overcome performance degradation problems encountered in series mode while rotor is spinning at high speeds and improve stability over entire speed range. The effectiveness of the proposed method was experimentally tested on a high-speed centrifugal blower with magnetic bearing. Zhong and Palazzolo (2015) dealt with multi-optimization of rotor system supported on homopolar AMBs to optimize control law and simultaneously achieve minimum actuator mass, the best steady state vibration performance of rotor, and least actuator power losses using non-dominated sorting genetic algorithm (NSGA). For searching the control law, twelve design variables, eleven constraints were handled with the NSGA-II code using parameter less penalty method with spinning rotor levitation and dynamic stability as constraint conditions.

Various AMB control laws in conjunction with suitable filters have been developed, implemented and compared in pursuit towards better vibration suppression. While for low speed applications, time tested SISO controllers are still in vogue, MIMO control laws have found place in high-speed applications where accuracy and robustness of AMB systems are critical. Despite the complexity associated with their implementation advantages of these controllers cannot be overstated.

1.15 Identification of Cracked Rotors with AMBs

Fatigue cracks have great potential to cause catastrophic failures in rotating machinery, if undetected in time. There have been numerous case studies in industries,

where undetected fatigue cracks have led to catastrophic failures. Cracks may be caused by mechanical stress raisers, such as sharp keyways, abrupt cross sectional changes, metallurgical factors, heavy shrink fits, grooves, and other stress concentration factors that promote crack initiation. Once a crack is initiated it propagates and stress required for propagation is smaller than that required for crack initiation. After many cycles, operating stresses may be sufficient to propagate the crack. Operating rotating machinery with a rotor crack is dangerous since the crack grows with time that may lead to catastrophic accident. It is customary to check the occurrence of a rotor crack in periodical inspections during general system maintenance using ultrasonic testing method or dye testing method. However, these methods have disadvantages such as high cost and difficulty of early detection (Inagaki et al., 1982).

Over the last four decades, dynamics of rotors with various types of cracks have been investigated and it continues to attract interest of researchers as an inter-disciplinary area. Wauer (1990) presented a review on studies and investigations done on cracked rotor including the modelling of cracked part of the structure and finding different detection procedures to diagnose fracture damage. Sabnavis et al. (2004) and Kumar and Rastogi (2009) reviewed detection and diagnosis techniques of cracked rotors. Bachschmid et al. (2010) in their monograph described crack modelling procedures, simulation of dynamical behaviour of cracked shaft and tests for detecting cracks along with procedures in model based crack identification for finding crack position and its depth.

Zhu et al. (2003) studied dynamic characteristics of a cracked rotor supported on AMBs; they concluded that if optimal controller parameters are not considered in designing AMB controller for a cracked rotor an unstable motion in some regions of rotational speed range is possible. It was found that only 2X and 3X revolution super-harmonic components in sub-critical speed region can be used to detect a crack in rotor–AMB system as against the traditional method, where 2X and 3X revolutions super-harmonic frequency components in super-critical speed region are used for detection. Bash (2005) studied use of AMBs as an actuator for health monitoring of rotor supported by conventional support bearings. A variety of known forces, i.e. chirp, Gaussian input were applied to a spinning rotor system to investigate rotordynamic faults, such as shaft rub and shaft crack. The test rig consisted of a shaft supported on ball bearings. An AMB

was placed at approximately midspan with two position probes located nearby for AMB control (Refer Figure 1-37). Four proximity probes were located along the shaft with two at approximately ¼ span and two at ¾ span. A shaft rub was investigated by applying contact from a brass screw at both inboard and outboard locations. A wide notch was made at midspan with progressive depths of 10, 25, and 40 percent of shaft diameter to simulate cracks.

Mani et al. (2006), Quinn et al. (2005) used multiple scales analysis to estimate a combination resonance among critical shaft frequencies, shaft rotational speed, and external frequency of AMB excitation. The rig used is shown in Figure 1-38. It is supported on rolling element bearings, while AMB is used as exciter and not for support. When a cracked rotor is excited by a force at combination resonance, a re-excitation of first natural frequency occurs with increased response amplitude compared to healthy shaft condition. It is shown that response amplitude increases as crack depth increases. Alternatively, when a healthy (non-cracked) rotor is excited by combination resonance, no increase in amplitude of response at first natural frequency occurs. Sawicki et al. (2008), and Sawicki (2009) present similar experimental results on combination frequencies technique.

Storozhev (2009) conducted experiments where in cracked rotor was supported/ levitated using AMBs unlike the earlier work where AMB was used as an exciter and not as a support. Each AMB is an 8-pole radial or conical heteropolar design and is equipped with four variable reluctance type position sensors. The main advantage of conical AMBs over radial AMBs is that conical bearings can provide radial and axial forces/excitations at pre-calculated frequency simultaneously to perturb the suspended spinning rotor. Therefore, there is no need for an extra AMB for axial support of the rotor. A healthy rotor, 25% cracked and 40% cracked rotors with different force injections were tested (Refer Figure 1-38).

Kasarda et al. (2007) experimentally demonstrated the capability of an AMB to be used as an actuator for identification of a shaft crack that might otherwise go undetected in conventional steady-state vibration monitoring approaches (Figure 1-37).

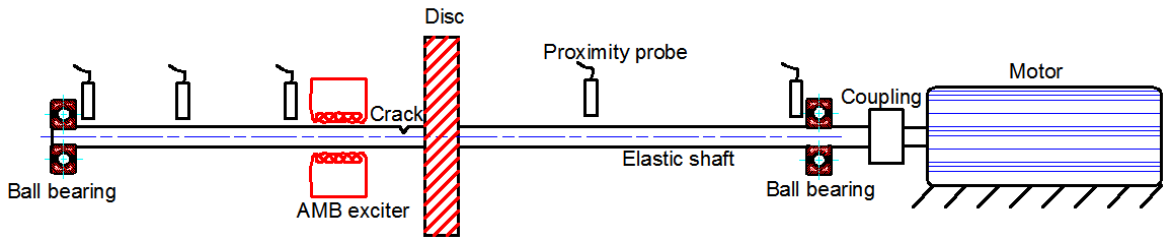

Figure 1-37 Test rig schematic: Kasarda et al. (2007)

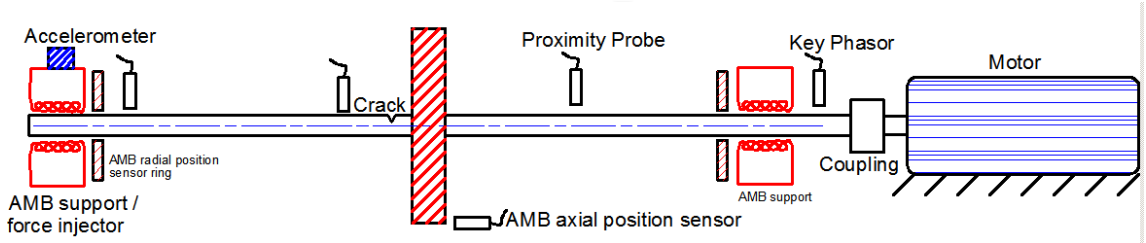

Figure 1-38 Test rig schematic: Sawicki et al. (2008)

A distinct shift in 3rd natural frequency was detected in frequency response function, when rotor was excited by an AMB. However, no changes in 1st or 2nd natural frequencies were detected. Since 3rd natural frequency is much above the rotor operating speed, the fault will be undetected in typical vibration monitoring systems.

Friswell et al. (2010) used recurrence plots of simulated and measured responses of a cracked rotor to determine the state of the machine. The reader can refer to Litak et al. (2009) who previously used these plots to detect faults in cracked rotors. It was found that AMB excitation reduces the periodicity of response of a healthy machine, which is recovered in the presence of a cracked shaft.

Sawicki et al. (2011a, 2011b) proposed harmonic balance method as an alternative to multiple scales analysis to estimate combination frequencies and associated response amplitudes for a cracked rotor system excited by unbalance force and external AMB force. The shaft was levitated on conical AMBs in simply supported arrangement and a radial AMB is used as an actuator/exciter to apply specified, time-dependent forcing on the shaft at mid-span or outboard location. Later the shaft was supported on rolling element bearings and AMB is used as exciter at mid span. The actuators are axially adjustable, i.e., can be placed at almost any axial location. (Figure 1-37).

Morais et al. (2012) numerically studied the control of breathing mechanism of crack, called self-healing, by using a mid-span electro-magnetic actuator. Minimizing the

crack opening was, however, found to increase the rotor vibration level. A multi-criteria optimization, called the particle swarm optimization, was devised to arrive at a current combination that is capable of minimizing the crack opening and, simultaneously, which does not induce either large vibrations or instability.

Table 1-2 A chronological summary of papers on smart condition monitoring in rotors

Authors (Year)	**Bearings**	**Type**	**Poles**	**RPM**	**Control**	**Sensors**	**Objective**	**Nature of work**
Kim and Lee (1999)	2 AMBR, 1 AMBT	-	-	3000	PID	PP, MFT, LC,GS	Idn. of i, K_s and F_{Mag}	Num. & Exp.
Baun and Flack (1999)	3 AMBR, 1 AMBT	-	8	620	PID	PP,	Meas. Of HF in pump	Exp.
Guinzburg and Buse(1995)	2 AMBR, 1 AMBT	HEMB	4	900 - 1780	-	PP	Meas. Of HF in CP	Exp.
Marshall et al. (2001)	1 AMBT	HEMB	8	-	PID	PP	Meas. of F_{Mag}	Num. & Exp.
Raymer and Childs (2001)	2 AMBR	-	-	-	-	FOSG	Meas. of F_{Mag}	Exp.
Zhu et al. (2003)	1 AMBR, 2 RIB	-	8	-	-	-	Cracked shaft CM	Num.
Nordmann and Aenis (2004)	2 AMBR, 1 AMBT	-	-	-	-	PP	CP Fault diagnostics	Exp.
Bash (2005)	1 AMBR, 2 BB	HEMB	8	5100	PID	PP	Study of RD faults	Exp.
Quinn et al. (2005)	1 AMBR, 2 BB	HEMB	8	5100	PID	PP	Cracked shaft CM	Num. & Exp.
Cade et al. (2005)	2 AMBR	-	-	-	PID	PP	Detection of sudden Unb.	Num. & Exp.
Mani et al. (2006)	1 AMBR	-	-	-	-	-	Cracked shaft CM	Num.
Pesch et al. (2008)	2 AMBC, 1 AMBR, 2 BB	HEMB	8	-	PID	PP	Cracked shaft CM	Num. & Exp.
Kozanecka et al. (2007)	2 AMBR, 1 AMBT	HEMB	8	2100	-	PT, PP, CT	Idn. of forces in LS	Exp.

Table 1-2 cont…

Authors (Year)	Bearings	Type	Poles	RPM	Control	Sensors	Objective	Nature of work
Kasarda et al. (2007)	1 AMBR, 2 BB	HEMB	8	2400	PID	PP	Cracked shaft CM	Exp.
Zhou et al. (2007)	1 AMBR, 2 BB	-	-	-	PID	PP	Cracked shaft CM	Num.
Friswell et al. (2010)	1 AMBR, 2 BB	HEMB	8	5100	PID	PP	Idn. of rotor cracks	Num.
Kozanecka et al.(2008)	1 AMBR, 1 REB	-	-	-	-	PP, CT	Idn. of eq. K and C of AMB	Num. & Exp.
Zutavern and Childs (2005,2008)	2 AMBR	-	-	-	-	FOSG	Idn. of an gas seal parameters	Exp.
Sawicki et al. (2008, 2011a, 2011b)	2 AMBC	HEMB	8	1560	PID	PP	Cracked shaft CM	Num. & Exp.
Storozhev (2009)	2 AMBC	HEMB	8	1560	PID	PP	Cracked shaft CM	Num. & Exp.
Morais et al. (2012)	1 EMA, 2 BB, 1 RB	HOMB	4	1500	-	PP	Control of breathing mechanism	Num.
Tiwari and Chougale (2014)	2 AMBR	HEMB	8	5000	PID	PP, CT	Estimation of K_s, K_i, U	Num. & Exp.
Tiwari and Viswanadh (2015)	2 AMBR	HEMB	8		PID	PP, CT	Estimation of K_s, K_i, U	Num. & Exp.
Chasalevris et al. (2011, 2014)	1 AMBR, 2 JB	HEMB	8	1850	-	-	Wear detection in JB	Exp.
Chasalevris and Papadopoulos (2015)	1 AMBR, 2 JB	-	-	950	-	-	Early crack detection	Exp.
Jiang et al.(2015)	2 AMBR, 1 AMBT	-	-	-	PID	PP	Estimation of K and C of AMB	Num. & Exp.
Singh and Tiwari (2015, 2016)	1 AMBR	HEMB	8	4300	PID	PP	Idn. of BC parameters	Num.
Xu et al. (2016)	2 AMBR, 2 AMBT	HEMB	8	1200-30000	PID	PP	Idn. of K and C of AMB	Exp.

Table 1-2 cont…

Authors (Year)	Bearings	Type	Poles	RPM	Control	Sensors	Objective	Nature of work
Xu et al. (2016)	1 AMBR, 2 BB	HEMB	8	1500	PID	ACC	Idn. of bearing outer race defects	Num. & Exp.
Zhou et al. (2016)	2 AMBR	HEMB	16	600 - 6000	μ-synthesis	-	Idn. of *K* and *C* of AMB	Exp.
Xu et al. (2018, 2020)	2 AMBR, 2 AMBT	HEMB	8	1200 - 30000	PID	PP	Idn. of *K* and *C* of AMB	Exp.
Sarmah and Tiwari(2018, 2020)	1 AMBR	HEMB	8	-	PID	PP	Modal Idn. of crack parameters	Num.
Prabhat and Tiwari(2020)	2 AMBR	HEMB	8	-	PID	PP	Modal Idn. of unbalance parameters	Num.

Abbreviations. ACC: Accelerometer; AMBC: Conical active magnetic bearing; AMBR: Radial active magnetic bearing; AMBT: Thrust active magnetic bearing; BB: Ball bearing; BC: Breathing crack; CP: Centrifugal pump; CT: Current transducer; EMA: Electromagnetic actuator; Exp.: Experimental; FOSG: Fiber optic strain gauge; Idn. : Identification; JB: Journal bearing; LS: Labyrinth seal; Meas.: Measurement; Num.: Numerical; PD: Proportional – derivative; PID: Proportional- integral-derivative; PT: Pressure transducer; REB: Rolling element bearing; RIB: Rigid bearing; Unb.: Unbalance

Symbols. C: equivalent AMB damping; K: Equivalent AMB stiffness; i: Current; K_s: Displacement stiffness; K_i: Current stiffness; F_H: Hydraulic force; F_{Mag}: Magnetic force; U: Unbalance.

Chasalevris and Papadopoulos (2015) presented a method for early detection of shallow cracks (< 5% of shaft radius) in rotating shafts using AMBs. A rotor-bearing system, consisting of an elastic rotor mounted on fluid-film bearings was used to detect the presence of crack at a depth of around 5 percent of shaft radius (Refer Figure 1-32). The variation of coupling property that a crack or a notch introduces into the system and the concept of localization of coupling in time domain were used to detect cracks. Signal processing techniques, such as Hilbert transforms, Fast Fourier transform (FFT) and Continuous wavelet transform (CWT) were used on response signals obtained from

system monitoring. Singh and Tiwari (2015, 2016) investigated the behaviour of a rotor-bearing system with a breathing crack under the support action of AMB. Since the AMB suppresses vibration induced on account of the presence of crack and unbalance, controller current was utilized for the purpose of identifying crack parameters. This is contrary to the traditional method of exciting the cracked rotor, which can affect its structural integrity. Sarmah and Tiwari (2018, 2020) considered the effects of both internal and external damping in the identification of crack parameters in rotor systems supported by auxiliary AMBs.

Rotors which are supported on REBs and excited by AMBs, as well as rotors that are both levitated and excited by support AMBs have used combination resonance technique for crack detection. However it was found that rotors with shallow cracks are indistinguishable from healthy rotors with this method. The application of variety of signal processing techniques on AMB signature has enabled early identification of shallow cracks. Control of crack breathing mechanism so as not induce either large vibrations or instability by choosing proper AMB current combination has been numerically studied. The behaviour of breathing crack on a Jeffcott rotor under AMB support has been studied. Identification of depth and location of multiple cracks using AMBs has not yet been explored. Acoustic emission techniques in conjunction with AMBs can help detect minute changes in transient elastic waves arising from multiple cracks excited by AMBs.

1.16 Identification of Bearing Faults with AMBs

Chasalevris et al. (2011, 2014) investigated the operation of worn journal bearings by incorporating an AMB on the same shaft, which acts as a collocated sensor/actuator unit (Refer Figure 1-32). The shaft was excited by transient electromagnetic external excitation with linearly varying frequency (chirp). The occurrence of additional sub- and super-harmonic components was observed when external frequency lies in the region of first natural frequency of the operating system. The time-frequency analysis revealed beginning of additional frequency components, especially in sub-harmonic domain. In the same work, the authors investigated the vibration behaviour when wear pattern is misaligned with respect to bearing longitudinal axis. An external excitation force of variable frequency was applied while the system is in nominal operation at steady rotational speed. Time histories of response under combined excitation of unbalance at

fixed frequency and linearly variable AMB forcing frequency were analysed in time and frequency domains with short-time Fourier transform (STFT) and Continuous wavelet transform (CWT). Two different cases of wear pattern and variable wear depths were investigated. It was found that ½ order AMB excitation was the most sensitive sub-harmonic component to wear depth.

Xu et al. (2016) studied the active health monitoring of rotordynamic systems in the presence of bearing outer race defect with the mid-span AMB exciter, which extracts the defect characteristic frequency of Outer Race Ball Pass Frequency (BPFO) during the bearing incipient faulty stage of rolling element bearings. It was found that there was an increase in the acceleration response as a result of the defect in outer race.

The wear in journal bearings, and defects in races of rolling element bearings have been identified with AMBs using signal processing techniques. Identification of faults in a shaft excited by AMB using the signature obtained from bearing caps can be explored.

1.17 Identification of AMB Forces

Guinzburg and Buse (1995), and Baun and Flack (1999) investigated the hydrodynamic axial and radial forces acting on centrifugal pump impellers by direct measurement of reaction forces with the help of retrofitted AMBs. The AMBs, besides supporting pump rotor, also functioned as calibrated load cells. Kasarda et al. (2000) developed improved AMB force measurement algorithms and calibration procedure that makes AMB a more reliable tool for the static and dynamic load measurement. Marshall et al. (2001) used multi-point technique for static force measurement in AMBs based only on basic actuator geometry and control current without requiring the knowledge of actual operating air gaps. This technique utilizes multiple sets of current pairs for force determination as opposed to a single point technique that utilizes bearing current information and assumed gaps or Hall sensors that measure the magnetic flux density. Raymer and Childs (2001) used fibre-optic strain gages (FOSG) mounted on the magnetic poles for the measurement of force generated by AMB that is exerted on the rotor.

Nordmann and Aenis et al. (2004) made a comparative study of various force measurement techniques employed in AMBs, such as *i-s* method, reluctance network method, and flux based methods using Hall sensors. Kozanecka et al. (2007) developed an identification procedure to measure the unsteady forces exerted by labyrinth seal on the

rotor-bearing system. This was done by simultaneous measurement of the journal position with respect to the bush and control currents that flow in the magnetic bearing bush winding. Experimental investigations were carried out on the vertical rotor levitating in the magnetic field. A comparison of forces of bearing magnetic response with and without seal gives measurable changes in static and dynamic loads of magnetic bearing, which makes it possible to determine the forces that act on shaft when the seal is in operation. Zutavern and Childs (2005, 2008) developed a method for parameter identification of an annular gas seal on a flexible rotor test rig. Dynamic loads applied by magnetic bearings that support the rotor were measured using four fibre-optic strain gauges (FOSG) bonded to the four poles of the AMBs. These forces were used for the parameter identification.

There are two main types of force measurements used in an AMB system. The first is based on the measurement of coil currents and rotor displacements (*i-s* method, reluctance network model) and the second method uses the direct measurement of magnetic flux density with a Hall sensor at each pole. Force measurements in AMB system has been done in mainly two different ways i.e. from current measurement and direct magnetic flux measurement. Use of AMB as a device to measure forces applied by labyrinth seal on rotor systems and to identify annular seal parameters have been reported.

1.18 Identification of AMB Current and Displacement Stiffness

Kozanecka et al. (2008) identified AMB dynamic parameters by means of a relationship between magnetic response, control current and magnetic gaps. The test rig consists of horizontal flexible power-transmission shaft supported on two rolling bearings at one end and a magnetic bearing at the other end (Figure 1-39). Measured gaps obtained from instantaneous position of journal with respect to centre of bush and measured magnetic forces enable the estimation of bearing dynamic parameters based on the relationship between the three parameters.

Tiwari and Chougale (2014) developed an identification algorithm for the estimation of dynamic parameters of AMBs and rotor residual unbalances for a flexible rotor systems levitated on AMBs. Unlike conventional bearings, AMBs partially attenuate the unbalance responses, which makes it difficult to correctly estimate the dynamic parameters from unbalance responses alone.

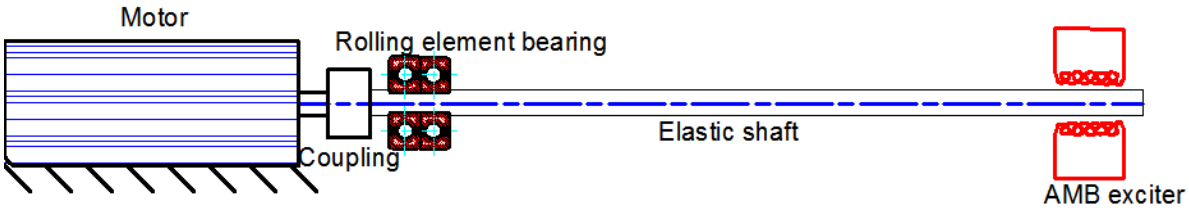

Figure 1-39 Test rig schematic: Kozanecka et al. (2008)

Keeping this in view the algorithm took care of both measured AMB controlling currents and rotor unbalance responses. The numerically estimated parameters were compared with the experimental parameters, which was previously obtained by Tiwari et al. (2009). Tiwari and Viswanadh (2015) developed an identification algorithm to estimate displacement stiffness and current stiffness of AMBs, and residual unbalances in a rigid rotor system levitated on AMBs. A Simulink™ model was used to generate numerical responses, which were further used in the estimation of AMB parameters and residual unbalances. Jiang et al. (2015) proposed a method for measuring equivalent stiffness and equivalent damping of AMB-rotor system with multi-frequency excitation. The multi-DOF rotor model based method is used as against the single-DOF system. Error in the identification of parameters is minimized, if the peak value of the multi-frequency excitation is large, but this can lead to large rotor vibration or force saturation of AMB. On the other hand, decreasing the excitation amplitudes of every component results in weak perturbations in the frequency domain and will consequently increase identification error. Schroeder-phased harmonic sequences was made use to superimpose the components with appropriate selection of relative phasing so that the lowest possible peak value signal is produced while the components retain the same higher value. This minimizes the possibility of vibration displacement exceeding clearance or AMB reaching saturation.

Zhou et al. (2016) presented a two-step identification procedure for closed-loop AMB stiffness and damping coefficients based on rotor unbalance response. The test was performed on the rig shown in Figure 1-40.

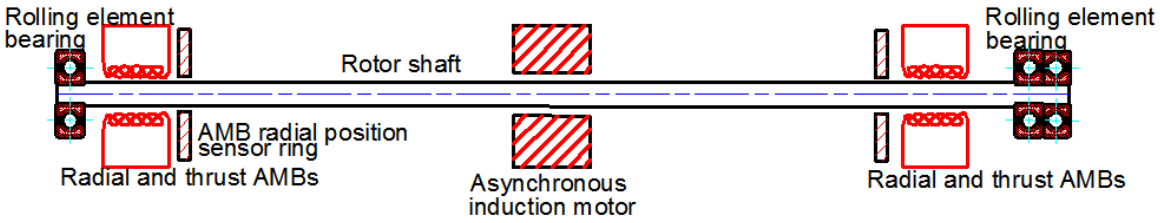

Figure 1-40 Test rig schematic: Xu et al. (2016)

A rigid body rotor model was used to compute the nominal values of the bearing stiffness and damping coefficients at a given rotating speed from the experimentally measured rotor unbalance response. Later based on a FEM model of the rotor, an error response surface is constructed for each parameter, to estimate the identification errors induced by rotor flexibility. The eventual closed-loop AMB stiffness and damping coefficients equal the sums of the nominal values initially computed from experimental unbalance response and identification errors determined by error response surfaces. The AMB stiffness and damping coefficients thus identified are input to finite element model of the rotor from which model unbalance responses at various rotating speeds are determined through simulation and compared with experimental measurements.

Xu et al. (2016) developed a rotor unbalance response based approach to identifying the AMB stiffness and damping coefficients. The rotor is supported by two radial and two thrust AMBs. An asynchronous induction motor rotor is located in the middle of the rotor between the front AMB and rear AMB (Refer Figure 1-40). A Timoshenko beam finite element rotor model was created and an identification procedure based on FE model was proposed. Then based on the experimental rotor unbalance response data at various speeds of operation the AMB stiffness and damping were obtained. Band-pass filters were employed to remove noise from the experimental data. The measured displacement values go through unbalance signal filter using zero-phase digital filters to extract the steady state amplitude and phase information upon which first order Fourier series based least-squares method was used to fit the filtered signals. Xu et al (2017, 2018) performed identification of AMB stiffness and current stiffness coefficients from the unbalance response of rotor. Experimental study showed good matching with the numerical estimates.

The identification of AMB dynamic parameters i.e. k_s and k_i by different magnetic force measurement methods and different excitation methods such as unbalance excitation, multi-frequency excitation has been reported in present subsection.

1.19 Other Applications of AMB in CM

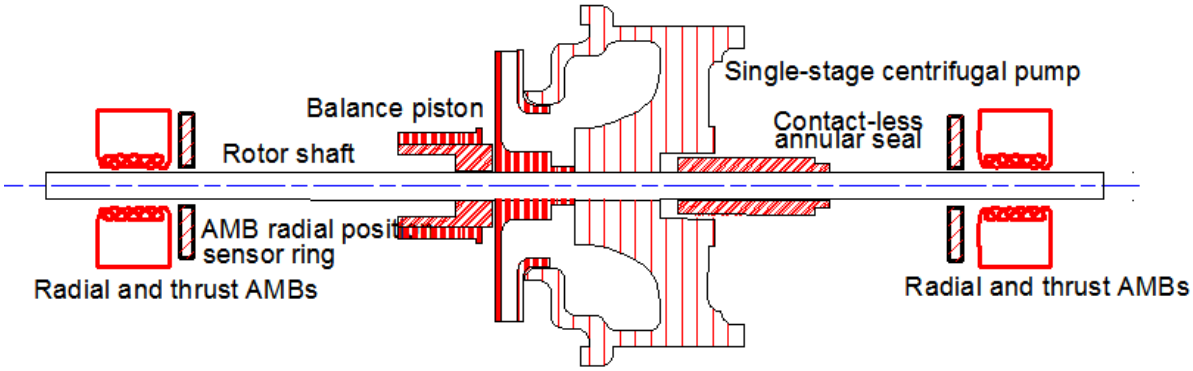

Figure 1-41 Test rig schematic: Nordmann and Aenis (2004)

Kim and Lee (1999) identified the dynamic characteristics of an oil-lubricated, short squeeze film damper (SFD) with a central feeding groove using an AMB system as an exciter. The experimentally identified damping and inertia coefficients of the SFD were compared with analytically derived dynamic coefficients.

Nordmann and Aenis (2004) developed a model-based diagnostic procedure for detection and diagnosis of dry-run condition as a fault in a magnetically suspended single stage centrifugal pump (Figure 1-41). The rotor of the pump was modelled through a finite element model after which the model was updated by an experimental modal analysis to guarantee an accurate description of physical model. Cade et al. (2005) used wavelet analysis to detect faults in rotor-magnetic bearing systems. Haar wavelet was chosen as mother wavelet, since its shape is suited for step changes in unbalance and short duration rotor/bearing contacts. A controller was formulated in wavelet coefficient domain with control forces derived from proportional feedback of displacement wavelet coefficients. Experimental validation through mass-loss tests were performed on flexible rotor/active magnetic bearing assembly to provide sudden changes in synchronous disturbance resulting in transient vibration responses.

Bouaziz et al. (2015) studied the influence of defects in high-speed milling spindle and AMB defects on dynamic behaviour of spindle supported by two AMBs. Some defects such as windings defect, misalignment between opposite AMB poles, and eccentricity defect due to non-uniform air gap around AMB and spindle unbalance have been studied for their impact on electromagnetic forces, and subsequently the dynamic behaviour of the spindle. The authors found that windings effect produced the largest change in the electromagnetic force, closely followed by misalignment, and eccentricity coming in the last.

The speed dependent stiffness and damping coefficients of SFD have been experimentally identified with AMB exciter. Defects in centrifugal pumps, milling spindles, AMB windings have been studied. This could be extended to identification of faults in motors.

1.20 General Remarks on AMB Applications

In this section the summary of the research work done on the application of AMBs mainly in flexible rotordynamic systems is presented. The primary focus was laid on vibration suppression, stability improvement and condition monitoring. While the aforesaid topics on AMBs were independently addressed in majority of papers, the above areas overlap each other in the work done by a few researchers. The following points have been found to be notable

(a) In flexible rotor systems, AMBs have been used in place of conventional bearings as stand-alone bearing supports to levitate the rotor and pass through several critical speeds.

(b) In the area of synchronous vibration suppression in the rigid and flexible rotors, it is felt that controller design, actuator design and actuator placement have been devoted research importance in about the same order.

(c) AMBs have been used as supplementary inboard/ outboard/inside-out magnetic damper(s) along the length of shafts supported on rolling element bearings or oil film bearings to suppress synchronous transverse vibration due to the unbalance.

(d) Apart from synchronous vibration suppression, AMBs have been used to suppress vibrations caused by driveline misalignment, periodic base/seismic excitation, presence of breathing cracks, faults in bearings, faults in gears, sub-synchronous excitation,

compressor surge instability in centrifugal compressors, coupled bending and torsional vibration, and chatter instability in high speed milling spindles.

(e) AMBs have been used in conjunction with fluid-film bearings to remove the oil whirl, oil whip, dry whip due to rubs, and increase instability threshold by introducing additional stiffness and damping into the system.

(f) Conversely, AMBs have been used to simulate destabilizing aerodynamic forces caused by seals and gyroscopic effects caused by large flywheels. Using AMBs in laboratory to simulate cross coupling forces and subsequently control them, gives the benefit of checking apriori the performance and robustness of controller's algorithm. Any errors in algorithm that might otherwise compromise the safety of fully levitated large industrial rotors can be avoided.

(g) They are capable of replacing non-rotating damping provided by static bearing support and foundation with contra-rotating damping for the dynamic stabilization of high speed rotors.

(h) AMBs have been used as exciters to produce characteristic signatures that correspond to the presence of various faults. From the point of view of fault identification and post processing the results, exciting faults is more straight forward and intuitive way of performing CM, than suppressing them. AMBs have been used to apply various types of excitation inputs such as harmonic, step, square, chirp forcing functions on rotors.

(i) AMBs are being used as prognostic tools in smart machines. Various faults such as unbalance eccentricity, internal damping, breathing cracks, faults in races of anti-friction bearings, wear in oil film bearings, and dry run condition in centrifugal pumps have been identified with AMBs.

(j) Combination frequency technique, a frequency domain tool, has been employed successfully for the detecting deep cracks. This technique is, however, reported to be not successful in clearly setting apart rotors with shallow cracks from uncracked rotors.

(k) AMBs in conjunction with wavelets have been used to effectively extract the weak signature corresponding to shallow cracks that are otherwise indistinguishable from the spectrum of un-cracked rotor.

(l) AMBs have been used in conjunction with full spectrum for modal based identification of breathing crack and, amplitude and phase of individual harmonics of crack excitation force.

(m) In the design of actuators, AMBs have been integrated with tilting pad bearings. Theoretical studies on integration of AMB with journal bearing have been found to be effective by resulting in lower bearing size, and higher load carrying capacity. The effect of number of electromagnets on transient behavior of purely angular misaligned rotor has been investigated.

(n) AMBs have been used for balancing of magnetically levitated flexible rotors below the bending critical speed by injecting synchronous electromagnetic forces in what has been called as virtual trail weights method in single start-up.

(o) AMBs have been used to perform in-situ high-speed balancing of flexible rotor-bearing system using virtual trial unbalances, while rotating the system below its critical speed.

(p) It is felt that AMBs as tools for ACM have not been exploited on the same level as in vibration suppression. Modal based CM has been found to be given less focus than the vibration based CM. There have been a few works related to the identification of crack, unbalance, and AMB dynamic parameters using modal based techniques.

1.21 Future Directions in AMB Applications

The following areas offer scope for further research in the application of AMBs in rotordynamic systems

(a) Power turbine shafts of gas turbine engines are long and slender. They are supported on rolling element bearings and balanced *near* operational critical speeds. The vibration displacement is measured with proximity probes and the correction mass is estimated. Since critical speed cannot be traversed through *before* balancing, this procedure becomes *iterative*. When AMB is placed at anti-node locations, it allows the rotor to run *at* the critical speed, as it suppresses the vibration simultaneously. This minimizes the bending stress experienced by the shaft- irrespective of the magnitude of unbalance- since AMB adjusts the control current in real time to limit the rotor whirling within clearance. Finally, the AMB current and displacement signals could be utilized to estimate the correction unbalance and phase in multiple planes in *one-shot*.

(b) It is known that the 1st bending critical speed of free-free supported rotor is almost 1.7 times more than that of fixed-fixed supported rotor. This characteristic in conjunction with controllable support stiffness characteristics of AMB can be used in flexible rotor balancing. The rotor to be balanced can be taken up to the required higher operating speeds using the lower support stiffness supplied by AMB, without crossing the first

critical speed. Since ODS is a function of support stiffness, besides unbalance distribution and operating speed, the rotor undergoes lesser deflection thereby requiring lesser power to control. After the desired speed has been reached, AMB stiffness can be increased through the controller to the actual support stiffness. The rotor now assumes true mode shape and undergoes actual deflection at the same speed. The current and displacement signature from AMB supports placed at anti nodal points could be captured and correction unbalance can be estimated. As long as the rigid critical speeds are stable (since very low support stiffness tends to shift the 1st rigid critical speed into unstable zone), this method can be used for balancing with lower power consumption.

(c) The above method is particularly useful to independently balance higher mode shapes without having to balance the lower mode shapes.

(d) Some practical problems that entail the usage of core - which is compulsory when using AMBs are as follows: When core is slid around the shaft in an interference fit, besides adding to actual rotor mass at specific locations, it increases bending stiffness, thus shifting the bending critical speed away from the actual resonance. This stiffening effect and additional core mass at the anti-nodal point affect the amplitude at the actual resonance.

(e) In the above situations (a), (b), (c), (d) when AMB is used as vibration suppressor in the form of intermediate support, the current signal from AMB has to be decomposed to separate the signal corresponding to actual suppressed vibration and the signal due to spurious vibrations arising on account of core placement effect. A study of correction factors that may be required to be applied to balancing speed and displacement/current signal from AMB, so that the actual rotor deflection is correctly determined could be made.

(f) In AMB application for balancing, presence of larger amount of residual unbalance requires more power for vibration suppression. This pushes the AMB size upwards, making implementation challenging.

(g) AMBs face challenge from actual industrial rotors due to their lesser load carrying capacity and therefore lesser stiffness. Hybrid bearings, by using permanent magnets for generating bias currents, have brought down the size of AMBs to some extent. The concept of integrating JBs with AMBs has been implemented by some authors. Integrated JB/TPB and AMB meets twofold requirements: 1) more load carrying

capacity and 2) active CM without the need for a separate and bigger AMB. Optimization of such hybrid bearings to increase load carrying capacity within space constraints could be explored.

(h) It is a common situation in flexible rotors that are balanced to acceptable levels of residual unbalance on balancing machine to experience higher vibration on actual engine owing to different dynamic support stiffness values on balancing machine and engine. This leads to different values of amplitude of operating deflection shape (ODS) in the two conditions. By simulating the actual bearing plane dynamic stiffness with AMB supports this problem could be addressed.

(i) Bearings with non-isotropic stiffness ($K_{xx} \neq K_{yy}$) have a zone of unstable backward critical speed between consecutive forward critical speeds corresponding to transverse orthogonal (x and y) directions. The extent of the zone depends on the damping present within the system. Two support AMBs can be used to introduce non-isotropic stiffness there by exciting the backward critical speed of the rotor system. As the backward whirl component in the full spectrum grows prominent, an intermediate AMB is activated to introduce directional harmonic force to suppress the vibrations due to backward whirl. The possibility of sensing the whirl direction in real time and introducing corresponding directional force which negates the vibration can be explored.

(j) The effect of number of poles of AMB support bearings on vibration suppression caused due to the pure angular misalignment has been explored. Auxiliary AMB and full-spectrum can be used to further investigate the directional vibration behavior of rotor-trains subject to both angular and parallel misalignments, while simultaneously suppressing the vibrations.

(k) Faults in gears such as tooth cracks can be investigated with auxiliary AMB exciter/supports. The periodicity of frequencies corresponding to gear faults is expected to interact with AMB forcing frequencies that may result in either pronounced peaks in spectra or appearance of altogether new frequency components

(l) Wavelets which are used to localize sudden changes in system dynamics- due to their ability to have finer time resolution at high frequencies and finer frequency resolution at lower frequencies-could be used in conjunction with full spectrum. When multiple faults such as crack, misalignment and rub develop in a rotor system over a period of time in unknown order, wavelet transform could be applied to time signal of AMB's current and

displacement to precisely identify the time of each defect inception. However since all the above mentioned faults have full spectrum components, distinguishing and identifying faults from one another would be a challenge which could be explored. AMBs on their part help in mitigating the vibration caused by these faults.

(m) Identification of depth and location of multiple cracks using AMBs has not yet been explored. Acoustic emission techniques in conjunction with AMBs can help detect minute changes in transient elastic waves arising from multiple cracks excited by AMBs.

(n) There exists a vast amount of literature on CM of electrical motors using various automated tools which are not covered in this chapter. Nandi et al. (2005) can be referred for a review of such techniques. Integration of AMBs into the rotor systems driven by these motors for the detection of various faults in motors could be explored.

भारतीय प्रौद्योगिकी संस्थान गुवाहाटी
Indian Institute of Technology Guwahati

CHAPTER 2

Identification of Misalignment in Coupled Simple Rotor-AMB Systems with Central Discs

2.1 Introduction

In the present chapter, the modelling, analysis and identification of various system faults in a coupled simple rotor system with auxiliary active magnetic bearing (AMB) support has been presented. The mathematical model of coupling in the presence of angular misalignmentis is developed. The coupled rotor system is modelled with two simple rotors each with a central disc. The coupling is assumed to be flexible and is modelled by a helical torsion (in bending) spring. This relaxation in modelling of the coupling makes it possible to establish a linear relationship between the slope at bearing/coupling location and the translational deflection at the disc location. Lagrange's equations are used to develop the equations of motion of the coupled rotor system. A steering function has been selected such that the forced reponse due to coupling misalignment yields both odd and even harmonics in full spectrum (with positive and negative frequencies). An identification algorithm based on least-squares regression technique in frequency domain has been developed using the forward and backward harmonics of rotor vibration and AMB current for the estimation of coupling direct stiffness, coupling additive stiffness, unbalance magnitude and its phase, equivalent viscous damping in each rotor, and current and displacement constants of the AMB. The robustness of identification algorithm is tested against various levels of measurement noise.

2.2 System Configuration

Figure 2-1 shows a coupled rotor system with central discs, with two bearings supporting each rotor. The drive is transmitted from rotor-1 to rotor-2 with the help of a coupling. An AMB placed on the second rotor next to the disc serves to attenuate the vibration as well as to perform the condition monitoring to characterise the faults present in the rotor

system. Figure 2-2 shows the inertial and rotating coordinate systems used in the present work .

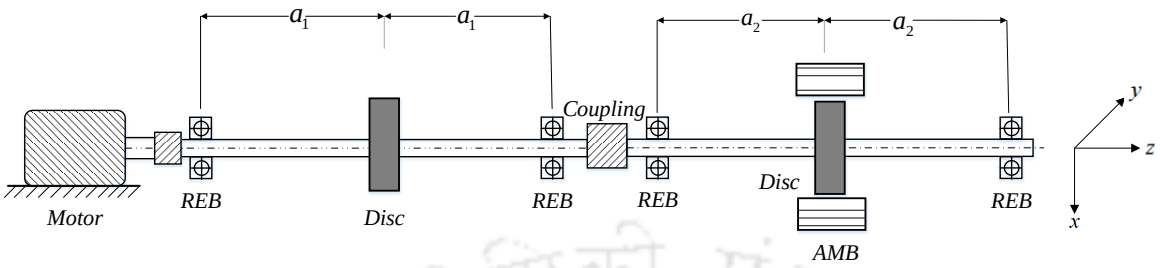

Figure 2-1General arrangement of a simple coupled rotor-AMB system

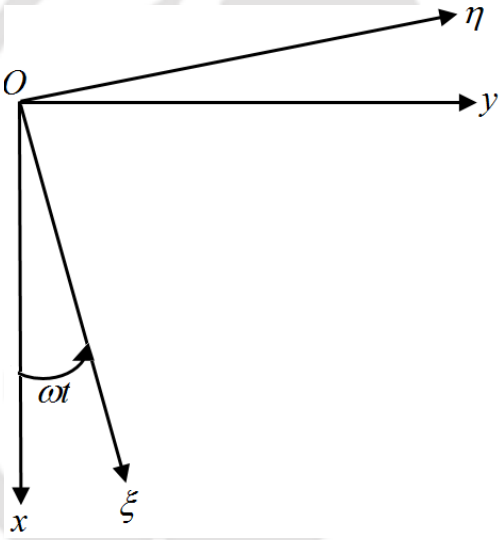

Figure 2-2 Inertial and rotating frames of reference

2.3 Assumptions

a) Only angular misalignment is present between the bearing centres. No parallel misalignment is considered in the present chapter. So coupling is modelled as helical torsion (in bending) spring.

b) Simply supported condition is assumed at bearing location i.e. there is no restriction to slope at the location.

c) The coupling is flexible and the disc is heavy. Under these conditions weight of the disc contributes more to the static slopes at coupling location than does the reaction

moment of the coupling. This makes it possible to establish linear relation between slopes at the coupling and translational displacements at the disc location.

d) The overhang of rotor between inboard bearings at the intermediate coupling location is considerably less compared to span of the shafts. It ensures that coupling has only angular displacement and no translatory displacement.

e) The mass and damping properties of coupling are ignored. The angular stiffness of coupling about two transverse axes is equal

2.4 Generalized Coordinates of Rotors and Relation with Coupling Slopes

(a)

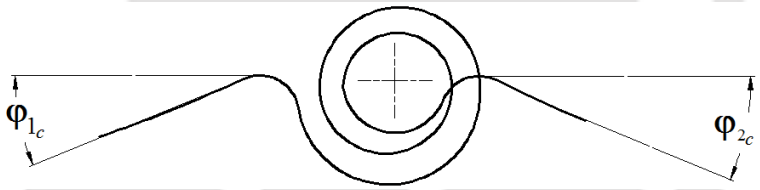

(b)

Figure 2-3 Coupled simple rotor system: (a) Displacements at disc locations (b) Slopes of helical torsion (bending) spring at coupling location

Figure 2-3 shows the displacments at disc and coupling locations with simple rotor model. The *generalized coordinate vectors* of the rotor-1 and rotor-2 represented by $\mathbf{q}_1(t)$ and $\mathbf{q}_2(t)$ are the total displacements of two degree-of-freedom (2-DOFs) coupled rotor system mounted with central discs. They are composed of static components, $\mathbf{q}_{10}$ and $\mathbf{q}_{20}$ and vibratory components $\Delta\mathbf{q}_1(t)$ and $\Delta\mathbf{q}_2(t)$. Mathematically they can be expressed as

$$\left.\begin{aligned}\mathbf{q}_1(t) &= \Delta\mathbf{q}_1(t) + \mathbf{q}_{10}\\ \mathbf{q}_2(t) &= \Delta\mathbf{q}_2(t) + \mathbf{q}_{20}\end{aligned}\right\} \tag{2.1}$$

with

$\Delta\mathbf{q}_1(t)=\begin{pmatrix}x_1 & y_1\end{pmatrix}^T;\mathbf{q}_{10}=\begin{pmatrix}\delta_{x_{10}} & \delta_{y_{10}}\end{pmatrix}^T$ and $\Delta\mathbf{q}_2(t)=\begin{pmatrix}x_2 & y_2\end{pmatrix}^T;\mathbf{q}_{20}=\begin{pmatrix}\delta_{x_{20}} & \delta_{y_{20}}\end{pmatrix}^T$

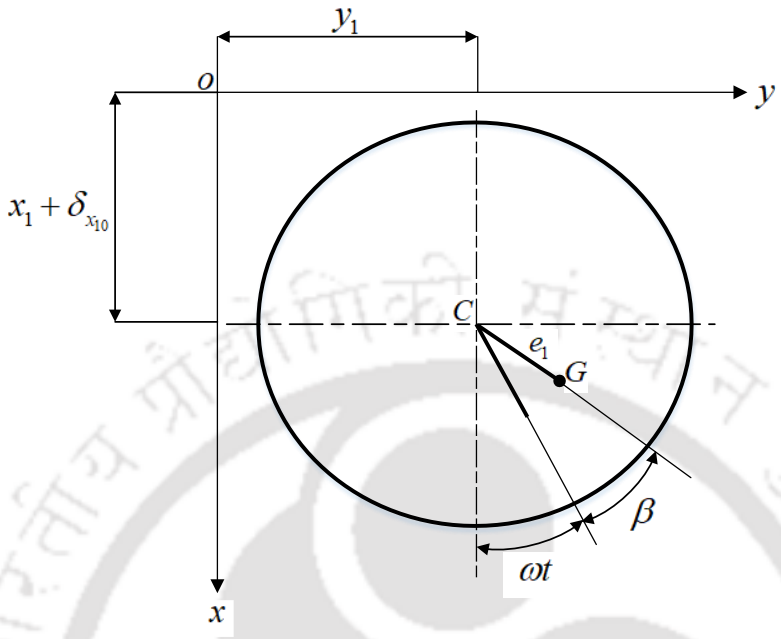

Figure 2-4 Angular position of unbalance

Total angular displacements i.e. slopes at coupling location for rotor-1 and rotor-2 are denoted by

$$\boldsymbol{\varphi}_{1c}=\begin{pmatrix}\varphi_{y_{c_1}} & \varphi_{x_{c_1}}\end{pmatrix}^T \tag{2.2}$$

$$\boldsymbol{\varphi}_{2c}=\begin{pmatrix}\varphi_{y_{c_2}} & \varphi_{x_{c_2}}\end{pmatrix}^T \tag{2.3}$$

Working under the assumptions mentioned in Section 2.3, slopes at coupling location for rotor-1 given by $\begin{pmatrix}\varphi_{y_{c_1}} & \varphi_{x_{c_1}}\end{pmatrix}^T$ and the translational displacement part in vector $\Delta\mathbf{q}_1$ given by $\begin{pmatrix}x_1 & y_1\end{pmatrix}^T$ at disc-1 location are linearly related by a constant λ_1, as

$$\boldsymbol{\varphi}_{1c}=\lambda_1\begin{pmatrix}x_1 & y_1\end{pmatrix}^T \tag{2.4}$$

with $\lambda_1=\left(\dfrac{3}{2a_1}\right)$

Likewise, for rotor-2, the corresponding relation can be written as

$$\boldsymbol{\varphi}_{2c}=\lambda_2\begin{pmatrix}x_2 & y_2\end{pmatrix}^T \tag{2.5}$$

with $\lambda_2 = \left(\frac{3}{2a_2}\right)$

where a_1 and a_2 are the respective distances of discs of rotor-1 and rotor-2 from their left and right supports (refer Figure 2-1). Eqns. (2.4) and (2.5) representing the relations between slopes at bearings and deflection at any section are obtained from the formulae given in **Appendix A**. The relative position of disc unbalance is shown in Figure 2-4. *O* is the bearing centre line, C is the geometric centre of the disc and G is the location of the mass unbalance, β is the initial phase angle.

2.5 Equations of Motion of Coupled Rotor System

Equations of motion for the coupled rotor-train system shall be derived from energy equations. The kinetic energy of rigid discs on rotor-1 and rotor-2 due to the translation and rotation motion is given by

$$T = \tfrac{1}{2} m_1(\dot{x}_1^{\,2} + \dot{y}_1^{\,2}) + \tfrac{1}{2}\Omega^2 I_{p_1} + \tfrac{1}{2} m_2(\dot{x}_2^{\,2} + \dot{y}_2^{\,2}) + \tfrac{1}{2}\Omega^2 I_{p_2} \qquad (2.6)$$

The potential energy in the shafts and coupling is given by

$$V = \tfrac{1}{2} k_{1xx} x_1^2 + \tfrac{1}{2} k_{1yy} y_1^2 + \tfrac{1}{2} k_{2xx} x_2^2 + \tfrac{1}{2} k_{2yy} y_2^2 + \tfrac{1}{2} k_{\varphi_{x_c}} (\varphi_{x_{c_1}} + \varphi_{x_{c_2}})^2 + \tfrac{1}{2} k_{\varphi_{y_c}} (\varphi_{y_{c_1}} + \varphi_{y_{c_2}})^2 \qquad (2.7)$$

where m_i, I_{d_i} and I_{p_i} are the mass, diametrical mass moment of inertia and polar mass moment of inertia of discs. k_{1ij}, k_{2ij} are the stiffness of the shafts and c_{1ij}, c_{2ij} are the viscous damping of the shafts. $k_{\varphi_{x_c}}$, $k_{\varphi_{y_c}}$ are the angular stiffness of coupling about *x* and *y* axes. For rotor-1, it is assumed that $k_{1xx} = k_{1yy}$. Likewise, for rotor-2, it is assumed that $k_{2xx} = k_{2yy}$. For the coupling, it has been assumed that angular (bending) stiffness is same about both axes, i.e. $k_{\varphi_{c_x}} = k_{\varphi_{c_y}}$. Substituting Eqns. (2.4) and (2.5) into Eqn. (2.7) we get potential energy purely in terms of generalized coordinates, as

$$V = \tfrac{1}{2} k_{1xx} x_1^2 + \tfrac{1}{2} k_{1yy} y_1^2 + \tfrac{1}{2} k_{2xx} x_2^2 + \tfrac{1}{2} k_{2yy} y_2^2 + \tfrac{1}{2} k_{\varphi_{x_c}} \left(\lambda_1 y_1 + \lambda_2 y_2\right)^2 + \tfrac{1}{2} k_{\varphi_{y_c}} \left(\lambda_1 x_1 + \lambda_2 x_2\right)^2 \qquad (2.8)$$

The last two terms signify potential energy of coupling represented in terms of translational displacements of rotor-1 and rotor-2. Likewise, the Rayleigh's dissipative function due to viscous damping in shafts can be written as

$$\Im = \tfrac{1}{2}c_{1xx}\dot{x}_1^2 + \tfrac{1}{2}c_{1yy}\dot{y}_1^2 + \tfrac{1}{2}c_{2xx}\dot{x}_2^2 + \tfrac{1}{2}c_{2yy}\dot{y}_2^2 \tag{2.9}$$

where c_{1ij}, c_{2ij} are the viscous damping of the shafts. To derive equations of motion, we use Lagrange's equation given by

$$\frac{d}{dt}\left(\frac{\partial T}{\partial \dot{q}_i}\right) - \frac{\partial T}{\partial q_i} + \frac{\partial V}{\partial q_i} + \frac{\partial \Im}{\partial \dot{q}_i} = Q_i \qquad (i = 1, 2, \ldots n) \tag{2.10}$$

The vector of generalized coordinates is given by $q_i = \begin{pmatrix} x_1 & y_1 & x_2 & y_2 \end{pmatrix}^T$.

Applying Eqn. (2.10) on energy expressions given by Eqns.(2.6), (2.8) and (2.9) sequentially, the equation of motion corresponding to each DOF is obtained. Thus there are four equations for four DOFs given by

$$m_1\ddot{x}_1 + k_{1xx}x_1 + \lambda_1^2 k_{\varphi_{y_c}} x_1 + \lambda_1\lambda_2 k_{\varphi_{y_c}} x_2 + c_{1xx}\dot{x}_1 = m_1 e_1 \omega^2 \cos(\omega t + \beta_1) + k_{1xx}\delta_{x_{10}} \tag{2.11}$$

$$m_1\ddot{y}_1 + k_{1yy}y_1 + \lambda_1^2 k_{\varphi_{x_c}} y_1 + \lambda_1\lambda_2 k_{\varphi_{x_c}} y_2 + c_{1yy}\dot{y}_1 = m_1 e_1 \omega^2 \sin(\omega t + \beta_1) + k_{1yy}\delta_{y_{10}} \tag{2.12}$$

$$m_2\ddot{x}_2 + k_{2xx}x_2 + \lambda_2^2 k_{\varphi_{y_c}} x_2 + \lambda_1\lambda_2 k_{\varphi_{y_c}} x_1 + c_{2xx}\dot{x}_2 = m_2 e_2 \omega^2 \cos(\omega t + \beta_2) + k_{2xx}\delta_{x_{20}} \tag{2.13}$$

$$m_2\ddot{y}_2 + k_{2yy}y_2 + \lambda_2^2 k_{\varphi_{x_c}} y_2 + \lambda_1\lambda_2 k_{\varphi_{y_c}} y_1 + c_{2yy}\dot{y}_2 = m_2 e_2 \omega^2 \sin(\omega t + \beta_2) + k_{2yy}\delta_{y_{20}} \tag{2.14}$$

The right hand side of each equation gives the static force and unbalance. It can be seen from the above equations that coupling stiffness terms appear only in the equations of motion (EOMs) corresponding to translational displacements. This is a direct consequence of relations given by Eqns. (2.4) and (2.5). Now Eqns. (2.11) to (2.14) can be written in the following form

$$\mathbf{M}_1\ddot{\mathbf{q}}_1 + \mathbf{C}_1\dot{\mathbf{q}}_1 + \mathbf{K}_1\mathbf{q}_1 + \mathbf{K}'_{\varphi_c}\mathbf{q}_1 + \mathbf{K}'''_{\varphi_c}\mathbf{q}_2 = \mathbf{f}_{unb_1} + \mathbf{f}_{st_1} \tag{2.15}$$

$$\mathbf{M}_2\ddot{\mathbf{q}}_2 + \mathbf{C}_2\dot{\mathbf{q}}_2 + \mathbf{K}_2\mathbf{q}_2 + \mathbf{K}'''_{\varphi_c}\mathbf{q}_1 + \mathbf{K}''_{\varphi_c}\mathbf{q}_2 = \mathbf{f}_{unb_2} + \mathbf{f}_{st_2} \tag{2.16}$$

where $\mathbf{M}_i, \mathbf{C}_i, \mathbf{K}_i, \mathbf{G}_i$ are the mass, damping, stiffness and gyroscopic matrices of rotors. $\mathbf{f}_{unb_i}$, $\mathbf{f}_{st_i}$ are the forces due to unbalance and static deflection. The system matrices of coupled rotor system are given in **Appendix B**. In Eqns. (2.15) and (2.16) the contribution of coupling to the rotor system stiffness comes from $\mathbf{K}'_{\varphi_c}, \mathbf{K}''_{\varphi_c}$ and $\mathbf{K}'''_{\varphi_c}$ matrices, which

are given by $\mathbf{K}'_{\varphi_c} = \lambda_1^2 \mathbf{K}_{\varphi_c}$; $\mathbf{K}''_{\varphi_c} = \lambda_2^2 \mathbf{K}_{\varphi_c}$; $\mathbf{K}'''_{\varphi_c} = \lambda_1 \lambda_2 \mathbf{K}_{\varphi_c}$, where $\mathbf{K}_{\varphi_c}$ is the coupling stiffness matrix.

2.6 Coupling Stiffness Matrix

Parallel misalignment, also referred to as the static misalignment, has a *hardening* effect on the bearings, and the angular misalignment, referred to as a dynamic misalignment, has *softening* effect on bearings as reported by Ertas and Vance (2004) and Friswell et al (2010). Lees (2007) proposed that in the presence of misalignment, the stiffness of coupling has two components: first the intact stiffness, which has steady contribution, and second the time dependent additive coupling stiffness(ACS) which varies with rotary motion. The parallel misalignment was considered in his work and the fluctuating component of coupling stiffness was assigned a (+) sign. In the present work, since the angular misalignment is considered, the latter component has a (-) sign. Therefore, the stiffness of the coupling is written as

$$\mathbf{K}_{\varphi_c}(t) = \mathbf{K}_{\varphi_c} - \Delta\mathbf{K}_{\varphi_c ROT}(t) \tag{2.17}$$

with

$$\mathbf{K}_{\varphi_c}(t) = \begin{bmatrix} k_{\varphi_c} & 0 \\ 0 & k_{\varphi_c} \end{bmatrix} - \begin{bmatrix} \Delta k_{\xi}(t) & 0 \\ 0 & \Delta k_{\eta}(t) \end{bmatrix} \tag{2.18}$$

where $\Delta k_{\xi}(t)$ and $\Delta k_{\eta}(t)$ are the ACS coefficients due to angular misalignment in ξ and η directions. Substituting Eqns. (2.1) and (2.17) in equation (2.15), it gives

$$\begin{aligned} &\mathbf{M}_1\ddot{\mathbf{q}}_1 + \mathbf{C}_1\dot{\mathbf{q}}_1 + \mathbf{K}_1\left(\mathbf{q}_{10} + \Delta\mathbf{q}_1\right) + \lambda_1^2\left(\mathbf{K}_{\varphi_c} - \Delta\mathbf{K}_{\varphi_c}\right)\left(\mathbf{q}_{10} + \Delta\mathbf{q}_1\right) \\ &+\lambda_1\lambda_2\left(\mathbf{K}_{\varphi_c} - \Delta\mathbf{K}_{\varphi_c}\right)\left(\mathbf{q}_{20} + \Delta\mathbf{q}_2\right) = \mathbf{f}_{unb_1} + \mathbf{f}_{st_1} \end{aligned} \tag{2.19}$$

In Eq. (2.19) force due to self weight $\mathbf{f}_{st_1}$ in the RHS cancels out with the $\mathbf{K}_1\mathbf{q}_{10}$ term in the LHS.

Ignoring the product of smaller terms, such as $\Delta\mathbf{K}_{\varphi_c}\Delta\mathbf{q}_1$ and $\Delta\mathbf{K}_{\varphi_c}\Delta\mathbf{q}_2$, we get

$$\mathbf{M}_1\Delta\ddot{\mathbf{q}}_1 + \mathbf{C}_1\Delta\dot{\mathbf{q}}_1 + (\mathbf{K}_1 + \mathbf{K}'_{\varphi_c})\Delta\mathbf{q}_1 + \mathbf{K}''_{\varphi_c}\Delta\mathbf{q}_2 = \mathbf{f}_{unb_1} + \mathbf{f}_{mis_1} - \mathbf{f}_{const_1} \tag{2.20}$$

with

$$\mathbf{f}_{const_1} = (\mathbf{K}'_{\varphi_c}\mathbf{q}_{10} + \mathbf{K}'''_{\varphi_c}\mathbf{q}_{20}) \tag{2.21}$$

$$\mathbf{f}_{mis_1} = (\Delta\mathbf{K}'_{\varphi_c}\mathbf{q}_{10} + \Delta\mathbf{K}'''_{\varphi_c}\mathbf{q}_{20}) \tag{2.22}$$

$\mathbf{f}_{mis_1}$, $\mathbf{f}_{const_1}$ are the time-varying and static coupling misalignment forces acting on rotor-1. Likewise Eqn. (2.16) transforms to,

$$\mathbf{M}_2\Delta\ddot{\mathbf{q}}_2 + \mathbf{C}_2\Delta\dot{\mathbf{q}}_2 + (\mathbf{K}_2 + \lambda_2^2\mathbf{K}_{\varphi_c})\Delta\mathbf{q}_2 + \lambda_1\lambda_2\mathbf{K}_{\varphi_c}\Delta\mathbf{q}_1 = \mathbf{f}_{unb_2} + \mathbf{f}_{mis_2} - \mathbf{f}_{const_2} \tag{2.23}$$

where

$$\mathbf{f}_{const_2} = (\mathbf{K}'''_{\varphi_c}\mathbf{q}_{10} + \mathbf{K}''_{\varphi_c}\mathbf{q}_{20}) \tag{2.24}$$

$$\mathbf{f}_{mis_2} = (\Delta\mathbf{K}'''_{\varphi_c}\mathbf{q}_{10} + \Delta\mathbf{K}''_{\varphi_c}\mathbf{q}_{20}) \tag{2.25}$$

$\mathbf{f}_{mis_2}$, $\mathbf{f}_{const_2}$ are the time-varying and static coupling misalignment forces acting on rotor-2.

with

$$\mathbf{K}'_{\varphi_c} = \lambda_1^2\mathbf{K}_{\varphi_c}; \mathbf{K}''_{\varphi_c} = \lambda_2^2\mathbf{K}_{\varphi_c}; \mathbf{K}'''_{\varphi_c} = \lambda_1\lambda_2\mathbf{K}_{\varphi_c}; \Delta\mathbf{K}'_{\varphi_c} = \lambda_1^2\Delta\mathbf{K}_{\varphi_c}; \Delta\mathbf{K}''_{\varphi_c} = \lambda_2^2\Delta\mathbf{K}_{\varphi_c}; \Delta\mathbf{K}'''_{\varphi_c} = \lambda_1\lambda_2\Delta\mathbf{K}_{\varphi_c}$$

where $\mathbf{f}_{mis_2}$ and $\mathbf{f}_{const_2}$ are the time-varying and static coupling misalignment forces acting on rotor-2. $\Delta\mathbf{K}_{\varphi_c}$ is the additive coupling stiffness matrix. In Eqns. (2.20) and (2.23) there are three types of forcing terms on the right hand side, viz. unbalance force due to disc eccentricity, time dependant coupling misalignment force, and constant coupling misalignment force. Due to the assumptions made in Section 2.3, it is possible to express coupling misalignment forces in terms of translational displacements of the rotors at disc locations.

ACS given in Eqn. (2.17) is written as the product of a periodic time function $s(t)$ and a matrix containing additive direct stiffness coefficients Δk_ξ and Δk_η , where the cross-coupled stiffness terms are ignored, as

$$\Delta\mathbf{K}_{\varphi_c\ ROT}(t) = \begin{bmatrix} \Delta k_\xi(t) & 0 \\ 0 & \Delta k_\eta(t) \end{bmatrix} = s(t)\begin{bmatrix} \Delta k_\xi & 0 \\ 0 & \Delta k_\eta \end{bmatrix} \tag{2.26}$$

Here $s(t)$ is also called the coupling excitation function and its Fourier expansion directly influences the harmonic nature of coupling misalignment force. In Rao et al. (2001) and,

Patel and Darpe (2008), it is shown that such multi-harmonic force can be generated in real rotors by introducing misalignment in the form of shims under the bearing blocks. The magnitude of Δk_ξ or Δk_η depends on the type of coupling and the amount of misalignment. Thus Δk_ξ or Δk_η generated due to a given amount of misalignment is more for a stiffer rigid coupling than it is for a flexible coupling.

Eqns. (2.20) and (2.23) are written in the stationary frame of reference, it is necessary to transform the time dependent coupling stiffness of rotating coupling into the inertial frame of reference (Figure 2-2). This is accomplished by change of axes using a transformation matrix given by (Shrawan and Tiwari, 2012, Singh and Tiwari, 2016)

$$\mathbf{T}_{RS} = \begin{bmatrix} \cos\omega t & \sin\omega t \\ -\sin\omega t & \cos\omega t \end{bmatrix} \tag{2.27}$$

Eqn. (2.17) then transforms to the following form in the stationary frame of reference

$$\mathbf{K}_{\varphi_{c\ STAT}} - \Delta\mathbf{K}_{\varphi_c STAT}(t) = \mathbf{K}_{\varphi_{c\ ROT}} - \mathbf{T}_{RS}^{T}\Delta\mathbf{K}_{\varphi_{c\ ROT}}(t)\mathbf{T}_{RS} \tag{2.28}$$

where $\mathbf{K}_{\varphi_{c\ STAT}}$ matrix in Eqn. (2.17) representing static coupling stiffness matrix remains unaltered during coordinate transformation. However, $\Delta\mathbf{K}_{\phi_{c\ STAT}}$ denotes time dependent stiffness, and it becomes

$$\Delta\mathbf{K}_{\varphi_{c\ STAT}}(t) = s(t)\begin{bmatrix} \Delta k_\xi \cos^2\omega t + \Delta k_\eta \sin^2\omega t & \Delta k_\xi \cos\omega t \sin\omega t - \Delta k_\eta \cos\omega t \sin\omega t \\ \Delta k_\xi \cos\omega t \sin\omega t - \Delta k_\eta \cos\omega t \sin\omega t & \Delta k_\xi \sin^2\omega t + \Delta k_\eta \cos^2\omega t \end{bmatrix} \tag{2.29}$$

Note that both Δk_ξ and Δk_η coefficients appear in Eqn. (2.29). The coupling becomes asymmetric once misalignment is introduced. As a result misalignment in one direction produces reactions in another direction (Ganesan and Padmanabhan, 2011). *Soft foot* a common term used for the improper contact between machine casing and the base plate can cause alignment problems in the vertical plane. This is in turn caused by improper amount of shims, dirt under machine feet or damaged base plates. In real world, the angular misalignment can exist in vertical plane or horizontal plane or both planes. As an example, Patel and Darpe (2008) introduced angular misalignment in horizontal plane by the relative movement of bearing pedestals. It is assumed in the present work that ACS in η direction, i.e. $\Delta k_\eta = 0$.

Equation (2.29) then transforms to

$$\Delta\mathbf{K}_{\varphi_{c\ STAT}}(t)=\frac{1}{2}\Delta k_{\xi}s(t)\begin{bmatrix}1+\cos 2\omega t & \sin 2\omega t\\ \sin 2\omega t & 1-\cos 2\omega t\end{bmatrix} \tag{2.30}$$

The time-dependent coupling misalignment force acting on rotor-1, which is present in the right hand side of Eqn. (2.20), is obtained by substituting Eqn. (2.30) into Eqn. (2.22) and is given by

$$\mathbf{f}_{mis_1}=\frac{1}{2}\Delta k_{\xi}s(t)\left(\lambda_1^2\begin{bmatrix}1+\cos 2\omega t & \sin 2\omega t\\ \sin 2\omega t & 1-\cos 2\omega t\end{bmatrix}\begin{Bmatrix}\delta_{x_{10}}\\ \delta_{y_{10}}\end{Bmatrix}+\lambda_1\lambda_2\begin{bmatrix}1+\cos 2\omega t & \sin 2\omega t\\ \sin 2\omega t & 1-\cos 2\omega t\end{bmatrix}\begin{Bmatrix}\delta_{x_{20}}\\ \delta_{y_{20}}\end{Bmatrix}\right) \tag{2.31}$$

The static deflection in *y* direction and static angular deflections about *x* and *y* axes are zero, i.e. $\delta_{y_{10}}=\delta_{y_{20}}=\delta_{\varphi_{y10}}=\delta_{\varphi_{y20}}=\delta_{\varphi_{x10}}=\delta_{\varphi_{x20}}=0$. Hence,

$$\mathbf{f}_{mis_1}=\frac{1}{2}\Delta k_{\xi}s(t)\left(\lambda_1^2\delta_{x_{10}}\begin{Bmatrix}1+\cos 2\omega t\\ \sin 2\omega t\end{Bmatrix}+\lambda_1\lambda_2\delta_{x_{20}}\begin{Bmatrix}1+\cos 2\omega t\\ \sin 2\omega t\end{Bmatrix}\right) \tag{2.32}$$

Equation (2.32) represents the time dependent coupling misalignment force acting on rotor-1. Likewise the time dependent coupling misalignment force acting on rotor-2, which is present in the RHS of Eqn. (2.23) is obtained by substituting Eqn. (2.30) in Eqn. (2.25) and is given by

$$\mathbf{f}_{mis_2}=\frac{1}{2}s(t)\Delta k_{\xi}\left(\lambda_1\lambda_2\delta_{x_{10}}\begin{Bmatrix}1+\cos 2\omega t\\ \sin 2\omega t\end{Bmatrix}+\lambda_2^2\delta_{x_{20}}\begin{Bmatrix}1+\cos 2\omega t\\ \sin 2\omega t\end{Bmatrix}\right) \tag{2.33}$$

In Eqns. (2.32) and (2.33), coupling misalignment force has been represented in terms of $\delta_{x_{10}}$ and $\delta_{x_{20}}$ the static deflection of discs; λ_1 and λ_2, numeric constants that depend on the disc location from supports; and $s(t)$, the coupling misalignment excitation function.

2.7 Coupling Misalignment Excitation Function

The stiffness matrix of coupling without misalignment is symmetrical and doesn't vary with rotation. A misaligned coupling on the other hand exhibits geometric asymmetry with the result that the stiffness varies periodically in one rotation. This causes the 2X harmonic to become predominant in physical systems. It is well established from numerous experiments that misalignment between bearing centers generates multiple

integer harmonics, both odd and even, in the rotor and bearing response spectrum. Hence, a suitable waveform function for time-varying coupling stiffness needs to be substituted in Eqns. (2.32) and (2.33). A rectangular wave with 40 % duty cycle as shown in Figure 2-5 has been chosen as the excitation function. All the integer harmonics needed to mimic the vibration response of real misaligned rotors are obtained in simulation when rectangular wave is used as steering function. This justifies its use in simulation. The Fourier expansion of the excitation function is given as (Kreyszig, 2008)

$$s(t) = a_0 + \sum_{n=1}^{\infty} a_n \cos(n\omega t) \tag{2.34}$$

with

$$a_0 = Average = 0.4;\ a_n = \frac{2A}{n\pi}\sin\left(n\pi\frac{t_p}{T}\right) = \frac{2A}{n\pi}\sin\left(0.4n\pi\right) \tag{2.35}$$

where A is amplitude, T is period and t_p is pulse width. The values of a_n for different values of n are given in Table 2-1.

On substituting the values of n and a_n in Eqn. (2.35) gives

$$\begin{aligned} s(t) = 0.4 &+ 0.6055\cos(\omega t) + 0.1871\cos(2\omega t) - 0.1247\cos(3\omega t) - 0.1514\cos(4\omega t) \\ &+ 0.1009\cos(6\omega t) + 0.0535\cos(7\omega t) - 0.0468\cos(8\omega t) - 0.0673\cos(9\omega t) \\ &+ 0.055\cos(11\omega t) + 0.0312\cos(12\omega t) - 0.0288\cos(13\omega t) - 0.0432\cos(14\omega t) \\ &+ 0.0378\cos(16\omega t) + 0.022\cos(17\omega t) \end{aligned} \tag{2.36}$$

Table 2-1 Fourier coefficients of square wave with 40% duty cycle

n	a_n	n	a_n
0	0.4	8	-0.0468
1	0.6055	9	-0.0673
2	0.1871	10	0.0000
3	-0.1247	11	0.0550
4	-0.1514	12	0.0312
5	0.0000	13	-0.0288
6	0.1009	14	-0.0432
7	0.0535	15	0.0000

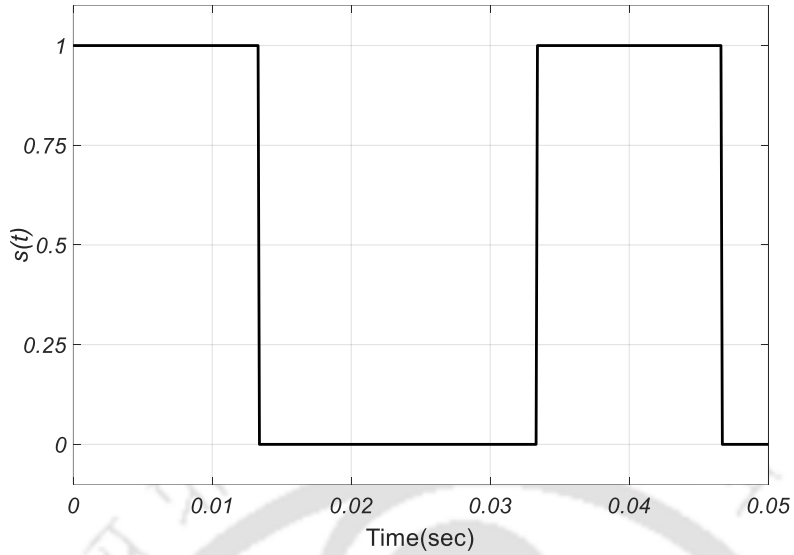

Figure 2-5 Rectangular wave with 40% duty cycle

It has been found that upon substituting Eqn. (2.36) into Eqns. (2.32) and (2.33) all the integer harmonics needed in response spectrum are generated. As such the phase relation that exists between the various integer harmonics of rectangular wave is taken the default value. Thus the arbitrarily chosen square waveform satisfies the suitability criteria to represent coupling misalignment excitation function. It is to be noted that as the severity of misalignment increases the number of harmonics that appear in the spectrum increases. In the experimental work conducted on real systems by Patel and Darpe (2008) it was found the number of harmonics that appeared in spectrum is not more than 5 with the result that the value of *n* when conducting experiment would be generally less than or equal to 5**.** There is, however, no limitation on the number of harmonics that may be used as inputs for the identification algorithm presented in subsequent sections.

2.8 EOM of Rotor-2 in the Presence of AMB Support

Sawicki et al. (2009, 2011) in their works used AMB as an exciter for crack detection. Singh and Tiwari (2015) used AMB as a *support*, whose current signature has been used along with rotor vibration signature for a model-based identification of fatigue crack parameters. In the current work AMB is used as an auxiliary support. The force exerted by AMB is given by

$$\mathbf{f}_{AMB} = \begin{Bmatrix} -k_{sx}x_2 + k_{ix}i_x \\ -k_{sy}y_2 + k_{iy}i_y \end{Bmatrix} \tag{2.37}$$

The AMB force becomes nonlinear when the AMB journal (laminated core) operates radially close to the actuator. With the nominal unbalance and misalignment values and proper tuning of the PID, the AMB magnetic force can be simplified to its linear form. Tiwari (2008) gives the magnetic force expression exerted by an AMB as shown in Eqn. (2.37). Here k_{ix} and k_{iy} are AMB current stiffness constants in x_2 and y_2 directions, respectively, and k_{sx} and k_{sy} are AMB displacement stiffness constants in x_2 and y_2 transverse directions, respectively. i_x and i_y are AMB currents in x_2 and y_2 transverse directions, respectively. The stiffness constants of AMB depend on number of poles in the armature. Various researchers have used magnetic actuators with 3, 4, 6, 8 and 16 numbers of poles. The number of poles is mainly dictated by the load carrying capacity requirement of AMB. An isotropic 8-pole actuator hetero-polar actuator is being used in the current work. Thus Eqn. (2.37) transforms to

$$\mathbf{f}_{AMB} = \begin{bmatrix} -k & 0 \\ 0 & -k \end{bmatrix} \begin{Bmatrix} x_2 \\ y_2 \end{Bmatrix} + \begin{bmatrix} k_i & 0 \\ 0 & k_i \end{bmatrix} \begin{Bmatrix} i_x \\ i_y \end{Bmatrix} \tag{2.38}$$

It can been seen that magnetic force depends on the instantaneous displacements and currents in the direction of translational coordinates only. AMB currents i_x and i_y are related to the instantaneous translational displacements of the rotor at the point of support. The real time displacements of rotor at AMB location are input to controller, which uses specific control law to generate current. The choice of control law depends on application, operational speed and accuracy required. There is a vast amount of literature on various controllers, their advantages and applications. A comprehensive list of controllers is given in Schweitzer et al. (2009). In the present work Proportional–Integral–Derivative (PID) controller, which is more popular, owing to its comparitive simplicity, has been used. The governing equation for the PID control law is given by

$$i_x(t) = K_p x_2(t) + K_i \int x_2(t)dt + K_D \frac{dx_2(t)}{dt} \tag{2.39}$$

$$i_y(t) = K_p y_2(t) + K_i \int y_2(t)dt + K_D \frac{dy_2(t)}{dt} \tag{2.40}$$

where K_p is the proportional gain, K_I is the integral gain and K_D is the derivative gain of the controller, $x_2(t)$ and $y_2(t)$ are the instantaneous displacements of rotor-2 at the AMB

location in *x* and *y* directions, respectively. The choice of gain constants affects the resonant speeds and dynamic response of the rotor being supported by AMB (Tiwari, 2018). The gain constants used in this paper are taken from the work of Bordoloi and Tiwari (2013) and are found based on Routh-Hurwitz criteria of stability. A few works that deal with the tuning a PID controller for AMBs are Anantachaisilip and Lin (2013), Psonis et al. (2015) and Martin et al (2018). In the present formulation (Figure 2-1), an AMB is used as an auxiliary support for rotor-2, which provided controlling force. The corresponding magnetic forcing term appears additionally in the right hand side and Eqn. (2.23) changes to

$$\mathbf{M}_2\Delta\ddot{\mathbf{q}}_2+\mathbf{C}_2\Delta\dot{\mathbf{q}}_2+(\mathbf{K}_2+\mathbf{K}''_{\varphi_c})\Delta\mathbf{q}_2+\mathbf{K}'''_{\varphi_c}\Delta\mathbf{q}_1=\mathbf{f}_{unb_2}+\mathbf{f}_{mis_2}-\mathbf{f}_{AMB}-\mathbf{f}_{const_2} \tag{2.41}$$

The sign of the magnetic force takes + or – sign depending on whether AMB is exciting or supporting the rotor system. Physically, it means that when the AMB acts as an excitation force it adds to other external forces and when it acts as suppression force, it gets subtracted from other external forces. The reader can refer to the works of Sawicki et al. (2009, 2011) to gain better perspective on this.

2.9 Equations of Motion in Complex Form

For ease of computation the translational and rotational vibration responses of rotors is written in a complex form by multiplying the equations of motion in *y*-direction with '$\mathrm{j}=\sqrt{-1}$' and adding to the equation of motion in *x*-direction. The complex vibration response of rotors is then given by

$$\mathbf{v}_1=x_1+\mathrm{j}y_{11};\qquad \mathbf{v}_2=x_2+\mathrm{j}y_2 \tag{2.42}$$

Upon substituting Eqn. (2.42), the equations of motion of rotor-1 and rotor-2 given by Eqns. (2.20) and (2.41) transform into the following complex form

$$\bar{\mathbf{M}}_1\ddot{\mathbf{v}}_1+\bar{\mathbf{C}}_1\dot{\mathbf{v}}_1+\tilde{\mathbf{K}}_1\mathbf{v}_1+\bar{\mathbf{K}}_{t_3}\mathbf{v}_2=\bar{\mathbf{f}}_{unb_1}+\bar{\mathbf{f}}_{mis_1}-\bar{\mathbf{f}}_{const_1} \tag{2.43}$$

$$\bar{\mathbf{M}}_2\ddot{\mathbf{v}}_2+\bar{\mathbf{C}}_2\dot{\mathbf{v}}_2+\tilde{\mathbf{K}}_2\mathbf{v}_2+\bar{\mathbf{K}}_{t_3}\mathbf{v}_1=\bar{\mathbf{f}}_{unb_2}+\bar{\mathbf{f}}_{mis_2}-\bar{\mathbf{f}}_{cur}-\bar{\mathbf{f}}_{const_2} \tag{2.44}$$

with

$$\bar{\mathbf{M}}_1=m_1;\ \bar{\mathbf{M}}_2=m_2;\ \bar{\mathbf{C}}_1=c_{1xx};\ \bar{\mathbf{C}}_2=c_{2xx};\bar{\mathbf{K}}_1=k_{1xx}\ ;\ \bar{\mathbf{K}}_2=k_{2xx};$$

$$\bar{\mathbf{K}}_{t_3} = \lambda_1\lambda_2 k_{\phi_c}\,;\tilde{\mathbf{K}}_1 = k_{1xx} + \lambda_1^2 k_{\phi_c}\,;\tilde{\mathbf{K}}_2 = k_{2xx} + \lambda_2^2 k_{\phi_c} - k_s$$

Forcing terms on the RHS of Eqns. (2.43) and (2.44) are given by

$$\bar{\mathbf{f}}_{unb_1} = m_1 e_1 \omega^2 e^{\mathrm{j}(\omega t+\beta_1)};\ \bar{\mathbf{f}}_{unb_2} = m_2 e_2 \omega^2 e^{\mathrm{j}(\omega t+\beta_2)};\ \bar{\mathbf{f}}_{cur} = k_i i_c$$

$$\bar{\mathbf{f}}_{mis_1} = 0.5 s(t)\Delta k_{\xi}(1+e^{2\mathrm{j}\omega t})(\lambda_1^2\mathbf{v}_{10} + \lambda_1\lambda_2\mathbf{v}_{20});\ \bar{\mathbf{f}}_{mis_2} = 0.5 s(t)\Delta k_{\xi}(1+e^{2\mathrm{j}\omega t})(\lambda_1\lambda_2\mathbf{v}_{10} + \lambda_2^2\mathbf{v}_{20})$$

$$\bar{\mathbf{f}}_{const_1} = \lambda_1^2\bar{\mathbf{K}}_{\phi_c}\mathbf{v}_{10} + \lambda_1\lambda_2\bar{\mathbf{K}}_{\phi_c}\mathbf{v}_{20};\ \ \bar{\mathbf{f}}_{const_2} = \lambda_1\lambda_2\bar{\mathbf{K}}_{\phi_c}\mathbf{v}_{10} + \lambda_2^2\bar{\mathbf{K}}_{\phi_c}\mathbf{v}_{20};\ \ i_c = i_x + \mathrm{j}i_y$$

The static displacement is given by

$$\mathbf{v}_{10} = \delta_{x_{10}};\ \mathbf{v}_{20} = \delta_{x_{20}}$$

The forcing terms in Eqns. (2.43) and (2.44) are multi harmonic in nature and are of the form $ke^{\mathrm{j}i\omega t}$. Hence, the assumed solution or particular integral that represents the vibration response of rotors takes the form (Kreyszig, 2008)

$$\mathbf{v}_1(t) = \sum_{i=-\infty}^{i=\infty} R_{1i}e^{\mathrm{j}i\omega t};\qquad \mathbf{v}_2(t) = \sum_{i=-\infty}^{i=\infty} R_{2i}e^{\mathrm{j}i\omega t} \tag{2.45}$$

Likewise, the AMB current in time domain can be decomposed into its multi harmonic form, as

$$i_c(t) = \sum_{i=-\infty}^{i=\infty} I_i e^{\mathrm{ij}\omega t} \tag{2.46}$$

On substituting Eqns. (2.45) and (2.46) into Eqn. (2.43), the frequency domain representation of rotor-1 EOM is given as

$$\begin{aligned}&\left[\left(-(i\omega)^2\bar{\mathbf{M}}_1 + \mathrm{j}i\omega\bar{\mathbf{C}}_1 + \bar{\mathbf{K}}_1\right)R_{1i} + \tilde{\mathbf{K}}_{t_3}R_{2i}\right]\\ &= m_1 e_1\omega^2 e^{\mathrm{j}\beta_1} + \Delta k_{\xi}\left(\lambda_1^2\delta_{x_{10}} + \lambda_1\lambda_2\delta_{x_{20}}\right)p_i - k_{\varphi_c}\left(\lambda_1^2\delta_{x_{10}} + \lambda_1\lambda_2\delta_{x_{20}}\right)\end{aligned} \tag{2.47}$$

where p_i is the participation factor of the i^{th} harmonic of the misalignment excitation force. Likewise, upon substituting Eqns. (2.45) and (2.46) into Eqn. (2.44) the frequency domain representation of rotor-2 EOM is obtained as

$$\begin{aligned}&\left[\left(-(i\omega)^2\bar{\mathbf{M}}_2 + \mathrm{j}i\omega\bar{\mathbf{C}}_2 + \bar{\mathbf{K}}_2\right)R_{2i} + \tilde{\mathbf{K}}_{t_3}R_{1i}\right]\\ &= m_2 e_2\omega^2 e^{\mathrm{j}\beta_2} + \Delta k_{\xi}\left(\lambda_1\lambda_2\delta_{x_{10}} + \lambda_2^2\delta_{x_{20}}\right)p_i - K_I I_i - k_{\varphi_c}\left(\lambda_1\lambda_2\delta_{x_{10}} + \lambda_2^2\delta_{x_{20}}\right)\end{aligned} \tag{2.48}$$

Eqns. (2.47) and (2.48) represent the frequency domain equations for the coupled rotor system with integrated AMB, for harmonic indices ranging from $i = -n, \cdots, -2, -1, 0, 1, 2, \cdots, n$, which are characteristic of a system excited by coupling misalignment.

2.10 Estimation of Rotor, Coupling and AMB Parameters

In parameter identification in rotor-bearing systems, Lees and Friswell (1997), Sekhar (2005), and Tiwari et al. (2004) have used modal based methods for the identification of faults, such as unbalance, crack and bearing parameters. The identification has been performed using the least-squares fitting in either time or frequency domain. In the present section, an identification algorithm that estimates the system parameters from a least-squares problem by utilizing the bi-directional frequency data of rotor vibration and AMB current shall be developed.

The complex Eqns. (2.47) and (2.48) are expanded and rearranged so as to arrange the known parameters on the left hand side and unknown parameters on the right hand side. The identifiable parameters are $c_1, c_2, k_\varphi, \Delta k_\xi, e_1, \beta_1, e_2, \beta_2, k_s$ and k_i , which represent rotor-1 equivalent viscous damping in *x*-direction, rotor–2 equivalent viscous damping in *x*-direction, coupling static angular stiffness, coupling ACS, eccentricity of disc-1, phase of unbalance on disc-1, eccentricity of disc-2, phase of unbalance on disc-2, AMB displacement constant and AMB current constant, respectively. The development of regression equations for rotor-1 and rotor-2 are provided in next section.

2.11 Regression Equations of Rotor-1

Rearranging Eqn. (2.47) by segregating known and unknown quantities, we get

$$\left(\mathrm{j}i\omega c_{1xx} R_{1i} + \lambda_1^2 k_{\varphi_c} R_{1i} + \lambda_1\lambda_2 k_{\varphi_c} R_{2i}\right) - m_1 e_1 \omega^2 e^{\mathrm{j}(\beta_1)} - \Delta k_\xi \left(\lambda_1^2 \delta_{x_{10}} + \lambda_1\lambda_2 \delta_{x_{20}}\right) p_i$$
$$+ k_{\varphi_c}\left(\lambda_1^2 \delta_{x_{10}} + \lambda_1\lambda_2 \delta_{x_{20}}\right) = \left\{m_1 (i\omega)^2 - k_{1xx}\right\} R_{1i} \tag{2.49}$$

R_{1i}, R_{2i} represent the complex displacements of harmonics of rotor-1 and rotor-2. Eqn. (2.49) can be expanded for various harmonic indices, i.e. $i = -n, \ldots, -2, -1, 0, 1, 2, \ldots, n$.

2.11.1 *i* = 0: Constant Coupling Misalignment Force

Extracting terms corresponding to $i = 0$ from Eqn. (2.49), we get

$$k_{\varphi_c}\left(\lambda_1^2 R_{10} + \lambda_1\lambda_2 R_{20}\right) - \Delta k_\xi\left(\lambda_1^2\delta_{x_{10}} + \lambda_1\lambda_2\delta_{x_{20}}\right)p_0 + k_{\varphi_c}\left(\lambda_1^2\delta_{x_{10}} + \lambda_1\lambda_2\delta_{x_{20}}\right) = -k_{1xx}R_{10} \quad (2.50)$$

The real and imaginary displacement components of 0^{th} harmonic of rotor-1 are

$$R_{10} = R_{10,\mathrm{Re}} + \mathrm{j}R_{10,Im};\; R_{20} = R_{20,\mathrm{Re}} + \mathrm{j}R_{20,Im} \quad (2.51)$$

Upon substituting Eqn. (2.51), Eqn. (2.50) becomes

$$\begin{aligned} &k_{\varphi_c}\left\{\lambda_1^2\left(R_{10,\mathrm{Re}} + \mathrm{j}R_{10,Im}\right) + \lambda_1\lambda_2\left(R_{20,\mathrm{Re}} + \mathrm{j}R_{20,Im}\right)\right\} - \Delta k_\xi\left(\lambda_1^2\delta_{x_{10}} + \lambda_1\lambda_2\delta_{x_{20}}\right)p_0 \\ &+k_{\varphi_c}\left(\lambda_1^2\delta_{x_{10}} + \lambda_1\lambda_2\delta_{x_{20}}\right) = -k_{1xx}\left(R_{10,\mathrm{Re}} + \mathrm{j}R_{10,Im}\right) \end{aligned} \quad (2.52)$$

Eqn. (2.52) can be further separated into the real and imaginary parts, as

$$k_{\varphi_c}\left\{\lambda_1^2\left(R_{10,\mathrm{Re}} + \delta_{x_{10}}\right) + \lambda_1\lambda_2\left(R_{20,\mathrm{Re}} + \delta_{x_{20}}\right)\right\} - \Delta k_\xi\left(\lambda_1^2\delta_{x_{10}} + \lambda_1\lambda_2\delta_{x_{20}}\right)p_0 = -k_{1xx}\left(R_{10,\mathrm{Re}}\right) \quad (2.53)$$

$$k_{\varphi_c}\left(\lambda_1^2 R_{10,Im} + \lambda_1\lambda_2 R_{20,Im}\right) = -k_{1xx}R_{10,Im} \quad (2.54)$$

2.11.2 *i* = 1: Unbalance force and 1st harmonic of time dependent coupling misalignment force

Extracting terms corresponding to $i = 1$ from Eqn. (2.49), we get

$$\begin{aligned} &\left(\mathrm{j}\omega c_{1xx}R_{11} + z_1^2 k_{\varphi_c}R_{11} + z_1 z_2 k_{\varphi_c}R_{21}\right) - m_1 e_1\omega^2 e^{\mathrm{j}\beta_1} - \Delta k_\xi\left(z_1^2\delta_{x_{10}} + z_1 z_2\delta_{x_{20}}\right)p_1 \\ &= \left(m_1\omega^2 - k_{1xx}\right)R_{11} \end{aligned} \quad (2.55)$$

The real and imaginary displacement components of 1^{st} harmonic of rotor-1 are

$$R_{11} = R_{11,\mathrm{Re}} + \mathrm{j}R_{11,Im};\quad R_{21} = R_{21,\mathrm{Re}} + \mathrm{j}R_{21,Im} \quad (2.56)$$

Upon substituting Eqn. (2.56), Eqn. (2.55) becomes

$$\begin{aligned} &\left\{\mathrm{j}\omega c_{1xx}\left(R_{11,\mathrm{Re}} + \mathrm{j}R_{11,Im}\right) + z_1^2 k_{\varphi_c}\left(R_{11,\mathrm{Re}} + \mathrm{j}R_{11,Im}\right) + z_1 z_2 k_{\varphi_c}\left(R_{21,\mathrm{Re}} + \mathrm{j}R_{21,Im}\right)\right\} - m_1 e_1\omega^2 e^{\mathrm{j}\beta_1} \\ &-\Delta k_\xi\left(z_1^2\delta_{x_{10}} + z_1 z_2\delta_{x_{20}}\right)p_1 = \left(m_1\omega^2 - k_{1xx}\right)\left(R_{11,\mathrm{Re}} + \mathrm{j}R_{11,Im}\right) \end{aligned} \quad (2.57)$$

Eqn. (2.57) can be further separated into the real and imaginary parts, as

$$-\omega c_{1xx}R_{11,Im}+k_{\varphi_c}\left(z_1^2R_{11,\mathrm{Re}}+z_1z_2R_{21,\mathrm{Re}}\right)-m_1\omega^2e_{1,\mathrm{Re}}-\Delta k_{\xi}\left(z_1^2\delta_{x_{10}}+z_1z_2\delta_{x_{20}}\right)p_1 = \left(m_1\omega^2-k_{1xx}\right)R_{11,\mathrm{Re}} \tag{2.58}$$

$$\omega c_{1xx}R_{11,\mathrm{Re}}+k_{\varphi_c}\left(z_1^2R_{11,Im}+z_1z_2R_{21,Im}\right)-m_1\omega^2e_{1,\mathrm{Im}}=\left(m_1\omega^2-k_{1xx}\right)R_{11,Im} \tag{2.59}$$

2.11.3 $i \neq 0$ and $i \neq 1$: Other harmonics of time dependent coupling misalignment force

Extracting terms corresponding to $i \neq 0$ and $i \neq 1$ from Eqn. (2.49), we get

$$\left(\mathrm{j}i\omega c_{1xx}R_{1i}+z_1^2k_{\varphi_c}R_{1i}+z_1z_2k_{\varphi_c}R_{2i}\right)-\Delta k_{\xi}\left(z_1^2\delta_{x_{10}}+z_1z_2\delta_{x_{20}}\right)p_i = \left\{m_1\left(i\omega\right)^2-k_{1xx}\right\}R_{1i} \tag{2.60}$$

The real and imaginary displacement components of i^{th} harmonic of rotor-1 are

$$R_{1i}=R_{1i,\mathrm{Re}}+\mathrm{j}R_{1i,Im};\qquad R_{2i}=R_{2i,\mathrm{Re}}+\mathrm{j}R_{2i,Im} \tag{2.61}$$

Upon substituting Eqn. (2.61), Eqn. (2.60) becomes

$$\left\{ji\omega c_{1xx}\left(R_{1i,\mathrm{Re}}+\mathrm{j}R_{1i,Im}\right)+z_1^2k_{\varphi_c}\left(R_{1i,\mathrm{Re}}+\mathrm{j}R_{1i,Im}\right)+z_1z_2k_{\varphi_c}\left(R_{2i,\mathrm{Re}}+\mathrm{j}R_{2i,Im}\right)\right\}- \Delta k_{\xi}\left(z_1^2\delta_{x_{10}}+z_1z_2\delta_{x_{20}}\right)p_i=\left\{m_1\left(i\omega\right)^2-k_{1xx}\right\}\left(R_{1i,\mathrm{Re}}+\mathrm{j}R_{1i,Im}\right) \tag{2.62}$$

Eqn. (2.62) can be further separated into the real and imaginary parts, as

$$-i\omega c_{1xx}R_{1i,Im}+k_{\varphi_c}\left(z_1^2R_{1i,\mathrm{Re}}+z_1z_2R_{2i,\mathrm{Re}}\right)-\Delta k_{\xi}\left(z_1^2\delta_{x_{10}}+z_1z_2\delta_{x_{20}}\right)p_i = \left\{m_1\left(i\omega\right)^2-k_{1xx}\right\}R_{1i,\mathrm{Re}} \tag{2.63}$$

$$i\omega c_{1xx}R_{1i,\mathrm{Re}}+k_{\varphi_c}\left(z_1^2R_{1i,Im}+z_1z_2R_{2i,Im}\right)=\left\{m_1\left(i\omega\right)^2-k_{1xx}\right\}R_{1i,Im} \tag{2.64}$$

2.12 Regression Equations of Rotor-2

Rearranging Eqn. (2.48) by segregating the known and unknown quantities, we get

$$\left(\mathrm{j}i\omega c_{2xx}R_{2i}+z_2^2k_{\varphi_c}R_{2i}+z_1z_2k_{\varphi_c}R_{1i}\right)-m_2e_2\omega^2e^{\mathrm{j}(\beta_2)}-\Delta k_{\xi}\left(z_1z_2\delta_{x_{10}}+z_2^2\delta_{x_{20}}\right)p_i +\left(k_II_i+k_sR_{2i}\right)+k_{\varphi_c}\left(z_1z_2\delta_{x_{10}}+z_2^2\delta_{x_{20}}\right)=m_2\left(i\omega\right)^2-k_{2xx}R_{2i} \tag{2.65}$$

Eqn. (2.65) takes the following modified form

$$\begin{aligned}\left(\mathrm{j}i\omega c_{2xx}R_{2i}+z_2^2k_{\varphi_c}R_{2i}+z_1z_2k_{\varphi_c}R_{1i}\right)-m_2e_2\omega^2e^{\mathrm{j}(\beta_2)}-\Delta k_{\xi}\left(z_1z_2\delta_{x_{10}}+z_2^2\delta_{x_{20}}\right)p_i+k_II_i\\+k_sR_{2i}+k_{\varphi_c}\left(z_1z_2\delta_{x_{10}}+z_2^2\delta_{x_{20}}\right)=\left\{m_2\left(i\omega\right)^2-k_{2xx}\right\}R_{2i}\end{aligned} \tag{2.66}$$

Eqn. (2.66) can be expanded for various harmonic indices, i.e. $i = -n,\ldots,-2,-1,0,1,2,\ldots,n$.

2.12.1 i = 0: Constant Coupling Misalignment Force

Extracting terms corresponding to $i = 0$ from Eqn. (2.66), we get

$$k_{\varphi_c}\left(z_2^2R_{20}+z_1z_2R_{10}\right)-\Delta k_{\xi}\left(z_1z_2\delta_{x_{10}}+z_2^2\delta_{x_{20}}\right)p_0+k_II_0+k_sR_{20}+k_{\varphi_c}\left(z_1z_2\delta_{x_{10}}+z_2^2\delta_{x_{20}}\right)=-k_2'R_{20} \tag{2.67}$$

0^{th} harmonic of rotor-2 displacement is made of the real and imaginary components, i.e.

$$R_{10}=R_{10,\mathrm{Re}}+\mathrm{j}R_{10,Im};\quad R_{20}=R_{20,\mathrm{Re}}+\mathrm{j}R_{20,Im};\quad I_0=I_{0,\mathrm{Re}}+\mathrm{j}I_{0,Im} \tag{2.68}$$

Upon substituting Eqn. (2.68), Eqn. (2.67) becomes

$$\begin{aligned}k_{\varphi_c}\left\{z_2^2\left(R_{20,\mathrm{Re}}+\mathrm{j}R_{20,Im}\right)+z_1z_2\left(R_{10,\mathrm{Re}}+\mathrm{j}R_{10,Im}\right)\right\}-\Delta k_{\xi}\left(z_1z_2\delta_{x_{10}}+z_2^2\delta_{x_{20}}\right)p_0\\+K_I\left(I_{0,\mathrm{Re}}+\mathrm{j}I_{0,Im}\right)+k_s(R_{20,\mathrm{Re}}+\mathrm{j}R_{20,Im})+k_{\varphi_c}\left(z_1z_2\delta_{x_{10}}+z_2^2\delta_{x_{20}}\right)=-k_{2xx}\left(R_{20,\mathrm{Re}}+\mathrm{j}R_{20,Im}\right)\end{aligned} \tag{2.69}$$

Eqn. (2.69) can be further separated into the real and imaginary parts, as

$$\begin{aligned}k_{\varphi_c}\left\{z_2^2\left(R_{20,\mathrm{Re}}+\delta_{x_{20}}\right)+z_1z_2\left(R_{10,\mathrm{Re}}+\delta_{x_{10}}\right)\right\}-\Delta k_{\xi}\left(z_1z_2\delta_{x_{10}}+z_2^2\delta_{x_{20}}\right)p_0\\+k_II_{0,\mathrm{Re}}+k_sR_{20,\mathrm{Re}}=-k_{2xx}R_{20,\mathrm{Re}}\end{aligned} \tag{2.70}$$

$$k_{\varphi_c}\left(z_2^2R_{20,Im}+z_1z_2R_{10,Im}\right)+k_II_{0,Im}+k_sR_{20,Im}=-k_{2xx}R_{20,Im} \tag{2.71}$$

2.12.2 i = 1: Unbalance force and 1st harmonic of time dependent coupling misalignment force

Extracting terms corresponding to $i = 1$ from Eqn. (2.66), we get

$$\left(\mathrm{j}\omega c_{2xx}R_{21}+z_2^2k_{\varphi_c}R_{21}+z_1z_2k_{\varphi_c}R_{11}\right)-m_2e_2\omega^2e^{\mathrm{j}\beta_2}-\Delta k_{\xi}\left(z_1z_2\delta_{x_{10}}+z_2^2\delta_{x_{20}}\right)p_1 \\ +k_II_1+k_sR_{21,\mathrm{Re}}=\left(m_2\omega^2-k_{2xx}\right)R_{21} \tag{2.72}$$

The real and imaginary components of 1st harmonic of rotor-2 complex displacement and current are

$$R_{11}=R_{11,\mathrm{Re}}+\mathrm{j}R_{11,Im};\quad R_{21}=R_{21,\mathrm{Re}}+\mathrm{j}R_{21,Im};\quad I_1=I_{1,\mathrm{Re}}+\mathrm{j}I_{1,Im} \tag{2.73}$$

Upon substituting Eqn. (2.73), Eqn. (2.72) becomes

$$\left\{\mathrm{j}\omega c_{2xx}\left(R_{21,\mathrm{Re}}+\mathrm{j}R_{21,Im}\right)+z_2^2k_{\varphi_c}\left(R_{21,\mathrm{Re}}+\mathrm{j}R_{21,Im}\right)+z_1z_2k_{\varphi_c}\left(R_{11,\mathrm{Re}}+\mathrm{j}R_{11,Im}\right)\right\} \\ -m_2e_2\omega^2e^{j\beta_2}-\Delta k_{\xi}\left(z_1z_2\delta_{x_{10}}+z_2^2\delta_{x_{20}}\right)p_1+k_i\left(I_{1,\mathrm{Re}}+\mathrm{j}I_{1,Im}\right)+k_s(R_{21,\mathrm{Re}}+\mathrm{j}R_{21,Im}) \\ =\left(m_2\omega^2-k_{2xx}\right)\left(R_{21,\mathrm{Re}}+\mathrm{j}R_{21,Im}\right) \tag{2.74}$$

Eqn. (2.74) can be further separated into the real and imaginary parts, as

$$-\omega c_{2xx}R_{21,Im}+k_{\varphi_c}(z_2^2R_{21,\mathrm{Re}}+z_1z_2R_{11,\mathrm{Re}})-m_2\omega^2e_{2,\mathrm{Re}}-\Delta k_{\xi}\left(z_1z_2\delta_{x_{10}}+z_2^2\delta_{x_{20}}\right)p_1+k_II_{1,\mathrm{Re}}+k_sR_{21,\mathrm{Re}} \\ =\left(m_2\omega^2-k_{2xx}\right)R_{21,\mathrm{Re}} \tag{2.75}$$

$$\omega c_{2xx}R_{21,\mathrm{Re}}+k_{\varphi_c}\left(z_2^2R_{21,Im}+z_1z_2R_{11,Im}\right)-m_2\omega^2e_{2,\mathrm{Im}}+K_II_{1,Im}+k_sR_{21,\mathrm{Im}} \\ =\left(m_2\omega^2-k_{2xx}\right)R_{21,Im} \tag{2.76}$$

2.12.3 $i\neq 0$ and $i\neq 1$: **Other harmonics of time dependent coupling misalignment force**

Extracting terms corresponding to $i\neq 0$ and $i\neq 1$ from Eqn. (2.66), we get

$$\left(\mathrm{j}i\omega c_{2xx}R_{2i}+z_2^2k_{\varphi_c}R_{2i}+z_1z_2k_{\varphi_c}R_{1i}\right)-\Delta k_{\xi}\left(z_1z_2\delta_{x_{10}}+z_2^2\delta_{x_{20}}\right)p_i+k_II_i+k_sR_{2i} \\ =\left\{m_2\left(i\omega\right)^2-k_{2xx}\right\}R_{2i} \tag{2.77}$$

The real and imaginary displacement components of i^{th} harmonic of rotor-2 complex displacement and current are

$$R_{1i}=R_{1i,\mathrm{Re}}+jR_{1i,Im};\quad R_{2i}=R_{2i,\mathrm{Re}}+jR_{2i,Im};\quad I_i=I_{i,\mathrm{Re}}+jI_{i,Im} \tag{2.78}$$

Upon substituting Eqn. (2.78), Eqn. (2.77) becomes

$$\left\{ ji\omega c_{2xx}\left(R_{2i,\mathrm{Re}}+\mathrm{j}R_{2i,Im}\right)+z_2^2k_{\varphi_c}\left(R_{2i,\mathrm{Re}}+\mathrm{j}R_{2i,Im}\right)+z_1z_2k_{\varphi_c}\left(R_{1i,\mathrm{Re}}+\mathrm{j}R_{1i,Im}\right)\right\}-$$
$$\Delta k_{\xi}\left(z_1z_2\delta_{x_{10}}+z_2^2\delta_{x_{20}}\right)p_i+k_I\left(I_{i,\mathrm{Re}}+\mathrm{j}I_{i,Im}\right)+k_s\left(R_{2i,\mathrm{Re}}+\mathrm{j}R_{2i,Im}\right)= \quad (2.79)$$
$$\left\{m_2\left(i\omega\right)^2-k_{2xx}\right\}\left(R_{2i,\mathrm{Re}}+\mathrm{j}R_{2i,Im}\right)$$

Eqn. (2.79) can be further separated into the real and imaginary parts, as

$$-i\omega c_{2xx}R_{2i,Im}+k_{\varphi_c}\left(z_2^2R_{2i,\mathrm{Re}}+z_1z_2R_{1i,\mathrm{Re}}\right)-\Delta k_{\xi}\left(z_1z_2\delta_{x_{10}}+z_2^2\delta_{x_{20}}\right)p_i+k_iI_{i,\mathrm{Re}}+k_sR_{2i,\mathrm{Re}}$$
$$=\left\{m_2\left(i\omega\right)^2-k_{2xx}\right\}R_{2i,\mathrm{Re}} \quad (2.80)$$

$$i\omega c_{2xx}R_{2i,\mathrm{Re}}+k_{\varphi_c}\left(z_2^2R_{2i,Im}+z_1z_2R_{1i,Im}\right)+k_iI_{i,Im}+k_sR_{2i,Im}=\left\{m_2\left(i\omega\right)^2-k_{2xx}\right\}R_{2i,Im} \quad (2.81)$$

Regression Eqns. (2.53), (2.54), (2.58), (2.59), (2.63) and (2.64) of rotor-1 and Eqns. (2.70), (2.71), (2.75), (2.76), (2.80), (2.81) of rotor-2 are arranged in a matrix form, as

$$\mathbf{A}_1\mathbf{x}_1=\mathbf{b}_1 \quad (2.82)$$

$$\mathbf{A}_1=\begin{bmatrix}
0 & 0 & 0 & 0 & 0 & 0 & \lambda_1^2\left(R_{10,\mathrm{Re}}+\delta_{x_{10}}\right)+\lambda_1\lambda_2\left(R_{20,\mathrm{Re}}+\delta_{x_{20}}\right) & -\left(\lambda_1^2\delta_{x_{10}}+\lambda_1\lambda_2\delta_{x_{20}}\right)p_0 & 0 & 0\\
0 & 0 & 0 & 0 & 0 & 0 & \lambda_1^2R_{10,Im}+\lambda_1\lambda_2R_{20,Im} & 0 & 0 & 0\\
-\omega R_{11,Im} & 0 & -m_1\omega^2 & 0 & 0 & 0 & \lambda_1^2R_{11,\mathrm{Re}}+\lambda_1\lambda_2R_{21,\mathrm{Re}} & -\left(\lambda_1^2\delta_{x_{10}}+\lambda_1\lambda_2\delta_{x_{20}}\right)p_1 & 0 & 0\\
\vdots & \vdots & \vdots & \vdots & \vdots & \vdots & \vdots & \vdots & \vdots & \vdots\\
5\omega R_{15,\mathrm{Re}} & 0 & 0 & 0 & 0 & 0 & \lambda_1^2R_{15,Im}+\lambda_1\lambda_2R_{25,Im} & 0 & 0 & 0\\
0 & 0 & 0 & 0 & 0 & 0 & \lambda_2^2\left(R_{20,\mathrm{Re}}+\delta_{x_{20}}\right)+\lambda_1\lambda_2\left(R_{10,\mathrm{Re}}+\delta_{x_{10}}\right) & -\left(\lambda_1\lambda_2\delta_{x_{10}}+\lambda_2^2\delta_{x_{20}}\right)p_0 & I_{0,\mathrm{Re}} & R_{20,\mathrm{Re}}\\
0 & 0 & 0 & 0 & 0 & 0 & \lambda_2^2R_{20,Im}+\lambda_1\lambda_2R_{10,Im} & 0 & I_{0,Im} & R_{20,Im}\\
0 & 0 & 0 & 0 & -m_2\omega^2 & 0 & \lambda_2^2R_{21,\mathrm{Re}}+\lambda_1\lambda_2R_{11,\mathrm{Re}} & -\left(\lambda_1\lambda_2\delta_{x_{10}}+\lambda_2^2\delta_{x_{20}}\right)p_1 & I_{1,\mathrm{Re}} & R_{21,\mathrm{Re}}\\
\vdots & \vdots & \vdots & \vdots & \vdots & \vdots & \vdots & \vdots & \vdots & \vdots\\
0 & 5\omega R_{25,\mathrm{Re}} & 0 & 0 & 0 & 0 & \lambda_2^2R_{25,Im}+\lambda_1\lambda_2R_{15,Im} & 0 & I_{5,Im} & R_{25,\mathrm{Im}}\\
\omega R_{-11,Im} & 0 & 0 & 0 & 0 & 0 & \lambda_1^2R_{-11,\mathrm{Re}}+\lambda_1\lambda_2R_{-21,\mathrm{Re}} & -\left(\lambda_1^2\delta_{x_{10}}+\lambda_1\lambda_2\delta_{x_{20}}\right)p_{-1} & 0 & 0\\
-\omega R_{-11,\mathrm{Re}} & 0 & 0 & 0 & 0 & 0 & \lambda_1^2R_{-11,Im}+\lambda_1\lambda_2R_{-21,Im} & 0 & 0 & 0\\
\vdots & \vdots & \vdots & \vdots & \vdots & \vdots & \vdots & \vdots & \vdots & \vdots\\
5\omega R_{-15,Im} & 0 & 0 & 0 & 0 & 0 & \lambda_1^2R_{-15,\mathrm{Re}}+\lambda_1\lambda_2R_{-25,\mathrm{Re}} & -\left(\lambda_1^2\delta_{x_{10}}+\lambda_1\lambda_2\delta_{x_{20}}\right)p_{-5} & 0 & 0\\
-5\omega R_{-15,\mathrm{Re}} & 0 & 0 & 0 & 0 & 0 & \lambda_1^2R_{-15,Im}+\lambda_1\lambda_{22}R_{-25,Im} & 0 & 0 & 0\\
0 & \omega R_{-21,Im} & 0 & 0 & 0 & 0 & 0 & -\left(\lambda_1\lambda_2\delta_{x_{10}}+\lambda_2^2\delta_{x_{20}}\right)p_{-1} & 0 & 0\\
0 & -\omega R_{-21,\mathrm{Re}} & 0 & 0 & 0 & 0 & 0 & 0 & 0 & 0\\
0 & \vdots & \vdots & \vdots & \vdots & \vdots & \vdots & \vdots & \vdots & \vdots\\
0 & 5\omega R_{-25,Im} & 0 & 0 & 0 & 0 & \lambda_2^2R_{-25,\mathrm{Re}}+\lambda_1\lambda_2R_{-15,\mathrm{Re}} & -\left(\lambda_1\lambda_2\delta_{x_{10}}+\lambda_2^2\delta_{x_{20}}\right)p_{-5} & I_{-5,\mathrm{Re}} & R_{-25,\mathrm{Re}}\\
0 & -5\omega R_{-25,\mathrm{Re}} & 0 & 0 & 0 & 0 & \lambda_2^2R_{-25,Im}+\lambda_1\lambda_2R_{-15,Im} & 0 & I_{-5,\mathrm{Im}} & R_{-25,\mathrm{Im}}
\end{bmatrix} \quad (2.83)$$

$$\mathbf{b}_1 = \begin{Bmatrix} -k_{1xx}R_{10,\mathrm{Re}} \\ -k_{1xx}R_{10,\mathrm{Im}} \\ (\omega^2 m_1 - k_{1xx})R_{11,\mathrm{Re}} \\ \vdots \\ (25\omega^2 m_1 - k_{1xx})R_{15,\mathrm{Im}} \\ -k_{2xx}R_{20,\mathrm{Re}} \\ -k_{2xx}R_{20,\mathrm{Im}} \\ (\omega^2 m_2 - k_{2xx})R_{21,\mathrm{Re}} \\ \vdots \\ (25\omega^2 m_2 - k_{2xx})R_{25,\mathrm{Im}} \\ (\omega^2 m_1 - k_{1xx})R_{-11,\mathrm{Re}} \\ (\omega^2 m_1 - k_{1xx})R_{-11,\mathrm{Im}} \\ \vdots \\ (25\omega^2 m_1 - k_{1xx})R_{-15,\mathrm{Re}} \\ (25\omega^2 m_1 - k_{1xx})R_{-15,\mathrm{Im}} \\ (\omega^2 m_2 - k_{2xx})R_{-21,\mathrm{Re}} \\ (\omega^2 m_2 - k_{2xx})R_{-21,\mathrm{Im}} \\ \vdots \\ (25\omega^2 m_2 - k_{2xx})R_{-25,\mathrm{Re}} \\ (25\omega^2 m_2 - k_{2xx})R_{-25,\mathrm{Im}} \end{Bmatrix} \tag{2.84}$$

$$\mathbf{x}_1 = \begin{Bmatrix} c_{1xx} & c_{2xx} & e_{1,\mathrm{Re}} & e_{1,\mathrm{Im}} & e_{2,\mathrm{Re}} & e_{2,\mathrm{Im}} & k_{\varphi_c} & \Delta k_{\xi} & k_i & k_s \end{Bmatrix}^T \tag{2.85}$$

The regression matrix $\mathbf{A}_1$, vector of known quantities $\mathbf{b}_1$ and vector of identifiable parameters $\mathbf{x}_1$ used in the estimation of various system faults and parameters are shown in Eqns. (2.83), (2.84) and (2.85). Vector x_1 containing the identifiable parameters can be obtained by solving inverse problem

$$\mathbf{x_1} = \left(\mathbf{A_1}^{\mathrm{T}}\mathbf{A_1}\right)^{-1}\mathbf{A_1}^{\mathrm{T}}\mathbf{b_1} \tag{2.86}$$

The effect of including data from a range of spin speeds on the estimates can be studied from

$$\begin{Bmatrix} \mathbf{A_1}(\omega_1) \\ \mathbf{A_1}(\omega_2) \\ \vdots \\ \mathbf{A_1}(\omega_n) \end{Bmatrix} \mathbf{x_1} = \begin{Bmatrix} \mathbf{b_1}(\omega_1) \\ \mathbf{b_1}(\omega_2) \\ \vdots \\ \mathbf{b_1}(\omega_n) \end{Bmatrix} \tag{2.87}$$

The advantage of using cumulative data from a range of speeds in Eqn. (2.87) is that the condition number of the matrix $\mathbf{A_1}$ improves thereby resulting in estimates closer to the actual values.

2.13 Estimation of Harmonics of Displacement and Current

Both left and right hand sides of Eqns. (2.82) and (2.87) contain the real and imaginary components of complex vibration outputs of rotor-1 and rotor-2, and complex current output of AMB for harmonic indices ranging from $i = -n,\ldots,-2,-1,0,1,2,\ldots,n$. These components can be obtained by two different methods discussed in the next subsections.

2.13.1Least Squares Regression Method in Time Domain

The harmonic content, i.e. the fundamental frequencies of time domain signal of complex current and displacement signals, represented by Eqns. (2.45) and (2.46) can be extracted using least-squares regression method, which is of the form

$$\left(\mathbf{A}_2\right)_{n\times i}\left(\mathbf{x}_{R_1}\right)_{i\times 1} = \left(\mathbf{b}_{r_1}\right)_{n\times 1} \tag{2.88}$$

with

$$\left(\mathbf{A}_1\right)_{n\times i} = \begin{bmatrix} 1 & e^{j\omega t_1} & \cdots & e^{j(5\omega)t_1} & \cdots & e^{j(-\omega)t_1} & \cdots & e^{j(-5\omega)t_1} \\ 1 & e^{j\omega t_2} & \cdots & e^{j(5\omega)t_2} & \cdots & e^{j(-\omega)t_2} & \cdots & e^{j(-5\omega)t_2} \\ \vdots & \vdots & \vdots & \vdots & \vdots & \vdots & \vdots & \vdots \\ \vdots & \vdots & \vdots & \vdots & \vdots & \vdots & \vdots & \vdots \\ 1 & e^{j\omega t_n} & \cdots & e^{j(5\omega)t_n} & \cdots & e^{j(-\omega)t_n} & \cdots & e^{j(-5\omega)t_n} \end{bmatrix} \tag{2.89}$$

The vector of complex vibration signal obtained at different instants of time is given by

$$\left(\mathbf{b}_{r_1}\right)_{n\times 1} = \left\{r_{1_c}(t_1) \quad r_{1_c}(t_2) \quad r_{1_c}(t_3) \quad \cdots \quad \cdots \quad \cdots \quad r_{1_c}(t_n)\right\}^T \tag{2.90}$$

And the vector of unknowns representing the complex harmonics is given by

$$\left(\mathbf{x}_{R_1}\right)_{i\times 1} = \left\{R_{10}(\omega) \quad R_{11}(\omega) \quad \cdots \quad R_{15}(\omega) \quad \cdots \quad R_{-11}(\omega) \quad \cdots \quad R_{-15}(\omega)\right\}^T \tag{2.91}$$

Similar relations exist for rotor-2 vibration response and the AMB current, and they can be collectively written in a single matrix equation, as

$$\begin{bmatrix}\mathbf{x}_{R_1} & \mathbf{x}_{R_2} & \mathbf{x}_I\end{bmatrix} = \left(\mathbf{A}_2^T\mathbf{A}_2\right)^{-1}\mathbf{A}_2^T\begin{bmatrix}\mathbf{b}_{r_1} & \mathbf{b}_{r_2} & \mathbf{b}_i\end{bmatrix} \tag{2.92}$$

2.13.2 Full Spectrum through FFT

Alternatively the complex harmonics obtained through Eqn. (2.92) can also be obtained directly by passing the time domain vibration and current signals- sent from “To

Workspace" block in Simulink model to the Matlab workspace - through Fast Fourier Transform (FFT) algorithm. Since both positive and negative frequencies exist in the signal, a full spectrum plot needs to be made use of to understand the qualitative nature of fault the time domain signal represents. Full spectrum contains information about the forward and backward whirl modes which is the uniqueness of rotor system with gyroscopic effect. This bidirectional data is useful in the estimation of both unbalance which has only forward whirl contribution and misalignment which has both forward and backward whirl contribution parameters. A comprehensive treatment of the mathematical procedure to obtain full spectrum and its application to rotating machinery diagnostics has been given in Goldman and Muszynska (1999). However, it requires phase corrections as explained in the following subsection.

2.13.3 Phase Abnormality and Compensation

It has been noticed that two different time domain signals of same amplitude and frequency content, which are acquired at different instants of time undergo a variation in the phase when passed through the FFT. The FFT algorithm on the other hand doesn't affect the amplitude information of harmonics of the two signals. Passing these complex harmonics to Eqns. (2.82) and (2.87) would result in incorrect estimation of system parameters.

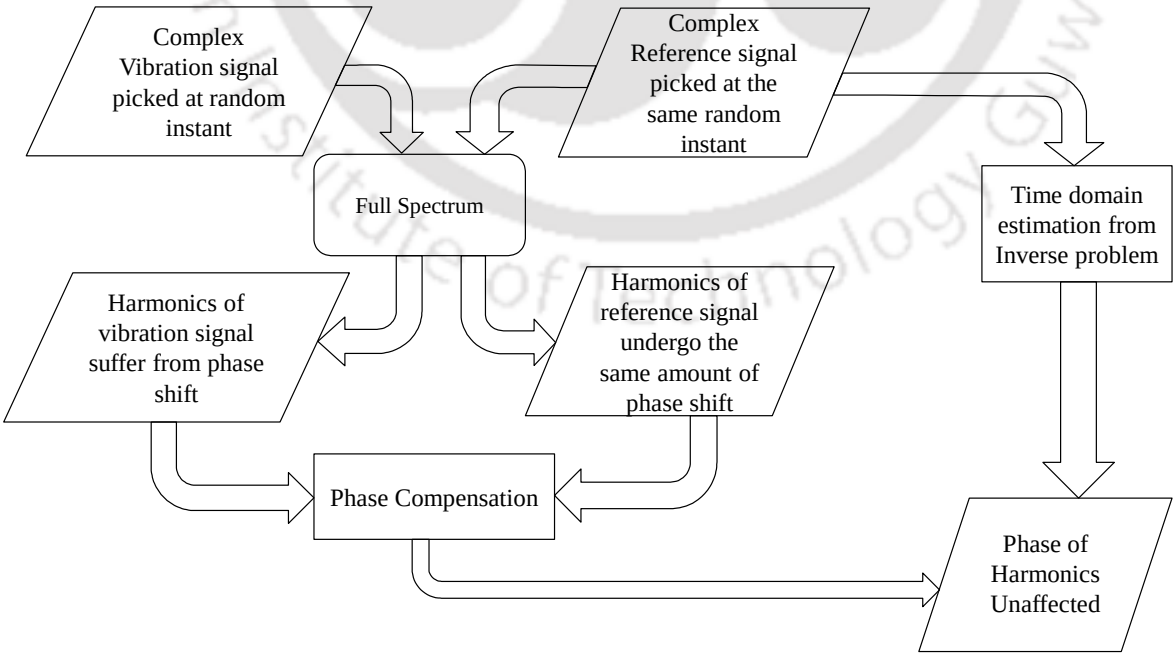

Figure 2-6 Phase compensation in full spectrum

To overcome this shortcoming, Singh and Tiwari (2015) envisaged a complex multi-harmonic reference signal to account for the phase variation that occurs in the usage of FFT algorithm.

$$r(t) = \cos(i\omega t) + \mathrm{j}\sin(i\omega t) \tag{2.93}$$

with $i = -n, -(n-1), \ldots, -1, 0, 1, \ldots, (n-1), n$

The number i represents the harmonic number of the fundamental frequency. The number of harmonics here depend on the amount of misalignment. Ideally the sampling frequency of data acquisition, which should be 2.0 times the frequency corresponding to the maximum operating speed so as not to lose the information of the required harmonics of interest. Applying FFT algorithm on the signal given by Eqn. (2.93) gives amplitude and phase of harmonics contained in the signal. The harmonic content present in the signal can be mathematically represented by

$$R(\omega) = |R_i| \angle \varphi_i(\omega) \tag{2.94}$$

Figure 2-6 shows the diagrammatic representation of the phase compensation procedure. A complex reference signal is obtained simultaneously along with the complex displacement and current signals and passed to the full spectrum algorithm. This causes the reference signal to undergo the same amount of phase shift as the vibration or current signal of interest. Subtracting the phase of the harmonics of the reference signal from that of the current and vibration signals reveals the true phase content of the latter signals. Mathematically, this is represented as

$$R_{1i} = |R_{1i}| \angle (\theta_{1i} - \varphi_i); \quad R_{2i} = |R_{2i}| \angle (\theta_{2i} - \varphi_i); \quad I_i = |I_i| \angle (\theta_{3i} - \varphi_i) \tag{2.95}$$

Where R_{1i}, R_{2i} and I_i represent the amplitudes of the i^{th} harmonic of rotor-1, rotor-2 and AMB current, respectively. θ_{1i}, θ_{2i} and θ_{3i} represent the phase angles of the respective i^{th} harmonics. φ_i is the phase angle of the i^{th} harmonic of complex reference signal. On a test rig, this can be realized by acquiring the vibratory displacement data from eddy current proximity sensors that are orthogonally placed above the shaft close to drive end. A complex reference signal is obtained from real (x-axis) and quadrature (y-axis) signals simultaneously along with other complex output signals (vibration and current) of interest.

2.14 Results and Discussion

The values of various rotor, coupling an AMB parameters assumed for simulation are listed in Table 2-2. Eqns. (2.43) and (2.44) are used to build the representative Simulink™ model shown in Figure 2-7. The model has two primary sub blocks representing rotor-1 and rotor-2, respectively. A reference signal is generated for implementing phase correction. The solution was run with fourth order Runge-Kutta (ode4) solver for a duration of 3 seconds acquiring 2^{16} (65536) samples per second of simulation time. However, for experimental purpose a lower sampling rate will be sufficient as it will save on the hardware memory requirements.

Table 2-2 Assumed values of coupled rotor system used in numerical simulation

Parameter	Value	Parameter	Value
m_1, kg	2	k_s, N/m	105210
m_2, kg	2.5	k_i, N/A	42.1
k_{1xx}, N/m	7.5×10^{5}	e_1, m	240×10^{-6}
$k_{2x\varphi_y}$, N/m	7.5×10^{5}	e_2, m	240×10^{-6}
c_{1xx}, N-s/mm	27	β_1, rad	$\pi/18$
c_{2xx}, N-s/mm	50	β_2, rad	$\pi/18$
a_1, m	0.25	$\delta_{x_{10}}$, m	2.33×10^{-5}
b_1, m	0.25	$\delta_{x_{20}}$, m	2.91×10^{-5}
a_2, m	0.25	K_P, A/m	12200
b_2, m	0.25	K_I, A/(m-s)	2000
k_{φ_c}, N-m/rad	300	K_D, (A-s)/m	3
Δk_{ξ}, N-m/rad	50	l_i, m	0.5

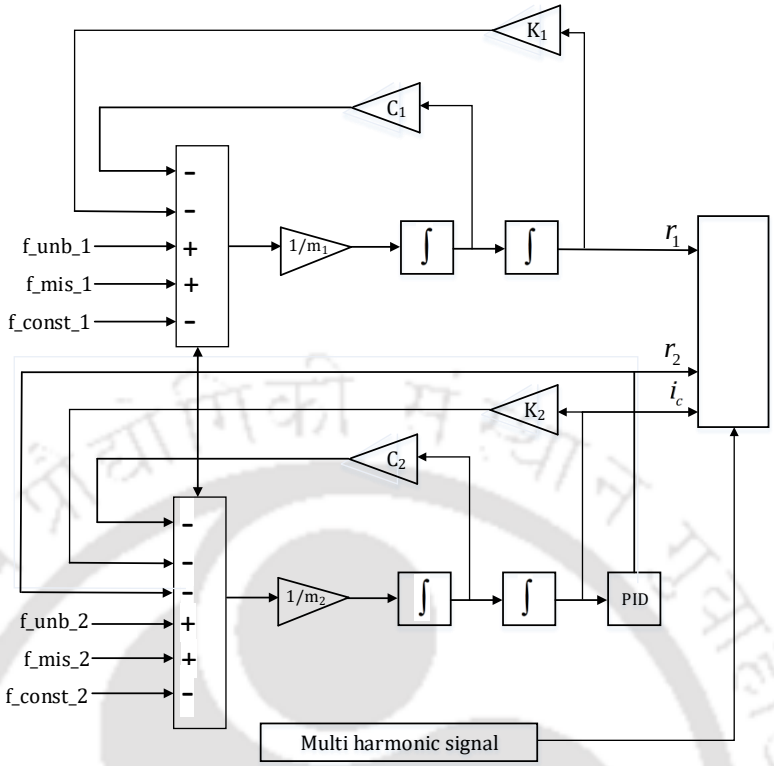

Figure 2-7 Simulink model of coupled rotor-AMB system

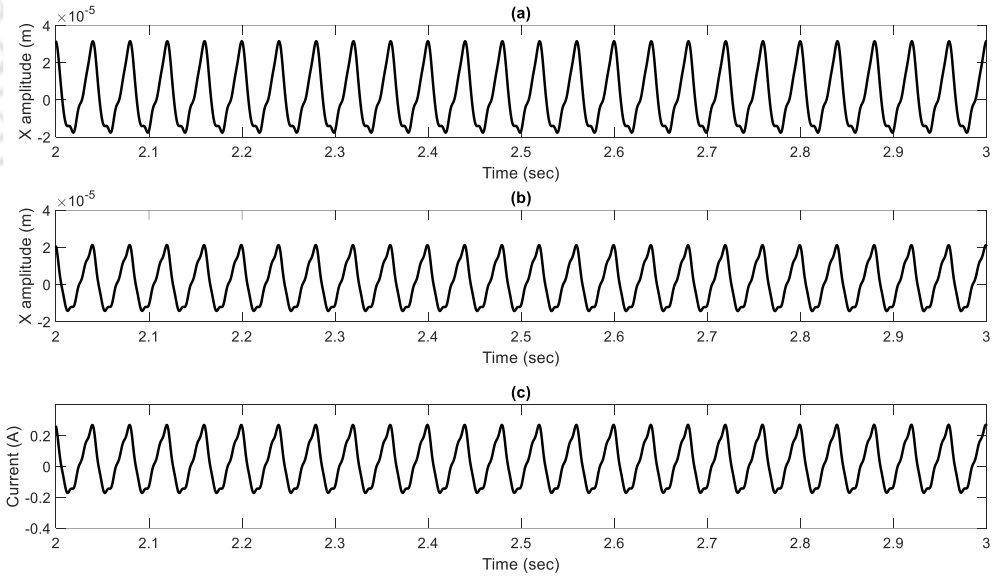

Figure 2-8 Time domain response at 25 Hz for unbalance and misalignment (a) Rotor-1 displacement (b) Rotor-2 displacement (c) AMB Current

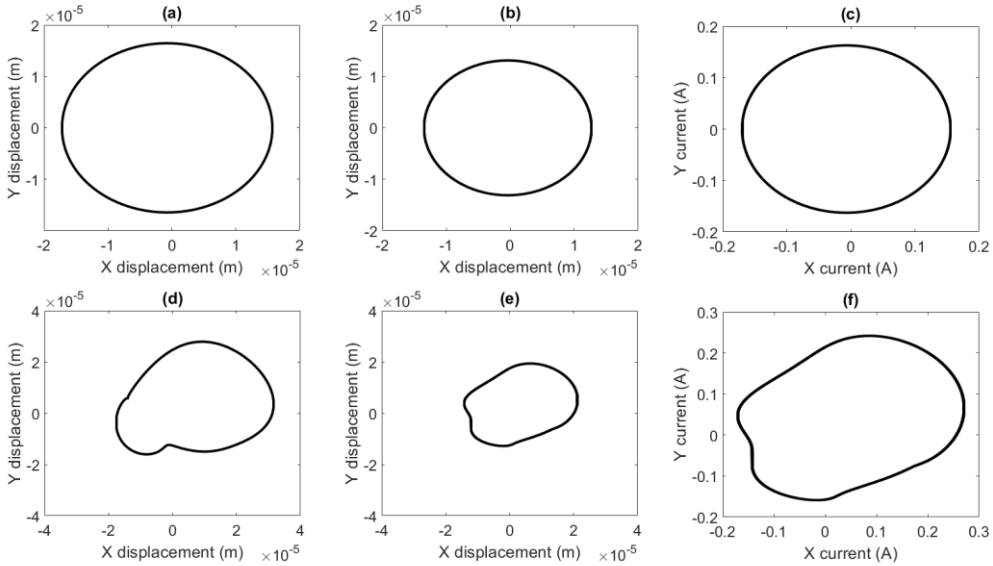

Figure 2-9 Orbit plots of Rotor-1, Rotor-2, and AMB at 25 Hz: (a, b, c) when unbalance is present; (d, e, f) when both unbalance and misalignment are present

To avoid the influence of transient response on the steady-state output the response from the last second has been considered. This model generates time domain responses of coupled rotor system supported by AMB when the system is excited by the unbalance force, and the couplings static and time- dependent misalignment couples. The vibration output from rotor-1, rotor-2 and current output from AMB are sent to “Bus creator” block and finally to “To Workspace” block.

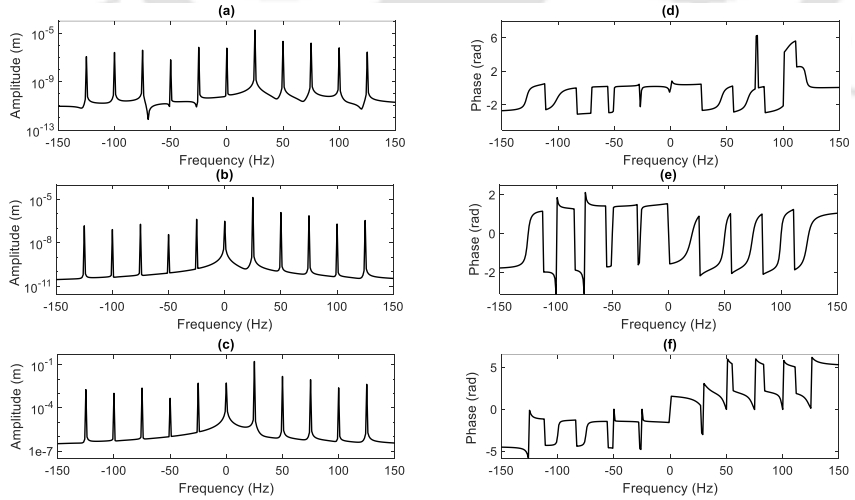

Figure 2-10 Full spectrum plots at 25 Hz (a, d) Amplitude and phase of rotor-1 complex displacement (b, e) Amplitude and phase of rotor-2 complex displacement (c, f) Amplitude and phase of complex AMB Current

The displacement response of rotor-1, rotor-2 and current response of AMB at 25 Hz when both unbalance and misalignment are present at a spin speed of 25 Hz are shown in Figure 2-8 (a-c). The time domain displacement responses are not pure sinusoids, which is indicative of presence of misalignment. The displacement and current orbits of rotor-1, rotor-2 and AMB are shown in Figure 2-9. The orbits shown in Figure 2-9 (a-c) are plotted when only unbalance is present. The orbits in Figure 2-9 (d-f) which is loopy in nature are plotted when both unbalance and misalignment are present. This is another striking characteristic of misalignment as reported by Vance (1988) and Ehrich (1998). The amplitude and phase of the various integer harmonics present in rotor-1, rotor-2 vibration responses and AMB current responses for cases Figure 2-9 (d-f) can be identified from full spectrum FFT plots shown in Figure 2-10.

Table 2-3 shows the comparison of amplitudes and phases of harmonics obtained from time domain and full spectrum with the phase compensation. It can be seen that the full spectrum shows good similarity to the values obtained from time domain inverse problem. Using full spectrum technique with "peak finding algorithm", the coefficients of harmonics of interest can be obtained quicker than it can be done with time domain analysis. Singh and Tiwari (2015) showed that the computational time for the problem of cracked Jeffcott rotor reduced from a few seconds to a few milli-seconds achieving almost 400 times reduction by using full spectrum.

Table 2-3 Harmonics of vibration and current obtained from time domain regression

	$\mathbf{R}_{1i}$		$\mathbf{R}_{2i}$		$\mathbf{I}_i$	
Harmonic i	Amplitude (m)	Phase (rad)	Amplitude (m)	Phase (rad)	Amplitude (m)	Phase (rad)
0	55.52×10^{-6}	3.14	4.36×10^{-6}	-3.14	0.11	3.14
1	54.96×10^{-6}	-2.57	22.4×10^{-6}	0.15	0.28	0.15
2	0.395×10^{-6}	-3.12	0.534×10^{-6}	-3.08	6.67×10^{-3}	-3.08
3	0.077×10^{-6}	-3.13	0.0673×10^{-6}	-3.13	8.41×10^{-4}	-3.11
4	0.003×10^{-6}	-3.13	0.0025×10^{-6}	2.93	3.08×10^{-5}	-3.11
5	0.0069×10^{-6}	-0.0004	0.0051×10^{-6}	0.09	6.39×10^{-5}	0.007

Table 2-3 cont…

-1	1.41×10^{-6}	3.08	0.423×10^{-6}	0.04	5.28×10^{-3}	0.039
-2	0.014×10^{-6}	3.11	0.0194×10^{-6}	3.13	2.4×10^{-4}	3.07
-3	0.019×10^{-6}	-0.003	0.0174×10^{-6}	-0.06	2.17×10^{-4}	-0.022
-4	0.044×10^{-6}	0.003	0.0035×10^{-6}	-0.16	4.32×10^{-5}	-0.008
-5	0.029×10^{-6}	3.12	0.0022×10^{-6}	-2.95	2.75×10^{-5}	3.123

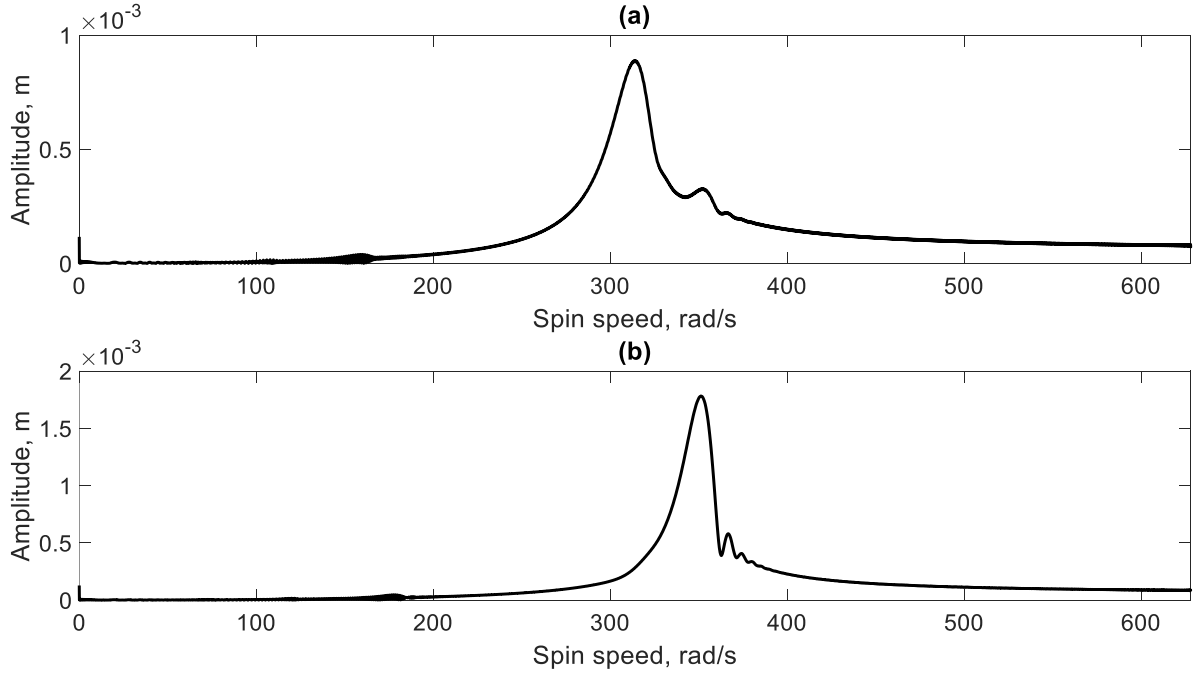

Figure 2-11 Hilbert envelope of (a) Rotor-1 (b) Rotor-2 with AMB

Figure 2-11 shows the Hilbert transform of *x* displacements of rotor-1 and rotor-2, when the system is ramped up with an angular acceleration of 20π rad/s^2. Industrial rotors such as aircraft gas turbines take about five seconds to reach from no-load condition to full load condition which is equivalent to covering a speed range of around 7000 rpm in five seconds (1400 rpm/sec). Steam turbines on the other hand reach the rated speed of 3000 rpm in 10 minutes (300 rpm/min). While crossing critical speeds however they run at 600 rpm/min. The chosen value 20pi rad/s^2 (600 rpm per sec) is arbitrary and falls between the two limits. The peaks in Figure 2-11 signify the critical speeds of rotor

system. The amplitude of peak in rotor-1 present at 314 rad/sec is 0.8×10^{-3} m. Due to the presence of auxiliary AMB support on rotor-2 the peak shifts to 350 rad/sec.

The speeds on the either side of half-power points can be taken for estimation of parameters (20 Hz to 30 Hz). Figure 2-12 shows the flow chart of parameter identification procedure for the estimation of system parameters.

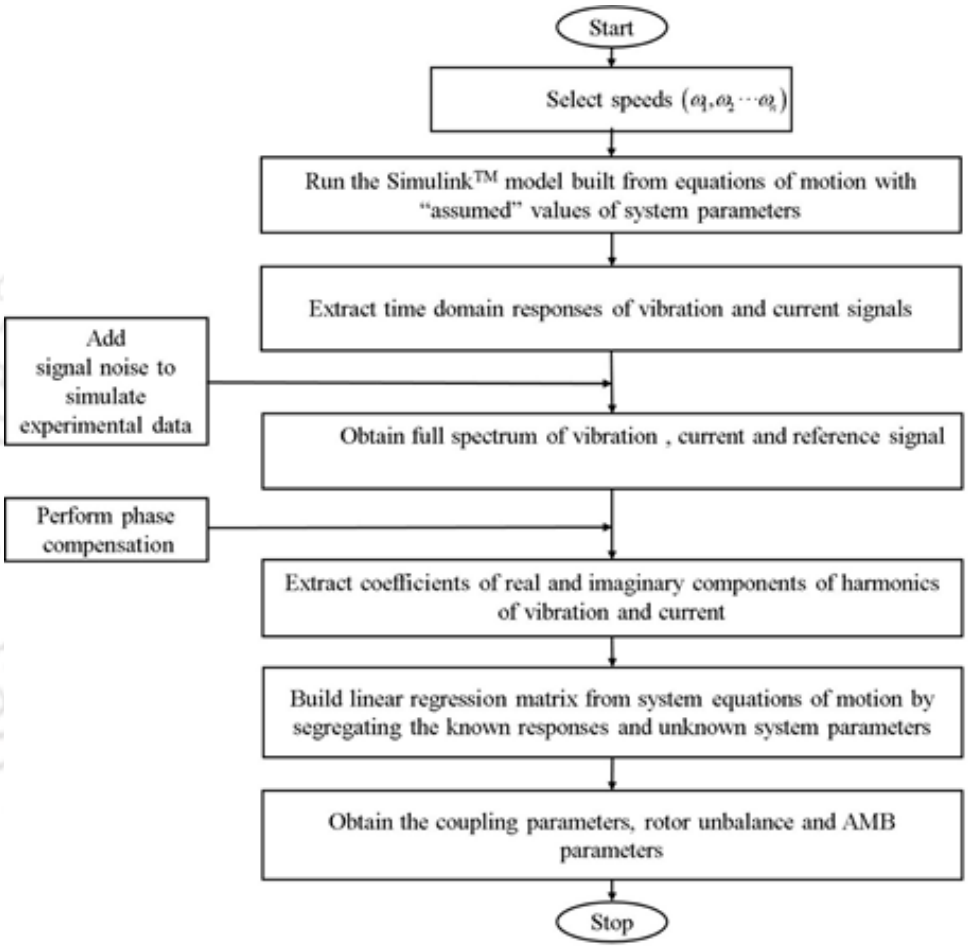

Figure 2-12 Flow chart of rotor-coupling-AMB parameter identification

Table 2-5 shows the estimates of rotor-coupling-AMB parameters obtained from the inverse problem given by Eqn. (2.82) at a spin speed of 18 Hz. The estimates obtained from clean signal are almost identical to the assumed values with error % less than -1%. Equivalent viscous damping of rotor-2, AMB constants undergo comparatively higher deviations compared to other estimates. Gaussian noise at various levels (1%, 2%, and 5%) has been added to the clean signal and estimation was carried out.

Table 2-4 Error percentage in identified parameters at various levels of measurement noise at 18 Hz

Parameters	Assumed values	Estimated values			
		0%	1%	2%	5%
c_1	75($Ns^{-1}m^{-1}$)	75.00	75.01	74.99	74.99
	% error	0.0	0.02	-0.02	-0.01
c_2	50($Ns^{-1}m^{-1}$)	49.82	49.32	48.65	48.72
	% error	-0.95	-1.36	-2.70	-2.56
k_t	10800(N-m/rad)	10800	10805.56	10725.78	10793.31
	% error	0.00	0.05	-0.69	-0.06
Δk_ξ	2000(N-m/rad)	20000	2001.07	1985.95	1998.52
	% error	0.0	0.05	-0.70	-0.07
e_1	240×10^{-6}(μm)	239.99×10^{-6}	241×10^{-6}	242×10^{-6}	243×10^{-6}
	% error	0.00	0.47	0.72	1.32
β_1	30(deg.)	30.00	30.00	30.00	30.00
	% error	0.00	0.00	0.00	0.01
e_2	240×10^{-6}(μm)	240×10^{-6}	1.93×10^{-6}	1.93×10^{-6}	1.95×10^{-6}
	% error	0.0	0.46	0.76	1.34
β_2	45(deg.)	44.99	45.00	44.99	44.99
	% error	-0.01	-0.01	-0.01	-0.01
k_s	105210(N/m)	104987	104189.74	104139.42	104200.22
	% error	-0.98	-0.97	-1.02	-0.96
k_i	42.1(N/A)	42.08	41.98	40.69	40.42
	% error	-0.16	-0.30	-3.35	-3.98

Table 2-5 Parameters estimated after considering cumulative data from 20 Hz to 30Hz in the identification algorithm

Parameter	Assumed values	Estimated values
c_1 (Ns^{-1}m^{-1})	75	74.99
c_2 (Ns^{-1}m^{-1})	50	50.6
k_t (N-m/rad)	10800	10800
Δk_ξ (N-m/rad)	2000	2000
e_1 (μm)	240×10^{-6}	239.99×10^{-6}
β_1 (deg.)	30	29.99
e_2 (μm)	240×10^{-6}	240×10^{-6}
β_2 (deg.)	45	45
k_s (N/m)	105210	105196
k_i (N/A)	42.1	42.09

Rotor-2 damping and AMB current stiffness have been underestimated by as much as 2.56% and 3.98%, respectively, at 5% noise level. The variation in the static and additive coupling stiffness values stands at a reasonable 0.7%. When collective data from the same speed range (20 Hz to 30 Hz) is considered and fed into Eqn. (2.87) the estimates show very good closeness to the assumed values as shown in Table 2-5. This exercise adequately justifies the usefulness of including multiple speeds in the identification algorithm.

2.15 Concluding Remarks

In the present chapter, EOMs of coupled rotor system with angular misalignment and supported on an auxiliary AMB have been formed from the generalized coordinates of simple rotors with central discs. An acceptable assumption based on the conditions of *weight dominance* and flexible coupling has made it possible to establish linear relationship between coupling slopes and disc translational displacements of the vibrating

system. The coupling angular stiffness is modelled as the sum of static and additive components. A time-varying periodic function that is necessary to correctly simulate the nature of coupling misalignment force in frequency domain has been selected. A Simulink^{TM} model is built to generate response in time domain. The amplitude and phase of harmonics of rotor vibration and AMB current are extracted from full spectrum. The identification algorithm based on least-squares regression is built by segregating the equations of motion in frequency domain into the known and unknown parameters. The algorithm is used to estimate coupling static stiffness, ACS, unbalance amplitude, unbalance phase, AMB displacement and current stiffness constants and was found to be robust up to measurement noise levels of 5%.The present chapter presents a new technique in the condition monitoring of misalignment in rotor systems. The identification algorithm developed helps in identifying angular misalignment by quantifying the ACS coefficient. The contribution of various positive and negative integer harmonics can be quantitatively assessed by this method.

Evidently, the present chapter concerns with modelling, algorithm development and identification in a simple rotor system. In the next chapter coupled Jeffcott rotors with offset discs and gyroscopic effect, which is closer to real rotors is considered. The rotor system has rotational DOFs at disc locations in addition to the translational DOFs. Since it is difficult to measure rotational DOFs in experiments a condensation procedure to eliminate them from the EOMs is presented in the next chapter.

CHAPTER 3

Identification of Misalignment in Coupled Simple Rotor-AMB Systems with Offset Discs

3.1 Introduction

In chapter 2, the modelling, analysis and identification of various system faults in coupled rotor-train systems with central discs was presented. In the present chapter, the study is extended to coupled rotor system with offset discs to have gyroscopic efffects. With the combination of flexible coupling and weight dominance assumption, the dynamic behaviour of rotor-bearing-coupling-AMB system has been characterized by the eight generalized coordinates of the two coupled rotors. Lagrange's equation is used to write the EOMs from the energy expressions of rotor-coupling system. The angular stiffness of the coupling has been modelled as the sum of direct stiffness and a time varying additive coupling stiffness (ACS) coefficient, whose magnitude is affected by the amount of angular misalignment. A steering function has been selected such that the forced reponse due to coupling misalignment yields both odd and even harmonics in full spectrum. Dynamic condensation is performed to remove the rotational DOFs and rewrite the EOMs in terms of translational DOFs. An identification algorithm based on least-squares regression technique in frequency domain has been developed using the forward and backward harmonics of rotor vibration and AMB current for the estimation of coupling direct stiffness, coupling additive stiffness, unbalance magnitude and its phase, equivalent viscous damping in each rotor, and current and displacement constants of AMB. The robustness of algorithm is checked against various levels of measurement noise.

3.2 Rotor System Configuration

Figure 3-1 shows a coupled rotor system with offset discs, with two bearings supporting each rotor. The drive is transmitted from rotor-1 to rotor-2 with the help of an intermediate coupling. An AMB placed on the second rotor next to the disc serves to attenuate the vibration as well as to perform the condition monitoring to characterise the faults present

in the rotor system The inertial and rotating coordinate systems used in the present chapter are shown in Figure 2-2.

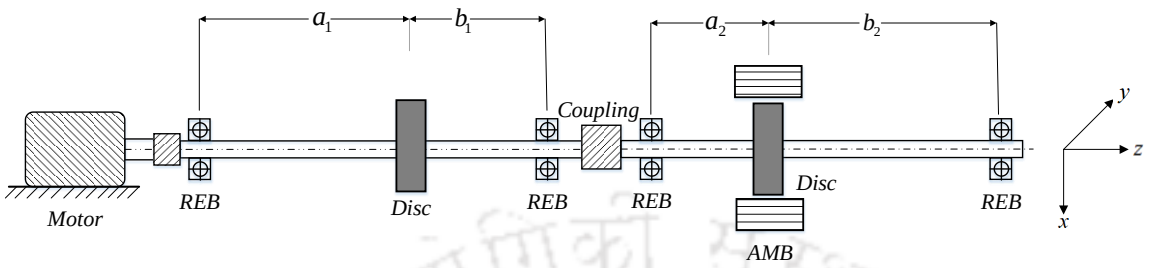

Figure 3-1 General arrangement of a simple coupled rotor-AMB system

3.3 Generalized Coordinates of Rotors and Relation with Coupling Slopes

Figure 3-2 shows the displacements at discs and coupling locations with simple rotor model. The *generalized coordinate vectors* of the rotor-1 and rotor-2 are represented by $\mathbf{q}_1(t)$ and $\mathbf{q}_2(t)$ are the total displacements of 4-DOF coupled rotor system mounted with offset discs. They are composed of static components, $\mathbf{q}_{10}$ and $\mathbf{q}_{20}$ and vibratory components $\Delta\mathbf{q}_1(t)$ and $\Delta\mathbf{q}_2(t)$. Mathematically, they can be expressed as

$$\left.\begin{aligned}\mathbf{q}_1(t) &= \Delta\mathbf{q}_1(t) + \mathbf{q}_{10}\\ \mathbf{q}_2(t) &= \Delta\mathbf{q}_2(t) + \mathbf{q}_{20}\end{aligned}\right\} \tag{3.1}$$

with

$$\Delta\mathbf{q}_1(t) = \begin{pmatrix} x_1 & y_1 & \varphi_{y_1} & \varphi_{x_1}\end{pmatrix}^T; \quad \mathbf{q}_{10} = \begin{pmatrix}\delta_{x_{10}} & \delta_{y_{10}} & \delta_{\varphi_{y_{10}}} & \delta_{\varphi_{x_{10}}}\end{pmatrix}^T$$

$$\Delta\mathbf{q}_2(t) = \begin{pmatrix} x_2 & y_2 & \varphi_{y_2} & \varphi_{x_2}\end{pmatrix}^T; \quad \mathbf{q}_{20} = \begin{pmatrix}\delta_{x_{20}} & \delta_{y_{20}} & \delta_{\varphi_{y_{20}}} & \delta_{\varphi_{x_{20}}}\end{pmatrix}^T$$

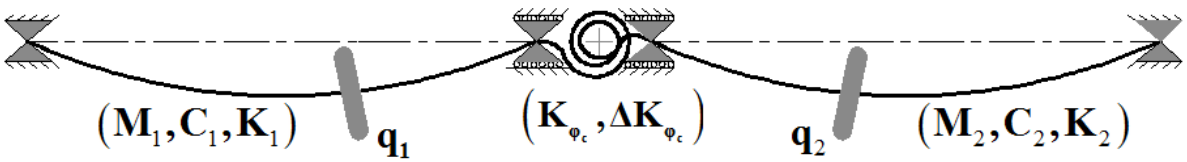

Figure 3-2 Coupled simple rotor system with displacements at disc locations

Total angular displacements i.e. slopes at coupling location for rotor-1 and rotor-2 are denoted by

$$\boldsymbol{\varphi}_{1c} = \begin{pmatrix} \varphi_{y_{c_1}} & \varphi_{x_{c_1}} \end{pmatrix}^T \tag{3.2}$$

$$\boldsymbol{\varphi}_{2c} = \begin{pmatrix} \varphi_{y_{c_2}} & \varphi_{x_{c_2}} \end{pmatrix}^T \tag{3.3}$$

Working under the assumptions mentioned in Section 2.3, the linear relationship between slopes at coupling location $\begin{pmatrix} \varphi_{y_{c_1}} & \varphi_{x_{c_1}} \end{pmatrix}^T$ and translational displacements at disc locations $\begin{pmatrix} x_1 & y_1 \end{pmatrix}^T$ is given by

$$\boldsymbol{\varphi}_{1c} = \lambda_1 \begin{pmatrix} x_1 & y_1 \end{pmatrix}^T \tag{3.4}$$

with $\lambda_1 = \left(\dfrac{2a_1 + b_1}{2a_1 b_1} \right)$

Likewise, for rotor-2, the corresponding relation can be written as

$$\boldsymbol{\varphi}_{2c} = \lambda_2 \begin{pmatrix} x_2 & y_2 \end{pmatrix}^T \tag{3.5}$$

with $\lambda_2 = \left(\dfrac{a_2 + 2b_2}{2a_2 b_2} \right)$

where (a_1, b_1) and (a_2, b_2) are the respective distances of discs of rotor-1 and rotor-2 from their left and right supports. Eqns. (3.4) and (3.5) representing the relations between slopes at bearings and deflection at any section are obtained from the formulae given in **Appendix A**. The relative position of disc unbalance is shown in Figure 2-4 in Chapter 2.

3.4 Equations of Motion of Coupled Rotor System

Equations of motion for the coupled rotor-train system shall be derived from energy equations. The kinetic energy (T) of rigid disks on rotor-1 and rotor-2 due to the translation and rotation motion is given by

$$\begin{aligned} T = {} & \tfrac{1}{2} m_1 (\dot{x}_1^{\,2} + \dot{y}_1^{\,2}) + \tfrac{1}{2} I_{d_1} (\dot{\varphi}_{x_1}^{\,2} + \dot{\varphi}_{y_1}^{\,2}) + \tfrac{1}{2} \Omega I_{p_1} (\dot{\varphi}_{x_1} \varphi_{y_1} - \varphi_{x_1} \dot{\varphi}_{y_1}) + \tfrac{1}{2} \Omega^2 I_{p_1} \\ & + \tfrac{1}{2} m_2 (\dot{x}_2^{\,2} + \dot{y}_2^{\,2}) + \tfrac{1}{2} I_{d_2} (\dot{\varphi}_{x_2}^{\,2} + \dot{\varphi}_{y_2}^{\,2}) + \tfrac{1}{2} \Omega I_{p_2} (\dot{\varphi}_{x_2} \varphi_{y_2} - \varphi_{x_2} \dot{\varphi}_{y_2}) + \tfrac{1}{2} \Omega^2 I_{p_2} \end{aligned} \tag{3.6}$$

The potential energy (V) in the shafts and coupling is given by

$$
\begin{aligned}
V = {} & \tfrac{1}{2}k_{1xx}x_1^2 + \tfrac{1}{2}k_{1x\varphi_y}x_1\varphi_{y_1} + \tfrac{1}{2}k_{1yy}y_1^2 + \tfrac{1}{2}k_{1y\varphi_x}y_1\varphi_{x_1} + \tfrac{1}{2}k_{1\varphi_y x}\varphi_{y_1}x_1 + \tfrac{1}{2}k_{1\varphi_y\varphi_y}\varphi_{y_1}\varphi_{y_1} \\
& + \tfrac{1}{2}k_{1\varphi_x y}\varphi_{x_1}y_1 + \tfrac{1}{2}k_{1\varphi_x\varphi_x}\varphi_{x_1}\varphi_{x_1} + \tfrac{1}{2}k_{2xx}x_2^2 + \tfrac{1}{2}k_{2x\varphi_y}x_2\varphi_{y_2} + \tfrac{1}{2}k_{2yy}y_2^2 + \tfrac{1}{2}k_{2y\varphi_x}y_2\varphi_{x_2} \\
& + \tfrac{1}{2}k_{2\varphi_y x}\varphi_{y_2}x_2 + \tfrac{1}{2}k_{2\varphi_y\varphi_y}\varphi_{y_2}\varphi_{y_2} + \tfrac{1}{2}k_{2\varphi_x y}\varphi_{x_2}y_2 + \tfrac{1}{2}k_{2\varphi_x\varphi_x}\varphi_{x_2}\varphi_{x_2} + \tfrac{1}{2}k_{\varphi_{x_c}}(\varphi_{x_{c_1}} + \varphi_{x_{c_2}})^2 \\
& + \tfrac{1}{2}k_{\varphi_{y_c}}(\varphi_{y_{c_1}} + \varphi_{y_{c_2}})^2
\end{aligned} \tag{3.7}
$$

where m_i, I_{d_i} and I_{p_i} are the mass, diametrical mass moment of inertia and polar mass moment of inertia of discs, respectively. k_{1ij}, k_{2ij} are the stiffness of the shafts and $k_{\varphi_{x_c}}$, $k_{\varphi_{y_c}}$ are the angular stiffness of coupling about *x* and *y* axes, respectively. For rotor-1, it is assumed that $k_{1xx} = k_{1yy}$, $k_{1\varphi_x\varphi_x} = k_{1\varphi_y\varphi_y}$, $k_{1x\varphi_y} = k_{1y\varphi_x}$, $k_{1\varphi_y x} = k_{1\varphi_x y}$. Likewise, for rotor-2, it is assumed that $k_{2xx} = k_{2yy}$, $k_{2\varphi_x\varphi_x} = k_{2\varphi_y\varphi_y}$, $k_{2x\varphi_y} = k_{2y\varphi_x}$, $k_{2\varphi_y x} = k_{2\varphi_x y}$. For the coupling, it has been assumed that angular (bending) stiffness is same about both axes, i.e. $k_{\varphi_{c_x}} = k_{\varphi_{c_y}}$. Substituting Eqns. (3.4) and (3.5) into Eqn. (3.7) the potential energy (*V*) purely in terms of generalized coordinates is obtained and is given by

$$
\begin{aligned}
V = {} & \tfrac{1}{2}k_{1xx}x_1^2 + \tfrac{1}{2}k_{1x\varphi_y}x_1\varphi_{y_1} + \tfrac{1}{2}k_{1yy}y_1^2 + \tfrac{1}{2}k_{1y\varphi_x}y_1\varphi_{x_1} + \tfrac{1}{2}k_{1\varphi_y x}\varphi_{y_1}x_1 + \tfrac{1}{2}k_{1\varphi_y\varphi_y}\varphi_{y_1}\varphi_{y_1} \\
& + \tfrac{1}{2}k_{1\varphi_x y}\varphi_{x_1}y_1 + \tfrac{1}{2}k_{1\varphi_x\varphi_x}\varphi_{x_1}\varphi_{x_1} + \tfrac{1}{2}k_{2xx}x_2^2 + \tfrac{1}{2}k_{2x\varphi_y}x_2\varphi_{y_2} + \tfrac{1}{2}k_{2yy}y_2^2 + \tfrac{1}{2}k_{2y\varphi_x}y_2\varphi_{x_2} \\
& + \tfrac{1}{2}k_{2\varphi_y x}\varphi_{y_2}x_2 + \tfrac{1}{2}k_{2\varphi_y\varphi_y}\varphi_{y_2}\varphi_{y_2} + \tfrac{1}{2}k_{2\varphi_x y}\varphi_{x_2}y_2 + \tfrac{1}{2}k_{2\varphi_x\varphi_x}\varphi_{x_2}\varphi_{x_2} + \tfrac{1}{2}k_{\varphi_{x_c}}\left(\lambda_1 y_1 + \lambda_2 y_2\right)^2 \\
& + \tfrac{1}{2}k_{\varphi_{y_c}}\left(\lambda_1 x_1 + \lambda_2 x_2\right)^2
\end{aligned} \tag{3.8}
$$

The last two terms signify potential energy of coupling represented in terms of translational displacements of rotor-1 and rotor-2. Likewise, the Rayleigh's dissipative function($\Im$) due to viscous damping in shafts can be written as

$$
\begin{aligned}
\Im = {} & \tfrac{1}{2}c_{1xx}\dot{x}_1^2 + \tfrac{1}{2}c_{1x\varphi_y}\dot{x}_1\dot{\varphi}_{y_1} + \tfrac{1}{2}c_{1yy}\dot{y}_1^2 + \tfrac{1}{2}c_{1y\varphi_x}\dot{y}_1\dot{\varphi}_{x_1} + \tfrac{1}{2}c_{1\varphi_y x}\dot{\varphi}_{y_1}\dot{x}_1 + \tfrac{1}{2}c_{1\varphi_y\varphi_y}\dot{\varphi}_{y_1}\dot{\varphi}_{y_1} \\
& + \tfrac{1}{2}c_{1\varphi_x y}\dot{\varphi}_{x_1}\dot{y}_1 + \tfrac{1}{2}c_{1\varphi_x\varphi_x}\dot{\varphi}_{x_1}\dot{\varphi}_{x_1} + \tfrac{1}{2}c_{2xx}\dot{x}_2^2 + \tfrac{1}{2}c_{2x\varphi_y}\dot{x}_2\dot{\varphi}_{y_2} + \tfrac{1}{2}c_{2yy}\dot{y}_2^2 + \tfrac{1}{2}c_{2y\varphi_x}\dot{y}_2\dot{\varphi}_{x_2} \\
& + \tfrac{1}{2}c_{2\varphi_y x}\dot{\varphi}_{y_2}\dot{x}_2 + \tfrac{1}{2}c_{2\varphi_y\varphi_y}\dot{\varphi}_{y_2}\dot{\varphi}_{y_2} + \tfrac{1}{2}c_{2\varphi_x y}\dot{\varphi}_{x_2}\dot{y}_2 + \tfrac{1}{2}c_{2\varphi_x\varphi_x}\dot{\varphi}_{x_2}\dot{\varphi}_{x_2}
\end{aligned} \tag{3.9}
$$

where c_{1ij}, c_{2ij} are the viscous damping coefficients of the shafts. To derive equations of motion, we use Lagrange's equation given by

$$
\frac{d}{dt}\left(\frac{\partial T}{\partial \dot{q}_i}\right) - \frac{\partial T}{\partial q_i} + \frac{\partial V}{\partial q_i} + \frac{\partial \Im}{\partial \dot{q}_i} = Q_i \qquad (i = 1, 2, \ldots n) \tag{3.10}
$$

The vector of generalized coordinates is given by $q_i = \begin{pmatrix} x_1 & y_1 & \varphi_{x_1} & \varphi_{y_1} & x_2 & y_2 & \varphi_{x_2} & \varphi_{y_2} \end{pmatrix}^T$. Q_i is the vector of generalized forces. Applying Eqn. (3.10) on energy expressions given by Eqns. (3.6), (3.8) and (3.9) sequentially, the equations of motion corresponding to each DOF is obtained. Thus there are eight equations for eight DOFs and are given by

$$m_1\ddot{x}_1 + k_{1xx}x_1 + k_{1x\varphi_y}\varphi_{y_1} + \lambda_1^2 k_{\varphi_{yc}} x_1 + \lambda_1\lambda_2 k_{\varphi_{yc}} x_2 + c_{1xx}\dot{x}_1 + c_{1x\varphi_y}\dot{\varphi}_{y_1} = m_1 e_1\omega^2\cos(\omega t + \beta_1) + k_{1xx}\delta_{x_{10}} \tag{3.11}$$

$$m_1\ddot{y}_1 + k_{1yy}y_1 + k_{1y\varphi_x}\varphi_{x_1} + \lambda_1^2 k_{\varphi_{xc}} y_1 + \lambda_1\lambda_2 k_{\varphi_{xc}} y_2 + c_{1yy}\dot{y}_1 + \dot{c}_{1y\varphi_x}\dot{\varphi}_{x_1} = m_1 e_1\omega^2\sin(\omega t + \beta_1) + k_{1yy}\delta_{y_{10}} \tag{3.12}$$

$$I_{d_1}\ddot{\varphi}_{x_1} + \Omega I_{p_1}\dot{\varphi}_{y_1} + k_{1y\varphi_x}y_{11} + k_{1\varphi_x\varphi_x}\varphi_{x_1} + c_{1y\varphi_x}\dot{y}_1 + c_{1\varphi_x\varphi_x}\dot{\varphi}_{x_1} = (I_{p_1} - I_{d_1})\varphi_{01}\omega^2\cos(\omega t + \phi_{01}) + k_{1y\varphi_x}\delta_{\varphi_{x_{10}}} \tag{3.13}$$

$$I_{d_1}\ddot{\varphi}_{y_1} - \Omega I_{p_1}\dot{\varphi}_{x_1} + k_{1x\varphi_y}x_{11} + k_{1\varphi_y\varphi_y}\varphi_{y_1} + c_{1x\varphi_y}\dot{x}_1 + c_{1\varphi_y\varphi_y}\dot{\varphi}_{y_1} = (I_{p_1} - I_{d_1})\varphi_{01}\omega^2\sin(\omega t + \phi_{01}) + k_{1x\varphi_y}\delta_{\varphi_{y_{10}}} \tag{3.14}$$

$$m_2\ddot{x}_2 + k_{2xx}x_2 + k_{2x\varphi_y}\varphi_{y_2} + \lambda_2^2 k_{\varphi_{yc}} x_2 + \lambda_1\lambda_2 k_{\varphi_{yc}} x_1 + c_{2xx}\dot{x}_2 + c_{2x\varphi_y}\dot{\varphi}_{y_2} = m_2 e_2\omega^2\cos(\omega t + \beta_2) + k_{2xx}\delta_{x_{20}} \tag{3.15}$$

$$m_2\ddot{y}_2 + k_{2yy}y_2 + k_{2y\varphi_x}\varphi_{x_2} + \lambda_2^2 k_{\varphi_{xc}} y_2 + \lambda_1\lambda_2 k_{\varphi_{yc}} y_1 + c_{2yy}\dot{y}_2 + c_{2y\varphi_x}\dot{\varphi}_{x_2} = m_2 e_2\omega^2\sin(\omega t + \beta_2) + k_{2yy}\delta_{y_{20}} \tag{3.16}$$

$$I_{d_2}\ddot{\varphi}_{x_2} + \Omega I_{p_2}\dot{\varphi}_{y_2} + k_{2\varphi_x y}y_2 + k_{2\varphi_x\varphi_x}\varphi_{x_2} + c_{2\varphi_x y}\dot{y}_2 + c_{2\varphi_x\varphi_x}\dot{\varphi}_{x_2} = (I_{p_2} - I_{d_2})\varphi_{02}\omega^2\cos(\omega t + \phi_{02}) + k_{2y\varphi_x}\delta_{\varphi_{x_{20}}} \tag{3.17}$$

$$I_{d_2}\ddot{\varphi}_{y_2} - \Omega I_{p_2}\dot{\varphi}_{x_2} + k_{2x\varphi_y}x_2 + k_{2\varphi_y\varphi_y}\varphi_{y_2} + c_{2x\varphi_y}\dot{x}_2 + c_{2\varphi_y\varphi_y}\dot{\varphi}_{y_2} = (I_{p_2} - I_{d_2})\varphi_{02}\omega^2\sin(\omega t + \phi_{02}) + k_{2x\varphi_y}\delta_{\varphi_{y_{20}}} \tag{3.18}$$

The right hand side of each equation gives the static force and unbalance. It can be seen from the above equations that coupling stiffness terms appear only in the EOMs corresponding to translational displacements. This is a direct consequence of relations given by Eqns. (3.4) and (3.5). Now Eqns. (3.11) to (3.18) can be written in the following form

$$\mathbf{M}_1\ddot{\mathbf{q}}_1+(\mathbf{C}_1+\Omega\mathbf{G}_1)\dot{\mathbf{q}}_1+\mathbf{K}_1\mathbf{q}_1+\mathbf{K}'_{\varphi_c}\mathbf{q}_1+\mathbf{K}'''_{\varphi_c}\mathbf{q}_2=\mathbf{f}_{unb_1}+\mathbf{f}_{st_1} \tag{3.19}$$

$$\mathbf{M}_2\ddot{\mathbf{q}}_2+(\mathbf{C}_2+\Omega\mathbf{G}_2)\dot{\mathbf{q}}_2+\mathbf{K}_2\mathbf{q}_2+\mathbf{K}'''_{\varphi_c}\mathbf{q}_1+\mathbf{K}''_{\varphi_c}\mathbf{q}_2=\mathbf{f}_{unb_2}+\mathbf{f}_{st_2} \tag{3.20}$$

where $\mathbf{M}_i$, $\mathbf{C}_i$, $\mathbf{K}_i$, $\mathbf{G}_i$ are the mass, damping, stiffness and gyroscopic matrices of rotors, respectively. $\mathbf{f}_{unb_i}$, $\mathbf{f}_{st_i}$ are the forces due to unbalance and static deflection, respectively. Moment unbalance generated due to the tilt of the disc has been ignored since the disc is thin. The system matrices of coupled 4-DOF rotor system are given in **Appendix C**. In Eqns. (3.19) and (3.20) the contribution of coupling to the rotor system stiffness comes from $\mathbf{K}'_{\varphi_c},\mathbf{K}''_{\varphi_c},\mathbf{K}'''_{\varphi_c}$ matrices which are given by $\mathbf{K}'_{\varphi_c}=\lambda_1^2\mathbf{K}_{\varphi_c}$, $\mathbf{K}''_{\varphi_c}=\lambda_2^2\mathbf{K}_{\varphi_c}$, $\mathbf{K}'''_{\varphi_c}=\lambda_1\lambda_2\mathbf{K}_{\varphi_c}$, where $\mathbf{K}_{\varphi_c}$ is the coupling stiffness matrix.

3.5 Coupling Stiffness Matrix

Lees (2007) proposed that in the presence of misalignment the stiffness of coupling has two components: intact stiffness, which has steady contribution, and time dependent additive coupling stiffness(ACS), which varies with rotary motion. The coupling stiffness is written as

$$\mathbf{K}_{\varphi_c}(t)=\mathbf{K}_{\varphi_c}-\Delta\mathbf{K}_{\varphi_c ROT}(t) \tag{3.21}$$

with

$$\mathbf{K}_{\varphi_c}(t)=\begin{bmatrix} k_{\varphi_c} & 0 & 0 & 0\\ 0 & k_{\varphi_c} & 0 & 0\\ 0 & 0 & 0 & 0\\ 0 & 0 & 0 & 0 \end{bmatrix}-\begin{Bmatrix} \Delta k_{\xi}(t) & 0 & 0 & 0\\ 0 & \Delta k_{\eta}(t) & 0 & 0\\ 0 & 0 & 0 & 0\\ 0 & 0 & 0 & 0 \end{Bmatrix} \tag{3.22}$$

where $\Delta k_{\xi}(t)$ and $\Delta k_{\eta}(t)$ are the ACS coefficients due to angular misalignment in ξ and η directions, respectively. Substituting Eqns. (3.1) and (3.21) in Eqn. (3.19) gives

$$\begin{aligned}&\mathbf{M}_1\ddot{\mathbf{q}}_1+(\mathbf{C}_1+\Omega\mathbf{G}_1)\dot{\mathbf{q}}_1+\mathbf{K}_1\left(\mathbf{q}_{10}+\Delta\mathbf{q}_1\right)+\lambda_1^2\left(\mathbf{K}_{\varphi_c}-\Delta\mathbf{K}_{\varphi_c}\right)\left(\mathbf{q}_{10}+\Delta\mathbf{q}_1\right)\\&+\lambda_1\lambda_2\left(\mathbf{K}_{\varphi_c}-\Delta\mathbf{K}_{\varphi_c}\right)\left(\mathbf{q}_{20}+\Delta\mathbf{q}_2\right)=\mathbf{f}_{unb_1}+\mathbf{f}_{st_1}\end{aligned} \tag{3.23}$$

Ignoring the product of smaller terms such as $\Delta\mathbf{K}_{\varphi_c}\Delta\mathbf{q}_1$ and $\Delta\mathbf{K}_{\varphi_c}\Delta\mathbf{q}_2$, we get

$$\mathbf{M}_1\Delta\ddot{\mathbf{q}}_1+(\mathbf{C}_1+\Omega\mathbf{G}_1)\Delta\dot{\mathbf{q}}_1+(\mathbf{K}_1+\mathbf{K}'_{\varphi_c})\Delta\mathbf{q}_1+\mathbf{K}''_{\varphi_c}\Delta\mathbf{q}_2=\mathbf{f}_{unb_1}+\mathbf{f}_{mis_1}-\mathbf{f}_{const_1} \quad (3.24)$$

with

$$\mathbf{f}_{const_1}=(\mathbf{K}'_{\varphi_c}\mathbf{q}_{10}+\mathbf{K}'''_{\varphi_c}\mathbf{q}_{20}) \quad (3.25)$$

$$\mathbf{f}_{mis_1}=(\Delta\mathbf{K}'_{\varphi_c}\mathbf{q}_{10}+\Delta\mathbf{K}'''_{\varphi_c}\mathbf{q}_{20}) \quad (3.26)$$

where $\mathbf{f}_{mis_1}$, $\mathbf{f}_{const_1}$ are the time-varying and static coupling misalignment forces acting on rotor-1, respectively.

Likewise Eqn. (3.20) transforms to,

$$\mathbf{M}_2\Delta\ddot{\mathbf{q}}_2+(\mathbf{C}_2+\Omega\mathbf{G}_2)\Delta\dot{\mathbf{q}}_2+(\mathbf{K}_2+\lambda_2^2\mathbf{K}_{\varphi_c})\Delta\mathbf{q}_2+\lambda_1\lambda_2\mathbf{K}_{\varphi_c}\Delta\mathbf{q}_1=\mathbf{f}_{unb_2}+\mathbf{f}_{mis_2}-\mathbf{f}_{const_2} \quad (3.27)$$

where

$$\mathbf{f}_{const_2}=(\mathbf{K}'''_{\varphi_c}\mathbf{q}_{10}+\mathbf{K}''_{\varphi_c}\mathbf{q}_{20}) \quad (3.28)$$

$$\mathbf{f}_{mis_2}=(\Delta\mathbf{K}'''_{\varphi_c}\mathbf{q}_{10}+\Delta\mathbf{K}''_{\varphi_c}\mathbf{q}_{20}) \quad (3.29)$$

with

$$\Delta\mathbf{K}'_{\varphi_c}=\lambda_1^2\Delta\mathbf{K}_{\varphi_c};\ \ \Delta\mathbf{K}''_{\varphi_c}=\lambda_2^2\Delta\mathbf{K}_{\varphi_c};\ \ \Delta\mathbf{K}'''_{\varphi_c}=\lambda_1\lambda_2\Delta\mathbf{K}_{\varphi_c}$$

where $\mathbf{f}_{mis_2}$, $\mathbf{f}_{const_2}$ are the time-varying and static coupling misalignment forces acting on rotor-2, respectively. $\Delta\mathbf{K}_{\varphi_c}$ is the additive coupling stiffness matrix. In Eqns. (3.24), (3.27) there are three types of forcing terms on the right hand side, viz. unbalance force due to disc eccentricity, time dependant coupling misalignment force, and constant coupling misalignment force. Due to the assumptions made in Section 2.3, it is possible to express coupling misalignment forces in terms of translational displacements of the rotors at disc locations.

ACS given in Eqn. (3.21) is written as the product of a periodic time function, $s(t)$ and a matrix containing additive direct stiffness coefficients Δk_ξ and Δk_η .The cross-coupled stiffness terms are ignored.

$$\Delta\mathbf{K}_{\varphi_c\ ROT}(t)=\begin{bmatrix}\Delta k_\xi(t) & 0 & 0 & 0\\ 0 & \Delta k_\eta(t) & 0 & 0\\ 0 & 0 & 0 & 0\\ 0 & 0 & 0 & 0\end{bmatrix}=s(t)\begin{bmatrix}\Delta k_\xi & 0 & 0 & 0\\ 0 & \Delta k_\eta & 0 & 0\\ 0 & 0 & 0 & 0\\ 0 & 0 & 0 & 0\end{bmatrix} \tag{3.30}$$

Herein, $s(t)$ is also called the *coupling excitation function* and its Fourier expansion directly influences the harmonic nature of coupling misalignment force. Eqns. 3.24 and 3.27 have been written in the stationary frame of reference, it is necessary to transform the time dependent coupling stiffness of rotating coupling into the inertial frame of reference (refer Figure 2-2). This is accomplished by change of axes using a transformation matrix, which is given by

$$\mathbf{T}=\begin{bmatrix}\cos\omega t & -\sin\omega t & 0 & 0\\ \sin\omega t & \cos\omega t & 0 & 0\\ 0 & 0 & \cos\omega t & -\sin\omega t\\ 0 & 0 & \sin\omega t & \cos\omega t\end{bmatrix} \tag{3.31}$$

Upon multiplying Eqn. (3.21) by Eqn. (3.31), we get

$$\mathbf{K}_{\varphi_c}-\Delta\mathbf{K}_{\varphi_c\,STAT}(t)=\mathbf{K}_{\varphi_c}-\mathbf{T}_{RS}^{T}\Delta\mathbf{K}_{\varphi_c\ ROT}(t)\mathbf{T}_{RS} \tag{3.32}$$

The subscript *STAT, ROT* refers to stationary and rotating frames of reference. $\mathbf{K}_{\varphi_c}$ in Eqn. (3.32) represents static coupling stiffness matrix that remains unaltered during coordinate transformation.However, $\Delta\mathbf{K}_{\phi_c\ STAT}$ which denotes time dependent stiffness is given by

$$\Delta\mathbf{K}_{\varphi_c\ STAT}(t)=s(t)\begin{bmatrix}\Delta k_\xi\cos^2\omega t+\Delta k_\eta\sin^2\omega t & \Delta k_\xi\cos\omega t\sin\omega t-\Delta k_\eta\cos\omega t\sin\omega t & 0 & 0\\ \Delta k_\xi\cos\omega t\sin\omega t-\Delta k_\eta\cos\omega t\sin\omega t & \Delta k_\xi\sin^2\omega t+\Delta k_\eta\cos^2\omega t & 0 & 0\\ 0 & 0 & 0 & 0\\ 0 & 0 & 0 & 0\end{bmatrix} \tag{3.33}$$

It is to be noted that both Δk_ξ and Δk_η coefficients appear in Eqn. (3.33). In the present work, it is assumed that ACS in η direction, i.e. $\Delta k_\eta = 0$. Eqn. (3.33) then transforms to

$$\Delta\mathbf{K}_{\varphi_c\ STAT}(t)=\frac{1}{2}\Delta k_\xi s(t)\begin{bmatrix}1+\cos 2\omega t & \sin 2\omega t & 0 & 0\\ \sin 2\omega t & 1-\cos 2\omega t & 0 & 0\\ 0 & 0 & 0 & 0\\ 0 & 0 & 0 & 0\end{bmatrix} \tag{3.34}$$

The time dependent coupling misalignment force acting on rotor-1, which is present in the RHS of Eqn. (3.24), is obtained by substituting Eqn. (3.34) in Eqn. (3.26) and is given by

$$\mathbf{f}_{mis_1}=\frac{1}{2}\Delta k_\xi s(t)\left(\lambda_1^2\begin{bmatrix}1+\cos 2\omega t & \sin 2\omega t & 0 & 0\\ \sin 2\omega t & 1-\cos 2\omega t & 0 & 0\\ 0 & 0 & 0 & 0\\ 0 & 0 & 0 & 0\end{bmatrix}\begin{Bmatrix}\delta_{x_{10}}\\ \delta_{y_{10}}\\ \delta_{\theta_{y10}}\\ \delta_{\theta_{x10}}\end{Bmatrix}+\lambda_1\lambda_2\begin{bmatrix}1+\cos 2\omega t & \sin 2\omega t & 0 & 0\\ \sin 2\omega t & 1-\cos 2\omega t & 0 & 0\\ 0 & 0 & 0 & 0\\ 0 & 0 & 0 & 0\end{bmatrix}\begin{Bmatrix}\delta_{x_{20}}\\ \delta_{y_{20}}\\ \delta_{\theta_{y20}}\\ \delta_{\theta_{x20}}\end{Bmatrix}\right) \tag{3.35}$$

The static deflection in *y* direction $\delta_{y_{10}}, \delta_{y_{20}}$ are zero. Eqn. (3.35) then simplifies to

$$\mathbf{f}_{mis_1}=\frac{1}{2}\Delta k_\xi s(t)\left(\lambda_1^2\delta_{x_{10}}\begin{Bmatrix}1+\cos 2\omega t\\ \sin 2\omega t\\ 0\\ 0\end{Bmatrix}+\lambda_1\lambda_2\delta_{x_{20}}\begin{Bmatrix}1+\cos 2\omega t\\ \sin 2\omega t\\ 0\\ 0\end{Bmatrix}\right) \tag{3.36}$$

Equation (3.36) represents the time dependent coupling misalignment force acting on rotor-1. Likewise the time dependent coupling misalignment force acting on rotor-2, which is present in the RHS of Eqn. (3.27) is obtained by substituting Eqn. (3.34) in Eqn. (3.29) and is given by

$$\mathbf{f}_{mis_2}=\frac{1}{2}s(t)\Delta k_\xi\left(\lambda_1\lambda_2\delta_{x_{10}}\begin{Bmatrix}1+\cos 2\omega t\\ \sin 2\omega t\\ 0\\ 0\end{Bmatrix}+\lambda_2^2\delta_{x_{20}}\begin{Bmatrix}1+\cos 2\omega t\\ \sin 2\omega t\\ 0\\ 0\end{Bmatrix}\right) \tag{3.37}$$

In Eqns. (3.36) and (3.37), the coupling misalignment force has been represented in terms of $\delta_{x_{10}}$ and $\delta_{x_{20}}$, the static deflection of discs, λ_1 and λ_2, numeric constants that depend on the disc location from supports, and $s(t)$, the coupling misalignment excitation function. The significance of $s(t)$ is descrived in Section 2.7.

3.6 EOM of Rotor-2 in the Presence of AMB Support

The magnetic force $\mathbf{f}_{AMB}$ exerted by the AMB on rotor-2 is given by

$$\mathbf{f}_{AMB} = \begin{Bmatrix} -k_{sx}x_2 + k_{ix}i_x \\ -k_{sy}y_2 + k_{iy}i_y \\ 0 \\ 0 \end{Bmatrix} \tag{3.38}$$

Here k_{ix} and k_{iy} are AMB current stiffness constants in x_2 and y_2 directions, respectively. k_{sx} and k_{sy} are AMB displacement stiffness constants in x_2 and y_2 transverse directions, respectively. i_x and i_y are AMB currents in x_2 and y_2 transverse directions, respectively. For the case of an isotropic 8-pole actuator used in the current work $k_{sx} = k_{sy} = k_s$ and $k_{ix} = k_{iy} = k_i$. Thus Eqn. (3.38) transforms to

$$\mathbf{f}_{AMB} = \begin{bmatrix} -k_s & 0 \\ 0 & -k_s \\ 0 & 0 \\ 0 & 0 \end{bmatrix} \begin{Bmatrix} x_2 \\ y_2 \end{Bmatrix} + \begin{bmatrix} k_i & 0 \\ 0 & k_i \\ 0 & 0 \\ 0 & 0 \end{bmatrix} \begin{Bmatrix} i_x \\ i_y \end{Bmatrix} \tag{3.39}$$

In the present formulation (Figure 3-1) AMB is used as an auxiliary support for rotor-2, which provided controlling force. The corresponding magnetic forcing term appears additionally in the right hand side and Eqn. (3.27) changes to

$$\mathbf{M}_2\Delta\ddot{\mathbf{q}}_2 + (\mathbf{C}_2 - \Omega\mathbf{G}_2)\Delta\dot{\mathbf{q}}_2 + (\mathbf{K}_2 + \mathbf{K}''_{\varphi_c})\Delta\mathbf{q}_2 + \mathbf{K}'''_{\varphi_c}\Delta\mathbf{q}_1 = \mathbf{f}_{unb_2} + \mathbf{f}_{mis_2} - \mathbf{f}_{AMB} - \mathbf{f}_{const_2} \tag{3.40}$$

The sign of the magnetic force takes + or – sign depending on whether AMB is exciting or supporting the rotor system.

3.7 Equations of Motion in Complex Form

For ease of computation translational and rotational vibration response of rotors is written in a complex form by multiplying the equations of motion in *y*-direction with '$\mathrm{j} = \sqrt{-1}$' and adding to the equation of motion in *x*-direction. The complex vibration response of rotors is then given by

$$\mathbf{v}_1 = \begin{pmatrix} r_1 & \varphi_1 \end{pmatrix}^T ; \mathbf{v}_2 = \begin{pmatrix} r_2 & \varphi_2 \end{pmatrix}^T \tag{3.41}$$

with

$$r_1 = x_1 + \mathrm{j}y_1 ; \quad r_2 = x_2 + \mathrm{j}y_2 ; \quad \varphi_1 = \varphi_{y_1} + \mathrm{j}\varphi_{x_1} ; \varphi_2 = \varphi_{y_2} + \mathrm{j}\varphi_{x_2}$$

where r_1, r_2, φ_1 and φ_2 are the complex displacement variables. Upon substituting Eqn. (3.41), the equations of motion of rotor-1 and rotor-2 given by Eqns. (3.24) and (3.40) transform into the following complex form

$$\bar{\mathbf{M}}_1 \ddot{\mathbf{v}}_1 + (\bar{\mathbf{C}}_1 - \mathrm{j}\omega\bar{\mathbf{G}}_1)\dot{\mathbf{v}}_1 + \tilde{\mathbf{K}}_1 \mathbf{v}_1 + \bar{\mathbf{K}}_{t_3} \mathbf{v}_2 = \bar{\mathbf{f}}_{unb_1} + \bar{\mathbf{f}}_{mis_1} - \bar{\mathbf{f}}_{const_1} \tag{3.42}$$

$$\bar{\mathbf{M}}_2 \ddot{\mathbf{v}}_2 + (\bar{\mathbf{C}}_2 - \mathrm{j}\omega\bar{\mathbf{G}}_2)\dot{\mathbf{v}}_2 + \tilde{\mathbf{K}}_2 \mathbf{v}_2 + \bar{\mathbf{K}}_{t_3} \mathbf{v}_1 = \bar{\mathbf{f}}_{unb_2} + \bar{\mathbf{f}}_{mis_2} - \bar{\mathbf{f}}_{cur} - \bar{\mathbf{f}}_{const_1} \tag{3.43}$$

with

$$\bar{\mathbf{M}}_1 = \begin{bmatrix} m_1 & 0 \\ 0 & I_{d_1} \end{bmatrix}; \bar{\mathbf{M}}_2 = \begin{bmatrix} m_2 & 0 \\ 0 & I_{d_2} \end{bmatrix}; \bar{\mathbf{C}}_1 = \begin{bmatrix} c_{1xx} & c_{1x\varphi_y} \\ c_{1\varphi_y x} & c_{1\varphi_y\varphi_y} \end{bmatrix}; \bar{\mathbf{C}}_2 = \begin{bmatrix} c_{2xx} & c_{2x\varphi_y} \\ c_{2\varphi_y x} & c_{2\varphi_y\varphi_y} \end{bmatrix}$$

$$\bar{\mathbf{K}}_1 = \begin{bmatrix} k_{1xx} & k_{1x\varphi_y} \\ k_{1\varphi_y x} & k_{1\varphi_y\varphi_y} \end{bmatrix}; \bar{\mathbf{K}}_2 = \begin{bmatrix} k_{2xx} & k_{2x\varphi_y} \\ k_{2\varphi_y x} & k_{2\varphi_y\varphi_y} \end{bmatrix}; \bar{\mathbf{G}}_1 = \begin{bmatrix} 0 & 0 \\ 0 & -I_{p_1} \end{bmatrix}; \bar{\mathbf{G}}_2 = \begin{bmatrix} 0 & 0 \\ 0 & -I_{p_2} \end{bmatrix};$$

$$\bar{\mathbf{K}}_{t_3} = \lambda_1\lambda_2 \begin{bmatrix} k_{\phi_c} & 0 \\ 0 & 0 \end{bmatrix}; \tilde{\mathbf{K}}_1 = \begin{bmatrix} k_{1xx} + \lambda_1^2 k_{\phi_c} & k_{1x\varphi_y} \\ k_{1\varphi_y x} & k_{1\varphi_y\varphi_y} \end{bmatrix}; \tilde{\mathbf{K}}_2 = \begin{bmatrix} k_{2xx} + \lambda_2^2 k_{\phi_c} - k_s & k_{2x\varphi_y} \\ k_{2\varphi_y x} & k_{2\varphi_y\varphi_y} \end{bmatrix};$$

$$\mathrm{j}I_{p_1}\omega\dot{\varphi}_1 = \left(-I_{p_1}\omega\dot{\varphi}_{x_1}\right) + \mathrm{j}\left(I_{p_1}\omega\dot{\varphi}_{y_1}\right); \ \mathrm{j}I_{p_2}\omega\dot{\varphi}_2 = \left(-I_{p_2}\omega\dot{\varphi}_{x_2}\right) + \mathrm{j}\left(I_{p_2}\omega\dot{\varphi}_{y_2}\right)$$

Forcing terms on the RHS of Eqns. (3.42) and (3.43) are given by

$$\bar{\mathbf{f}}_{unb_1} = \begin{Bmatrix} m_1 e_1 \omega^2 e^{\mathrm{j}(\omega t + \beta_1)} \\ 0 \end{Bmatrix}; \ \bar{\mathbf{f}}_{unb_2} = \begin{Bmatrix} m_2 e_2 \omega^2 e^{\mathrm{j}(\omega t + \beta_2)} \\ 0 \end{Bmatrix}; \ \bar{\mathbf{f}}_{cur} = k_i \begin{Bmatrix} i_c \\ 0 \end{Bmatrix}$$

$$\bar{\mathbf{f}}_{mis_1} = 0.5 s(t) \Delta k_\xi (1 + e^{2\mathrm{j}\omega t})(\lambda_1^2 \mathbf{v}_{10} + \lambda_1\lambda_2 \mathbf{v}_{20}); \ \bar{\mathbf{f}}_{mis_2} = 0.5 s(t) \Delta k_\xi (1 + e^{2\mathrm{j}\omega t})(\lambda_1\lambda_2 \mathbf{v}_{10} + \lambda_2^2 \mathbf{v}_{20})$$

$$\bar{\mathbf{f}}_{const_1} = \lambda_1^2 \bar{\mathbf{K}}_{\phi_c} \mathbf{v}_{10} + \lambda_1\lambda_2 \bar{\mathbf{K}}_{\phi_c} \mathbf{v}_{20}; \ \bar{\mathbf{f}}_{const_2} = \lambda_1\lambda_2 \bar{\mathbf{K}}_{\phi_c} \mathbf{v}_{10} + \lambda_2^2 \bar{\mathbf{K}}_{\phi_c} \mathbf{v}_{20}; \ i_c = i_x + \mathrm{j}i_y$$

i_c is the complex current variable. Static displacement vectors are given by

$$\mathbf{v}_{10}=\begin{Bmatrix}\delta_{x_{10}}\\0\end{Bmatrix};\ \mathbf{v}_{20}=\begin{Bmatrix}\delta_{x_{20}}\\0\end{Bmatrix}$$

The forcing terms in Eqns. (3.42) and (3.43) are multi harmonic in nature and are of the form $ke^{\mathrm{j}i\omega t}$. Hence, the assumed solution or particular integral that represents the complex vibration response of rotors takes the form (Kreyszig, 2007)

$$\mathbf{v}_1(t)=\sum_{i=-\infty}^{i=\infty}R_{1i}e^{\mathrm{j}i\omega t};\quad \mathbf{v}_2(t)=\sum_{i=-\infty}^{i=\infty}R_{2i}e^{\mathrm{j}i\omega t} \tag{3.44}$$

Likewise, the AMB complex current in time domain can be decomposed into its multi harmonic form

$$i_c(t)=\sum_{i=-\infty}^{i=\infty}I_i e^{\mathrm{ij}\omega t} \tag{3.45}$$

Substituting Eqns. (3.44) and (3.45) in equation (3.42), it gives

$$\begin{aligned}&\left[\left\{-(i\omega)^2\bar{\mathbf{M}}_1+\mathrm{j}i\omega\left(\bar{\mathbf{C}}_1-\mathrm{j}\Omega\bar{\mathbf{G}}_1\right)+\bar{\mathbf{K}}_1\right\}R_{1i}+\tilde{\mathbf{K}}_{t_3}R_{2i}\right]\\&=\begin{Bmatrix}m_1e_1\omega^2e^{\mathrm{j}\beta_1}\\0\end{Bmatrix}+\begin{Bmatrix}\Delta k_\xi\left(\lambda_1^2\delta_{x_{10}}+\lambda_1\lambda_2\delta_{x_{20}}\right)p_i\\0\end{Bmatrix}-\begin{Bmatrix}k_{\varphi_c}\left(\lambda_1^2\delta_{x_{10}}+\lambda_1\lambda_2\delta_{x_{20}}\right)\\0\end{Bmatrix}\end{aligned} \tag{3.46}$$

Likewise, upon substituting Eqns. (3.44) and (3.45) in Eqn. (3.43), we get

$$\begin{aligned}&\left[\left\{-(i\omega)^2\bar{\mathbf{M}}_2+\mathrm{j}i\omega\left(\bar{\mathbf{C}}_2-j\Omega\bar{\mathbf{G}}_2\right)+\bar{\mathbf{K}}_2\right\}R_{2i}+\tilde{\mathbf{K}}_{t_3}R_{1i}\right]\\&=\begin{Bmatrix}m_2e_2\omega^2e^{\mathrm{j}\beta_2}\\0\end{Bmatrix}+\begin{Bmatrix}\Delta k_\xi\left(\lambda_1\lambda_2\delta_{x_{10}}+\lambda_2^2\delta_{x_{20}}\right)p_i\\0\end{Bmatrix}-\begin{Bmatrix}K_I I_i\\0\end{Bmatrix}-\begin{Bmatrix}k_{\varphi_c}\left(\lambda_1\lambda_2\delta_{x_{10}}+\lambda_2^2\delta_{x_{20}}\right)\\0\end{Bmatrix}^T\end{aligned} \tag{3.47}$$

Eqns. (3.46) and (3.47) represent the frequency domain equations for the coupled rotor system with integrated AMB, for harmonic indices ranging from $i=-n,\cdots,-2,-1,0,1,2,\cdots,n$, which are characteristic of a system excited by the coupling misalignment.

3.8 Reduction of Angular Generalized Coordinates: Dynamic Condensation

Since it is difficult to measure angular displacements, i.e. tilt of discs in test conditions, it would be useful to remove the rotational coordinates of discs $(\varphi_{xi},\varphi_{yi})$ from generalized

coordinate vectors by the process of model order reduction. As a result the vibration information of rotational displacements, i.e. slopes will not be needed in the development of identification algorithm, which is difficult to measure accurately in practice. This is achieved by defining rotational coordinates as slave DOFs in the EOMs. Translational coordinates that can be measured with non-contact sensors are designated as master DOFs. Qu (2004) and Wagner et al. (2010) presented a comprehensive review of model order reduction methods for the rotor dynamic analysis. The DOFs for both rotors in Eqns. (3.46) and (3.47) are segregated as shown below, where *m* and *s* subscripts denote masters and slaves, respectively.

$$\left(-(i\omega)^2\begin{bmatrix}\mathbf{M}_{1mm} & 0\\ 0 & \mathbf{M}_{1ss}\end{bmatrix}+\mathrm{j}(i\omega)\left(\begin{bmatrix}\mathbf{C}_{1mm} & \mathbf{C}_{1ms}\\ \mathbf{C}_{1sm} & \mathbf{C}_{1ss}\end{bmatrix}-\mathrm{j}\omega\begin{bmatrix}0 & 0\\ 0 & \mathbf{G}_{1mm}\end{bmatrix}\right)+\begin{bmatrix}\mathbf{K}_{1mm} & \mathbf{K}_{1ms}\\ \mathbf{K}_{1sm} & \mathbf{K}_{1ss}\end{bmatrix}\right)\begin{Bmatrix}\mathbf{Q}_{1m}\\ \mathbf{Q}_{1s}\end{Bmatrix}+\begin{bmatrix}\mathbf{K}_{\varphi_{mm}} & 0\\ 0 & 0\end{bmatrix}\begin{Bmatrix}\mathbf{Q}_{2m}\\ \mathbf{Q}_{2s}\end{Bmatrix}=\begin{Bmatrix}\mathbf{f}_{1i}\\ 0\end{Bmatrix} \tag{3.48}$$

$$\left(-(i\omega)^2\begin{bmatrix}\mathbf{M}_{2mm} & 0\\ 0 & \mathbf{M}_{2ss}\end{bmatrix}+\mathrm{j}(i\omega)\left(\begin{bmatrix}\mathbf{C}_{2mm} & \mathbf{C}_{2ms}\\ \mathbf{C}_{2sm} & \mathbf{C}_{2ss}\end{bmatrix}-\mathrm{j}\omega\begin{bmatrix}0 & 0\\ 0 & \mathbf{G}_{2mm}\end{bmatrix}\right)+\begin{bmatrix}\mathbf{K}_{2mm} & \mathbf{K}_{2ms}\\ \mathbf{K}_{2sm} & \mathbf{K}_{2ss}\end{bmatrix}\right)\begin{Bmatrix}\mathbf{Q}_{2m}\\ \mathbf{Q}_{2s}\end{Bmatrix}+\begin{bmatrix}\mathbf{K}_{\varphi_{mm}} & 0\\ 0 & 0\end{bmatrix}\begin{Bmatrix}\mathbf{Q}_{1m}\\ \mathbf{Q}_{1s}\end{Bmatrix}=\begin{Bmatrix}\mathbf{f}_{2i}\\ 0\end{Bmatrix} \tag{3.49}$$

with

$$\mathbf{M}_{1mm}=\begin{bmatrix}m_1 & 0\\ 0 & m_1\end{bmatrix};\ \mathbf{M}_{1ss}=\begin{bmatrix}I_{d_1} & 0\\ 0 & I_{d_1}\end{bmatrix};\ \mathbf{M}_{2mm}=\begin{bmatrix}m_2 & 0\\ 0 & m_2\end{bmatrix};\ \mathbf{M}_{2ss}=\begin{bmatrix}I_{d_2} & 0\\ 0 & I_{d_2}\end{bmatrix};$$

$$\mathbf{C}_{1mm}=\begin{bmatrix}c_{1xx} & 0\\ 0 & c_{1yy}\end{bmatrix};\ \mathbf{C}_{1sm}=\mathbf{C}_{1ms}=\begin{bmatrix}c_{1x\varphi_y} & 0\\ 0 & c_{1y\varphi_x}\end{bmatrix};\ \mathbf{C}_{1ss}=\begin{bmatrix}c_{1\varphi_y\varphi_y} & 0\\ 0 & c_{1\varphi_x\varphi_x}\end{bmatrix}$$

$$\mathbf{C}_{2mm}=\begin{bmatrix}c_{2xx} & 0\\ 0 & c_{2yy}\end{bmatrix};\ \mathbf{C}_{2sm}=\mathbf{C}_{2ms}=\begin{bmatrix}c_{2x\varphi_y} & 0\\ 0 & c_{2y\varphi_x}\end{bmatrix};\ \mathbf{C}_{2ss}=\begin{bmatrix}c_{2\varphi_y\varphi_y} & 0\\ 0 & c_{2\varphi_x\varphi_x}\end{bmatrix}$$

$$\mathbf{K}_{1mm}=\begin{bmatrix}k_{1xx}+\lambda_1^2k_{\varphi_c} & 0\\ 0 & k_{1xx}+\lambda_1^2k_{\varphi_c}\end{bmatrix};\ \mathbf{K}_{1ms}=\mathbf{K}_{1sm}=\begin{bmatrix}k_{1x\varphi_y} & 0\\ 0 & k_{1y\varphi_x}\end{bmatrix};\ \mathbf{K}_{1ss}=\begin{bmatrix}k_{1\varphi_y\varphi_y} & 0\\ 0 & k_{1\varphi_x\varphi_x}\end{bmatrix}$$

$$\mathbf{K}_{2ss}=\begin{bmatrix} k_{2\varphi_y\varphi_y} & 0 \\ 0 & k_{2\varphi_x\varphi_x} \end{bmatrix};\mathbf{K}_{\varphi_{mm}}=\begin{bmatrix} \lambda_1\lambda_2 k_{\varphi_c} & 0 \\ 0 & \lambda_1\lambda_2 k_{\varphi_c} \end{bmatrix};\ \begin{Bmatrix}\mathbf{Q}_{1m}\\ \mathbf{Q}_{1s}\end{Bmatrix}=\begin{Bmatrix} U_{1i}^x \\ U_{1i}^y \\ \\ \varphi_{1i}^y \\ \varphi_{1i}^x \end{Bmatrix};\ \begin{Bmatrix}\mathbf{Q}_{2m}\\ \mathbf{Q}_{2s}\end{Bmatrix}=\begin{Bmatrix} U_{2i}^x \\ U_{2i}^y \\ \\ \varphi_{2i}^y \\ \varphi_{2i}^x \end{Bmatrix}$$

$$\mathbf{f}_{1i}=\begin{Bmatrix} m_1e_1\omega^2e^{\mathrm{j}\beta_1} \\ 0 \end{Bmatrix}e^{\mathrm{j}\omega t}+\begin{Bmatrix} \Delta k_\xi\left(\lambda_1^2\delta_{x_{10}}+\lambda_1\lambda_2\delta_{x_{20}}\right)\sum_{i=-\infty}^{i=\infty}p_ie^{\mathrm{j}i\omega t} \\ 0 \end{Bmatrix}-\begin{Bmatrix} k_\varphi\left(\lambda_1^2\delta_{x_{10}}+\lambda_1\lambda_2\delta_{x_{20}}\right) \\ 0 \end{Bmatrix}$$

$$\mathbf{f}_{2i}=\begin{Bmatrix} m_2e_2\omega^2e^{\mathrm{j}\beta_2} \\ 0 \end{Bmatrix}e^{j\omega t}+\begin{Bmatrix} \Delta k_\xi\left(\lambda_1\lambda_2\delta_{x_{10}}+\lambda_2^2\delta_{x_{20}}\right)\sum_{i=-\infty}^{i=\infty}p_ie^{\mathrm{j}i\omega t} \\ 0 \end{Bmatrix}$$
$$-\begin{Bmatrix} k_\varphi\left(\lambda_1\lambda_2\delta_{x_{10}}+\lambda_2^2\delta_{x_{20}}\right) \\ 0 \end{Bmatrix}-\begin{Bmatrix} K_I\sum_{i=-\infty}^{i=\infty}I_ie^{\mathrm{j}i\omega t} \\ 0 \end{Bmatrix}$$

A relationship between master and global DOF established through transformation matrix isas follows

$$\left.\begin{aligned}\begin{Bmatrix}\mathbf{Q}_{1m}\\ \mathbf{Q}_{1s}\end{Bmatrix}&=\mathbf{T}_{\boldsymbol{d}_1}\mathbf{Q}_{1m}\\ \begin{Bmatrix}\mathbf{Q}_{2m}\\ \mathbf{Q}_{2s}\end{Bmatrix}&=\mathbf{T}_{\boldsymbol{d}_2}\mathbf{Q}_{2m}\end{aligned}\right\} \tag{3.50}$$

where transformation matrices are given by

$$\left.\begin{aligned}\mathbf{T}_{d_1}&=\begin{bmatrix}1&0&t_{d_1}&0\\0&1&0&t_{d_1}\end{bmatrix}^T\\ \mathbf{T}_{d_2}&=\begin{bmatrix}1&0&t_{d_2}&0\\0&1&0&t_{d_2}\end{bmatrix}^T\end{aligned}\right\} \tag{3.51}$$

with

$$t_{d_1} = \left[\frac{k_{1\varphi_y x}}{\left\{ (i\omega)^2 I_{d_1} - k_{1\varphi_y \varphi_y} \right\}} \right]$$

$$t_{d_2} = \left[\frac{k_{2\varphi_y x}}{\left\{ (i\omega)^2 I_{d_2} - k_{2\varphi_y \varphi_y} \right\}} \right]$$

Substituting Eqn. (3.51) in Eqn. (3.48), we get

$$\left[\left\{ -(i\omega)^2 \bar{\mathbf{M}}_1 + \mathrm{j}i\omega\left(\bar{\mathbf{C}}_1 - \mathrm{j}\Omega\bar{\mathbf{G}}_1\right) + \overline{\mathbf{K}}_1 \right\} \mathbf{T}_{\boldsymbol{d}_1} \mathbf{Q}_{1m} + \tilde{\mathbf{K}}_{t_3} \mathbf{T}_{\boldsymbol{d}_2} \mathbf{Q}_{2m} \right] \sum_{i=-\infty}^{i=\infty} e^{\mathrm{j}i\omega t} = \mathbf{f}_{1i} \quad (3.52)$$

Pre multiplying by $\mathbf{T}_{d_1}^T$, we get

$$\left[\left\{ -(i\omega)^2 \mathbf{T}_{\boldsymbol{d}_1}^T \bar{\mathbf{M}}_1 \mathbf{T}_{\boldsymbol{d}_1} + \mathrm{j}i\omega\left(\mathbf{T}_{\boldsymbol{d}_1}^T \bar{\mathbf{C}}_1 \mathbf{T}_{\boldsymbol{d}_1} - \mathrm{j}\Omega \mathbf{T}_{\boldsymbol{d}_1}^T \bar{\mathbf{G}}_1 \mathbf{T}_{\boldsymbol{d}_1} \right) + \mathbf{T}_{\boldsymbol{d}_1}^T \overline{\mathbf{K}}_1 \mathbf{T}_{\boldsymbol{d}_1} \right\} \mathbf{Q}_{1m} + \mathbf{T}_{\boldsymbol{d}_1}^T \tilde{\mathbf{K}}_{t_3} \mathbf{T}_{\boldsymbol{d}_2} \mathbf{Q}_{2m} \right] \sum_{i=-\infty}^{i=\infty} e^{\mathrm{j}i\omega t} = \mathbf{T}_{\boldsymbol{d}_1}^T \mathbf{f}_{1i} \quad (3.53)$$

$$\left[\left\{ -(i\omega)^2 \bar{\mathbf{M}}_{d_1} + \mathrm{j}i\omega\left(\bar{\mathbf{C}}_{d_1} - \mathrm{j}\Omega\bar{\mathbf{G}}_{d_1}\right) + \overline{\mathbf{K}}_{d_1} \right\} \mathbf{Q}_{1m} + \tilde{\mathbf{K}}_{d_{t_3}} \mathbf{Q}_{2m} \right] \sum_{i=-\infty}^{i=\infty} e^{\mathrm{j}i\omega t} = \bar{\mathbf{f}}_{1i_d} \quad (3.54)$$

In the above equation subscript *d* denotes dynamically condensed matrix. The system matrices in condensed form are defined as

$$\bar{\mathbf{M}}_{d_1} = \mathbf{T}_{\boldsymbol{d}_1}^T \bar{\mathbf{M}}_1 \mathbf{T}_{\boldsymbol{d}_1} = \begin{bmatrix} m_1 + \left(t_{d_1}\right)^2 I_{d_1} & 0 \\ 0 & m_1 + \left(t_{d_1}\right)^2 I_{d_1} \end{bmatrix}$$

$$\bar{\mathbf{M}}_{d_2} = \mathbf{T}_{\boldsymbol{d}_2}^T \bar{\mathbf{M}}_2 \mathbf{T}_{\boldsymbol{d}_2} = \begin{bmatrix} m_2 + \left(t_{d_2}\right)^2 I_{d_2} & 0 \\ 0 & m_2 + \left(t_{d_2}\right)^2 I_{d_2} \end{bmatrix}$$

$$\bar{\mathbf{C}}_{d_1} = \mathbf{T}_{\boldsymbol{d}_1}^T \bar{\mathbf{C}}_1 \mathbf{T}_{\boldsymbol{d}_1} = \begin{bmatrix} c_{1xx} + t_{d_1}\left(c_{1x\varphi_y} + c_{1\varphi_y x}\right) + \left(t_{d_1}\right)^2 c_{1\varphi_y\varphi_y} & 0 \\ 0 & c_{1xx} + t_{d_1}\left(c_{1x\varphi_y} + c_{1\varphi_y x}\right) + \left(t_{d_1}\right)^2 c_{1\varphi_y\varphi_y} \end{bmatrix}$$

$$\bar{\mathbf{C}}_{d_2} = \mathbf{T}_{\boldsymbol{d}_2}^T \bar{\mathbf{C}}_2 \mathbf{T}_{\boldsymbol{d}_2} = \begin{bmatrix} c_{2xx} + t_{d_2}\left(c_{2x\varphi_y} + c_{2\varphi_y x}\right) + \left(t_{d_2}\right)^2 c_{2\varphi_y\varphi_y} & 0 \\ 0 & c_{2xx} + t_{d_2}\left(c_{2x\varphi_y} + c_{2\varphi_y x}\right) + \left(t_{d_2}\right)^2 c_{2\varphi_y\varphi_y} \end{bmatrix}$$

$$\bar{\mathbf{G}}_{d_1} = \mathbf{T}_{\boldsymbol{d}_1}^{T}\bar{\mathbf{G}}_1\mathbf{T}_{\boldsymbol{d}_1} = \begin{bmatrix} 0 & \left(t_{d_1}\right)^2 I_{p_1} \\ -\left(t_{d_1}\right)^2 I_{p_1} & 0 \end{bmatrix}$$

$$\bar{\mathbf{G}}_{d_2} = \mathbf{T}_{\boldsymbol{d}_2}^{T}\bar{\mathbf{G}}_2\mathbf{T}_{\boldsymbol{d}_2} = \begin{bmatrix} 0 & \left(t_{d_2}\right)^2 I_{p_2} \\ -\left(t_{d_2}\right)^2 I_{p_2} & 0 \end{bmatrix}$$

$$\bar{\mathbf{K}}_{d_2} = \mathbf{T}_{\boldsymbol{d}_1}^{T}\bar{\mathbf{K}}_2\mathbf{T}_{\boldsymbol{d}_1} =$$

$$\begin{bmatrix} k_{2xx} + \lambda_2^2 k_{\varphi_c} - k_s + t_{d_2}\left(k_{2x\varphi_y} + k_{2\varphi_y x}\right) + \left(t_{d_2}\right)^2 k_{2\varphi_y\varphi_y} & 0 \\ 0 & k_{2xx} + \lambda_2^2 k_{\varphi_c} - k_s + t_{d_2}\left(k_{2x\varphi_y} + k_{2\varphi_y x}\right) + \left(t_{d_2}\right)^2 k_{2\varphi_y\varphi_y} \end{bmatrix}$$

$$\bar{\mathbf{K}}_{d_1} = \mathbf{T}_{\boldsymbol{d}_1}^{T}\bar{\mathbf{K}}_1\mathbf{T}_{\boldsymbol{d}_1} =$$

$$\begin{bmatrix} k_{1xx} + \lambda_1^2 k_{\varphi_c} + t_{d_1}\left(k_{1x\varphi_y} + k_{1\varphi_y x}\right) + \left(t_{d_1}\right)^2 k_{1\varphi_y\varphi_y} & 0 \\ 0 & k_{1xx} + \lambda_1^2 k_{\varphi_c} + t_{d_1}\left(k_{1x\varphi_y} + k_{1\varphi_y x}\right) + \left(t_{d_1}\right)^2 k_{1\varphi_y\varphi_y} \end{bmatrix}$$

$$\tilde{\mathbf{K}}_{d_{t_3}} = \mathbf{T}_{\boldsymbol{d}_1}^{T}\tilde{\mathbf{K}}_{t_3}\mathbf{T}_{\boldsymbol{d}_2} = \begin{bmatrix} \lambda_1\lambda_2 k_{\varphi_c} & 0 \\ 0 & \lambda_1\lambda_2 k_{\varphi_c} \end{bmatrix}$$

$$\bar{\mathbf{f}}_{1i_d} = \begin{Bmatrix} m_1 e_1 \omega^2 \cos(\omega t + \beta_1) \\ m_1 e_1 \omega^2 \sin(\omega t + \beta_1) \end{Bmatrix} + \Delta k_\xi \left(\lambda_1^2 \delta_{x_{10}} + \lambda_1\lambda_2 \delta_{x_{20}}\right) p_i \begin{Bmatrix} \cos(i\omega t) \\ \sin(i\omega t) \end{Bmatrix} - \begin{Bmatrix} k_{\varphi_c}\left(\lambda_1^2 \delta_{x_{10}} + \lambda_1\lambda_2 \delta_{x_{20}}\right) \\ 0 \end{Bmatrix}$$

$$\bar{\mathbf{f}}_{2i_d} = \begin{Bmatrix} m_2 e_2 \omega^2 \cos(\omega t + \beta_2) \\ m_2 e_2 \omega^2 \sin(\omega t + \beta_2) \end{Bmatrix} + \Delta k_\xi \left(\lambda_1\lambda_2 \delta_{x_{10}} + \lambda_2^2 \delta_{x_{20}}\right) p_i \begin{Bmatrix} \cos(i\omega t) \\ \sin(i\omega t) \end{Bmatrix}$$
$$- \begin{Bmatrix} k_{\varphi_c}\left(\lambda_1\lambda_2 \delta_{x_{10}} + z_2^2 \delta_{x_{20}}\right) \\ 0 \end{Bmatrix} - k_I I_i \begin{Bmatrix} \cos(i\omega t) \\ \sin(i\omega t) \end{Bmatrix}$$

where p_i is the participation factor of the i^{th} harmonic of the misalignment excitation force. Upon converting Eqn. (3.54) into complex form, we get

$$\begin{bmatrix} -(i\omega)^2 \left\{ m_1 + \left(t_{d_1}\right)^2 I_{d_1} \right\} + \mathrm{j}i\omega \left\{ c_{1xx} + t_{d_1}\left(c_{1x\varphi_y} + c_{1\varphi_y x}\right) + \left(t_{d_1}\right)^2 c_{1\varphi_y\varphi_y} + jI_{p_1}\omega\left(t_{d_1}\right)^2 \right\} \\ \left\{ k_{1xx} + \lambda_1^2 k_{\varphi_c} + t_{d_1}\left(k_{1x\varphi_y} + k_{1\varphi_y x}\right) + \left(t_{d_1}\right)^2 k_{1\varphi_y\varphi_y} \right\} R_{1i} + \lambda_1\lambda_2 k_{\varphi_c} R_{2i} \end{bmatrix} \qquad (3.55)$$
$$= m_1 e_1 \omega^2 e^{\mathrm{j}(\beta_1)} + \Delta k_\xi \left(\lambda_1^2 \delta_{x_{10}} + \lambda_1\lambda_2 \delta_{x_{20}}\right) p_i - k_{\varphi_c}\left(\lambda_1^2 \delta_{x_{10}} + \lambda_1\lambda_2 \delta_{x_{20}}\right)$$

Likewise, upon substituting Eqn. (3.51) in Eqn. (3.49) and converting into complex form, we get

$$\left[-(i\omega)^2\left\{m_2+\left(t_{d_2}\right)^2 I_{d_2}\right\}+\mathrm{j}i\omega\left\{c_{2xx}+t_{d_2}\left(c_{2x\varphi_y}+c_{2\varphi_y x}\right)+\left(t_{d_2}\right)^2 c_{2\varphi_y\varphi_y}+\mathrm{j}I_{p_2}\omega\left(t_{d_2}\right)^2\right\}+\right.$$
$$\left.\left\{k_{2xx}+\lambda_2^2 k_{\varphi_c}-k_s+t_{d_2}\left(k_{2x\varphi_y}+k_{2\varphi_y x}\right)+\left(t_{d_2}\right)^2 k_{2\varphi_y\varphi_y}\right\}R_{2i}+\lambda_1\lambda_2 k_{\varphi_c}R_{1i}\right]=m_2 e_2\omega^2 e^{\mathrm{j}(\beta_2)} \qquad (3.56)$$
$$+\Delta k_\xi\left(\lambda_1\lambda_2\delta_{x_{10}}+\lambda_2^2\delta_{x_{20}}\right)p_i-k_I I_i-k_{\varphi_c}\left(\lambda_1\lambda_2\delta_{x_{10}}+\lambda_2^2\delta_{x_{20}}\right)$$

Eqns. (3.55) and (3.56) are the frequency domain equations for coupled rotor system with integrated AMB, represented purely in terms of master DOFs.

3.9 Estimation of Rotor, Coupling and AMB Parameters

The dynamically condensed complex Eqns. (3.55) and (3.56) are expanded and rearranged so as to arrange the known parameters on the left hand side and unknown parameters on the right hand side. The identifiable parameters are $c_1, c_2, k_\varphi, \Delta k_\xi, e_1, \beta_1, e_2, \beta_2, k_s$ and k_i, which represent rotor-1 equivalent viscous damping in *x*-direction, rotor–2 equivalent viscous damping in *x*-direction, coupling static angular stiffness, coupling ACS, eccentricity of disc-1, phase of unbalance on disc-1, eccentricity of disc-2, phase of unbalance on disc-2, AMB displacement constant and AMB current constant, respectively. The development of regression equations for rotor-1 and rotor-2 are provided in next section.

3.10 Regression Equations of Rotor-1

Rearranging Eqn. (3.55) by segregating known and unknown quantities, we get

$$\left(\mathrm{j}i\omega c_{1xx}R_{1i}+\lambda_1^2 k_{\varphi_c}R_{1i}+\lambda_1\lambda_2 k_{\varphi_c}R_{2i}\right)-m_1 e_1\omega^2 e^{\mathrm{j}(\beta_1)}-\Delta k_\xi\left(\lambda_1^2\delta_{x_{10}}+\lambda_1\lambda_2\delta_{x_{20}}\right)p_i$$
$$+k_{\varphi_c}\left(\lambda_1^2\delta_{x_{10}}+\lambda_1\lambda_2\delta_{x_{20}}\right)=\left[(i\omega)^2\left\{m_1+\left(t_{d_1}\right)^2 I_{d_1}\right\}-ji\omega\left\{t_{d_1}\left(c_{1x\varphi_y}+c_{1\varphi_y x}\right)+\left(t_{d_1}\right)^2 c_{1\varphi_y\varphi_y}\right\}\right.$$
$$\left.+i\omega^2 I_{p_1}\left(t_{d_1}\right)^2-\left\{k_{1xx}+t_{d_1}\left(k_{1x\varphi_y}+k_{1\varphi_y x}\right)+\left(t_{d_1}\right)^2 k_{1\varphi_y\varphi_y}\right\}\right]R_{1i}$$

(3.57)

For the sake of convenience, the following notations shall be adopted

$$m_1' = m_1 + \left(t_{d_1}\right)^2 I_{d_1}; c_1' = t_{d_1}\left(c_{1x\varphi_y} + c_{1\varphi_y x}\right) + \left(t_{d_1}\right)^2 c_{1\varphi_y\varphi_y}; k_1' = k_{22} + t_{d_1}\left(k_{23} + k_{32}\right) + \left(t_{d_1}\right)^2 k_{33} \quad (3.58)$$

Eqn. (3.57) then takes the following modified form

$$\begin{aligned}&\left(\mathrm{j}i\omega c_{1xx}R_{1i} + z_1^2 k_{\varphi_c} R_{1i} + z_1 z_2 k_{\varphi_c} R_{2i}\right) - m_1 e_1 \omega^2 e^{\mathrm{j}(\beta_1)} - \Delta k_\xi \left(z_1^2 \delta_{x_{10}} + z_1 z_2 \delta_{x_{20}}\right) p_i \\ &+ k_{\varphi_c}\left(z_1^2 \delta_{x_{10}} + z_1 z_2 \delta_{x_{20}}\right) = \left\{(i\omega)^2 m_1' - \mathrm{j}i\omega c_1' + i\omega^2 I_{p_1}\left(t_{d_1}\right)^2 - k_1'\right\} R_{1i}\end{aligned} \quad (3.59)$$

Eqn. (3.59) can be expanded for various harmonic indices, i.e. $i = -n, \ldots, -2, -1, 0, 1, 2, \ldots, n$.

3.10.1 *i* = 0: Constant Coupling Misalignment Force

Extracting terms corresponding to $i = 0$ from Eqn. (3.59), we get

$$k_{\varphi_c}\left(z_1^2 R_{10} + z_1 z_2 R_{20}\right) - \Delta k_\xi \left(z_1^2 \delta_{x_{10}} + z_1 z_2 \delta_{x_{20}}\right) p_0 + k_{\varphi_c}\left(z_1^2 \delta_{x_{10}} + z_1 z_2 \delta_{x_{20}}\right) = -k_1' R_{10} \quad (3.60)$$

The real and imaginary displacement components of 0^{th} harmonic of rotor-1 are

$$R_{10} = R_{10,\mathrm{Re}} + \mathrm{j}R_{10,Im}; R_{20} = R_{20,\mathrm{Re}} + \mathrm{j}R_{20,Im} \quad (3.61)$$

Upon substituting Eqn. (3.61), Eqn. (3.60) becomes

$$\begin{aligned}&k_{\varphi_c}\left\{z_1^2\left(R_{10,\mathrm{Re}} + \mathrm{j}R_{10,Im}\right) + z_1 z_2\left(R_{20,\mathrm{Re}} + \mathrm{j}R_{20,Im}\right)\right\} - \Delta k_\xi\left(z_1^2\delta_{x_{10}} + z_1 z_2 \delta_{x_{20}}\right) p_0 \\ &+ k_{\varphi_c}\left(z_1^2 \delta_{x_{10}} + z_1 z_2 \delta_{x_{20}}\right) = -k_1'\left(R_{10,\mathrm{Re}} + \mathrm{j}R_{10,Im}\right)\end{aligned} \quad (3.62)$$

Eqn. (3.62) can be further separated into the real and imaginary parts, as

$$k_{\varphi_c}\left\{z_1^2\left(R_{10,\mathrm{Re}} + \delta_{x_{10}}\right) + z_1 z_2\left(R_{20,\mathrm{Re}} + \delta_{x_{20}}\right)\right\} - \Delta k_\xi\left(z_1^2\delta_{x_{10}} + z_1 z_2 \delta_{x_{20}}\right) p_0 = -k_1' R_{10,\mathrm{Re}} \quad (3.63)$$

and

$$k_{\varphi_c}\left(z_1^2 R_{10,Im} + z_1 z_2 R_{20,Im}\right) = -k_1' R_{10,Im} \quad (3.64)$$

3.10.2 *i* = 1: Unbalance force and 1st harmonic of time-dependent coupling misalignment force

Extracting terms corresponding to $i = 1$ from Eqn. (3.59), we get

$$\begin{aligned}&\left(\mathrm{j}\omega c_{1xx}R_{11}+z_1^2k_{\varphi_c}R_{11}+z_1z_2k_{\varphi_c}R_{21}\right)-m_1e_1\omega^2e^{\mathrm{j}\beta_1}-\Delta k_\xi\left(z_1^2\delta_{x_{10}}+z_1z_2\delta_{x_{20}}\right)p_1\\&=\left\{(\omega)^2m_1'-\mathrm{j}\omega c_1'+\omega^2I_{p_1}\left(t_{d_1}\right)^2-k_1'\right\}R_{11}\end{aligned}\tag{3.65}$$

The real and imaginary displacement components of 1st harmonic of rotor-1 are

$$R_{11}=R_{11,\mathrm{Re}}+\mathrm{j}R_{11,Im};R_{21}=R_{21,\mathrm{Re}}+\mathrm{j}R_{21,Im}\tag{3.66}$$

Upon substituting Eqn. (3.66), Eqn. (3.65) becomes

$$\begin{aligned}&\left\{\mathrm{j}\omega c_{1xx}\left(R_{11,\mathrm{Re}}+\mathrm{j}R_{11,Im}\right)+z_1^2k_{\varphi_c}\left(R_{11,\mathrm{Re}}+\mathrm{j}R_{11,Im}\right)+z_1z_2k_{\varphi_c}\left(R_{21,\mathrm{Re}}+\mathrm{j}R_{21,Im}\right)\right\}-m_1e_1\omega^2e^{\mathrm{j}\beta_1}\\&-\Delta k_\xi\left(z_1^2\delta_{x_{10}}+z_1z_2\delta_{x_{20}}\right)p_1=\left\{(\omega)^2m_1'-\mathrm{j}\omega c_1'+\omega^2I_{p_1}\left(t_{d_1}\right)^2-k_1'\right\}\left(R_{11,\mathrm{Re}}+\mathrm{j}R_{11,Im}\right)\end{aligned}\tag{3.67}$$

Eqn. (3.67) can be further separated into the real and imaginary parts, as

$$\begin{aligned}&-\omega c_{1xx}R_{11,Im}+k_{\varphi_c}\left(z_1^2R_{11,\mathrm{Re}}+z_1z_2R_{21,\mathrm{Re}}\right)-m_1\omega^2e_{1,\mathrm{Re}}-\Delta k_\xi\left(z_1^2\delta_{x_{10}}+z_1z_2\delta_{x_{20}}\right)p_1\\&=\left\{(\omega)^2m_1'+\omega^2I_{p_1}\left(t_{d_1}\right)^2-k_1'\right\}R_{11,\mathrm{Re}}+\omega c_1'R_{11,Im}\end{aligned}\tag{3.68}$$

$$\omega c_{1xx}R_{11,\mathrm{Re}}+k_{\varphi_c}\left(z_1^2R_{11,Im}+z_1z_2R_{21,Im}\right)-m_1\omega^2e_{1,\mathrm{Im}}=\left\{(\omega)^2m_1'+\omega^2I_{p_1}\left(t_{d_1}\right)^2-k_1'\right\}R_{11,Im}-\omega c_1'R_{11,\mathrm{Re}}\tag{3.69}$$

3.10.3 $i\neq 0$ and $\mathrm{i}\neq 1$: Other harmonics of time dependent coupling misalignment force

Extracting terms corresponding to $i\neq 0$ and $i\neq 1$ from Eqn. (3.59), we get

$$\begin{aligned}&\left(\mathrm{j}i\omega c_{1xx}R_{1i}+z_1^2k_{\varphi_c}R_{1i}+z_1z_2k_{\varphi_c}R_{2i}\right)-\Delta k_\xi\left(z_1^2\delta_{x_{10}}+z_1z_2\delta_{x_{20}}\right)p_i\\&=\left\{(i\omega)^2m_1'-\mathrm{j}i\omega c_1'+i\omega^2I_{p_1}\left(t_{d_1}\right)^2-k_1'\right\}R_{1i}\end{aligned}\tag{3.70}$$

The real and imaginary displacement components of i^{th} harmonic of rotor-1 are

$$R_{1i}=R_{1i,\mathrm{Re}}+\mathrm{j}R_{1i,Im};R_{2i}=R_{2i,\mathrm{Re}}+\mathrm{j}R_{2i,Im}\tag{3.71}$$

Upon substituting Eqn. (3.71), Eqn. (3.70) changes to

$$\begin{aligned}&\left\{ji\omega c_{1xx}\left(R_{1i,\mathrm{Re}}+\mathrm{j}R_{1i,Im}\right)+z_1^2k_{\varphi_c}\left(R_{1i,\mathrm{Re}}+\mathrm{j}R_{1i,Im}\right)+z_1z_2k_{\varphi_c}\left(R_{2i,\mathrm{Re}}+\mathrm{j}R_{2i,Im}\right)\right\}-\\&\Delta k_\xi\left(z_1^2\delta_{x_{10}}+z_1z_2\delta_{x_{20}}\right)p_i=\left\{(i\omega)^2m_1'-\mathrm{j}i\omega c_1'+i\omega^2I_{p_1}\left(t_{d_1}\right)^2-k_1'\right\}\left(R_{1i,\mathrm{Re}}+\mathrm{j}R_{1i,Im}\right)\end{aligned}\tag{3.72}$$

Eqn. (3.72) can be further separated into the real and imaginary parts, as

$$-i\omega c_{1xx}R_{1i,Im}+k_{\varphi_c}\left(z_1^2R_{1i,\mathrm{Re}}+z_1z_2R_{2i,\mathrm{Re}}\right)-\Delta k_{\xi}\left(z_1^2\delta_{x_{10}}+z_1z_2\delta_{x_{20}}\right)p_i \\ =\left\{(i\omega)^2m_1'+i\omega^2I_{p_1}\left(t_{d_1}\right)^2-k_1'\right\}R_{1i,\mathrm{Re}}+i\omega c_1'R_{1i,Im} \tag{3.73}$$

and

$$i\omega c_{1xx}R_{1i,\mathrm{Re}}+k_{\varphi_c}\left(z_1^2R_{1i,Im}+z_1z_2R_{2i,Im}\right)=\left\{(i\omega)^2m_1'+i\omega^2I_{p_1}\left(t_{d_1}\right)^2-k_1'\right\}R_{1i,Im}-i\omega c_1'R_{1i,\mathrm{Re}} \tag{3.74}$$

3.11 Regression Equations of Rotor-2

Rearranging Eqn. (3.56) by segregating the known and unknown quantities, we get

$$\left(\mathrm{j}i\omega c_{2xx}R_{2i}+z_2^2k_{\varphi_c}R_{2i}+z_1z_2k_{\varphi_c}R_{1i}\right)-m_2e_2\omega^2e^{\mathrm{j}(\beta_2)}-\Delta k_{\xi}\left(z_1z_2\delta_{x_{10}}+z_2^2\delta_{x_{20}}\right)p_i \\ +\left(k_II_i+k_sR_{2i}\right)+k_{\varphi_c}\left(z_1z_2\delta_{x_{10}}+z_2^2\delta_{x_{20}}\right)= \\ (i\omega)^2\left\{m_2+\left(t_{d_2}\right)^2I_{d_2}\right\}-ji\omega\left\{t_{d_2}\left(c_{2x\varphi_y}+c_{2\varphi_yx}\right)+\left(t_{d_2}\right)^2c_{2\varphi_y\varphi_y}\right\} \\ +iI_{p_2}\omega^2\left(t_{d_2}\right)^2-\left\{k_{2xx}+t_{d_2}\left(k_{2x\varphi_y}+k_{2\varphi_yx}\right)+\left(t_{d_2}\right)^2k_{2\varphi_y\varphi_y}\right\}R_{2i} \tag{3.75}$$

For the sake of convenience, the following notations shall be adopted

$$m_2'=m_2+\left(t_{d_2}\right)^2I_{d_2};c_2'=t_{d_2}\left(c_{2x\varphi_y}+c_{2\varphi_yx}\right)+\left(t_{d_2}\right)^2c_{2\varphi_y\varphi_y};k_2'=k_{2xx}+t_{d_2}\left(k_{2x\varphi_y}+k_{2\varphi_yx}\right)+\left(t_{d_2}\right)^2k_{2\varphi_y\varphi_y} \tag{3.76}$$

Eqn. (3.75) takes the following modified form

$$\left(\mathrm{j}i\omega c_{2xx}R_{2i}+z_2^2k_{\varphi_c}R_{2i}+z_1z_2k_{\varphi_c}R_{1i}\right)-m_2e_2\omega^2e^{\mathrm{j}(\beta_2)}-\Delta k_{\xi}\left(z_1z_2\delta_{x_{10}}+z_2^2\delta_{x_{20}}\right)p_i+k_II_i \\ +k_sR_{2i}+k_{\varphi_c}\left(z_1z_2\delta_{x_{10}}+z_2^2\delta_{x_{20}}\right)=\left\{(i\omega)^2m_2'-\mathrm{j}i\omega c_2'+iI_{p_2}\omega^2\left(t_{d_2}\right)^2-k_2'\right\}R_{2i} \tag{3.77}$$

Eqn. (3.77) can be expanded for various harmonic indices, i.e. $i = -n,\ldots,-2,-1,0,1,2,\ldots,n$.

3.11.1 $i = 0$: constant coupling misalignment force

Extracting terms corresponding to $i = 0$ from Eqn. (3.77), we get

$$k_{\varphi_c}\left(z_2^2R_{20}+z_1z_2R_{10}\right)-\Delta k_{\xi}\left(z_1z_2\delta_{x_{10}}+z_2^2\delta_{x_{20}}\right)p_0+k_iI_0+k_sR_{20}+k_{\varphi_c}\left(z_1z_2\delta_{x_{10}}+z_2^2\delta_{x_{20}}\right)=-k_2'R_{20} \tag{3.78}$$

0^{th} harmonic of rotor-2 displacement is made of the real and imaginary components, i.e.

$$R_{10}=R_{10,\mathrm{Re}}+\mathrm{j}R_{10,Im};\quad R_{20}=R_{20,\mathrm{Re}}+\mathrm{j}R_{20,Im};\quad I_0=I_{0,\mathrm{Re}}+\mathrm{j}I_{0,Im} \tag{3.79}$$

Upon substituting Eqn. (3.79), Eqn. (3.78) becomes

$$\begin{aligned}&k_{\varphi_c}\left\{z_2^2\left(R_{20,\mathrm{Re}}+\mathrm{j}R_{20,Im}\right)+z_1z_2\left(R_{10,\mathrm{Re}}+\mathrm{j}R_{10,Im}\right)\right\}-\Delta k_{\xi}\left(z_1z_2\delta_{x_{10}}+z_2^2\delta_{x_{20}}\right)p_0\\&+k_i\left(I_{0,\mathrm{Re}}+\mathrm{j}I_{0,Im}\right)+k_s\left(R_{20,\mathrm{Re}}+\mathrm{j}R_{20,Im}\right)+k_{\varphi_c}\left(z_1z_2\delta_{x_{10}}+z_2^2\delta_{x_{20}}\right)=-k_2'\left(R_{20,\mathrm{Re}}+\mathrm{j}R_{20,Im}\right)\end{aligned} \tag{3.80}$$

Eqn. (3.80) can be further separated into the real and imaginary parts, as

$$\begin{aligned}k_{\varphi_c}\left\{z_2^2\left(R_{20,\mathrm{Re}}+\delta_{x_{20}}\right)+z_1z_2\left(R_{10,\mathrm{Re}}+\delta_{x_{10}}\right)\right\}-\Delta k_{\xi}\left(z_1z_2\delta_{x_{10}}+z_2^2\delta_{x_{20}}\right)p_0\\+k_iI_{0,\mathrm{Re}}+k_sR_{20,\mathrm{Re}}=-k_2'R_{20,\mathrm{Re}}\end{aligned} \tag{3.81}$$

$$k_{\varphi_c}\left\{z_2^2R_{20,Im}+z_1z_2R_{10,Im}\right\}+k_iI_{0,Im}+k_sR_{20,Im}=-k_2'R_{20,Im} \tag{3.82}$$

3.11.2 *i* = 1: unbalance force and 1st harmonic of time dependent coupling misalignment force

Extracting terms corresponding to $i = 1$ from Eqn. (3.77), we get

$$\begin{aligned}&\left(\mathrm{j}\omega c_{1xx}R_{21}+z_2^2k_{\varphi_c}R_{21}+z_1z_2k_{\varphi_c}R_{11}\right)-m_2e_2\omega^2e^{\mathrm{j}\beta_2}-\Delta k_{\xi}\left(z_1z_2\delta_{x_{10}}+z_2^2\delta_{x_{20}}\right)p_1\\&+k_iI_1+k_sR_{21,\mathrm{Re}}=\left\{(\omega)^2m_2'-\mathrm{j}\omega c_2'+I_{p_2}\omega^2\left(t_{d_2}\right)^2-k_2'\right\}R_{21}\end{aligned} \tag{3.83}$$

The real and imaginary components of 1st harmonic of rotor-2 complex displacement and current are

$$R_{11}=R_{11,\mathrm{Re}}+\mathrm{j}R_{11,Im};R_{21}=R_{21,\mathrm{Re}}+\mathrm{j}R_{21,Im};I_1=I_{1,\mathrm{Re}}+\mathrm{j}I_{1,Im} \tag{3.84}$$

Upon substituting Eqn. (3.84), Eqn. (3.83) turns into

$$\begin{aligned}&\left\{\mathrm{j}\omega c_{2xx}\left(R_{21,\mathrm{Re}}+\mathrm{j}R_{21,Im}\right)+z_2^2k_{\varphi_c}\left(R_{21,\mathrm{Re}}+\mathrm{j}R_{21,Im}\right)+z_1z_2k_{\varphi_c}\left(R_{11,\mathrm{Re}}+\mathrm{j}R_{11,Im}\right)\right\}\\&-m_2e_2\omega^2e^{j\beta_2}-\Delta k_{\xi}\left(z_1z_2\delta_{x_{10}}+z_2^2\delta_{x_{20}}\right)p_1+K_I\left(I_{1,\mathrm{Re}}+\mathrm{j}I_{1,Im}\right)+k_s\left(R_{21,\mathrm{Re}}+\mathrm{j}R_{21,Im}\right)\\&=\left\{(\omega)^2m_2'-\mathrm{j}\omega c_2'+I_{p_2}\omega^2\left(t_{d_2}\right)^2-k_2'\right\}\left(R_{21,\mathrm{Re}}+\mathrm{j}R_{21,Im}\right)\end{aligned} \tag{3.85}$$

Eqn. (3.85) can be further separated into the real and imaginary parts, as

$$-\omega c_{2xx}R_{21,Im}+k_{\varphi_c}(z_2^2R_{21,\mathrm{Re}}+z_1z_2R_{11,\mathrm{Re}})-m_2\omega^2e_{2,\mathrm{Re}}-\Delta k_\xi\left(z_1z_2\delta_{x_{10}}+z_2^2\delta_{x_{20}}\right)p_1+k_II_{1,\mathrm{Re}}+k_sR_{21,\mathrm{Re}}$$
$$=\left\{\omega^2m_2'+I_{p_2}\omega^2\left(t_{d_2}\right)^2-k_2'\right\}R_{21,\mathrm{Re}}+\omega c_2'R_{21,Im} \tag{3.86}$$

$$\omega c_{2xx}R_{21,\mathrm{Re}}+k_{\varphi_c}\left(z_2^2R_{21,Im}+z_1z_2R_{11,Im}\right)-m_2\omega^2e_{2,\mathrm{Im}}+K_II_{1,Im}+k_sR_{21,\mathrm{Im}}$$
$$=\left\{\omega^2m_2'+I_{p_2}\omega^2\left(t_{d_2}\right)^2-k_2'\right\}R_{21,Im}-\omega c_2'R_{21,\mathrm{Re}} \tag{3.87}$$

3.11.3 $i\neq 0$ and $i\neq 1$: Other harmonics of time dependent coupling misalignment force

Extracting terms corresponding to $i\neq 0$ and $i\neq 1$ from Eqn. (3.77), we get

$$\left(\mathrm{j}i\omega c_{2xx}R_{2i}+z_2^2k_{\varphi_c}R_{2i}+z_1z_2k_{\varphi_c}R_{1i}\right)-\Delta k_\xi\left(z_1z_2\delta_{x_{10}}+z_2^2\delta_{x_{20}}\right)p_i+k_II_i+k_sR_{2i}$$
$$=\left\{(i\omega)^2m_2'-\mathrm{j}i\omega c_2'+iI_{p_2}\omega^2\left(t_{d_2}\right)^2-k_2'\right\}R_{2i} \tag{3.88}$$

The real and imaginary displacement components of i^{th} harmonic of rotor-2 complex displacement and current are

$$R_{1i}=R_{1i,\mathrm{Re}}+jR_{1i,Im};\quad R_{2i}=R_{2i,\mathrm{Re}}+jR_{2i,Im};\quad I_i=I_{i,\mathrm{Re}}+jI_{i,Im} \tag{3.89}$$

Upon substituting Eqn. (3.89), Eqn. (3.88) becomes

$$\left\{ji\omega c_{2xx}\left(R_{2i,\mathrm{Re}}+\mathrm{j}R_{2i,Im}\right)+z_2^2k_{\varphi_c}\left(R_{2i,\mathrm{Re}}+\mathrm{j}R_{2i,Im}\right)+z_1z_2k_{\varphi_c}\left(R_{1i,\mathrm{Re}}+\mathrm{j}R_{1i,Im}\right)\right\}-$$
$$\Delta k_\xi\left(z_1z_2\delta_{x_{10}}+z_2^2\delta_{x_{20}}\right)p_i+k_I\left(I_{i,\mathrm{Re}}+\mathrm{j}I_{i,Im}\right)+k_s\left(R_{2i,\mathrm{Re}}+\mathrm{j}R_{2i,Im}\right)=$$
$$\left\{(i\omega)^2m_2'-\mathrm{j}i\omega c_2'+iI_{p_2}\omega^2\left(t_{d_2}\right)^2-k_2'\right\}\left(R_{2i,\mathrm{Re}}+\mathrm{j}R_{2i,Im}\right) \tag{3.90}$$

Eqn. (3.90) can be further separated into the real and imaginary parts, as

$$-i\omega c_{2xx}R_{2i,Im}+k_{\varphi_c}\left(z_2^2R_{2i,\mathrm{Re}}+z_1z_2R_{1i,\mathrm{Re}}\right)-\Delta k_\xi\left(z_1z_2\delta_{x_{10}}+z_2^2\delta_{x_{20}}\right)p_i+K_II_{i,\mathrm{Re}}+k_sR_{2i,\mathrm{Re}}$$
$$=\left\{(i\omega)^2m_2'+iI_{p_2}\omega^2\left(t_{d_2}\right)^2-k_2'\right\}R_{2i,\mathrm{Re}}+i\omega c_2'R_{2i,Im} \tag{3.91}$$

$$
\begin{aligned}
&i\omega c_{2xx}R_{2i,\mathrm{Re}} + k_{\varphi_c}\left(z_2^2 R_{2i,Im} + z_1 z_2 R_{1i,Im}\right) + K_I I_{i,Im} + k_s R_{2i,Im} \\
&= \left\{(i\omega)^2 m_2' + iI_{p_2}\omega^2\left(t_{d_2}\right)^2 - k_2'\right\} R_{2i,Im} - i\omega c_2' R_{2i,\mathrm{Re}}
\end{aligned}
\tag{3.92}
$$

Eqns. (3.63), (3.64), (3.68), (3.69), (3.73), (3.74) of rotor-1 and Eqns. (3.81), (3.82), (3.86), (3.87), (3.91) and (3.92) of rotor-2 are arranged in a matrix form, as

$$
\mathbf{A}_1\mathbf{x}_1 = \mathbf{b}_1 \tag{3.93}
$$

The regression matrix $\mathbf{A_1}$, vector of known quantities $\mathbf{b_1}$ and vector of identifiable parameters $\mathbf{x_1}$ used in the estimation of various system faults and parameters are shown below.

$$
\mathbf{A}_1 = \begin{bmatrix}
0 & 0 & 0 & 0 & 0 & 0 & \lambda_1^2\left(R_{10,\mathrm{Re}}+\delta_{x_{10}}\right)+\lambda_1\lambda_2\left(R_{20,\mathrm{Re}}+\delta_{x_{20}}\right) & -\left(\lambda_1^2\delta_{x_{10}}+\lambda_1\lambda_2\delta_{x_{20}}\right)p_0 & 0 & 0 \\
0 & 0 & 0 & 0 & 0 & 0 & \lambda_1^2 R_{10,Im}+\lambda_1\lambda_2 R_{20,Im} & 0 & 0 & 0 \\
-\omega R_{11,Im} & 0 & -m_1\omega^2 & 0 & 0 & 0 & \lambda_1^2 R_{11,\mathrm{Re}}+\lambda_1\lambda_2 R_{21,\mathrm{Re}} & -\left(\lambda_1^2\delta_{x_{10}}+\lambda_1\lambda_2\delta_{x_{20}}\right)p_1 & 0 & 0 \\
\vdots & \vdots & \vdots & \vdots & \vdots & \vdots & \vdots & \vdots & \vdots & \vdots \\
5\omega R_{15,\mathrm{Re}} & 0 & 0 & 0 & 0 & 0 & \lambda_1^2 R_{15,Im}+\lambda_1\lambda_2 R_{25,Im} & 0 & 0 & 0 \\
0 & 0 & 0 & 0 & 0 & 0 & \lambda_2^2\left(R_{20,\mathrm{Re}}+\delta_{x_{20}}\right)+\lambda_1\lambda_2\left(R_{10,\mathrm{Re}}+\delta_{x_{10}}\right) & -\left(\lambda_1\lambda_2\delta_{x_{10}}+\lambda_2^2\delta_{x_{20}}\right)p_0 & I_{0,\mathrm{Re}} & R_{20,\mathrm{Re}} \\
0 & 0 & 0 & 0 & 0 & 0 & \lambda_2^2 R_{20,Im}+\lambda_1\lambda_2 R_{10,Im} & 0 & I_{0,Im} & R_{20,Im} \\
0 & 0 & 0 & 0 & -m_2\omega^2 & 0 & \lambda_2^2 R_{21,\mathrm{Re}}+\lambda_1\lambda_2 R_{11,\mathrm{Re}} & -\left(\lambda_1\lambda_2\delta_{x_{10}}+\lambda_2^2\delta_{x_{20}}\right)p_1 & I_{1,\mathrm{Re}} & R_{21,\mathrm{Re}} \\
\vdots & \vdots & \vdots & \vdots & \vdots & \vdots & \vdots & \vdots & \vdots & \vdots \\
0 & 5\omega R_{25,\mathrm{Re}} & 0 & 0 & 0 & 0 & \lambda_2^2 R_{25,Im}+\lambda_1\lambda_2 R_{15,Im} & 0 & I_{5,Im} & R_{25,\mathrm{Im}} \\
\omega R_{-11,Im} & 0 & 0 & 0 & 0 & 0 & \lambda_1^2 R_{-11,\mathrm{Re}}+\lambda_1\lambda_2 R_{-21,\mathrm{Re}} & -\left(\lambda_1^2\delta_{x_{10}}+\lambda_1\lambda_2\delta_{x_{20}}\right)p_{-1} & 0 & 0 \\
-\omega R_{-11,\mathrm{Re}} & 0 & 0 & 0 & 0 & 0 & \lambda_1^2 R_{-11,Im}+\lambda_1\lambda_2 R_{-21,Im} & 0 & 0 & 0 \\
\vdots & \vdots & \vdots & \vdots & \vdots & \vdots & \vdots & \vdots & \vdots & \vdots \\
5\omega R_{-15,Im} & 0 & 0 & 0 & 0 & 0 & \lambda_1^2 R_{-15,\mathrm{Re}}+\lambda_1\lambda_2 R_{-25,\mathrm{Re}} & -\left(\lambda_1^2\delta_{x_{10}}+\lambda_1\lambda_2\delta_{x_{20}}\right)p_{-5} & 0 & 0 \\
-5\omega R_{-15,\mathrm{Re}} & 0 & 0 & 0 & 0 & 0 & \lambda_1^2 R_{-15,Im}+\lambda_1\lambda_{22} R_{-25,Im} & 0 & 0 & 0 \\
0 & \omega R_{-21,Im} & 0 & 0 & 0 & 0 & 0 & -\left(\lambda_1\lambda_2\delta_{x_{10}}+\lambda_2^2\delta_{x_{20}}\right)p_{-1} & 0 & 0 \\
0 & -\omega R_{-21,\mathrm{Re}} & 0 & 0 & 0 & 0 & 0 & 0 & 0 & 0 \\
0 & \vdots & \vdots & \vdots & \vdots & \vdots & \vdots & \vdots & \vdots & \vdots \\
0 & 5\omega R_{-25,Im} & 0 & 0 & 0 & 0 & \lambda_2^2 R_{-25,\mathrm{Re}}+\lambda_1\lambda_2 R_{-15,\mathrm{Re}} & -\left(\lambda_1\lambda_2\delta_{x_{10}}+\lambda_2^2\delta_{x_{20}}\right)p_{-5} & I_{-5,\mathrm{Re}} & R_{-25,\mathrm{Re}} \\
0 & -5\omega R_{-25,\mathrm{Re}} & 0 & 0 & 0 & 0 & \lambda_2^2 R_{-25,Im}+\lambda_1\lambda_2 R_{-15,Im} & 0 & I_{-5,\mathrm{Im}} & R_{-25,\mathrm{Im}}
\end{bmatrix}
\tag{3.94}
$$

$$\mathbf{b}_1 = \begin{Bmatrix} -k_1' R_{10,\mathrm{Re}} \\ -k_1' R_{10,\mathrm{Im}} \\ (\omega^2 m_1' + \omega^2 I_{p_1}(t_{d_1})^2 - k_1') R_{11,\mathrm{Re}} + \omega c_1' R_{11,\mathrm{Im}} \\ \vdots \\ (25\omega^2 m_1' + 5\omega^2 I_{p_1}(t_{d_1})^2 - k_1') R_{15,\mathrm{Im}} - 5\omega c_1' R_{15,\mathrm{Re}} \\ -k_2' R_{20,\mathrm{Re}} \\ -k_2' R_{20,\mathrm{Im}} \\ (\omega^2 m_2' + \omega^2 I_{p_2}(t_{d_2})^2 - k_2') R_{21,\mathrm{Re}} + \omega c_2' R_{21,\mathrm{Im}} \\ \vdots \\ (25\omega^2 m_2' + 5\omega^2 I_{p_2}(t_{d_2})^2 - k_2') R_{25,\mathrm{Im}} - 5\omega c_2' R_{25,\mathrm{Re}} \\ (\omega^2 m_1' - \omega^2 I_{p_1}(t_{d_1})^2 - k_1') R_{-11,\mathrm{Re}} - \omega c_1' R_{-11,\mathrm{Im}} \\ (\omega^2 m_1' - \omega^2 I_{p_1}(t_{d_1})^2 - k_1') R_{-11,\mathrm{Im}} + \omega c_1' R_{-11,\mathrm{Re}} \\ \vdots \\ (25\omega^2 m_1' - 5\omega^2 I_{p_1}(t_{d_1})^2 - k_1') R_{-15,\mathrm{Re}} - 5\omega c_1' R_{-15,\mathrm{Im}} \\ (25\omega^2 m_1' - 5\omega^2 I_{p_1}(t_{d_1})^2 - k_1') R_{-15,\mathrm{Im}} + 5\omega c_1' R_{-15,\mathrm{Re}} \\ (\omega^2 m_2' - I_{p_2}\omega^2 (t_{d_2})^2 - k_2') R_{-21,\mathrm{Re}} - \omega c_2' R_{-21,\mathrm{Im}} \\ (\omega^2 m_2' - I_{p_2}\omega^2 (t_{d_2})^2 - k_2') R_{-21,\mathrm{Im}} + \omega c_2' R_{-21,\mathrm{Re}} \\ \vdots \\ (25\omega^2 m_2' - 5I_{p_2}\omega^2 (t_{d_2})^2 - k_2') R_{-25,\mathrm{Re}} - 5\omega c_2' R_{-25,\mathrm{Im}} \\ (25\omega^2 m_2' - 5I_{p_2}\omega^2 (t_{d_2})^2 - k_2') R_{-25,\mathrm{Im}} + 5\omega c_2' R_{-25,\mathrm{Re}} \end{Bmatrix} \tag{3.95}$$

$$\mathbf{x}_1 = \begin{Bmatrix} c_{1xx} & c_{2xx} & e_{1,\mathrm{Re}} & e_{1,\mathrm{Im}} & e_{2,\mathrm{Re}} & e_{2,\mathrm{Im}} & k_{\varphi_c} & \Delta k_\xi & k_I & k_s \end{Bmatrix}^T \tag{3.96}$$

Matrices $\mathbf{A_1}$ and $\mathbf{b_1}$ of Eqn. (3.93) contain the known parameters of rotor-bearing-coupling system. The term t_{d_1} corresponding to dynamic condensation of rotational DOF at disc location appears in $\mathbf{b_1}$ matrix. These terms do not exist for the case of central disc discussed in Chapter 2. Vector x_1 contains the identifiable parameters, which can be obtained by solving inverse problem, as

$$\mathbf{x_1} = \left(\mathbf{A_1}^{\mathrm{T}} \mathbf{A_1}\right)^{-1} \mathbf{A_1}^{\mathrm{T}} \mathbf{b_1} \tag{3.97}$$

The effect of including cumulative data from a range of spin speeds on the estimates can be studied from Eqn. (3.98), as

$$\begin{Bmatrix} \mathbf{A_1}(\omega_1) \\ \mathbf{A_1}(\omega_2) \\ \vdots \\ \mathbf{A_1}(\omega_n) \end{Bmatrix} \mathbf{x_1} = \begin{Bmatrix} \mathbf{b_1}(\omega_1) \\ \mathbf{b_1}(\omega_2) \\ \vdots \\ \mathbf{b_1}(\omega_n) \end{Bmatrix} \tag{3.98}$$

The advantage of using cumulative data from a range of speeds is that the condition number of the matrix **A** improves, thereby resulting in estimates closer to the actual values.

3.12 Results and Discussions

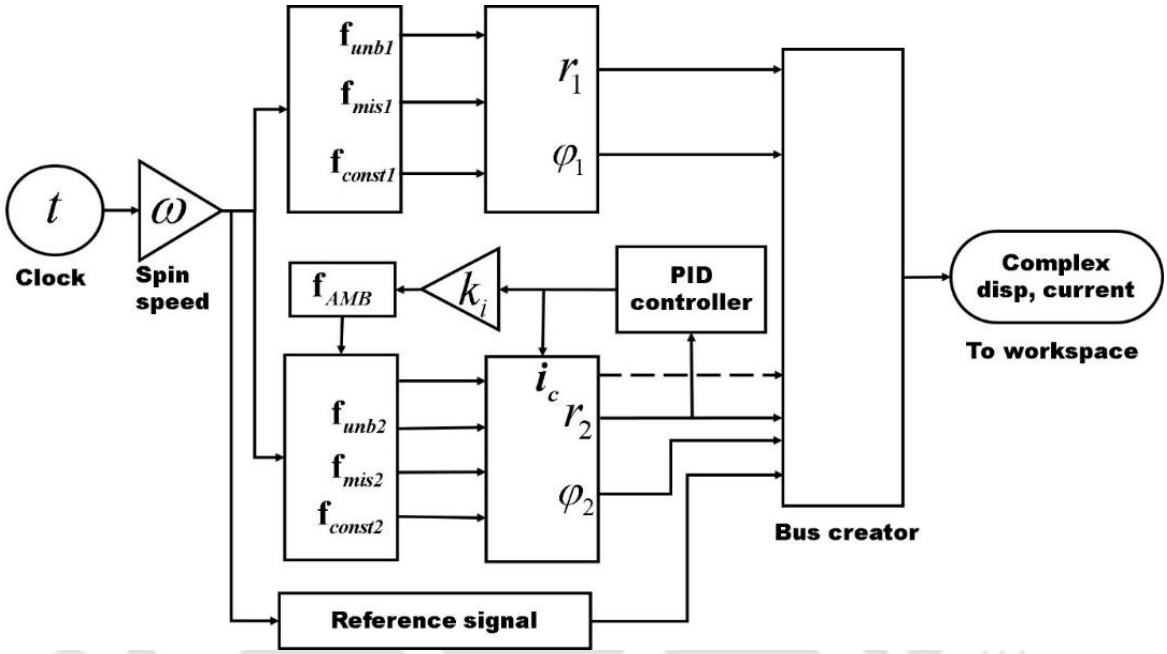

Figure 3-3 Simulink model of coupled rotor-AMB system

The values of various rotor, coupling and AMB parameters assumed for simulation are listed in Table 3-1. Eqns. (3.42) and (3.43) are used to build the Simulink^{TM} model shown in Figure 3-3, which is the simplified representation of the actual Simulink model. This model outputs both translational and rotational vibratory displacements at disc locations on rotor-1 and rotor-2. Additionally AMB current near the disc-2 is also obtained. The model in chapter 2 outputs only translatory displacements as gyroscopic moments are absent for the case of central disc. The solution was run with fourth order Runge-Kutta (ode4) solver acquiring 2^{16} (65536) samples per second of simulation time.

Table 3-1 Rotor, coupling and AMB system data for numerical simulation

Parameter	Value	Parameter	Value	Parameter	Value
m_1,kg	2	Δk_{ξ}, N-m/rad	50	k_s, N/m	105210
m_2,kg	2.5	c_{1xx}, N-s/mm	27	k_i, N/A	42.1
I_{p_1}, kg-m^2	0.0048	$c_{1x\varphi_y}$, N-s/mm	11	e_1,m	240×10^{-6}
I_{p_2}, kg-m^2	0.006	$c_{1\varphi_y\varphi_y}$, N-s/mm	6	e_2,m	240×10^{-6}
k_{1xx}, N/m	100220	c_{2xx}, N-s/mm	50	β_1,rad	π/18
$k_{1x\varphi_y}$, N/m	8590	$c_{2x\varphi_y}$, N-s/mm	11	β_2,rad	π/18
$k_{1\varphi_y\varphi_y}$, N/m	5154	$c_{2\varphi_y\varphi_y}$, N-s/mm	6	$\delta_{x_{10}}$,m	2.33×10^{-5}
$k_{2x\varphi_y}$, N/m	100220	a_1,m	0.3	$\delta_{x_{20}}$,m	2.91×10^{-5}
$k_{2x\varphi_y}$, N/m	8590	b_1,m	0.2	K_P,A/m	25000
$k_{2\varphi_y\varphi_y}$, N/m	5154	a_2,m	0.2	K_I, A/m-s	2000
k_{φ_c}, N-m/rad	300	b_2,m	0.3	K_D, A-s/m	2
λ_1	6.66	λ_2	5.83	l_i,m	0.5

Figure 3-4 shows the Hilbert transform of *x* displacements of rotor-1 and rotor-2, when the system is ramped up with an angular acceleration of 20π rad/s^2. The peaks in the figures represent the natural frequencies of rotors. From subplots Figure 3-4(a) and Figure 3-4(b) in Figure 3-4, it can be seen that the natural frequencies of coupled rotor system are ~100 rad/sec and ~210 rad/sec. To be able to operate the rotor system over a wider speed range the proportional constant of controller, k_p has been changed from 12200 to 25000 N/A. This has resulted in shift in the natural frequency of rotor-2 to 300 rad/sec as shown in Figure 3-4(d). However, peak of rotor-1 remains unchanged as shown in Figure 3-4(c).

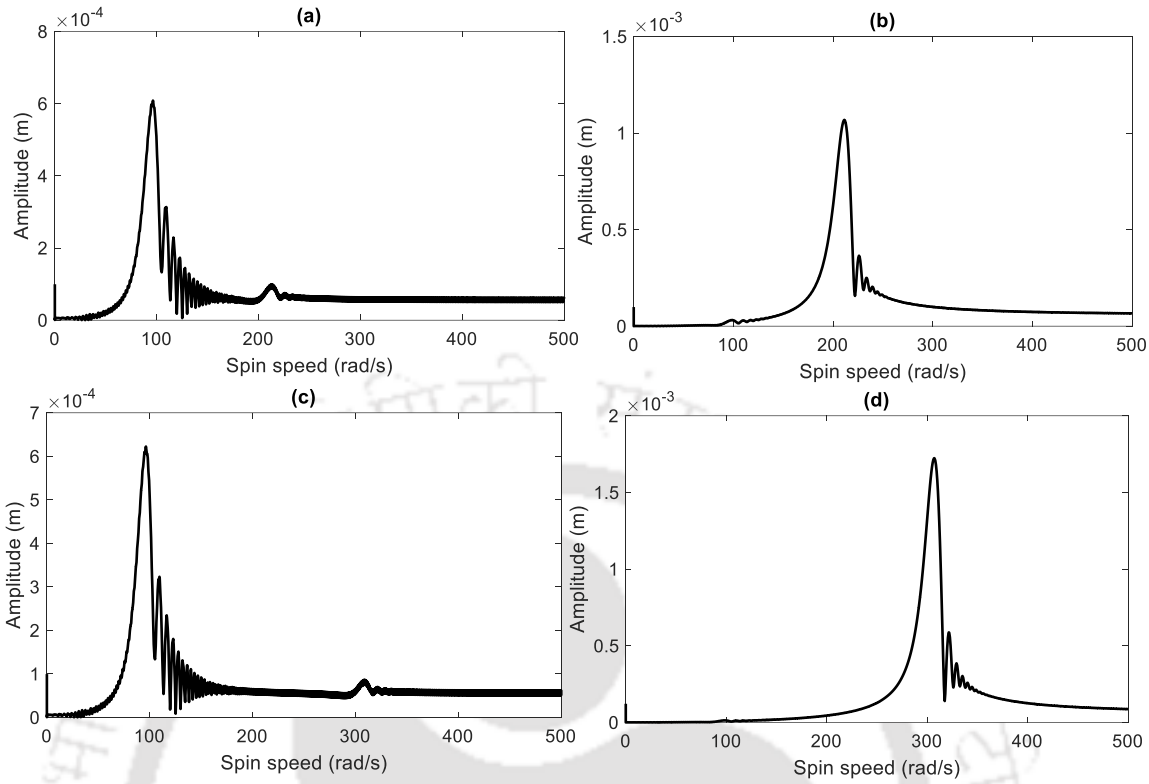

Figure 3-4 Effect of AMB on the dynamic response of coupled rotor system demonstrated through Hilbert envelope of AMB (a) Rotor-1 when k_p = 12200 (b) Rotor-2 when k_p = 12200 (c) Rotor-1 when k_p = 25000 (d) Rotor-2 when k_p = 25000

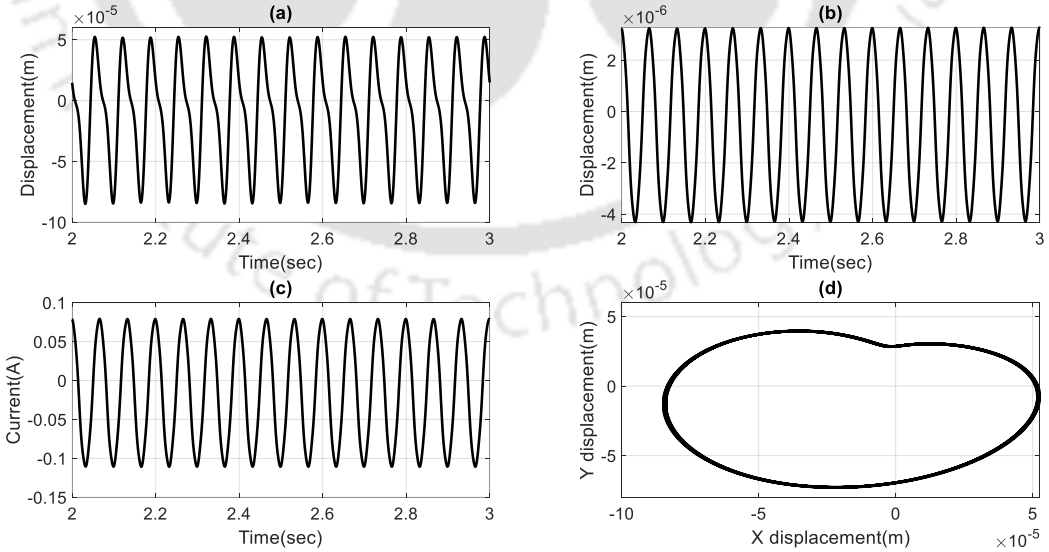

Figure 3-5 Time domain response at 15 Hz for nominal unbalance (a) Rotor-1 *x*-displacement (b) Rotor-2 *x*-displacement (c) AMB *x*-Current (d) Rotor -1 orbit

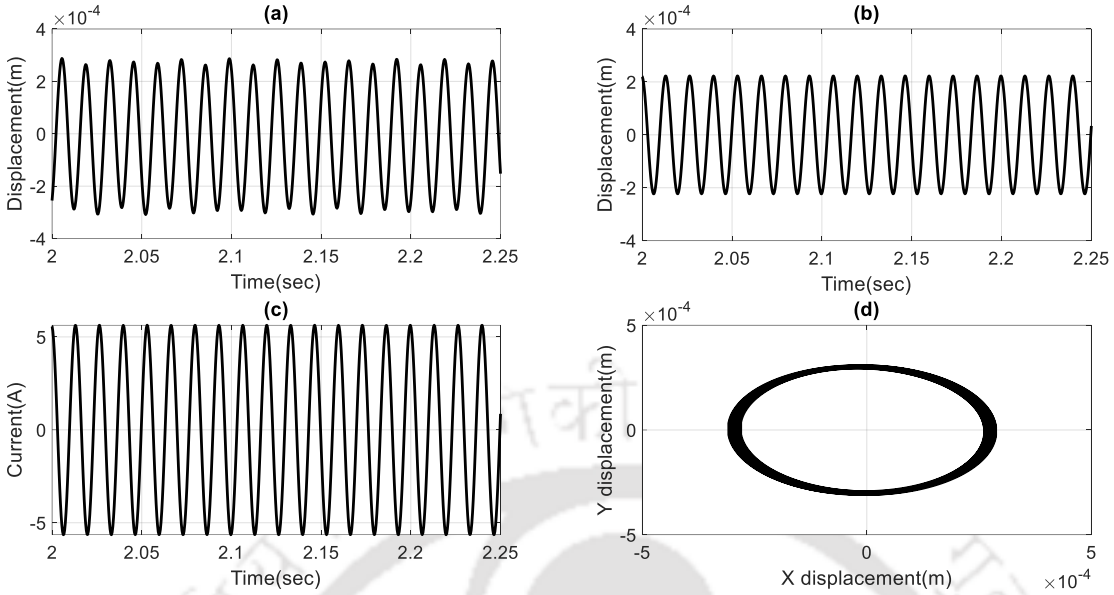

Figure 3-6 Time domain response at 75 Hz for nominal unbalance (a) Rotor-1 *x*-displacement (b) Rotor-2 *x*-displacement (c) AMB *x*-Current (d) Rotor-1 orbit

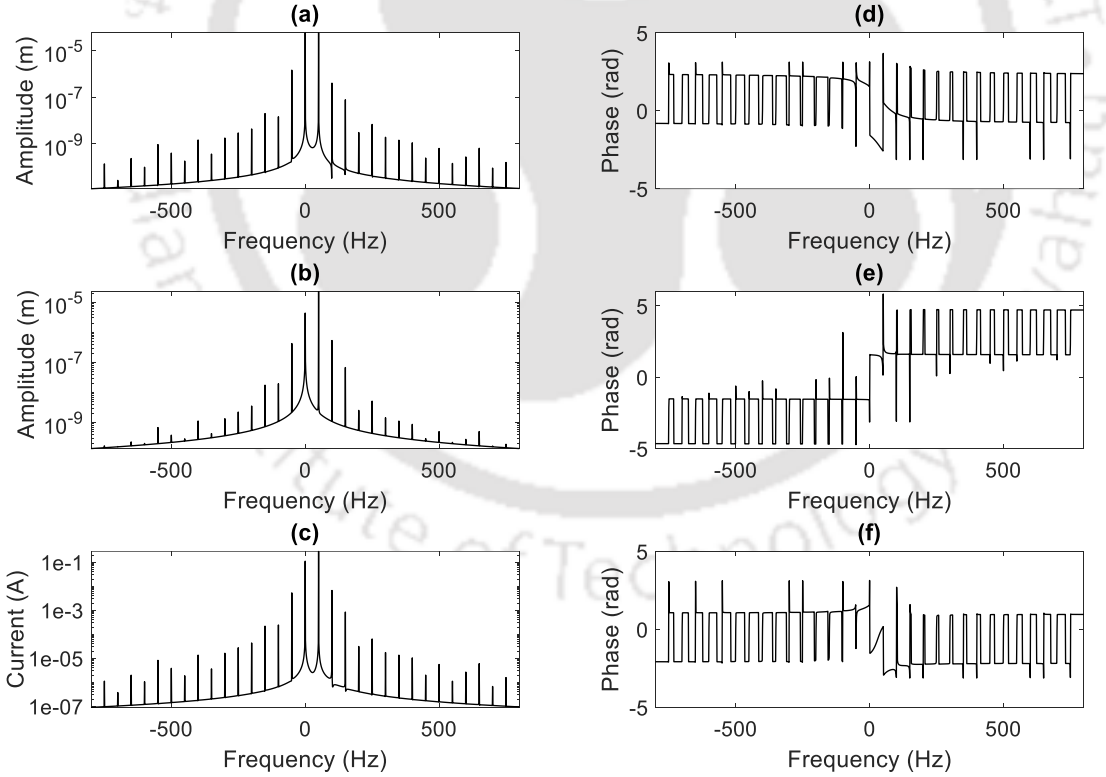

Figure 3-7 Full spectrum plots at 50 Hz(a) Amplitude of rotor-1 complex translational displacement (b) Amplitude of rotor-2 complex translational displacement (c) Amplitude of complex AMB Current (d) Phase of rotor-1 complex translational displacement (e) Phase of rotor-2

The steady-state displacement and current responses of rotor-1 is obtained for a duration of 3 seconds. To avoid the influence of transient response the waveform from 2 to 3 seconds has been considered. For a nominal value of unbalance given in Table 3-1 and a spin speed of 15 Hz, which is close to the critical speed of rotor-1, the reponses are shown in Figure 3-5(a-c). The time domain displacement responses of rotor-1 is not a pure sinusoids, which is indicative of presence of misalignment. The displacment orbit of rotor-1 in Figure 3-5(d) is loopy in nature, which is also the characteristic of misalignment.

At a spin speed of 75 Hz, the unbalance response overtakes the misalignment response and that affects the nature of time domain plot and orbit plot (Figure 3-6), which are smoother and circular compared to those at 15 Hz. The speeds are intentionally chosen to highlight the point that the misalignment response is not so easily detected from orbits at higher speeds as at lower speeds as the total vibration response is dominated by 1X component. Figure 3-7 shows the full spectrum plots of the of vibration of rotor-1, rotor-2 and AMB current at a spin speed of 50 Hz. Log scale has been used for Y axis to accurately identify the amplitudes of various harmonics from the plots which is not possible on linear scale. The real and imaginary coefficients of the displacement and current harmonics obtained from full spectrum plot are supplied to Eqn. (3.93) and identifiable parameters are estimated. The flow chart of parameter identification procedure for the estimation of system parameters is given in Chapter 2. Inititally parameter estimation was performed at individual speeds in the range of 24 Hz to 34 Hz, away from half-power points, i.e. operating speed points on either side of peak where amplitude is $0.707x_{resonant}$ In Figure 3-8(a), c_{1xx} and k_s show a variation of -18% and 15.4%, respectively, from the assumed values. The variation in estimates of other parameters fell within 10% of their assumed values. To account for the effect of possible presence of instrumentation and data acquisition errors in the vibration and current responses, random Gaussian noise is added to the signal obtained from the numerical simulation. Figure 3-8(b-d) show the trend of error percentage of estimated values with speed. For 1%, 2% and 5% levels of noise in data acquisition, both c_{1xx} and k_s displayed proportionately increasing deviation from their assumed values. With 5% noise level an error of -59% at 28 Hz and 69.2% at 34 Hz was noticed in the estimated values of k_s. This is attributed to the large condition number of regression matrix.

To get round the problem of ill-conditioning, cumulative data from the speed range of 24 Hz to 34 Hz, with central frequency of 29 Hz, was utilized in the identification procedure. In Eqn. (3.98), the size of regressor matrix now increases by *n* times, where '*n*' is the number of speeds from which data is gathered. From Table 3-2, it can be seen that there is a remarkable improvement in the accuracy of parameter estimation. At 0% noise level, the estimated parameters are almost identical to the assumed values. When noise is added to response, the error in estimates was confined to less than 10%. This demonstrates the usefulness of using cumulative data in the parameter identification algorithm.

From Table 2, the highest error percentages are: Rotor-2 equivalent viscous damping, k_s, and ACS, Δk_ξ, have displayed comparatively higher variation, -10.5% and 5% respectively, while c_{1xx} and c_{2xx} displayed a variation of 2.22% and -3.36%, respectively. It can be noticed that in Eqn. (3.93), the unknown identifiable parameters on the left hand side are $m_1, m_2, k_{1xx}, k_{2xx}, \delta_{x_{10}}$ and $\delta_{x_{20}}$.The direct bending stiffness of shaft can be measured from the static deflection test or by experimentally estimating the 1^{st} bending natural frequency of shaft by impact test. Any likely error in the measurement of the aforesaid parameters will reflect in the parameter estimation even when the response is noise free.

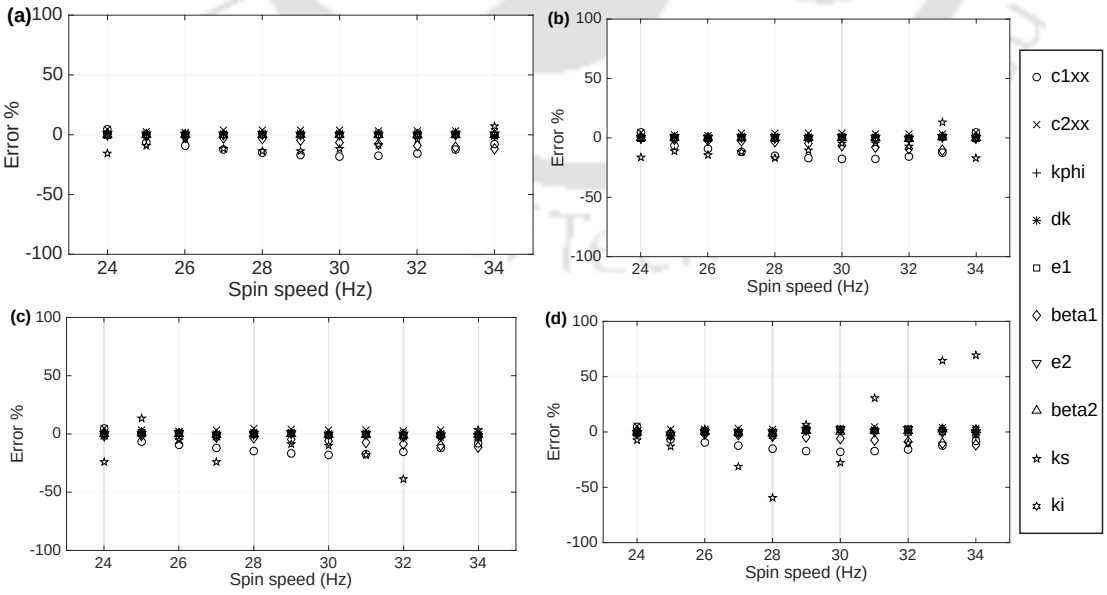

Figure 3-8 Error percentage in estimated parameters with various levels of error percentage in response at various speeds from 24 Hz to 34 Hz (a) 0% error (b) 1% error (c) 2% error (d) 5% error

Table 3-2 Effect of noise in measured vibration and current on estimated parameters speed range 24 Hz to 34 Hz

Parameter	Assumed values	Estimated values with noise			
		0%	1%	2%	5%
c_{1xx}	27($Ns^{-1}m^{-1}$)	26.89	26.4	26.53	26.57
	% error	-0.4	2.22	1.74	1.59
c_{2xx}	50($Ns^{-1}m^{-1}$)	49.9	52.5	51.68	50.68
	% error	-0.19	-5	-3.36	-1.36
k_{φ_c}	300(N-m/rad)	299.1	302.73	303.36	303.48
	% error	-0.3	-0.91	-1.12	-1.16
Δk_{ξ}	50(N-m/rad)	49.46	52.58	55.26	53.48
	% error	-1.07	-5.16	-10.52	-6.96
e_1	240(μm)	239.8	238.94	238.11	239.72
	% error	-0.08	0.44	0.79	0.12
β_1	30(deg.)	29.97	29.9	30.07	30.07
	% error	-0.03	0.33	-0.23	-0.23
e_1	240 (μm)	239.28	241.95	242.55	241.75
	% error	-0.3	-0.81	-1.06	-0.73
β_2	10 (deg.)	10	10.06	10	10.06
	% error	0	-0.6	0	-0.6
k_s	105210 (N/m)	105557	105885	99948	105113
	% error	0.33	-0.64	5	0.09
k_i	42.1 (N/A)	41.99	42.3	42.1	42.4
	% error	-0.24	-0.48	0	-0.71

Gaussian noise of 1%, 2% and 5% levels are deliberately added to the mass, stiffness and static deflection parameters. Identification is then performed at individual speeds in the range of 24 Hz to 34 Hz.

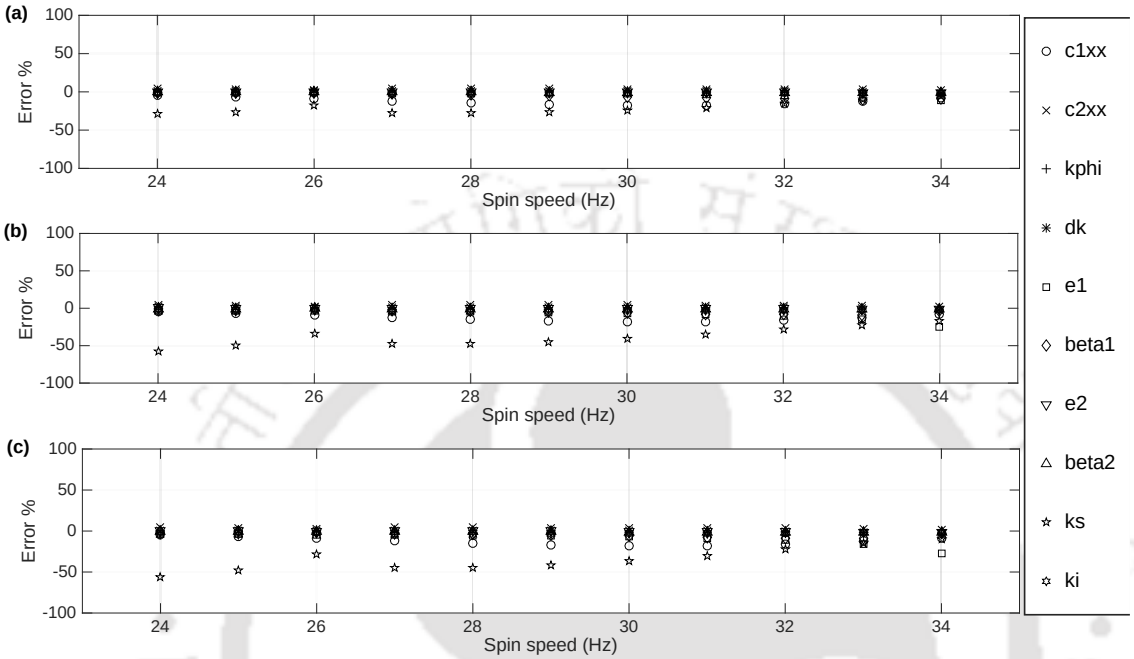

Figure 3-9 Error percentage in estimated parameters with various levels of error percentage in modelling at various speeds from 24 Hz to 34 Hz (a) 1% error (b) 2% error (c) 5% error

In all three test cases, the error in the estimation of AMB displacment stiffness k_s was comparatively larger, reaching as high as 57% (Figure 3-9). Next, the cumulative data from 11 speed points has been fed to regresssion matrix **A** and known matrix vector **b** in Eqn. (3.98) and system parameters are estimated. From Table 3-3, it is seen that there is significant improvement in the closeness of estimated parameters. At 5% noise , $\Delta k_\xi, k_s$ vary by a reasonable 12.3% and -6.49%, respectively, from the assumed values. It can be seen that all the estimated parameters undergo significant variation from their assumed values when the identification algorithm is used with data collected at individual speeds. However, cumulative data has a desirable effect on the closeness of estimated parameters. Of all the parameters additive coupling stiffness (Δk_ξ) and AMB displacement stiffness (k_s) have undergone comparatively higher variation, while shaft equivalent viscous damping c_{1xx} and c_{2xx} have varied by a moderate degree.

Table 3-3 Effect of noise in modelling parameters on estimated parameters for speed range 24 Hz to 34 Hz

Parameter	Assumed values	Estimated values with noise			
		0%	1%	2%	5%
c_{1xx}	27($Ns^{-1}m^{-1}$)	26.89	26.91	26.86	26.95
	% error	-0.4	-0.32	-0.49	-0.15
c_{2xx}	50($Ns^{-1}m^{-1}$)	49.9	48.68	50.16	49.89
	% error	-0.19	-0.62	0.33	-0.21
k_{φ_c}	300	299.1	305.84	295.46	308.01
	% error	-0.3	1.94	-1.5	2.67
Δk_{ξ}	50	49.46	55.92	46.42	56.19
	% error	-1.07	11.84	-7.14	12.39
e_1	240(μm)	239.8	239.77	239.8	239.75
	% error	-0.08	-0.09	-0.07	-0.1
β_1	30(deg.)	29.97	29.99	29.98	29.99
	% error	-0.03	-0.02	-0.03	-0.02
e_1	240 (μm)	239.28	245.39	235.28	245.77
	% error	-0.3	2.24	-1.96	2.4
β_2	10 (deg.)	10	9.99	10	9.99
	% error	0	-0.06	0	-0.06
β_1	105210 (N/m)	105557	99898	106749	98371
	% error	0.33	-5.04	1.46	-6.49
k_i	42.1 (N/A)	41.99	42.61	40.9	42.82
	% error	-0.24	1.23	-1.16	1.72

However, it is the unbalance eccentricity and phase of the discs that undergo least variation during the identification process. The development of global EOM with both translational and rotational DOFs, and the subsequent dynamic condensation of rotational DOF has resulted in estimates exhibiting comparatively more deviation than those estimated in Chapter 2. However the error percentages are still within acceptable limits. The performance of identification algorithm without condensation has been checked and it has shown better error percentages than the case with condensation particularly for the cases of noise. However it has not been tabulated as it would not be of use in physical systems where rotational degrees cannot be captured as easily as translational dof.

3.13 Concluding Remarks

In the present chapter, a coupled rotor system with offset discs and supported on 8-pole AMB in the presence of angular misalignment has been considered. Inclusion of gyroscopic effect by way of offset disc model has increased the number of generalized coordinates due to the presence of rotational DOF. EOMs have been derived using Lagranges's equation from the expressions of kinetic energy, potential energy and dissipative energy. An acceptable assumption based on the conditions of weight dominance and flexible coupling has made it possible to establish linear relationship between coupling slopes and disc translational displacements of the vibrating system. The coupling angular stiffness is modelled as the sum of static and additive components. A time-varying periodic function that is necessary to correctly simulate the nature of coupling misalignment force in frequency domain has been selected. The constants of PID controller (k_p) have been chosen to give a wide range of operation. A Simulink^{TM} model is built to generate respones in time domain. The amplitude and phase of harmonics of rotor vibration and AMB current are extracted from full spectrum. Dynamic condensation has been used to create the EOMs purely in terms of master DOFs i.e., measurable translational displacements of rotors. The identification algorithm based on least-squares regression is built by segregating the EOMs in frequency domain into the known and unknown parameters. The algorithm is used to estimate coupling static stiffness, ACS, unbalance amplitude, unbalance phase, AMB displacement and current stiffness constants and was found to be robust upto noise levels of 5%.

The coupling model is derived in terms of translational dispacements at disc locations. The effect of dynamic condensation is seen in the error percentages of results, which have shown marginally more deviation than the case of central discs considered in Chapter 2. The complexity of the present chapter is the inclusion of gyroscopic effects in the rotor model. The present mathematical model is representative of simple laboratory rotors and therefore cannot be directly applied to multistage industrial rotors with many discs and supported on flexible bearings. There is also a need to include the case of coupling that is subjected to both parallel and angular misalignments. In the next chapter a multi-stage industrial turbogenerator supported on rolling element bearings and auxiliary AMBs is considered. Timoshenko beam finite elements are used to discretize the rotor system. The coupling model considered is more realistic as both parallel and angular misalignements taken into acccount in its derivation.

CHAPTER 4

Analysis and Identification of Misalignment in Coupled Rotor-AMB Systems using Finite Elements

4.1 Introduction

In Chapters 2 and 3, modelling, analysis and identification procedure of angular misalignment in coupled simple rotors is presented. Lagrange's equations have been used to develop the EOM of the rotor system. A relationship between coupling slopes and disc displacements have been used to derive EOMs in terms of generalized coordinates. This chapter extends the work to industrial turbo-generators (TGs) having multiple stages of rotors supported on flexible rolling element bearings, and auxiliary AMBs. The rotor is modelled with two-node Timoshenko beam elements having four DOFs at each node. Global EOM is developed by assembling the elemental matrices of subsystems. Weight dominance assumption, which is valid for heavy TGs is considered in the derivation of coupling model. Both parallel and angular misalignments are considered in the coupling model. The steering function used in the model of coupling misalignment is chosen such that it produces the multi-harmonic vibration response as reported in various experimental studies. This coupling model is then integrated into the finite element model of rotor system. The AMBs used serve as auxiliary supports to reduce rotor vibration and also for condition monitoring (CM). The identification algorithm developed from global EOMs in frequency domain is a least-squares regression problem, which uses vibration and current data from full spectrum FFT plots. The system parameters are disc unbalance, AMB constants, bearing stiffness and coupling static stiffness and ACS coefficients. The robustness of identification algorithm is checked against various levels of measurement noise and modelling bias.

4.2 System Configuration

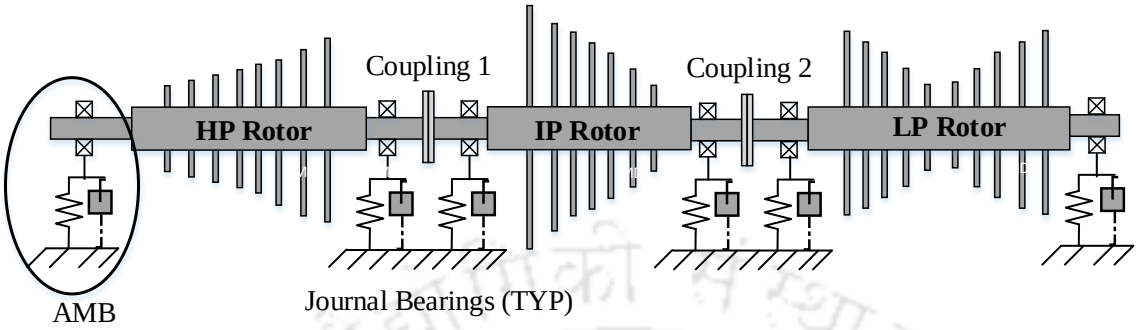

Figure 4-1A sub 500 MW turbo-generator with integrated AMB

A real industrial Turbine-Generator (TG) that has seven stages of rotors seated on hydrodynamic bearings and connected by intermediate rigid couplings with integrated AMB is described in Pilotto et al. (2017). TG sets with output power less than 500 MW typically have mono flow HP rotor, mono flow IP rotor and double flow LP rotor, where steam enters in the middle and flows in both directions toward the ends of the section. The sets with power larger than 500 MW have mono flow LP, double flow IP and LP rotors. A typical schematic of a sub 500 MW TG set is shown in Figure 4-1. Now modelling of the rotor, bearing, coupling and AMB in the element form are described in the next section.

4.3 Mathematical Model

This section deals with finite element analysis of a multi-stage turbogenerator model connected by intermediate couplings, supported on rolling element bearings and auxiliary AMB.

4.3.1 Shaft and Disc Model

Timoshenko beam finite elements have been used to discretize the rotor system. The elemental matrices with real coefficients are of the size 8×8 and are given in Nelson and McVaugh (1976), and Chen and Gunter (2007). Alternatively, matrices of size 4×4, corresponding to a complex nodal displacement vector as given by Nelson (1985) and Chen (1998) can be used for modelling each finite element. Besides reducing the computational effort, complex notation helps in identifying the coefficients of positive and negative harmonics of full spectrum arising due to multi-harmonic forcing from the

misalignment. In the matrix coefficients given by Nelson (1985) are imaginary and the nodal displacements of the left node are arranged in real domain and those of the right node are arranged in imaginary domain, as shown in Eqn. (4.1).

$$\mathbf{u}^e = \mathbf{u}_{left} + j\mathbf{u}_{right} = \left\{x_1 \quad \varphi_{x_1} \quad x_2 \quad \varphi_{x_2}\right\}^T + j\left\{y_1 \quad \varphi_{y_1} \quad y_2 \quad \varphi_{y_2}\right\}^T \tag{4.1}$$

The matrix coefficients given by Chen (1998) are real and the nodal displacements of *x-z* plane are arranged in real domain and those of *y-z* plane in imaginary domain as shown in Eqn. (4.2). These matrices are used in the present work for the finite element modelling the rotor system.

$$\mathbf{u}^e = \mathbf{u}_{xz} + j\mathbf{u}_{yz} = \left\{x_1 \quad \varphi_{y_1} \quad x_2 \quad \varphi_{y_2}\right\}^T + j\left\{y_1 \quad \varphi_{x_1} \quad y_2 \quad \varphi_{x_2}\right\}^T \tag{4.2}$$

The corresponding elemental matrices of shaft are given in **Appendix D.** The mass and gyroscopic matrices of rigid discs used in the present work are given in Friswell et al. (2010), Singh and Tiwari (2016).

4.3.2 Coupling Mathematical Model

The model of coupling and its generalized coordinates are shown in Figure 4-2. The convention followed in this paper for the stationary and rotating frames of reference is shown in Figure 4-3.

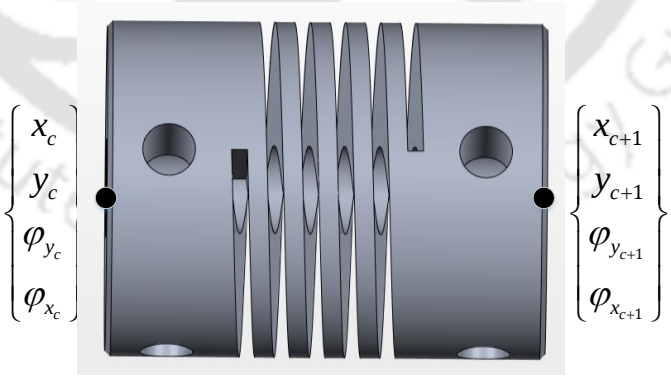

Figure 4-2 Generalized coordinates of coupling

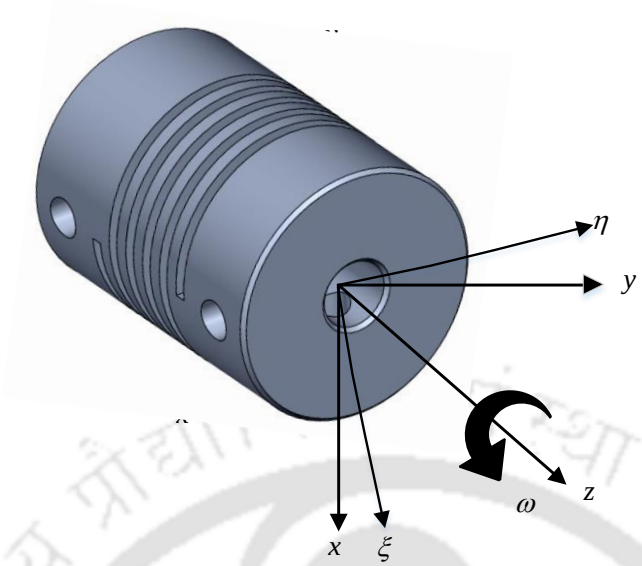

Figure 4-3 Stationary and rotating coordinate references

In Chapters 2 and 3 only angular misalignment was considered at coupling location. The slopes at coupling have been written in terms of translational locations at discs using weight dominance criteria. In the present chapter both parallel and angular misalignments are considered in the coupling. The translational and rotational displacements at either end of coupling are independent of those at other locations along the length of the rotor. This is a significant deviation from the previous coupling model.

Lees (2007) proposed that in the presence of misalignment, the coupling has the static coupling stiffness (SCS) and time-dependent additive coupling stiffness (ACS) components.The aforementioned hypothesis is the basis of the present mathematical formulation. When the bearing centres are perfectly aligned there is only the static stiffness component.

$$\mathbf{f}_c^{rot} = \mathbf{K}_c \left\{ \mathbf{u}_{0c}^{rot} + \mathbf{u}_c^{rot}(t) \right\} \tag{4.3}$$

where

$$\mathbf{u}_{0c}^{rot} = \left\{ \delta\xi_c \quad \delta\eta_c \quad \delta\varphi_{\eta_c} \quad \delta\varphi_{\xi_c} \quad \delta\xi_{c+1} \quad \delta\eta_{c+1} \quad \delta\varphi_{\eta_{c+1}} \quad \delta\varphi_{\xi_{c+1}} \right\}^T \tag{4.4}$$

$$\mathbf{u}_c^{rot} = \left\{ \xi_c \quad \eta_c \quad \varphi_{\eta_c} \quad \varphi_{\xi_c} \quad \xi_{c+1} \quad \eta_{c+1} \quad \varphi_{\eta_{c+1}} \quad \varphi_{\xi_{c+1}} \right\}^T \tag{4.5}$$

where $\mathbf{K}_c$ is the static stiffness matrix of coupling, $\mathbf{u}_c^{rot}$ is the vector of generalized coordinates of coupling, $\mathbf{u}_{0c}^{rot}$ is the vector of static deflections of coupling. When there is misalignment between bearing centres, then the additive component comes into play. The force vector due to static deflections given by $\mathbf{K}_c\mathbf{u}_{0c}^{re}$ is equal to the self-weight ($\mathbf{f}_{st} = \mathbf{Mg}$) of the rotor. In such case

$$\begin{aligned}\mathbf{f}_c^{rot} &= \left[\mathbf{K}_c + \Delta\mathbf{K}_c^{rot}(t)\right]\left\{\mathbf{u}_{0c}^{rot} + \mathbf{u}_c^{rot}(t)\right\} \\ &= \underbrace{\mathbf{K}_c\mathbf{u}_c^{rot}(t)}_{\mathbf{f}_{SCS}^{rot}} + \underbrace{\Delta\mathbf{K}_c^{rot}(t)\mathbf{u}_{0c}^{rot} + \Delta\mathbf{K}_c^{rot}(t)\mathbf{u}_c^{rot}(t)}_{\mathbf{f}_{ACS}^{rot}}\end{aligned} \tag{4.6}$$

where $\Delta\mathbf{K}_c^{rot}(t)$ is the matrix of additive coupling stiffness coefficients. Eqn. (4.6) has two parts $\mathbf{f}_{SCS}^{rot}$ and $\mathbf{f}_{ACS}^{rot}$, which are in rotating frame of reference. Next section deals with derivation of the static coupling stiffness force in the stationary frame of reference.

4.3.2.1 Static Coupling Stiffness Force: Coordinate Transformation

Coordinate transformation to stationary frame of reference of the $\mathbf{f}_{SCS}^{rot}$ part of Eqn. (4.6) is performed as shown below.

$$\mathbf{f}_{SCS}^{stat} = \left(\mathbf{T}^T\mathbf{K}_c\mathbf{T}\right)\mathbf{u}_c^{stat}(t) = \tilde{\mathbf{K}}_c\mathbf{u}_c^{stat}(t) \tag{4.7}$$

where

$$\mathbf{K}_c = \begin{bmatrix} k_{xx} & k_{xy} & 0 & 0 & -k_{xx} & -k_{xy} & 0 & 0 \\ k_{yx} & k_{yy} & 0 & 0 & -k_{yx} & -k_{yy} & 0 & 0 \\ 0 & 0 & k_{\varphi_y\varphi_y} & 0 & 0 & 0 & -k_{\varphi_y\varphi_y} & 0 \\ 0 & 0 & 0 & k_{\varphi_x\varphi_x} & 0 & 0 & 0 & -k_{\varphi_x\varphi_x} \\ -k_{xx} & -k_{xy} & 0 & 0 & k_{xx} & k_{xy} & 0 & 0 \\ -k_{yx} & -k_{yy} & 0 & 0 & k_{yx} & k_{yy} & 0 & 0 \\ 0 & 0 & -k_{\varphi_y\varphi_y} & 0 & 0 & 0 & k_{\varphi_y\varphi_y} & 0 \\ 0 & 0 & 0 & -k_{\varphi_x\varphi_x} & 0 & 0 & 0 & k_{\varphi_x\varphi_x} \end{bmatrix} \tag{4.8}$$

$$\mathbf{u}_c^{stat} = \begin{Bmatrix} x_c & y_c & \varphi_{y_c} & \varphi_{x_c} & x_{c+1} & y_{c+1} & \varphi_{y_{c+1}} & \varphi_{x_{c+1}} \end{Bmatrix}^T \tag{4.9}$$

$$\mathbf{T}=\begin{bmatrix} \cos\omega t & \sin\omega t & 0 & 0 & 0 & 0 & 0 & 0 \\ -\sin\omega t & \cos\omega t & 0 & 0 & 0 & 0 & 0 & 0 \\ 0 & 0 & \cos\omega t & \sin\omega t & 0 & 0 & 0 & 0 \\ 0 & 0 & -\sin\omega t & \cos\omega t & 0 & 0 & 0 & 0 \\ 0 & 0 & 0 & 0 & \cos\omega t & \sin\omega t & 0 & 0 \\ 0 & 0 & 0 & 0 & -\sin\omega t & \cos\omega t & 0 & 0 \\ 0 & 0 & 0 & 0 & 0 & 0 & \cos\omega t & \sin\omega t \\ 0 & 0 & 0 & 0 & 0 & 0 & -\sin\omega t & \cos\omega t \end{bmatrix} \tag{4.10}$$

where $\mathbf{u}_c^{stat}$ is the vector of coupling coordinates in the stationary frame of reference. **Appendix F** gives the terms of the $\tilde{\mathbf{K}}_c$ matrix and $\mathbf{f}_{SCS}^{stat}$ is a vector of real coordinates. To convert into the complex form, column wise operations are performed on Eqn. (4.7), to get

$$\mathbf{f}_{SCS}=\begin{Bmatrix} \tilde{k}_{xx}(x_c-x_{c+1})+\tilde{k}_{xy}\left(y_c-y_{c+1}\right)+\mathrm{j}\left[\tilde{k}_{yx}\left(x_c-x_{c+1}\right)+\tilde{k}_{yy}\left(y_c-y_{c+1}\right)\right] \\ \tilde{k}_{\varphi_y\varphi_y}\left(\varphi_{y_c}-\varphi_{y_{c+1}}\right)+\tilde{k}_{\varphi_y\varphi_x}\left(\varphi_{x_c}-\varphi_{x_{c+1}}\right)+\mathrm{j}\left[\tilde{k}_{\varphi_y\varphi_x}\left(\varphi_{y_c}-\varphi_{y_{c+1}}\right)+\tilde{k}_{\varphi_x\varphi_x}(\varphi_{x_c}-\varphi_{x_{c+1}})\right] \\ -\tilde{k}_{xx}(x_c-x_{c+1})-\tilde{k}_{xy}\left(y_c-y_{c+1}\right)-\mathrm{j}\left[\tilde{k}_{yx}\left(x_c-x_{c+1}\right)+\tilde{k}_{yy}\left(y_c-y_{c+1}\right)\right] \\ -\tilde{k}_{\varphi_y\varphi_y}\left(\varphi_{y_c}-\varphi_{y_{c+1}}\right)-\tilde{k}_{\varphi_y\varphi_x}\left(\varphi_{x_c}-\varphi_{x_{c+1}}\right)-\mathrm{j}\left[\tilde{k}_{\varphi_y\varphi_x}\left(\varphi_{y_c}-\varphi_{y_{c+1}}\right)+\tilde{k}_{\varphi_x\varphi_x}(\varphi_{x_c}-\varphi_{x_{c+1}})\right] \end{Bmatrix} \tag{4.11}$$

The complex notation of translational and rotational displacements is denoted by $u_c=x_c+\mathrm{j}y_c$, $u_{c+1}=x_{c+1}+\mathrm{j}y_{c+1}$, $\varphi_c=\varphi_{y_c}+\mathrm{j}\varphi_{x_c}$, $\varphi_{c+1}=\varphi_{y_{c+1}}+\mathrm{j}\varphi_{x_{c+1}}$. Eqn. (4.11) can be rewritten in the following complex form, herein superscript * represents the complex conjugate.

$$\mathbf{f}_{SCS}=0.5\begin{Bmatrix}\tilde{k}_{xx}\left((u_c+u_c^*)-(u_{c+1}+u_{c+1}^*)\right)-\mathrm{j}\tilde{k}_{xy}\left((u_c-u_c^*)-(u_{c+1}-u_{c+1}^*)\right)\\+\mathrm{j}\left[\tilde{k}_{yx}\left((u_c+u_c^*)-(u_{c+1}+u_{c+1}^*)\right)-\mathrm{j}\tilde{k}_{yy}\left((u_c-u_c^*)-(u_{c+1}-u_{c+1}^*)\right)\right]\\\tilde{k}_{\varphi_y\varphi_y}\left((\varphi_c+\varphi_c^*)-(\varphi_{c+1}+\varphi_{c+1}^*)\right)-\mathrm{j}\tilde{k}_{\varphi_y\varphi_x}\left((\varphi_c-\varphi_c^*)-(\varphi_{c+1}-\varphi_{c+1}^*)\right)\\+\mathrm{j}\left[\tilde{k}_{\varphi_y\varphi_x}\left((\varphi_c+\varphi_c^*)-(\varphi_{c+1}+\varphi_{c+1}^*)\right)-\mathrm{j}\tilde{k}_{\varphi_x\varphi_x}\left((\varphi_c-\varphi_c^*)-(\varphi_{c+1}-\varphi_{c+1}^*)\right)\right]\\\tilde{k}_{xx}\left((u_{c+1}+u_{c+1}^*)-(u_c+u_c^*)\right)-\mathrm{j}\tilde{k}_{xy}\left((u_{c+1}-u_{c+1}^*)-(u_c-u_c^*)\right)\\+\mathrm{j}\left[\tilde{k}_{yx}\left((u_{c+1}+u_{c+1}^*)-(u_c+u_c^*)\right)-\mathrm{j}\tilde{k}_{yy}\left((u_{c+1}-u_{c+1}^*)-(u_c-u_c^*)\right)\right]\\\tilde{k}_{\varphi_y\varphi_y}\left((\varphi_{c+1}+\varphi_{c+1}^*)-(\varphi_c+\varphi_c^*)\right)-\mathrm{j}\tilde{k}_{\varphi_y\varphi_x}\left((\varphi_{c+1}-\varphi_{c+1}^*)-(\varphi_c-\varphi_c^*)\right)\\+\mathrm{j}\left[\tilde{k}_{\varphi_y\varphi_x}\left((\varphi_{c+1}+\varphi_{c+1}^*)-(\varphi_c+\varphi_c^*)\right)-\mathrm{j}\tilde{k}_{\varphi_x\varphi_x}\left((\varphi_{c+1}-\varphi_{c+1}^*)-(\varphi_c-\varphi_c^*)\right)\right]\end{Bmatrix} \tag{4.12}$$

If cross-coupled coupling coefficients are not considered then $k_{xy}=k_{yx}=0$. Cross-coupled stiffness coefficients are ignored to keep the coupling force vector simple when it is converted to complex form.Even though coupling asymmetry does not pose any difficulty, we assume that it is symmetric (in aligned condition) since most catalogues only specify radial and angular stiffness values. In such case $k_{xx}=k_{yy}=k_{rad}$ and $k_{\varphi_{yy}}=k_{\varphi_{xx}}=k_{\varphi_{ang}}$. The final form of static coupling force obtained from Eqn. (4.12) is

$$\mathbf{f}_{SCS}=\begin{bmatrix}k_{rad}&0&-k_{rad}&0\\0&k_{ang}&0&-k_{ang}\\-k_{rad}&0&k_{rad}&0\\0&-k_{ang}&0&k_{ang}\end{bmatrix}\begin{Bmatrix}u_c\\\varphi_c\\u_{c+1}\\\varphi_{c+1}\end{Bmatrix} \tag{4.13}$$

4.3.2.2 Additive Coupling Stiffness Force

In previous chapters additive coupling stiffness force for the case of angular misalignment was derived. In the present chapter both parallel and angular misalignments have been considered. Additive stiffness force of coupling in Eqn. (4.6) can be expanded as

$$\mathbf{f}_{ACS}^{rot}=\Delta\mathbf{K}_c^{rot}(t)\left(\mathbf{u}_{0c}^{rot}+\mathbf{u}_c^{rot}e^{\mathrm{j}i\omega t}\right) \tag{4.14}$$

where $\mathbf{u}_{0c}^{rot}$, $\mathbf{u}_c^{rot}$ defined by Eqns. (4.4) and (4.5) denote the static and vibratory deflections of coupling nodes in rotating coordinate system. Turbo generators run up to multiple stages and each stage generally weighs a few tens of tons. It can be safely assumed that

the vibratory displacement at coupling nodes is less than static deflection due to the self-weight of rotor. (Friswell et al., 2010). If *weight dominance* (Singh and Tiwari, 2016) criterion is assumed, then

$$\mathbf{u}_c^{rot} << \mathbf{u}_{0c}^{rot} \tag{4.15}$$

And Eqn. (4.14) becomes

$$\mathbf{f}_{ACS}^{rot} = \Delta\mathbf{K}_c^{rot}(t)\mathbf{u}_{0c}^{rot} \tag{4.16}$$

$\Delta\mathbf{K}_c^{rot}(t)$ which is the additive stiffness of coupling varies in time with rotation angle. Hence, Eqn. (4.16) can be written as the product of a suitable time waveform and a matrix of constant coefficients $\Delta\mathbf{K}_c^{rot}$. This waveform $s(t)$ is called steering function and further discussion is made in later section. The additive coupling force in real form is given by

$$\mathbf{f}_{ACS}^{rot} = s(t)\Delta\mathbf{K}_c^{rot}\mathbf{u}_{0c}^{rot} \tag{4.17}$$

with

$$\Delta\mathbf{K}_c^{rot} = \begin{bmatrix} \Delta k_{\xi\xi} & 0 & 0 & 0 & -\Delta k_{\xi\xi} & 0 & 0 & 0 \\ 0 & \Delta k_{\eta\eta} & 0 & 0 & 0 & -\Delta k_{\eta\eta} & 0 & 0 \\ 0 & 0 & \Delta k_{\varphi_\eta\varphi_\eta} & 0 & 0 & 0 & -\Delta k_{\varphi_\eta\varphi_\eta} & 0 \\ 0 & 0 & 0 & \Delta k_{\varphi_\xi\varphi_\xi} & 0 & 0 & 0 & -\Delta k_{\varphi_\xi\varphi_\xi} \\ -\Delta k_{\xi\xi} & 0 & 0 & 0 & \Delta k_{\xi\xi} & 0 & 0 & 0 \\ 0 & -\Delta k_{\eta\eta} & 0 & 0 & 0 & \Delta k_{\eta\eta} & 0 & 0 \\ 0 & 0 & -\Delta k_{\varphi_\eta\varphi_\eta} & 0 & 0 & 0 & \Delta k_{\varphi_\eta\varphi_\eta} & 0 \\ 0 & 0 & 0 & -\Delta k_{\varphi_\xi\varphi_\xi} & 0 & 0 & 0 & \Delta k_{\varphi_\xi\varphi_\xi} \end{bmatrix} \tag{4.18}$$

The subscripts ξ, η, φ_η and φ_ξ in Eqn. (4.18) represent the directions in rotating coordinate system shown in Figure 4-3. Coordinate transformation to stationary frame of reference of Eqn. (4.17) is performed as shown below.

$$\mathbf{f}_{ACS}^{stat} = s(t)\left(\mathbf{T}^T\Delta\mathbf{K}_c^{rot}\mathbf{T}\right)\mathbf{u}_{0c}^{stat} \tag{4.19}$$

where the vector of static deflections at coupling nodes is given by

$$\mathbf{u}_{0c}^{stat} = \left\{\delta x_c \quad \delta y_c \quad \delta\varphi_{y_c} \quad \delta\varphi_{x_c} \quad \delta x_{c+1} \quad \delta y_{c+1} \quad \delta\varphi_{y_{c+1}} \quad \delta\varphi_{x_{c+1}}\right\}^T \tag{4.20}$$

The next section describes the procedure to numerically estimate static deflections, $\mathbf{u}_{0c}^{stat}$ at various locations along the rotor axis.

4.3.3.3 Catenary curve of turbogenerator

The 'catenary curve' is the graphical representation of the static deflections and slopes due to self-weight at each node along the length of the rotor modelled by finite elements. A detailed discussion on this topic is presented in Friswell et al. (2010). The coupling static deflection vector $\mathbf{u}_{0c}^{stat}$ in Eqn. (4.19) is the subset of global static deflection vector, $\mathbf{u}_{0}^{stat}$ which for a finite element model with *n* nodes, is obtained by solving the equation

$$\left(\mathbf{u}_{0}^{stat}\right)_{4n\times 1} = -\left(\mathbf{K}_{4n\times 4n}^{re}\right)^{-1}\left(\mathbf{M}_{4n\times 4n}^{re}\right)\left\{\mathbf{g}_{4n\times 1}\right\} \tag{4.21}$$

In Eqn. (4.21) the coordinate system and elemental matrices of size 8×8 given in Nelson and McVaugh (1976) (refer **Appendix E**) are used. The superscript *re* is used to differentiate from other elemental matrices of size 4×4 used throughout the paper. The global gravity vector **g** is obtained by assembling the gravity vector of each element given by

$$\mathbf{g}^{e} = \begin{Bmatrix} 0 & 9.81 & 0 & 0 & 0 & 9.81 & 0 & 0 \end{Bmatrix}^{T} \tag{4.22}$$

For a horizontal rotor, the self-weight acts in the transverse (vertically downward) direction. In case of journal bearings, the horizontal force arising from the oil-film acts on the rotor and produces the horizontal static deflections (Friswell et al., 2010). Since we consider rolling element bearings in the present work, the horizontal static deflections can be safely ignored. Hence, as per the convention followed, as shown in Figure 4-3, we have

$$\delta y_1 = \delta y_2 = \delta\varphi_{x_1} = \delta\varphi_{x_2} = 0 \tag{4.23}$$

The remaining coefficients of the vector given by Eqn. (4.21) are the static deflections and slopes at the due to the self-weight of the coupled rotor system. The derivation of $\mathbf{f}_{ACS}^{stat}$ is given in the next section.

4.3.3.4 Additive coupling stiffness force in stationary frame of reference

The physical meaning of ACS matrix given by Eqn. (4.18) is pictorially represented in Figure 4-4. Parallel misalignment generates time dependent additive coupling stiffness coefficients $\Delta k_{\xi\xi}$ and $\Delta k_{\eta\eta}$ in the rotating frame of reference. Likewise, $\Delta k_{\varphi_\eta\varphi_\eta}$ and $\Delta k_{\varphi_\xi\varphi_\xi}$ are additive coupling stiffness coefficients generated due to angular misalignment. In real rotor systems, unequal amounts of misalignment exist in $x-y$ and $x-z$ planes, and therefore the coefficients are assumed to be unequal, i.e. $\Delta k_{\xi\xi} \neq \Delta k_{\eta\eta}$ and $\Delta k_{\varphi_\eta\varphi_\eta} \neq \Delta k_{\varphi_\xi\varphi_\xi}$, which makes the total number of direct ACS coefficients four. The unequal magnitudes of these coefficients mean that the coupling exhibits asymmetric dynamic behaviour during operation. All cross-coupling coefficients are ignored in this work. The matrix $\Delta\mathbf{K}_c^{rot}(t)$ in Eqn. (4.19) is in rotating frame of reference. We convert to stationary frame of reference using the below transformation (Friswell et al., 2010),

$$\mathbf{f}_{ACS}^{stat} = s(t)\left(\mathbf{T}^T \Delta\mathbf{K}_c^{rot}\mathbf{T}\right)\mathbf{u}_{0c}^{stat} = s(t)\Delta\mathbf{K}_c^{stat}\mathbf{u}_{0c}^{stat} \tag{4.24}$$

where $\mathbf{T}$ is the transformation matrix is given by Eqn. (4.10)

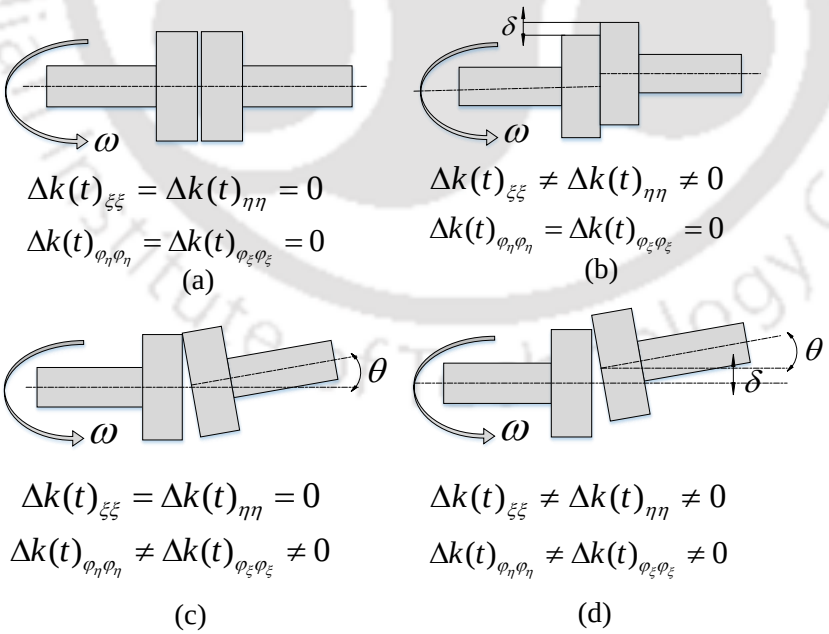

Figure 4-4 ACS coefficients for various misalignment conditions (a) No misalignment (b) Parallel (c) Angular (d) Combined

Table 4-1 Correlation between misalignment type and coupling additive stiffness coefficients

Misalignment type	Direction	$\Delta k_{\xi\xi}$	$\Delta k_{\eta\eta}$	$\Delta k_{\varphi_\eta\varphi_\eta}$	$\Delta k_{\varphi_\xi\varphi_\xi}$
Parallel	x	✓	✗	✗	✗
	y	✗	✓	✗	✗
Angular	φ_x	✗	✗	✓	✗
	φ_y	✗	✗	✗	✓
Combined	x, y	✓	✓	✗	✗
	φ_x, φ_y	✗	✗	✓	✓

Eqn. (4.24) then becomes

$$\Delta\mathbf{K}_c^{stat} = \begin{bmatrix} a & b & 0 & 0 & -a & -b & 0 & 0 \\ b & c & 0 & 0 & -b & -c & 0 & 0 \\ 0 & 0 & d & e & 0 & 0 & -d & -e \\ 0 & 0 & e & f & 0 & 0 & -e & -f \\ -a & -b & 0 & 0 & a & b & 0 & 0 \\ -b & -c & 0 & 0 & b & c & 0 & 0 \\ 0 & 0 & -d & -e & 0 & 0 & d & e \\ 0 & 0 & -e & -f & 0 & 0 & e & f \end{bmatrix} \tag{4.25}$$

where

$$a = \cos^2 \omega t(\Delta k_{\xi\xi}) + \sin^2 \omega t(\Delta k_{\eta\eta}); b = \cos \omega t \sin \omega t(\Delta k_{\xi\xi} - \Delta k_{\eta\eta})$$

$$c = \cos^2 \omega t\left(\Delta k_{\eta\eta}\right) + \sin^2 \omega t\left(\Delta k_{\xi\xi}\right) d = \cos^2 \omega t\left(\Delta k_{\varphi_\eta\varphi_\eta}\right) + \sin^2 \omega t\left(\Delta k_{\varphi_\xi\varphi_\xi}\right)$$

$$e = \cos \omega t \sin \omega t(\Delta k_{\varphi_\eta\varphi_\eta} - \Delta k_{\varphi_\xi\varphi_\xi}); f = \cos^2 \omega t\left(\Delta k_{\varphi_\xi\varphi_\xi}\right) + \sin^2 \omega t\left(\Delta k_{\varphi_\eta\varphi_\eta}\right)$$

On substituting Eqns. (4.25) and (4.20) in Eqn. (4.24), we obtain the ACS force vector in real coordinates of size 8×1, as

$$\mathbf{f}_{ACS}^{stat} = s(t)\Delta\mathbf{K}_c^{stat}\mathbf{u}_{0c}^{stat} = s(t)\begin{bmatrix} a(\delta x_c - \delta x_{c+1}) + b(\delta y_c - \delta y_{c+1}) \\ b(\delta x_c - \delta x_{c+1}) + c(\delta y_c - \delta y_{c+1}) \\ e(\delta\varphi_{x_c} - \delta\varphi_{x_{c+1}}) + d(\delta\varphi_{y_c} - \delta\varphi_{y_{c+1}}) \\ f(\delta\varphi_{x_c} - \delta\varphi_{x_{c+1}}) + e(\delta\varphi_{y_c} - \delta\varphi_{y_{c+1}}) \\ a(\delta x_{c+1} - \delta x_c) + b(\delta y_{c+1} - \delta y_c) \\ b(\delta x_{c+1} - \delta x_c) + c(\delta y_{c+1} - \delta y_c) \\ e(\delta\varphi_{x_{c+1}} - \delta\varphi_{x_c}) + d(\delta\varphi_{y_{c+1}} - \delta\varphi_{y_c}) \\ f(\delta\varphi_{x_{c+1}} - \delta\varphi_{x_c}) + e(\delta\varphi_{y_{c+1}} - \delta\varphi_{y_c}) \end{bmatrix} \tag{4.26}$$

Rewriting the force vector due to additive coupling stiffness in the complex form, we have

$$\mathbf{f}_{ACS} = s(t)\begin{Bmatrix} (\delta x_c - \delta x_{c+1})(a + \mathrm{j}b) + (\delta y_c - \delta y_{c+1})(b + \mathrm{j}c) \\ (\delta\varphi_{x_c} - \delta\varphi_{x_{c+1}})(e + \mathrm{j}f) + (\delta\varphi_{y_c} - \delta\varphi_{y_{c+1}})(d + \mathrm{j}e) \\ (\delta x_{c+1} - \delta x_c)(a + \mathrm{j}b) + (\delta y_{c+1} - \delta y_c)(b + \mathrm{j}c) \\ (\delta\varphi_{x_{c+1}} - \delta\varphi_{x_c})(e + \mathrm{j}f) + (\delta\varphi_{y_{c+1}} - \delta\varphi_{y_c})(d + \mathrm{j}e) \end{Bmatrix} \tag{4.27}$$

where

$$(a + \mathrm{j}b) = 0.5\left(\Delta k_{\xi\xi}\left(1 + e^{\mathrm{j}2\omega t}\right) + \Delta k_{\eta\eta}(1 - e^{\mathrm{j}2\omega t})\right)$$
$$(d + \mathrm{j}e) = 0.5\left(\Delta k_{\varphi_\eta\varphi_\eta}\left(1 + e^{\mathrm{j}2\omega t}\right) + \Delta k_{\varphi_\xi\varphi_\xi}(1 - e^{\mathrm{j}2\omega t})\right)$$

Upon substituting Eqn. (4.23) in Eqn. (4.27), the final form of the ACS force in the complex form is given by

$$\mathbf{f}_{ACS} = 0.5s(t)\begin{Bmatrix} (\delta x_c - \delta x_{c+1})\left\{\Delta k_{\xi\xi}(1 + e^{\mathrm{j}2\omega t}) + \Delta k_{\eta\eta}(1 - e^{\mathrm{j}2\omega t})\right\} \\ (\delta\varphi_{y_c} - \delta\varphi_{y_{c+1}})\left\{\Delta k_{\varphi_\xi\varphi_\xi}(1 + e^{\mathrm{j}2\omega t}) + \Delta k_{\varphi_\eta\varphi_\eta}(1 - e^{\mathrm{j}2\omega t})\right\} \\ (\delta x_{c+1} - \delta x_c)\left\{\Delta k_{\xi\xi}(1 + e^{\mathrm{j}2\omega t}) + \Delta k_{\eta\eta}(1 - e^{\mathrm{j}2\omega t})\right\} \\ (\delta\varphi_{y_{c+1}} - \delta\varphi_{y_c})\left\{\Delta k_{\varphi_\xi\varphi_\xi}(1 + e^{\mathrm{j}2\omega t}) + \Delta k_{\varphi_\eta\varphi_\eta}(1 - e^{\mathrm{j}2\omega t})\right\} \end{Bmatrix} \tag{4.28}$$

where the steering function is assumed to be rectangular wave with 40% duty cycle as discussed in Section 2.7. Eqn. (4.28) is rearranged as below by taking the steering function inside and multiplying with exponential terms.

$$\mathbf{f}_{ACS} = 0.5\begin{Bmatrix} \left(\delta x_c - \delta x_{c+1}\right)\left(\Delta k_{\xi\xi}\sum_{i=-n}^{i+n} p_i e^{\mathrm{j}i\omega t} + \Delta k_{\eta\eta}\sum_{i=-n}^{i+n} q_i e^{\mathrm{j}i\omega t}\right) \\ \left(\delta\varphi_{y_c} - \delta\varphi_{y_{c+1}}\right)\left(\Delta k_{\varphi_\eta\varphi_\eta}\sum_{i=-n}^{i+n} p_i e^{\mathrm{j}i\omega t} + \Delta k_{\varphi_\xi\varphi_\xi}\sum_{i=-n}^{i+n} q_i e^{\mathrm{j}i\omega t}\right) \\ \left(\delta x_{c+1} - \delta x_c\right)\left(\Delta k_{\xi\xi}\sum_{i=-n}^{i+n} p_i e^{\mathrm{j}i\omega t} + \Delta k_{\eta\eta}\sum_{i=-n}^{i+n} q_i e^{\mathrm{j}i\omega t}\right) \\ \left(\delta\varphi_{y_{c+1}} - \delta\varphi_{y_c}\right)\left(\Delta k_{\varphi_\eta\varphi_\eta}\sum_{i=-n}^{i+n} p_i e^{\mathrm{j}i\omega t} + \Delta k_{\varphi_\xi\varphi_\xi}\sum_{i=-n}^{i+n} q_i e^{\mathrm{j}i\omega t}\right) \end{Bmatrix} \tag{4.29}$$

The values of p_i and q_i in Eqn. (4.29), which denote the participation factors of the steering function, are tabulated in Table 4-1. In the case of experimental data from rotor test setup the values of $\Delta k_{\xi\xi}\, p_i$, $\Delta k_{\eta\eta}\, q_i$, $\Delta k_{\varphi_\eta\varphi_\eta}\, p_i$, and $\Delta k_{\varphi_\xi\varphi_\xi}\, q_i$ can be obtained from linear regression (Shravan and Tiwari, 2012). The physical interpretation Eqn. (4.29) is as follows: With weight-dominance assumption, ACS forces and moments are written as the product of additive stiffness coefficients, an appropriate steering function and the static deflection at the coupling nodes. Assigning values to the additive stiffness coefficients in a particular direction in numerical simulation would physically represent the existence of misalignment and therefore fluctuating forces/moments in the corresponding direction. As the severity of misalignment increases the vibration amplitude spills over to higher harmonics in the full spectrum. Experimental data from real rotors has shown that the maximum number of predominant positive and negative harmonics is not more than five. For the present problem, the number of harmonics *i* considered in **A** and **b** is defined in Section 2.9 is taken from -5 to $+5$.

4.3.3 AMB Force

The lateral force exerted by the AMB on the rotor has two components: the one which is proportional to the rotor vibration at the AMB location and the other proportional to the current in the AMB actuator (Singh and Tiwari, 2016)

$$\mathbf{f}_{AMB} = -k_s \mathbf{u}_{AMB} + k_i \mathbf{i}_c \tag{4.30}$$

where $\mathbf{u}_{AMB}$ is the complex displacement vector at AMB nodal locations. The control current in AMB coils controlled by proportional-integral-derivative (PID) law is given by

$$\mathbf{i}_c = k_P \mathbf{u}_{AMB} + k_I \int \mathbf{u}_{AMB} dt + k_D \dot{\mathbf{u}}_{AMB} \tag{4.31}$$

4.3.4 Unbalance Force

The unbalance force vector due to the mass eccentricities at the nodal locations of discs is

$$\mathbf{f}_{unb} = m_d e\omega^2 e^{\mathrm{j}\omega t} e^{\mathrm{j}\beta} \tag{4.32}$$

where e is the disc unbalance eccentricity located at the phase angle β.

4.3.5 Bearing Force

The bearing support force vector acting at the bearing node locations due to the stiffness

$$\mathbf{f}_{bk} = 0.5\left\{k_{bxx}(\mathbf{u}_b + \mathbf{u}_b^*) - \mathrm{j}k_{bxy}(\mathbf{u}_b - \mathbf{u}_b^*) + \mathrm{j}k_{byx}(\mathbf{u}_b + \mathbf{u}_b^*) + k_{byy}(\mathbf{u}_b - \mathbf{u}_b^*)\right\} \tag{4.33}$$

where $\mathbf{u}_b$ and $\mathbf{u}_b^*$ are the vectors of complex translational displacements at bearing nodal locations and their conjugates, respectively. Parameters $k_{bxx}, k_{bxy}, k_{byx}$, and k_{byy} represent the direct and cross-coupled stiffness coefficients. Likewise, the force acting at the bearing nodal locations due to the direct coefficients of damping of bearings is

$$\mathbf{f}_{bc} = 0.5\left\{c_{bxx}(\dot{\mathbf{u}}_b + \dot{\mathbf{u}}_b^*) - \mathrm{j}c_{bxy}(\dot{\mathbf{u}}_b - \dot{\mathbf{u}}_b^*) + \mathrm{j}c_{byx}(\dot{\mathbf{u}}_b + \dot{\mathbf{u}}_b^*) + c_{byy}(\dot{\mathbf{u}}_b - \dot{\mathbf{u}}_b^*)\right\} \tag{4.34}$$

where $\dot{\mathbf{u}}_b$, $\dot{\mathbf{u}}_b^*$ are the vector of complex translational velocities at bearing nodal locations and their conjugates, respectively. Parameters $c_{bxx}, c_{byy}, c_{bxy}$ and c_{byx} represent the direct and cross-coupled bearing damping coefficients.

4.3.6 Global EOM and Simulink Model

Eqn. (4.35) is the global EOM in complex form, obtained by assembling the sub system matrices, as

$$\mathbf{M}\ddot{\mathbf{u}} + \left(\mathbf{C} - \mathrm{j}\omega\mathbf{G}\right)\dot{\mathbf{u}} + \mathbf{K}\mathbf{u} = \mathbf{f}_{unb} + \mathbf{f}_{AMB} - \mathbf{f}_{ACS} \tag{4.35}$$

$$\mathbf{M} = \mathbf{M}_{sh} + \mathbf{M}_d;\ \mathbf{C} = \mathbf{C}_b + \mathbf{C}_c + \mathbf{C}_{sh};\ \mathbf{K} = \mathbf{K}_b + \mathbf{K}_{scs} + \mathbf{K}_{sh};\ \mathbf{G} = \mathbf{G}_{sh} + \mathbf{G}_d$$

From Eqn. (4.35), it can be noticed that the external forces acting on the system are (i) unbalance force (ii) ACS force stiffness due to misalignment and (iii) AMB restitution force. The assumed solution to Eqn. (4.35) is

$$\mathbf{u} = \sum_{i=-\infty}^{i=+\infty} \bar{\mathbf{u}} e^{\mathrm{j}i\omega t} \tag{4.36}$$

The complex current vector $\mathbf{i}_c$ of AMB in Eqn. (4.30) too will have the same multi-harmonic nature as rotor displacement, so that

$$\mathbf{i}_c = \sum_{i=-\infty}^{i=+\infty} \bar{\mathbf{i}}_c e^{\mathrm{j}i\omega t} \tag{4.37}$$

The force vectors, on the right side of Eqn. (4.35) are given by

$$\bar{\mathbf{f}}_{unb} = \bar{\mathbf{f}}_{unb} e^{i\omega t}; \quad \bar{\mathbf{f}}_{AMB} = \bar{\mathbf{f}}_{AMB} e^{\mathrm{j}i\omega t}; \quad \bar{\mathbf{f}}_{ACS} = \bar{\mathbf{f}}_{ACS} e^{\mathrm{j}i\omega t}$$

Substituting Eqn. (4.36) in Eqn. (4.35), it converts EOM in time domain to frequency domain, as

$$\left(-\mathbf{M}(i\omega)^2 + \mathrm{j}(i\omega)(\mathbf{C} - \mathrm{j}\omega\mathbf{G}) + \mathbf{K}\right)\bar{\mathbf{u}} = \bar{\mathbf{f}}_{unb} + \bar{\mathbf{f}}_{AMB} - \bar{\mathbf{f}}_{ACS} \tag{4.38}$$

4.3.7 Application of Condensation Schemes

Due to the inconvenience of taking measurements at all nodal locations along the length of the rotor, condensation/reduction of global EOMs is performed to reduce the measurable DOFs. Qu (2004) has presented various reduction techniques in finite elements. Table 4-2 lists the recent papers where condensation technique has been performed. The nodes where the external forces act on the rotor system are usually chosen as master DOFs. Rest of the DOFs are grouped as slave DOFs. The master DOFs that correspond to the nodal locations of *all identifiable parameters* are the translational DOFs at bearings, discs, coupling, AMBs and rotational DOFs at coupling nodes.

$$\bar{\mathbf{u}}_m^d = \{u_{b_1} \quad u_{d_1} \quad u_{AMB_1} \quad u_{d_2} \quad u_{b_2} \quad u_{c_2} \quad \varphi_{c_1} \quad u_{c_2} \quad \varphi_{c_2} \quad u_{b_3} \quad u_{d_3} \quad u_{AMB_2} \quad u_{d_4} \quad u_{b_4}$$
$$\ldots \quad u_{b_{n-1}} \quad u_{d_{n-1}} \quad u_{AMB_{n-1}} \quad \ldots \quad \ldots \quad u_{c_{n-1}} \quad \varphi_{c_{n-1}} \quad u_{c_n} \quad \varphi_{c_n} \quad \ldots \quad u_{AMB_n} \quad \ldots \quad u_{b_n}\} \tag{4.39}$$

The derivation of the transformation matrix $\mathbf{T}^d$, which links master DOFs to the total DOFs is explained in Lal and Tiwari (2012) and is expressed as

$$\mathbf{u} = \begin{Bmatrix} \bar{\mathbf{u}}_m^d \\ \bar{\mathbf{u}}_s^d \end{Bmatrix} = \mathbf{T}^d \bar{\mathbf{u}}_m^d \tag{4.40}$$

where

$$\mathbf{T}^d = \begin{Bmatrix} \mathbf{I} \\ -[\mathbf{K}_{ss} - \omega_0^2 \mathbf{M}_{ss}]^{-1} [\mathbf{K}_{sm} - \omega_0^2 \mathbf{M}_{sm}] \end{Bmatrix} \tag{4.41}$$

In Eqn. (4.41), ω_0 is the mean speed at which dynamic condensation is performed. Prasad and Tiwari (2018) considered the gyroscopic matrix in the derivation of transformation matrix, which resulted in better estimates of the AMB and unbalance parameters. However, since there are no overhanging discs in the present formulation $\mathbf{G}$ matrix is not considered in the derivation of $\mathbf{T}^d$. The EOM in terms of reduced coordinates is given by

$$\left(-\mathbf{M}^d (i\omega)^2 + \mathrm{j}(i\omega)\left(\mathbf{C}^d - \mathrm{j}\omega\mathbf{G}^d\right) + \mathbf{K}^d\right)\bar{\mathbf{u}}_m^d = \bar{\mathbf{f}}_{unb}^d + \bar{\mathbf{f}}_{AMB}^d - \bar{\mathbf{f}}_{ACS}^d \tag{4.42}$$

where

$$\mathbf{M}^d = \left(\mathbf{T}^d\right)^T \mathbf{M}\mathbf{T}^d; \quad \mathbf{K}^d = \left(\mathbf{T}^d\right)^T \mathbf{K}\mathbf{T}^d; \quad \mathbf{C}^d = \left(\mathbf{T}^d\right)^T \mathbf{C}\mathbf{T}^d; \quad \mathbf{G}^d = \left(\mathbf{T}^d\right)^T \mathbf{G}\mathbf{T}^d$$

$$\bar{\mathbf{f}}_{unb}^d = \left(\mathbf{T}^d\right)^T \bar{\mathbf{f}}_{unb}; \bar{\mathbf{f}}_{AMB}^d = \left(\mathbf{T}^d\right)^T \bar{\mathbf{f}}_{AMB}; \bar{\mathbf{f}}_{ACS}^d = \left(\mathbf{T}^d\right)^T \bar{\mathbf{f}}_{ACS}$$

The superscript d refers to the dynamically reduced form of matrices and vectors. Before pre and post multiplying the elemental matrices and external force vectors, it is necessary that the matrices be reordered as shown in the example shown below.

$$\mathbf{M} = \begin{bmatrix} \mathbf{M}_{mm} & \mathbf{M}_{ms} \\ \mathbf{M}_{sm} & \mathbf{M}_{ss} \end{bmatrix} \tag{4.43}$$

Likewise, the force vectors too should be rearranged in the below form

$$\bar{\mathbf{f}} = \begin{Bmatrix} \bar{\mathbf{f}}_{mm} \\ \bar{\mathbf{f}}_{ss} \end{Bmatrix} \tag{4.44}$$

The operations shown in Eqns. (4.43) and (4.44) have to be performed in keeping with the rearranged form of global DOFs as shown in Eqn. (4.40). Eqn. (4.42) is used in the next section for the estimation of unknown system parameters.

4.3.8 Identification Algorithm for Parameter Estimation

The forcing terms containing the unknown parameters are grouped on the right side and known system parameters are grouped on the left side of equality. Eqn. (4.42) is rearranged in the form

$$\left(-\mathbf{M}^{d}\left(i\omega\right)^{2}+\mathrm{j}\left(i\omega\right)\left(\mathbf{C}_{sh}^{d}-\mathrm{j}\omega\mathbf{G}^{d}\right)+\mathbf{K}_{sh}^{d}\right)\bar{\mathbf{u}}_{m}^{d}=\mathbf{f}_{unb}^{d}+\mathbf{f}_{AMB}^{d}-\mathrm{j}i\omega(\mathbf{f}_{bc}^{d})-\mathbf{f}_{bk}^{d}-\mathbf{f}_{SCS}^{d}-\mathbf{f}_{ACS}^{d} \tag{4.45}$$

Equation. (4.45) is in the form

$$\mathbf{Ax}=\mathbf{b} \tag{4.46}$$

where **x** is the vector of all unknown system parameters, i.e. the disc unbalance eccentricities, stiffness of bearing in *x* and *y* directions, radial and angular stiffness of coupling, and coupling ACS coefficients. The vector **x** of identifiable parameters is given by

$$\begin{aligned}\mathbf{x}=\{&U_1^{re}\quad U_1^{im}\quad U_2^{re}\quad U_2^{im}\quad U_3^{re}\quad U_3^{im}\quad U_4^{re}\quad U_4^{im}\quad k_{1xx}\quad k_{2xx}\quad k_{3xx}\quad k_{4xx}\\ &k_{1yy}\quad k_{2yy}\quad k_{3yy}\quad k_{4yy}\quad k_s\quad k_i\quad k_{rad}\quad k_{ang}\quad \Delta k_{\xi\xi}\quad \Delta k_{\eta\eta}\quad \Delta k_{\varphi_\eta\varphi_\eta}\quad \Delta k_{\varphi_\xi\varphi_\xi}\}\end{aligned} \tag{4.47}$$

The complex displacements $\bar{\mathbf{u}}_m^d$ in Eqns. (4.45) can be written as

$$\bar{\mathbf{u}}_m^d=\bar{\mathbf{u}}^{dre}+\mathrm{j}\bar{\mathbf{u}}^{dim} \tag{4.48}$$

Likewise, the complex current in AMBs can be written as

$$\mathbf{i}=\mathbf{i}^{re}+\mathrm{j}\mathbf{i}^{im} \tag{4.49}$$

The real and imaginary parts of rotor vibration ($\bar{\mathbf{u}}^{dre}$, $\bar{\mathbf{u}}^{dim}$) and AMB current ($\bar{\mathbf{i}}^{re}$, $\bar{\mathbf{i}}^{im}$) obtained from the amplitude and phase of the harmonics of full spectrum plots are the inputs to Eqn. (4.48). To improve the condition number of the regression matrix **A** (refer **Appendix G**), the data from multiple speeds can be advantageously used. Equation. (4.49) then becomes

$$\begin{Bmatrix} \mathbf{A}(\omega_1) \\ \mathbf{A}(\omega_2) \\ \vdots \\ \vdots \\ \mathbf{A}(\omega_n) \end{Bmatrix} \mathbf{x} = \begin{Bmatrix} \mathbf{b}(\omega_1) \\ \mathbf{b}(\omega_2) \\ \vdots \\ \vdots \\ \mathbf{b}(\omega_n) \end{Bmatrix} \tag{4.50}$$

Solution to Eqns. (4.46), (4.50) is of the form

$$\mathbf{x} = \left(\mathbf{A}(\omega)^{\mathrm{T}}\mathbf{A}(\omega)\right)^{-1}\mathbf{A}(\omega)^{\mathrm{T}}\mathbf{b}(\omega) \tag{4.51}$$

The estimation the real and imaginary parts of the harmonics of rotor vibration and AMB current essential for solving Eqn. (4.54) is described in Chapter 2 in detail. The numerical experiment and parameter identification in a test rotor system is discussed in next section.

4.3.9 Results and Discussion

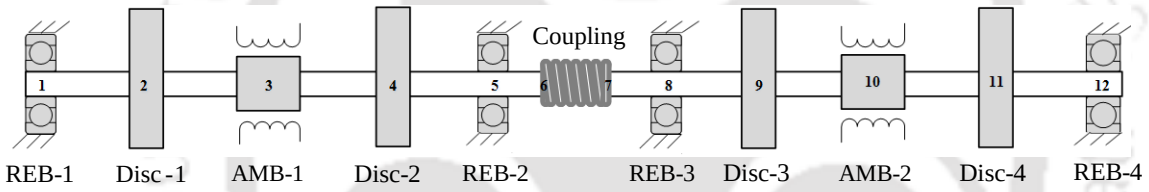

Figure 4-5 Coupled rotor system integrated with AMBs

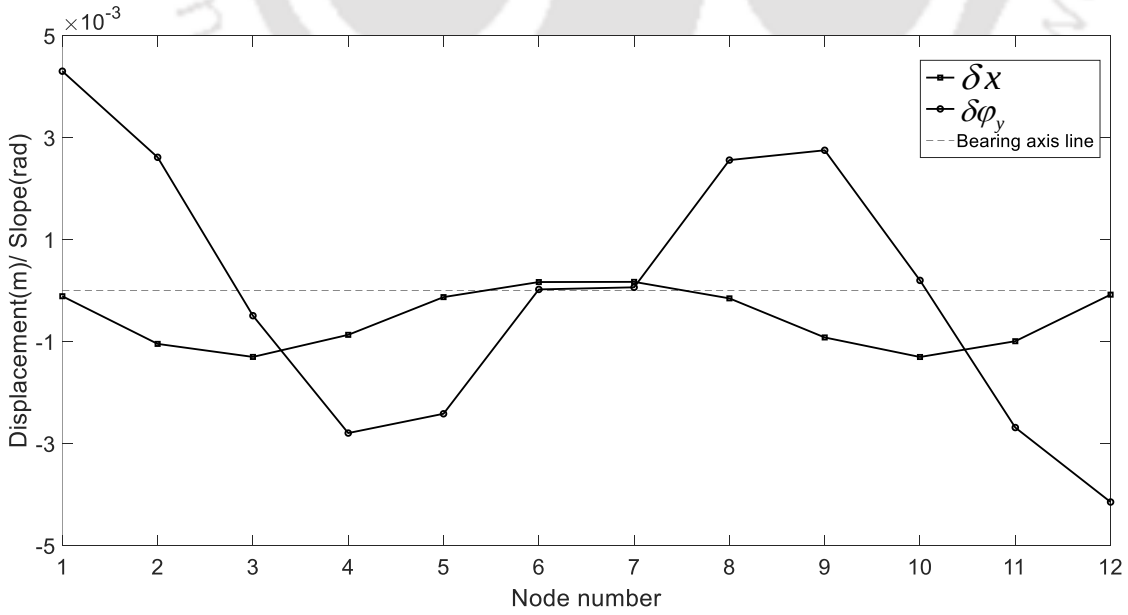

Figure 4-6 Static deflection curve

Table 4-2 Rotor geometric properties

Rotor						AMB		
m_{d_1}	2.25	kg	I_{d_4}	0.004	kg-m^2	k_p	12200	A/m
m_{d_2}	1.75	kg	I_{p_1}	0.0048	kg-m^2	k_I	2000	A/m-s
m_{d_3}	2.5	kg	I_{p_2}	0.007	kg-m^2	k_d	3	A-s/m
m_{d_4}	1.6	kg	I_{p_3}	0.009	kg-m^2	k_s	105210	N/m
I_{d_1}	0.0024	kg-m^2	I_{p_4}	0.008	kg-m^2	k_i	12.4	N/A
I_{d_2}	0.0035	kg-m^2	l_e	0.25	m			
I_{d_3}	0.0045	kg-m^2	d	0.017	m			

Figure 4-5 shows a simplified model of the TG with integrated AMB considered in the present work. It is similar to two-stage test rig set-up used in Mayes and Davies (1980) to study the vibratory behavior of *coupled rotating shafts* containing a transverse crack**.** Each rotor system is supported on rolling element bearings, has two rigid discs mounted on the flexible shaft, and an auxiliary AMB between the discs. An intermediate coupling transmits the drive from rotor-1 to rotor-2. The drive end coupling is not shown in the schematic and is not considered in the present formulation.

The geometric properties of a laboratory rotor model are given in Table 4-1. The stiffness and damping of bearings are shown in Figure 4-7 and Figure 4-8. Bearing stiffness and damping are assumed such that the net effect of bearing and housing is considered. The equivalent viscous damping of coupling $\mathbf{C}_c$ is ignored in the present work.The static and additive stiffness coefficients of the coupling are shown in Figure 4-9. The values of coupling stiffness coefficients are assumed such that they are lower than bearing stiffness coefficients. Figure 4-6 shows the catenary curve of the rotor-bearing system obtained from Eqn. (4.21). Figure 4-10 shows the Simulink model built from Eqn. (4.35) to

generate time domain responses of the vibration at each node along the length of rotor-bearing-coupling-AMB system and current in AMBs. The flow chart that shows analysis and identification procedure is shown in Figure 4-11. Numerical simulation was implemented in Matlab-Simulink environment (ODE15s variable step stiff solver is used to solve the system since it is found to be faster than non-stiff solvers such as ODE23 or ODE4). However, the time domain data is logged at fixed intervals of $1/2^{16}$ sec.

To study the effect of coupling stiffness and the AMB on the dynamic behaviour of system, the system is ramped up with the angular acceleration of 20π rad/s^2 for 10 s. The Hilbert envelope of *x*-displacement at the location of two AMBs (node 3 and node 10) for rotor-1 and rotor-2 are plotted to identify the critical speeds in three different cases. Figure 4-12 (a) and Figure 4-12 (d) illustrate the case when the rotors are uncoupled and there is no AMB. The peaks are noticed at 68 rad/s (108 μm) and 65 rad/s (109 μm). In Figure 4-12(b) and Figure 4-12(e) the rotors are coupled and the effect of coupling static and additive stiffness causes the peaks to shift to 81 rad/s (218 μm) and 80 rad/s (225 μm), respectively.

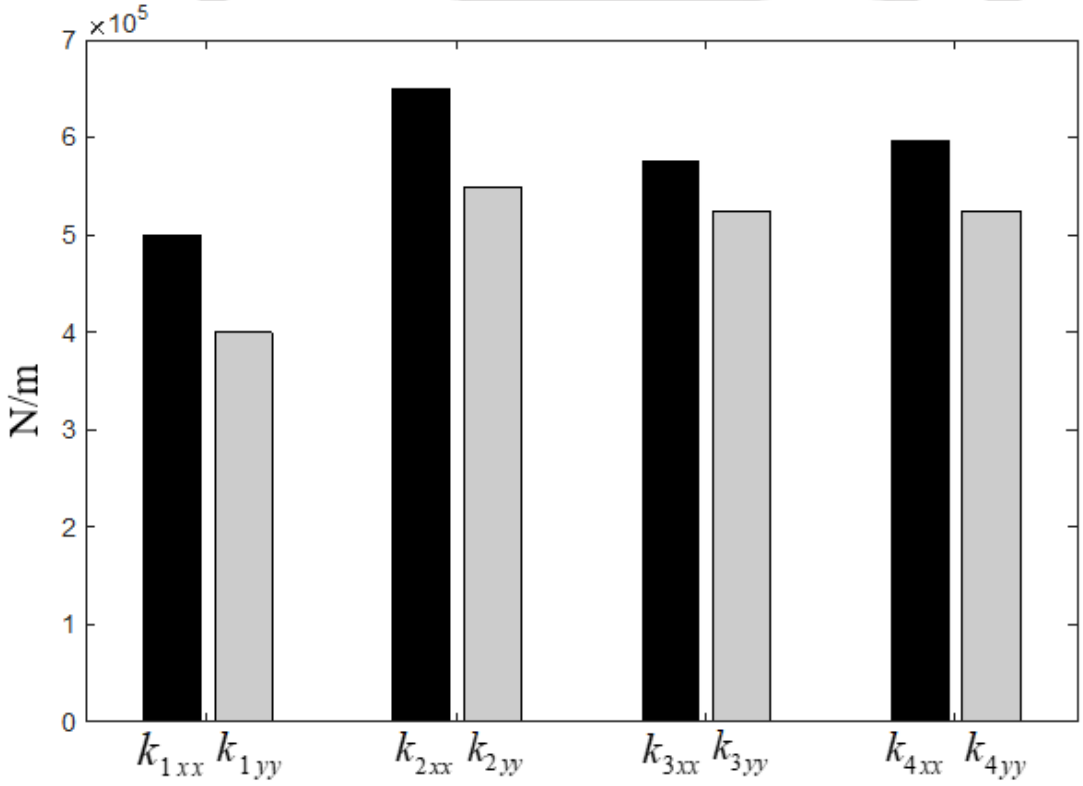

Figure 4-7 Stiffness of bearings

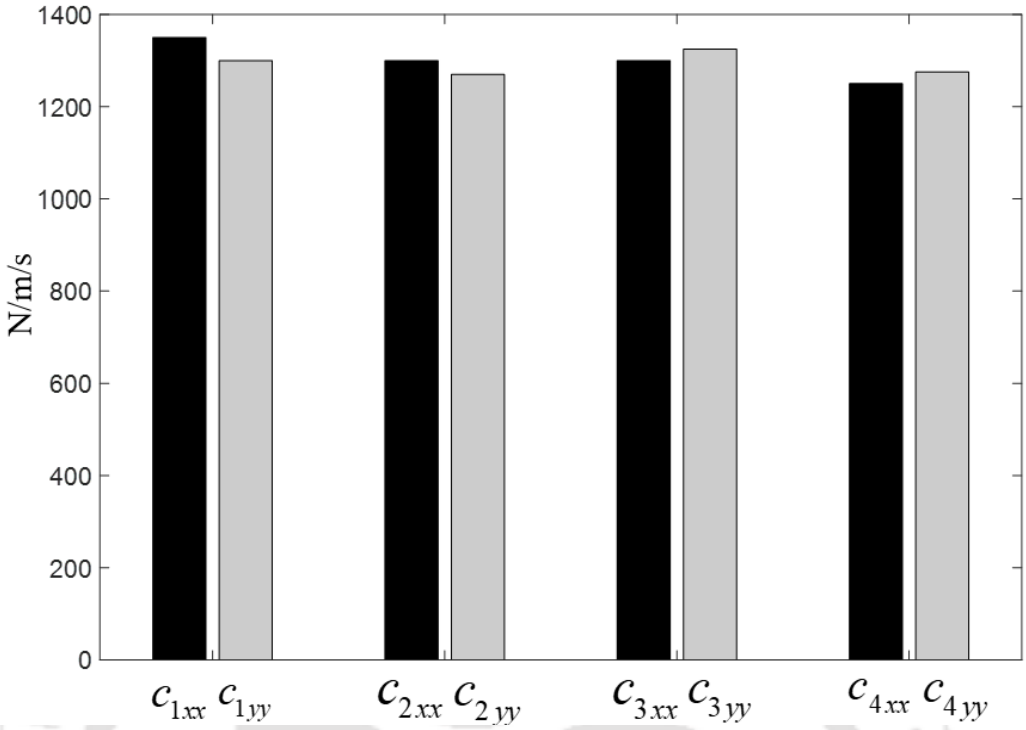

Figure 4-8 Damping of bearings

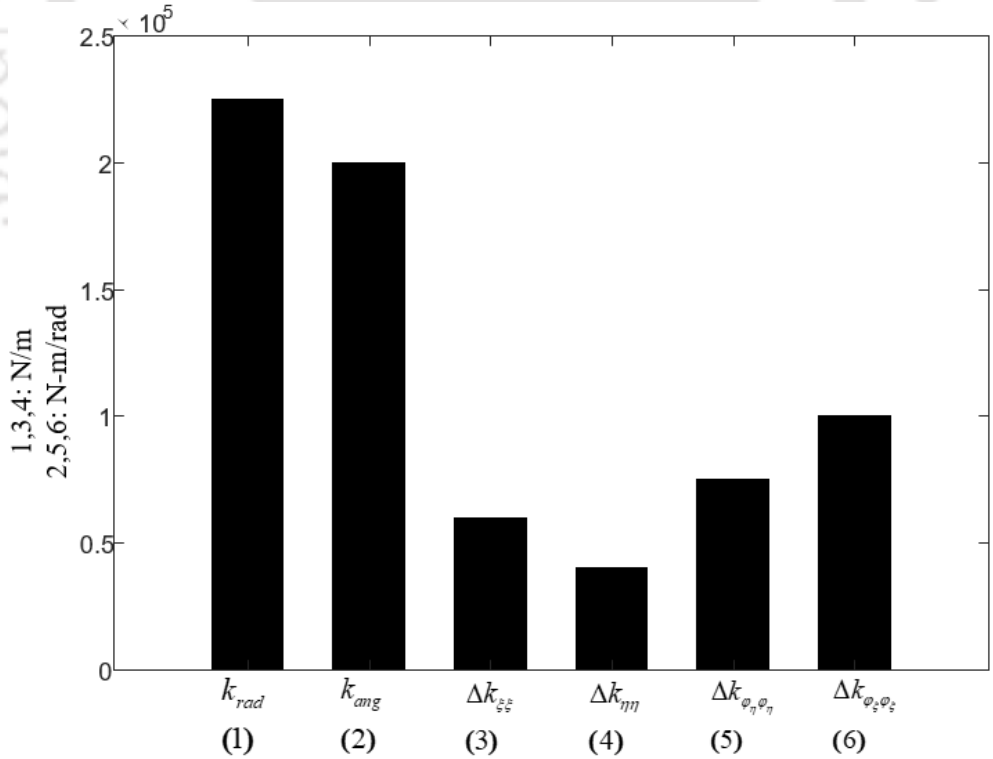

Figure 4-9 Static and additive stiffness coefficients of coupling

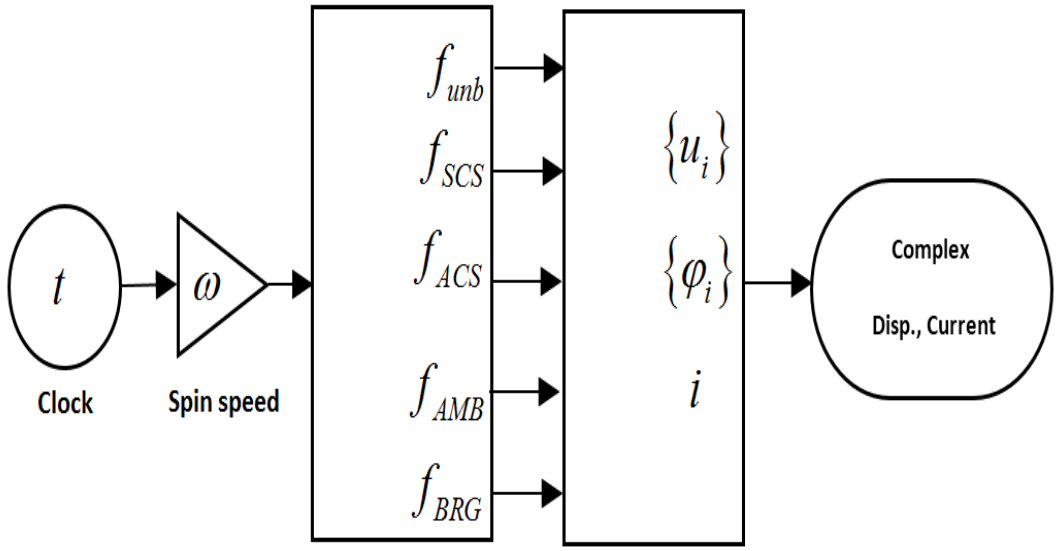

Figure 4-10 Simulink model of Rotor-Bearing-Coupling-AMB system

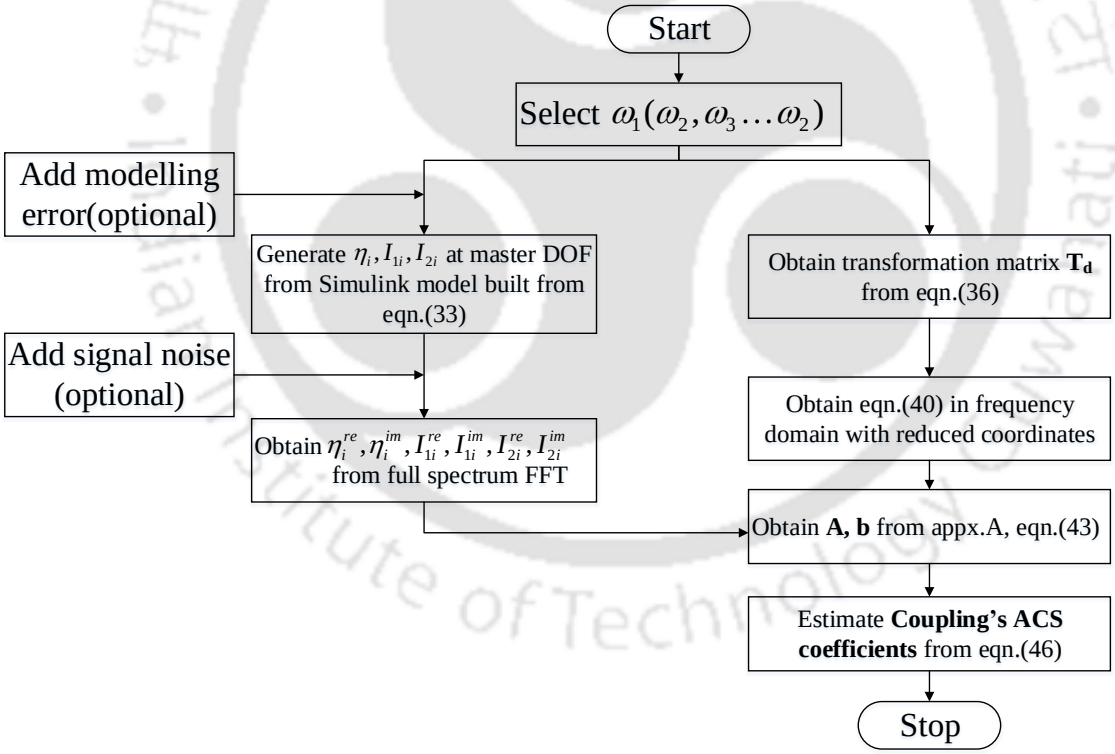

Figure 4-11 Analysis and identification flowchart

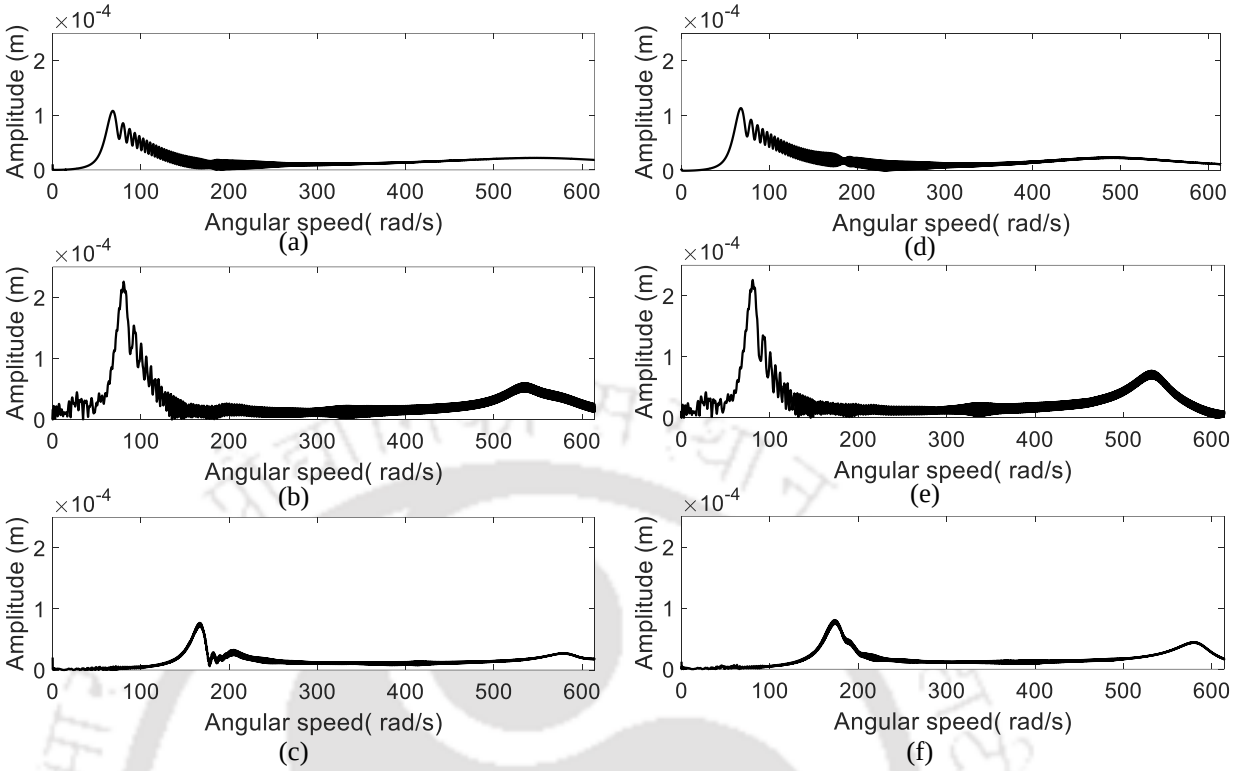

Figure 4-12 Ramp-up response of rotor-1 and rotor-2 at AMB nodal locations: (a), (d) Individual rotors without AMB (b), (e) Coupled rotors without AMB (c), (f) Coupled rotors with AMB

Figures 4-12(c) and Figure 4-12(f) show the effect of inclusion of AMBs at nodes 3 and 10. The resonant peaks move further to the right and the response also increases at 168 rad/s and 174 rad/s. At both locations there is a considerable decrease in response to 75 µm and 80 µm, respectively. This demonstrates the usefulness of AMB in controlling the dynamic behaviour of the system to advantage. In all the plots there is a trace of beating phenomenon, which is generally noticed in accelerating rotors and coupled rotors whose natural frequencies are in vicinity of each other. However, because of considerable bearing damping the phenomenon is not sustained for longer duration. For the purpose of parameter identification, the speeds outside the half-power points are chosen. Figure 4-13 shows the full spectrum plot of disc-1 vibration and AMB-1 current. The amplitude and phase of forward and backward whirl frequencies can be seen. The full spectrum plots obtained from the simulation look similar to the plots obtained by Patel and Darpe (2009), Monte et al. (2014) and Tuckmantel et al. (2014) in laboratory experiments. Shravan et al.

(2015) show that despite the presence of noise inherent in experimental data the displacement harmonics in the frequency domain were distinct and measurable.

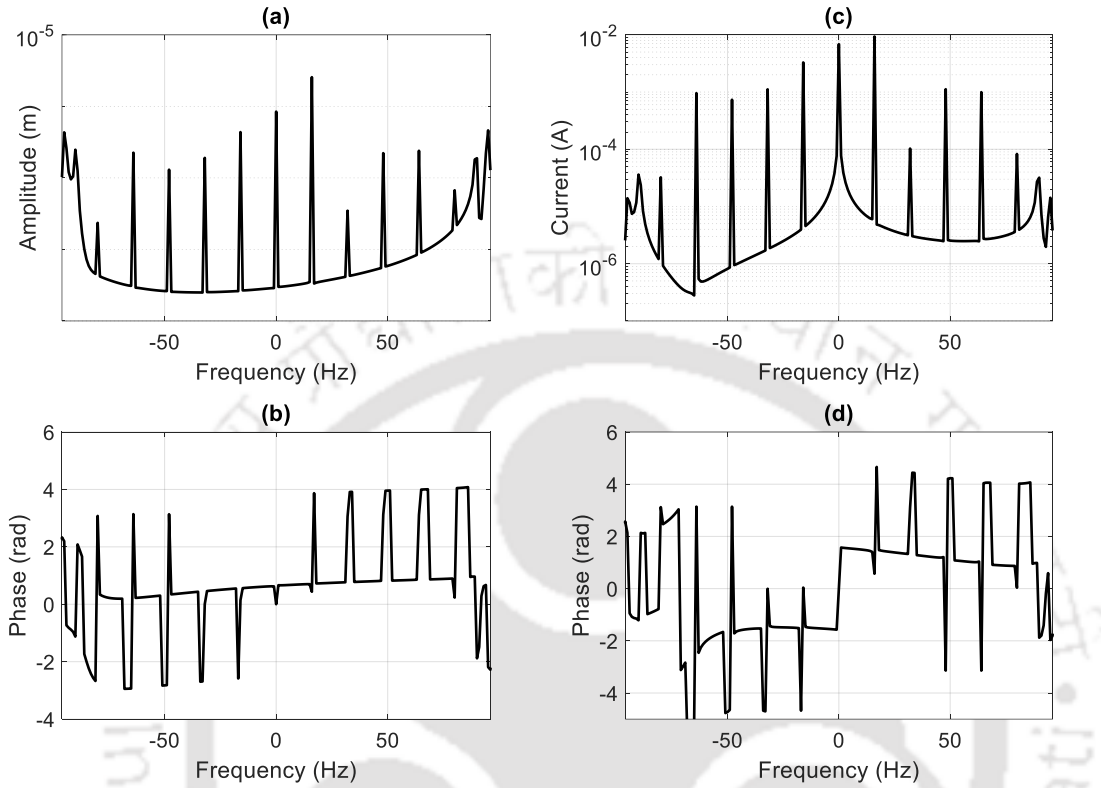

Figure 4-13 Full spectrum plot at 16 Hz (a) Amplitude at Disc 1 location (b) Phase at Disc 1 location (c) Amplitude of AMB current (d) Phase of AMB current

Identification of unknown parameters is performed through Eqn. (4.51) by using data from *master* DOFs. There are a total of fourteen master DOFs of which twelve DOFs are translational displacements of disc, bearings, AMB, couplings and two DOFs are rotational displacements of coupling. All the individual speeds in the range of 45 Hz - 55 Hz are chosen for parameter identification.

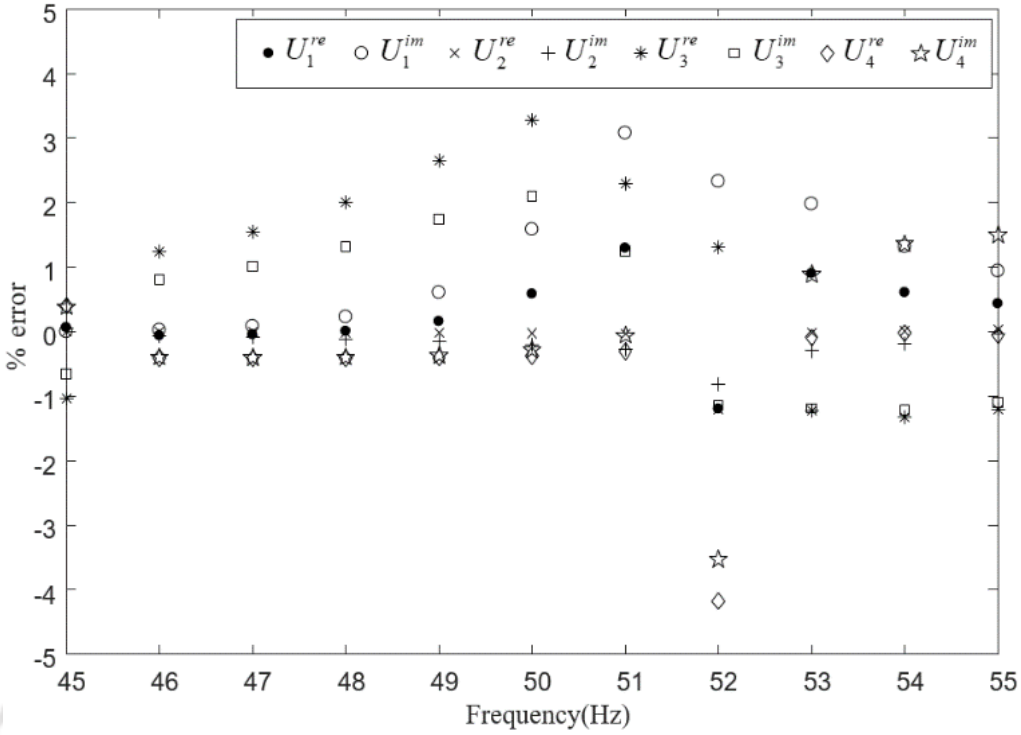

Figure 4-14 Effect of speed on estimates of unbalance

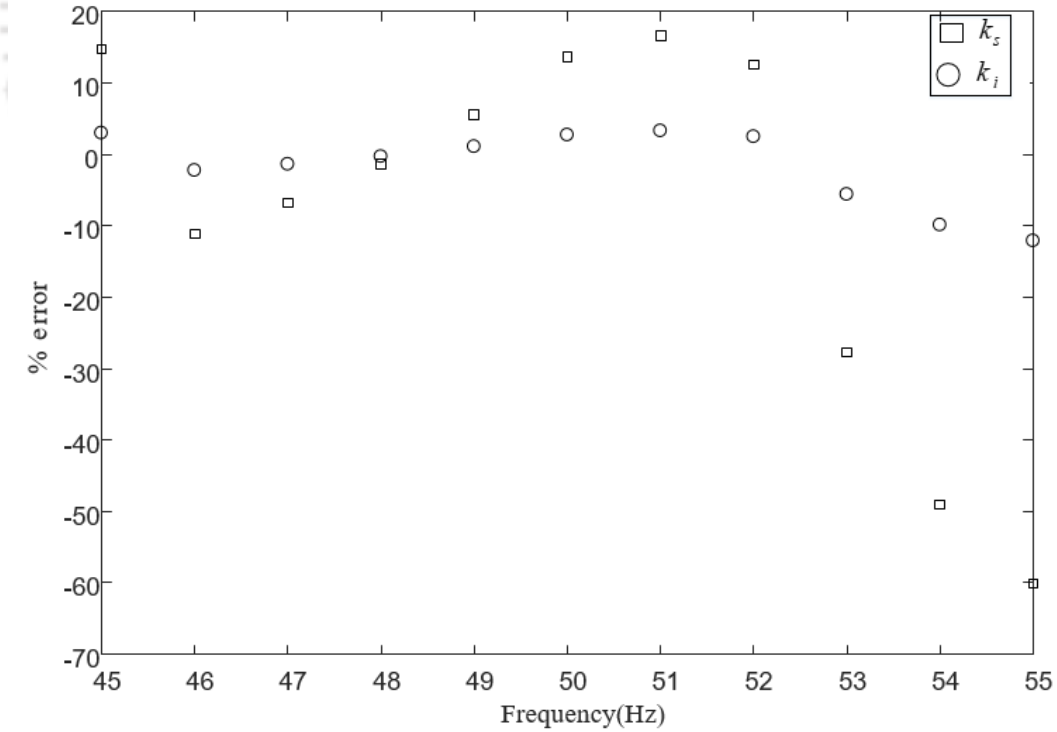

Figure 4-15 Effect of speed on estimates of AMB constants

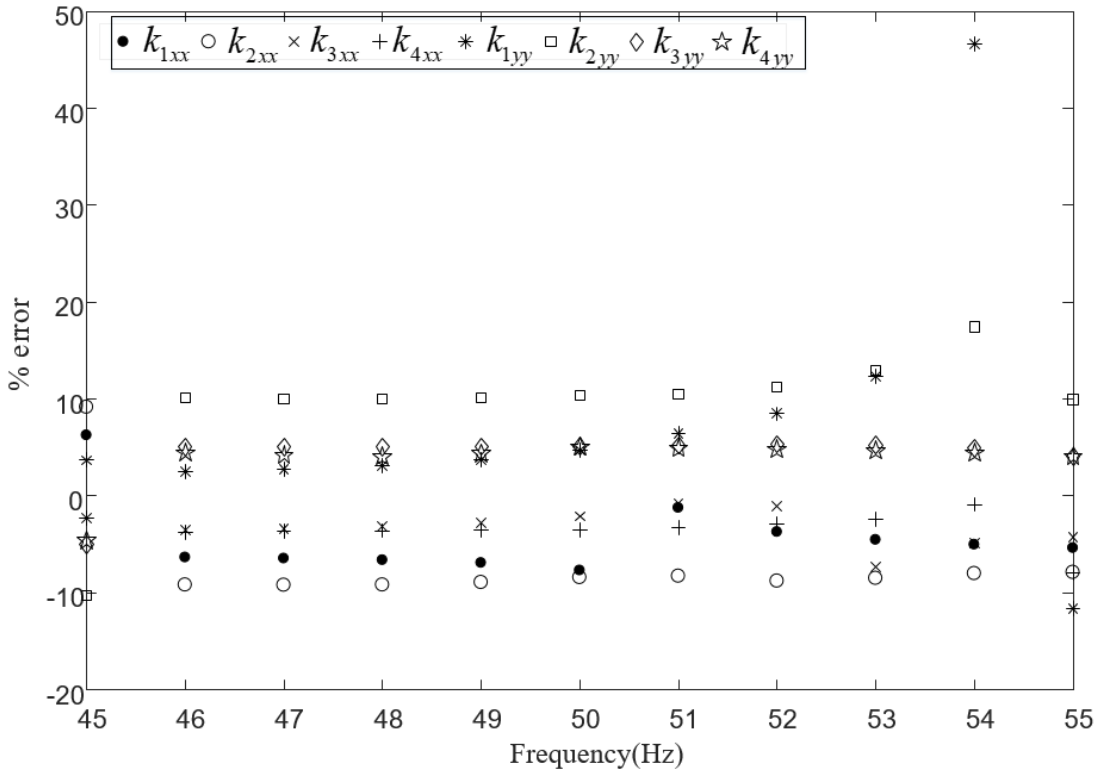

Figure 4-16 Effect of speed on estimates of bearing stiffness coefficients

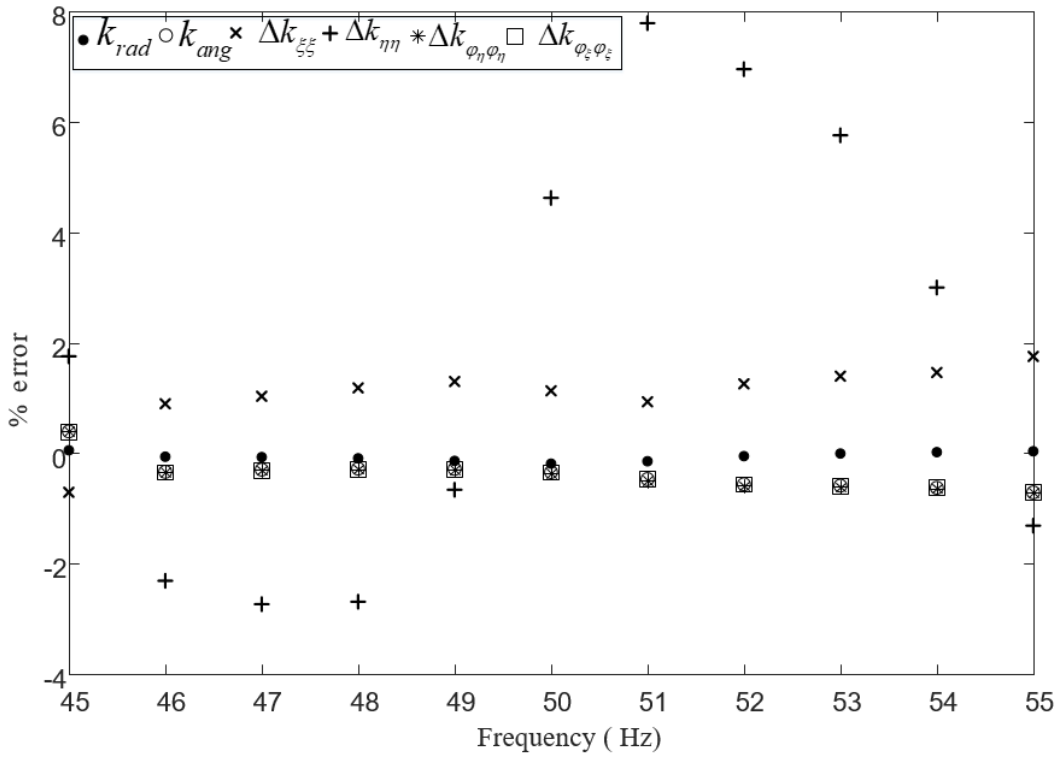

Figure 4-17 Effect of speed on estimates of coupling static and additive stiffness

This particular range is chosen since it is away from the critical speeds of the rotor system shown in Figure 4-12. The unknown parameters are first identified at individual speeds in this range using Eqn. (4.49). In Figure 4-14 for 50 - 52 Hz, the percentage error in the unbalance parameter U_4^{re} & U_4^{im} is 4%. Figure 4-15 shows that the error in the AMB displacement constant is as high as 50% at 53 Hz and 60% at 54 Hz. The percentage error in the bearing stiffness coefficients in Figure 4-16 is in the range $\pm 10\%$ across all speeds. However, at 54 Hz variation in k_{1yy} is as high as 47%. The percentage error in the estimation of $\Delta k_{\eta\eta}$ in Figure 4-17 varies from 4% to 8% between 50 Hz to 54 Hz.

The considerable error in the estimation of parameters in the range of 50 Hz to 54 Hz can be attributed to the fact that this speed range falls between almost twice the critical speed values of rotor-1 (168 rad/s) and rotor-2 (174 rad/s) with AMBs. Next cumulative data from all 11 speeds is considered for the identification and input into Eqn. (4.53). The comparison of the absolute values of all identifiable parameters with various levels of measurement noise is shown in Figure 4.18 through Figure 4.22. In Figure 4-29 the percentage error of estimated using the cumulative data from 11 speeds from 45 Hz to 54 Hz is shown. For 0% noisy signal, the maximum deviation from the assumed values is less than 4.6% for 21 parameters out of 24 parameters. The highest deviations are found in k_{1xx} , k_{1yy} and k_s with deviation of 8.2%, -11% and 10% respectively. For 1% noisy signals the highest deviations from assumed values are shown by U_3^{im}(-16.5%) , U_4^{im}(-26%) , k_{2yy}(-12.5%) and $\Delta k_{\xi\xi}$(-23%) . Rest of the parameters deviate by no more than 8%. For 5% noise the maximum deviations occur in $\Delta k_{\xi\xi}$(-51%), $\Delta k_{\eta\eta}$(-40%), U_4^{im}(-40%), U_3^{im}(-28%) and k_{2xx}(19.3%). Rest of the parameters deviate by no more than 8.2%.

The uncertainties in an engineering problem can be generally described by two groups of variables: random and interval. There are many approaches to model these uncertainties, such as probabilistic, fuzzy, interval, evidence, and grey system-based (Yan et al., 2013). In the present work instead of modelling the uncertainty in the formulation, a bias error is introduced in the rotor parameters to study the sensitivity of identification algorithm. The parameters that undergo bias are $m_{d_1}, m_{d_2}, m_{d_3}, m_{d_4}, \delta x_c, \delta x_{c+1}, \delta\varphi_{y_c}$ and $\delta\varphi_{y_{c+1}}$. Figure 4-23

through Figure 4-27 compare the absolute values of assumed and estimated parameters for various levels of bias errors. The percentage error when cumulative data is considered is graphically shown in Figure 4-28. The parameters that exhibit maximum deviation are k_{3xx}(8.1%), k_{3yy}(-11%) and k_i(11.75%). Rest of the estimates fall within ±5% of the assumed values. The algorithm is found to be more sensitive to measurement noise comparatively.

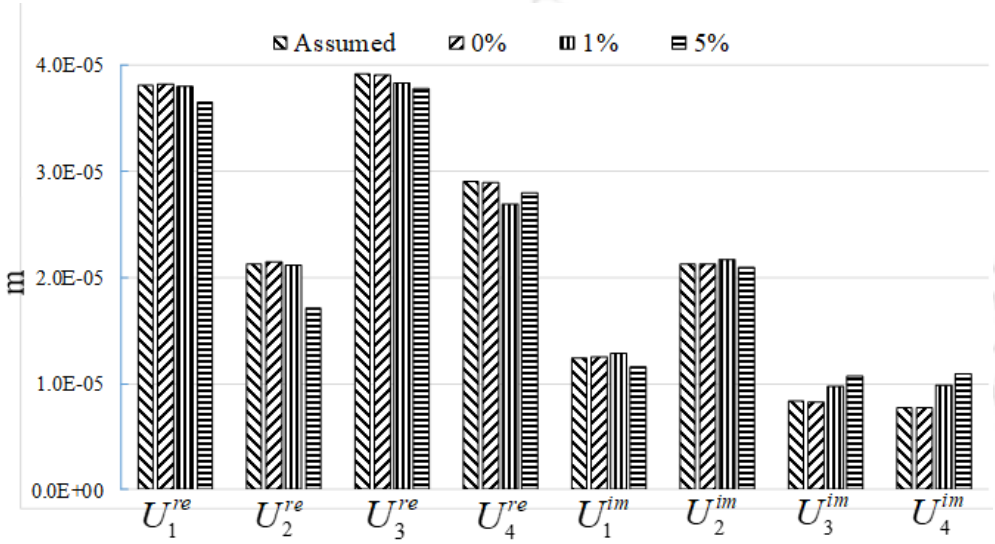

Figure 4-18 Sensitivity of disc unbalance eccentricity to various levels of noise

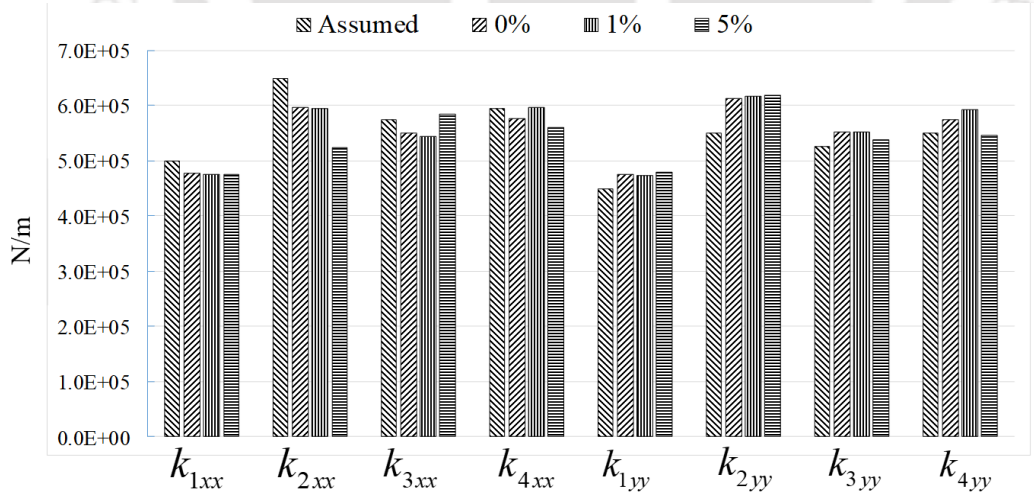

Figure 4-19 Sensitivity of bearing stiffness coefficients to various levels of noise

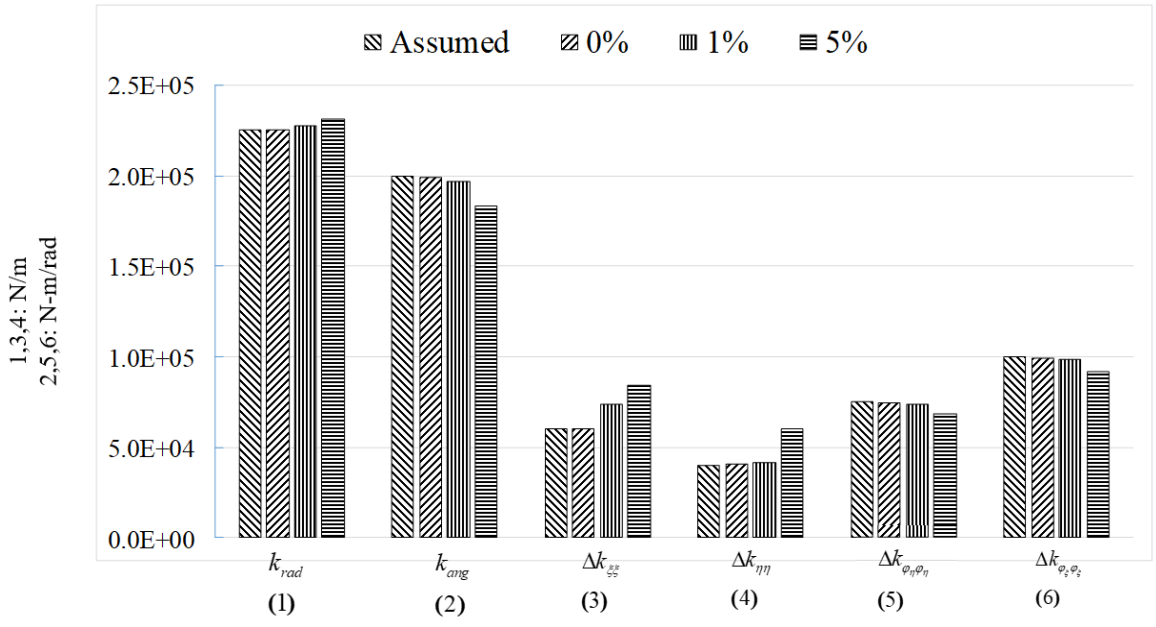

Figure 4-20 Sensitivity of static and additive stiffness coefficients of coupling to various levels of noise

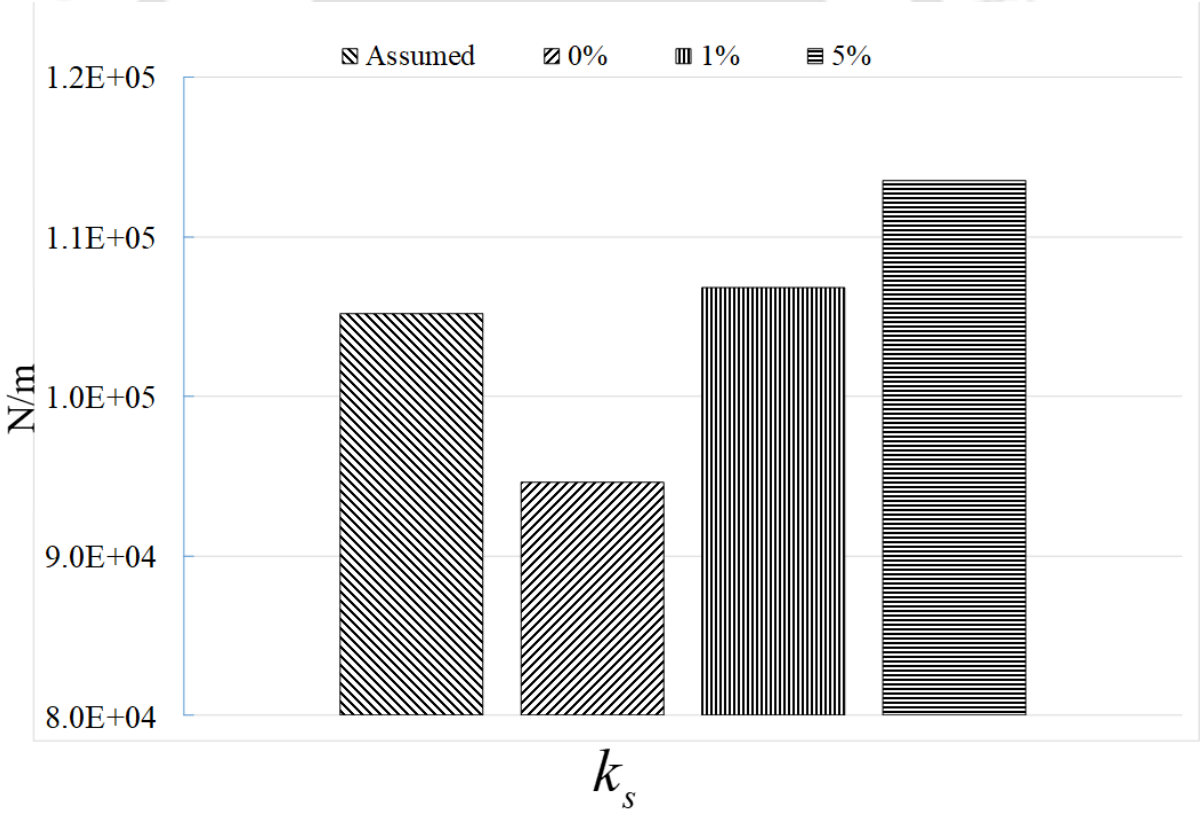

Figure 4-21 Sensitivity of AMB displacement constant to various levels of noise

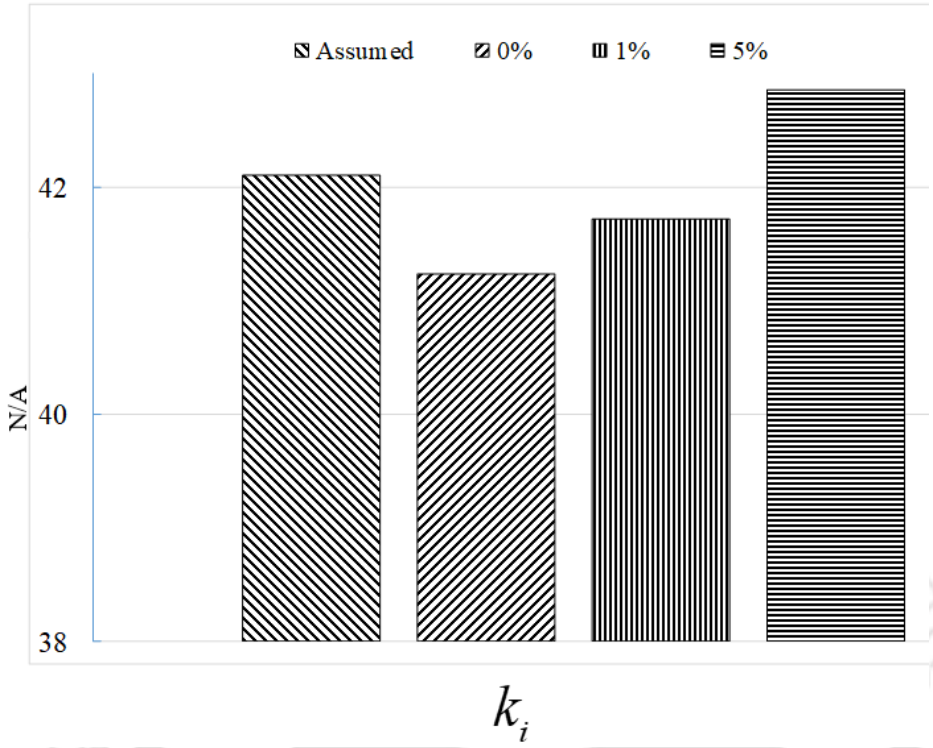

Figure 4-22 Sensitivity of AMB current constant to various levels of noise

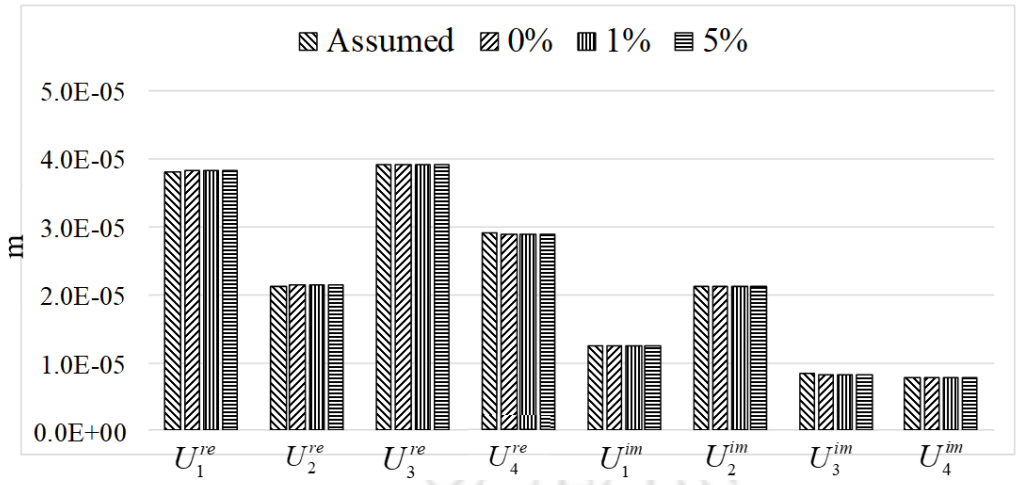

Figure 4-23 Sensitivity of disc unbalance eccentricity to errors in modelling

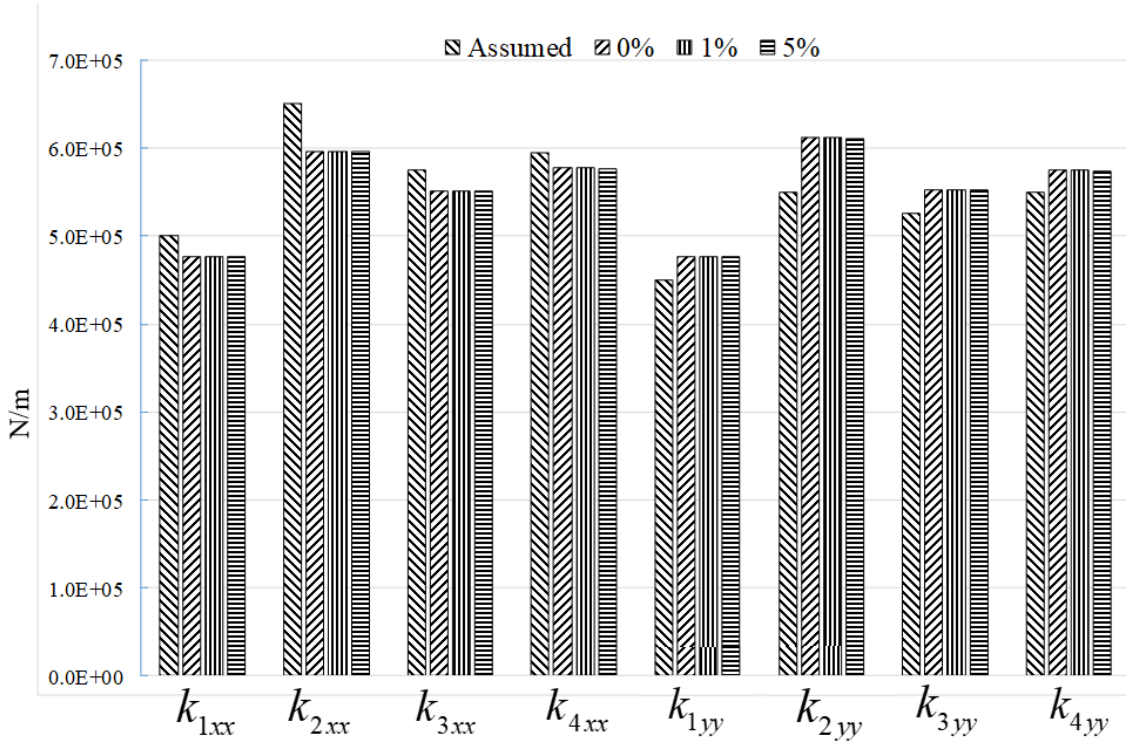

Figure 4-24 Sensitivity of bearing stiffness coefficients to errors in modelling

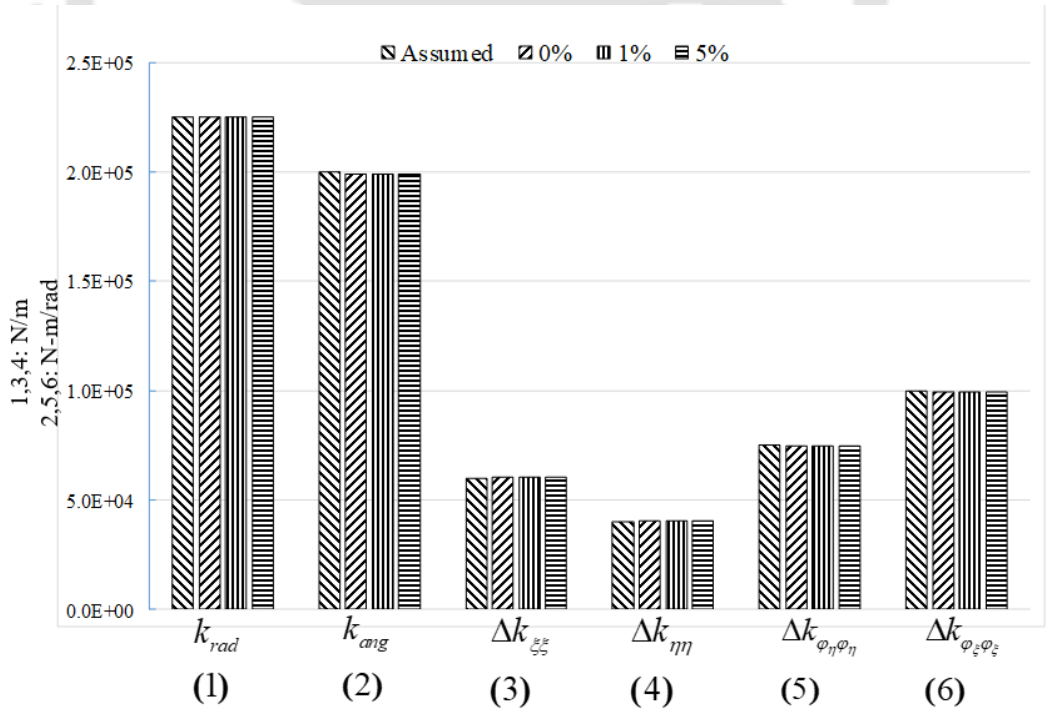

Figure 4-25 Sensitivity of coupling static and additive stiffness coefficients to errors in modelling

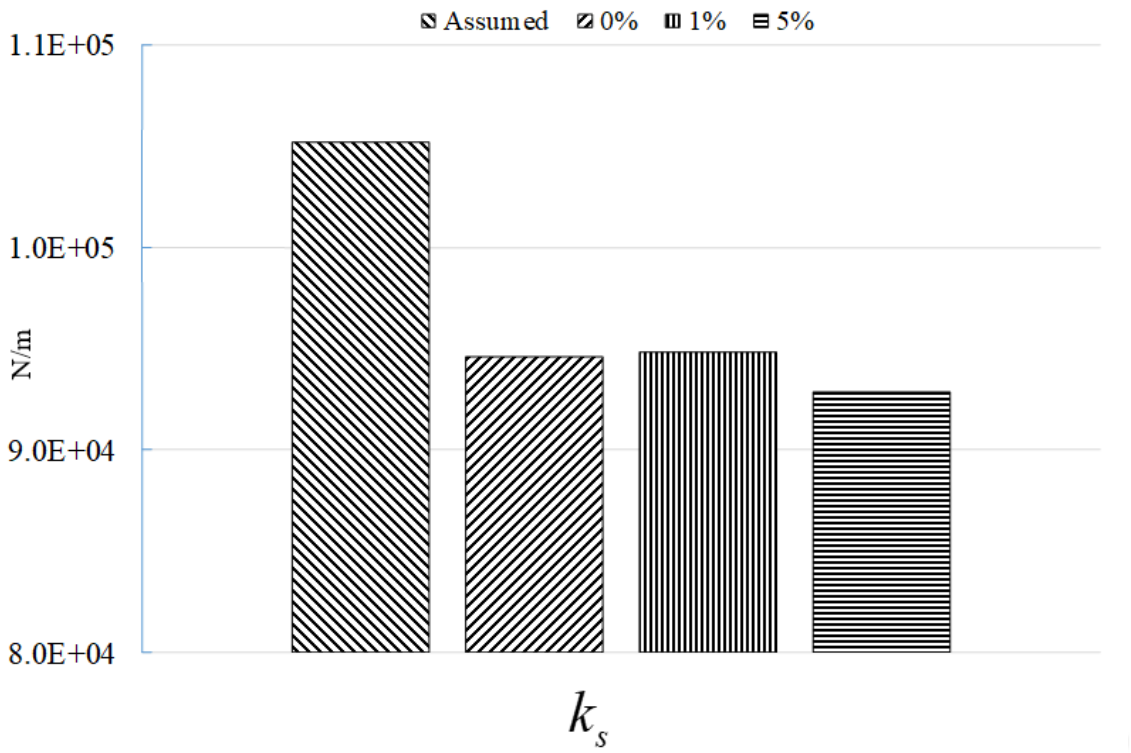

Figure 4-26 Sensitivity of AMB displacement constant to errors in modelling

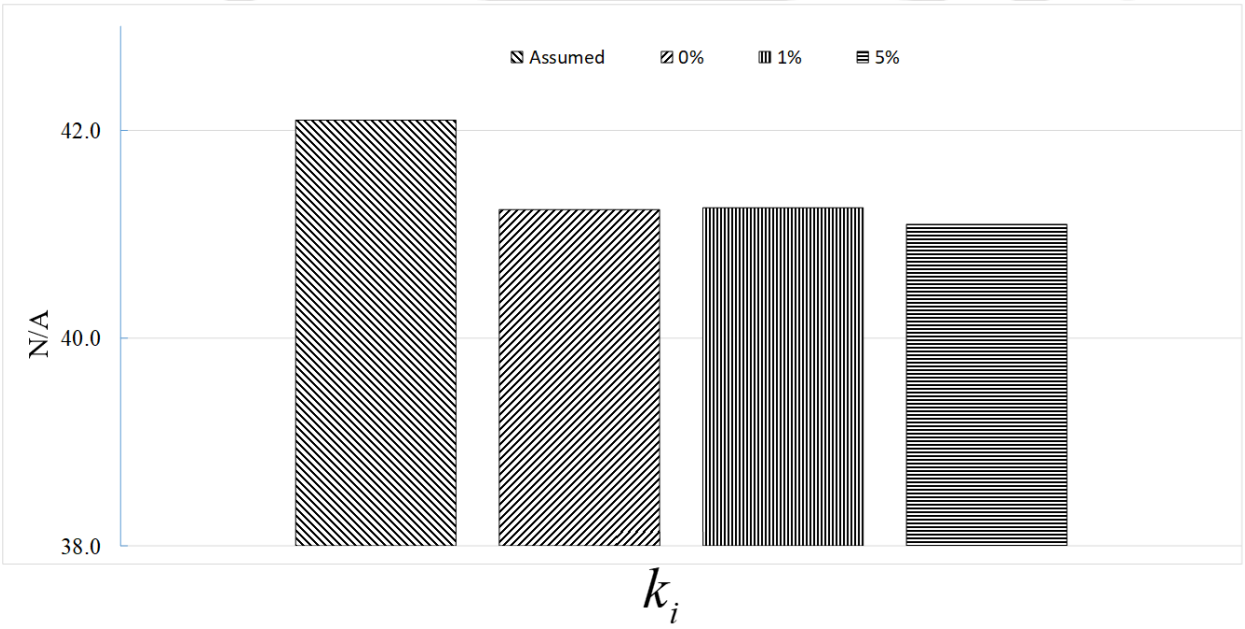

Figure 4-27 Sensitivity of AMB current constant to errors in modelling

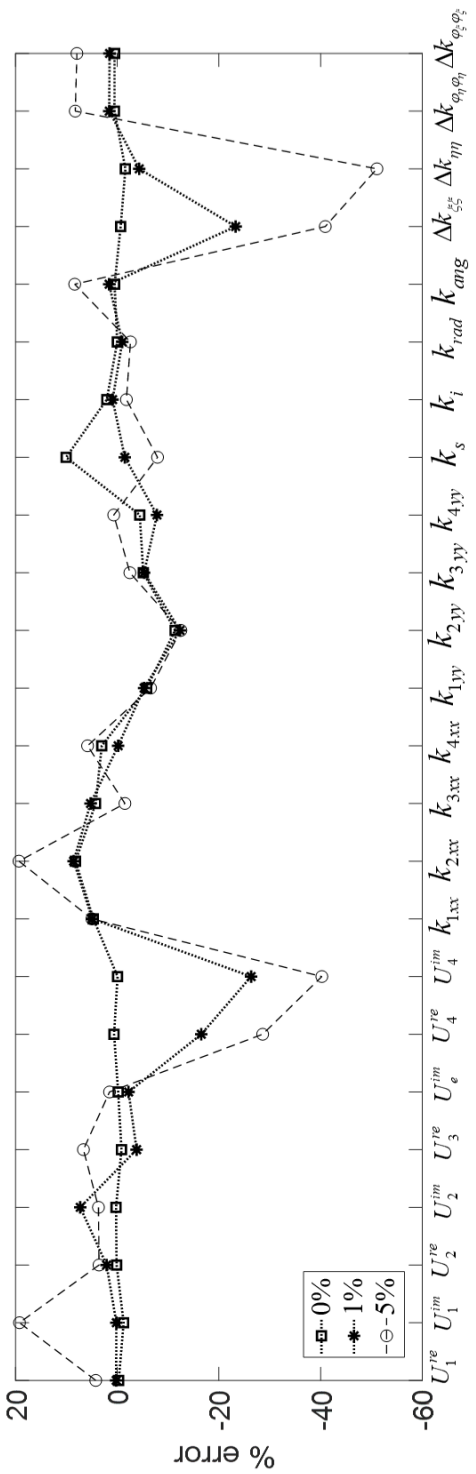

Figure 4-29 Sensitivity of unknown parameters obtained from multiple speeds to measurement noise

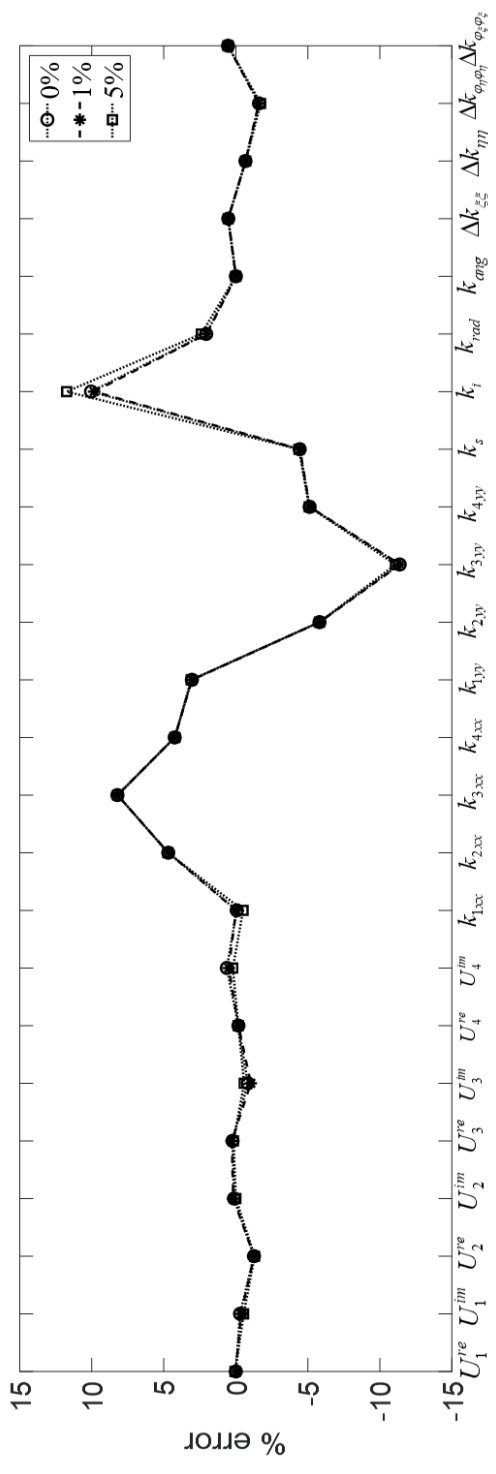

Figure 4-28 Sensitivity of identifiable parameters obtained from multiple speeds to modeling bias

4.4 Concluding Remarks

In the present chapter, the mathematical model of turbine-generator with auxiliary AMBs is developed using Timoshenko beam finite elements. The mathematical model of coupling in the presence of parallel and angular misalignments has been developed from the vector of static deflections at coupling nodes, unlike the previous chapters where it was developed from the static deflections at the disc locations. The present model is based on weight dominance and is applicable for both rigid and flexible couplings. The steering function is chosen in such a way that full spectra obtained from the numerical simulation look similar to the experimental spectra. The correlation between misalignment direction and ACS coefficients has been explained. A Simulink model that generates time domain vibration and current data is built from the global EOM.The effect of incorporating AMB by way of amplitude reduction and shift in the peaks of coupled rotor system is shown.

The global EOM is converted into frequency domain and has been rearranged in the form that can be solved by linear least-squares regression. The magnitude and phase of the positive and negative harmonics of the vibration at the master DOFs and the AMB current have been estimated from full spectrum plots. This data is input to the identification algorithm to estimate the unknown parameters of the rotor, bearing, AMB and coupling. The accuracy of solution is improved by considering cumulative data from multiple speeds. It has been found that data from multiple speeds yields better estimates compared to those obtained from individual speeds. The algorithm yielded reasonably correct estimates when signal is contaminated with measurement noise and modelling bias up to 5%. The magnitude of ACS coefficients, which depend on the amount of misalignment present between bearing centers are identified to fairly accurate degree using the present algorithm. The deviation of parameters estimated in the present chapter from their assumed values is more than that exhibited by the corresponding parameters of the previous chapters.

The identification algorithm, which is the outcome of the study, can be used in physical experiments. It takes amplitudes and phases of various harmonics of vibration and current as inputs and estimates ACS coefficients. They can in turn be used to estimate the fluctuating forces and moments. That way the misalignment condition in coupling between the rotors can be studied using the identification algorithm.

The identification algorithm developed in the present chapter considers data from both translational DOFs and rotational DOFs. The rotational DOFs which correspond to the both ends of coupling may pose more difficulty in data acquisition than translational DOFs. To get round this problem another stage of condensation is performed in Chapter 5. Also the present mathematical model is extended to TGs that run on speed-dependent journal bearings and AMB *support* bearings in Chapter 5.

CHAPTER 5

Finite Element Modelling, Analysis and Identification of Speed dependent Misalignment in Coupled Rotor-Bearing-AMB Systems

5.1 Introduction

In Chapter 4, finite element modelling, analysis and identification of misalignment in TGs supported on rolling element bearings with auxiliary AMBs is presented. The mathematical model of coupling subjected to both parallel and angular misalignments was developed using weight dominance criteria. The present chapter extends the work to TGs supported on speed-dependent tilting pad journal bearings (TPJB) and AMB support bearings. In the presence of speed-dependent excitations, AMBs exhibit speed-dependent behaviour. The stiffness and damping of TPJBs, ACS coefficients of coupling, displacement and current constants of AMB are modelled as speed-dependent parameters. The identification of these parameters is performed using an identification algorithm that has been developed from the condensed global EOMs in frequency domain. The algorithm developed in the present chapter uses only translational DOFs at the nodal locations. Speed dependent parameters at six different speeds have been identified. The robustness of algorithm is tested against various levels of measurement noise and modelling bias.

5.2 System Configuration

The model of a TG running up to multiple stages supported on TPJBs and AMBs is shown in Figure 4-1. In Pilotto et al. (2017) AMB was used as support bearing in a Turbo generator along with TPJBs. To simulate that case AMB was used as support bearings at two locations in place of TPJBs. The intermediate couplings that transmit drive from one rotor stage to the next is subject to misalignment. This causes the coupling to develop static and time-varying additive stiffness coefficients (Lees, 2007). The mathematical model of each sub system is discussed next.

5.3 Mathematical Model

5.3.1 Tilting Pad Journal Bearings

This section deals with finite element analysis of a multi-stage turbogenerator model connected by intermediate couplings, supported on tilting pad journal bearings (TPJB) and active magnetic bearings (AMB).

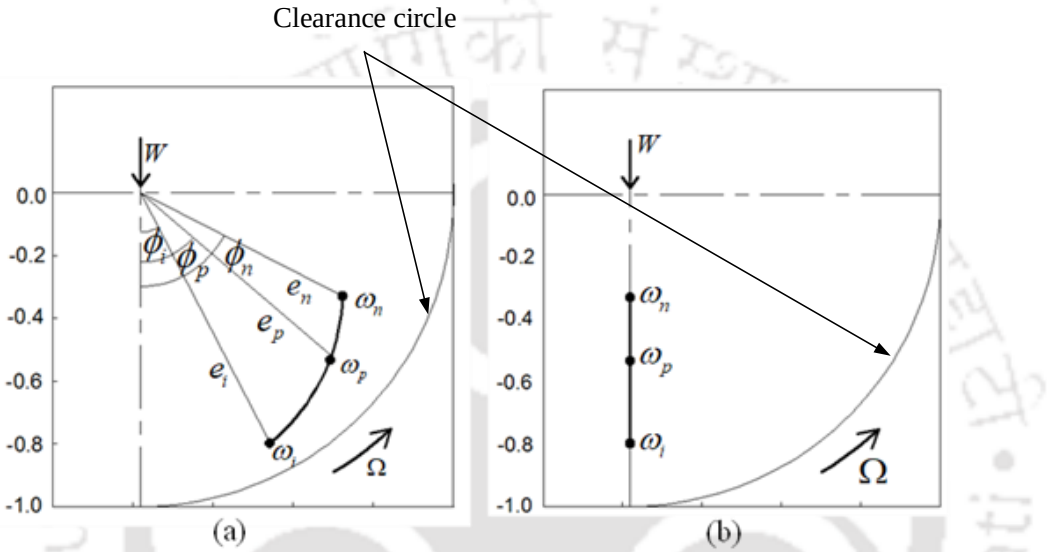

Figure 5-1 Journal equilibrium loci for (a) JB (b) TPJB

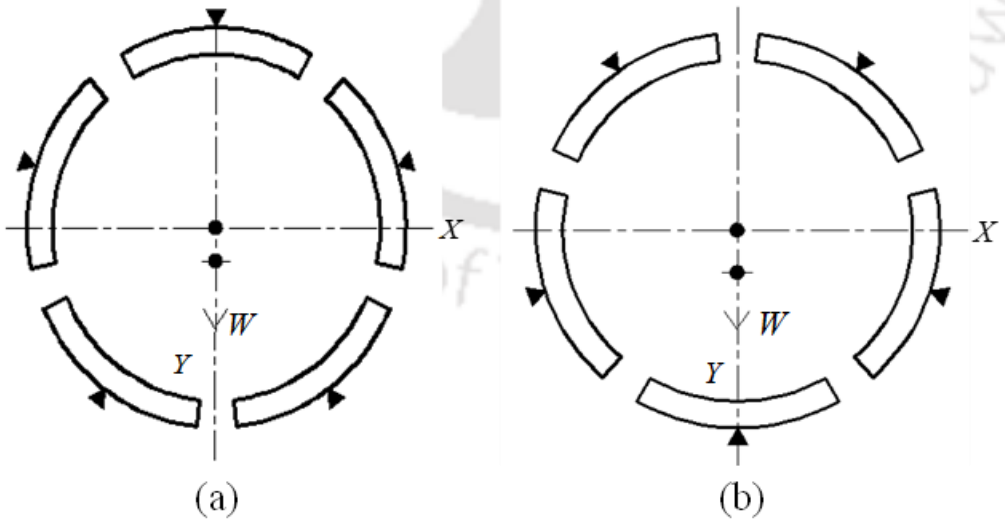

Figure 5-2 TPJB (a) load between pivot (b) load on pivot

For modelling shafts and discs, the elemental matrices given in Chapter 4 are used. The fundamental difference between a JB and a TPJB is explained now. Figure 5-1(a) is the

pictorial representation of the loci of the journal equilibrium position at various speeds $\omega_i, \omega_p, \omega_n$. Attitude angle ϕ_i is the angle between load direction and the line of centers, and is a function of rotational speed, ω, and static load, W. For a given static load and at a given rotor speed, the equilibrium position of journal is defined by journal eccentricity e and attitude angle ϕ_i. It can be seen that the attitude angles are non-zero at each speed. This generates a positive tangential force which produces non-zero cross-coupled coefficients which in turn give rise to *half-frequency whirl* instability at twice the first critical speed of the rotor. From the rotor stability point of view, the zero attitude angle is the most desirable configuration at all speeds (Chen and Gunter, 2007). When it comes to TPJBs the pads are supported on pivots, which can be either rigid or flexible. The pads can tilt on the pivots independently of one another in response to rotor motion. This causes the attitude angle to be zero at all speeds as shown in Figure 5-1(b), which is the cause of their inherent stability. Figure 5-2 shows a typical TPJB with five pads. The parameters which affect the stiffness and damping of TPJBs are operating speed, number of pads, pad length, pad diameter, load configuration (load on pivot (*lop*) / load between pivot (*lbp*)), load angle, preload, clearance, pivot flexibility and oil viscosity (Chen and Gunter, 2007). At a *given* speed ω the complex bearing dynamic forces due to stiffness and damping are given by (Chen and Gunter, 2007).

$$dF(\omega) = -\begin{bmatrix} k_{xx}(\omega) & 0 \\ 0 & k_{yy}(\omega) \end{bmatrix}\begin{Bmatrix} x \\ y \end{Bmatrix} - \begin{bmatrix} c_{xx}(\omega) & 0 \\ 0 & c_{yy}(\omega) \end{bmatrix}\begin{Bmatrix} \dot{x} \\ \dot{y} \end{Bmatrix} \tag{5.1}$$

The translational displacements are rewritten in terms of complex displacements as $x = (u+\bar{u})/2$, $y = -\mathrm{j}(u-\bar{u})/2$, where $u = x + \mathrm{j}y$, $\bar{u} = x - \mathrm{j}y$. Equation (4.52) then takes the following complex form

$$dF(\omega) = -0.5\begin{bmatrix} k_{xx}(\omega) & 0 \\ 0 & k_{yy}(\omega) \end{bmatrix}\begin{Bmatrix} u+\bar{u} \\ -j(u-\bar{u}) \end{Bmatrix} - \begin{bmatrix} c_{xx}(\omega) & 0 \\ 0 & c_{yy}(\omega) \end{bmatrix}\begin{Bmatrix} \dot{u}+\dot{\bar{u}} \\ -j(\dot{u}-\dot{\bar{u}}) \end{Bmatrix} \tag{5.2}$$

where $k_{xx}(\omega), k_{yy}(\omega)$, $c_{xx}(\omega), c_{yy}(\omega)$ are the direct stiffness and damping of TPJB in x and y directions. Since the attitude angle is zero in Figure 5-1(b), the cross-coupled coefficients are zero in TPJBs. For the *lbp* configuration (Figure 5-2(a)), the load is shared equally by the two bottom pads ($k_{xx}(\omega) = k_{yy}(\omega)$) and for the *lop* configuration

(Figure 5-2(b)), the majority of the load is felt totally by the bottom most pad ($k_{xx}(\omega) \neq k_{yy}(\omega)$) (Chen and Gunter, 2007).

5.3.2 Speed Dependent Active Magnetic Bearings

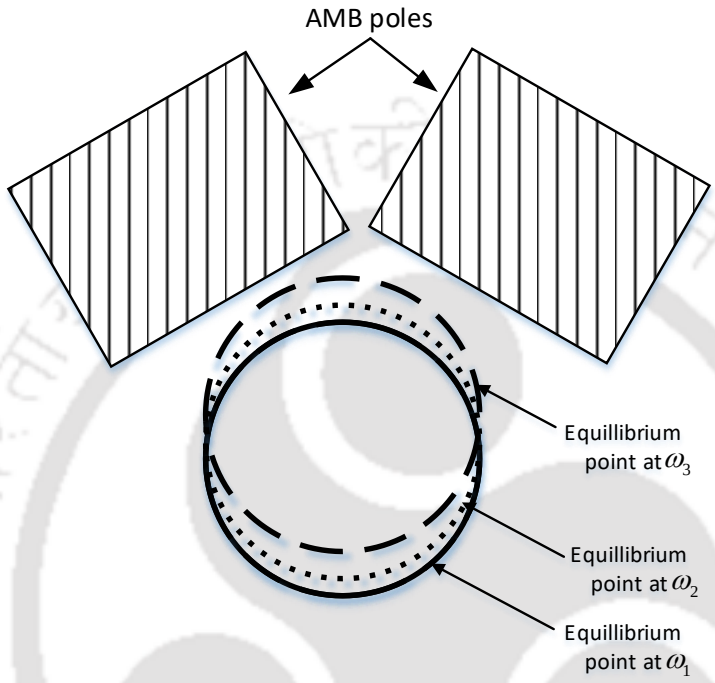

Figure 5-3 Operating point of rotor at various speeds inside AMB clearance

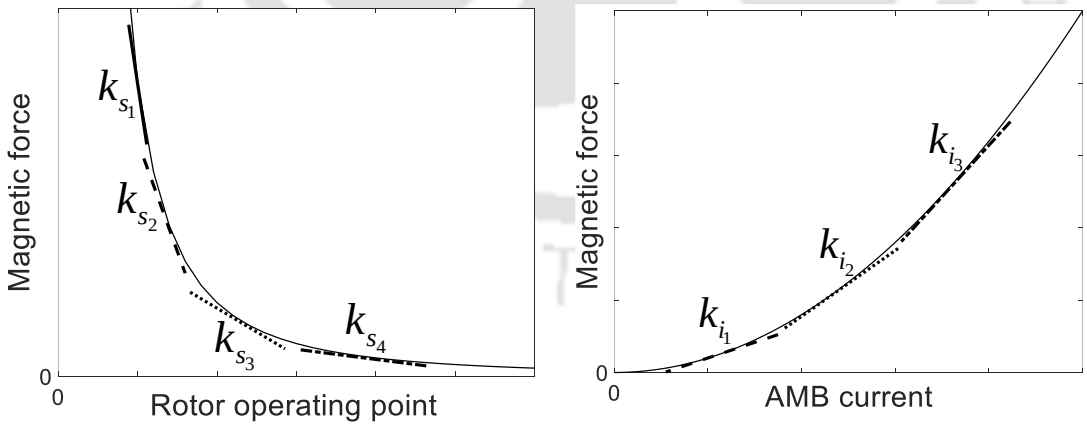

Figure 5-4 (a) AMB force versus operating point (b) AMB force versus AMB current

The control force exerted by AMBs is given by Tiwari (2017)

$$\mathbf{f}_{AMB} = -k_s \mathbf{u}_{AMB} + k_i \mathbf{i}_c \tag{5.3}$$

with $k_s = 4c_1 i_b^2 / l_g^3$ is the AMB displacement constant; $k_i = 4c_1 i_b^2 / l_g^3$ is the AMB current constant; i_b is the bias current; l_g is the airgap; $c_1 = 0.25\mu_0 N^2 A_g$; μ_0 is the free space permeability; N is the actuator windings; A_g is the leg area; and $\mathbf{u}_{AMB}$ is the complex displacement of rotor at AMB location. The control current in AMB coils controlled by proportional-integral-derivative (PID) law is given by

$$\mathbf{i}_c = k_P \mathbf{u}_{AMB} + k_I \int \mathbf{u}_{AMB} dt + k_D \dot{\mathbf{u}}_{AMB} \tag{5.4}$$

where k_P, k_I and k_D are the proportional, integral and derivative gains, respectively. Due to the speed-dependent nature of unbalance and misalignment forces there will be a shift in the equilibrium position of rotor within the AMB clearance about the geometric center line with the change in rotor speed (Figure 5-3). Figure 5-4(a) shows nonlinear nature of *magnetic force versus operating point* curve. Each point on the curve corresponds to a discrete rotor speed. As the operating speed of rotor changes the operating point shifts and there is a corresponding change in slope of the curve (k_s). This leads to a change in the AMB current required, which in turn causes a shift in the slope of the curve (k_i) in Figure 5-4(b). Thus stiffness constants of AMB, which are otherwise not varying, change due to the disturbances that vary with operating speed. Thus in the presence of external forces, such as unbalance and misalignment, it would be practical to rewrite as

$$\mathbf{f}_{AMB}(\omega) = -k_s(\omega)\mathbf{u}_{AMB} + k_i(\omega)\mathbf{i}_c \tag{5.5}$$

The speed dependent nature of AMB force is the result of vibratory motion of rotor excited due to speed-dependent forces, such as unbalance and misalignment.

5.3.3 Mathematical Model of Misaligned Coupling

Since the rotor is supported on TPJBs and AMBs, whose parameters are speed-dependent, for a given amount of misalignment, the forces and moments acting on coupling too change with speed (Kuppa and Lal, 2020) with the result that ACS coefficients too would become speed dependent, while the SCS coefficients would remain constant. The detailed derivation for the coupling force vectors $\mathbf{f}_{SCS}$ and $\mathbf{f}_{ACS}$ in the presence of parallel and angular misalignments is given in Chapter 4. The final form of speed-dependent SCS force

vector for a symmetric coupling with no cross-coupling stiffness coefficients $\mathbf{f}_{SCS}$ is given by

$$\mathbf{f}_{SCS} = \begin{bmatrix} k_{rad} & 0 & -k_{rad} & 0 \\ 0 & k_{ang} & 0 & -k_{ang} \\ -k_{rad} & 0 & k_{rad} & 0 \\ 0 & -k_{ang} & 0 & k_{ang} \end{bmatrix} \begin{Bmatrix} u_c \\ \varphi_c \\ u_{c+1} \\ \varphi_{c+1} \end{Bmatrix} \tag{5.6}$$

The final form of speed-dependent ACS force vector of coupling in complex form is as follows

$$\mathbf{f}_{ACS}(\omega) = 0.5 \begin{Bmatrix} \left(\delta x_c - \delta x_{c+1}\right)\left(\Delta k^{\omega}_{\xi\xi} \sum_{i=-n}^{i+n} p_i e^{\mathrm{j}i\omega t} + \Delta k^{\omega}_{\eta\eta} \sum_{i=-n}^{i+n} q_i e^{\mathrm{j}i\omega t} \right) \\ \left(\delta \varphi_{y_c} - \delta \varphi_{y_{c+1}}\right)\left(\Delta k^{\omega}_{\varphi_\xi\varphi_\xi} \sum_{i=-n}^{i+n} r_i e^{\mathrm{j}i\omega t} + \Delta k^{\omega}_{\varphi_\eta\varphi_\eta} \sum_{i=-n}^{i+n} s_i e^{\mathrm{j}i\omega t} \right) \\ \left(\delta x_{c+1} - \delta x_c\right)\left(\Delta k^{\omega}_{\xi\xi} \sum_{i=-n}^{i+n} p_i e^{\mathrm{j}i\omega t} + \Delta k^{\omega}_{\eta\eta} \sum_{i=-n}^{i+n} q_i e^{\mathrm{j}i\omega t} \right) \\ \left(\delta \varphi_{y_{c+1}} - \delta \varphi_{y_c}\right)\left(\Delta k^{\omega}_{\varphi_\xi\varphi_\xi} \sum_{i=-n}^{i+n} r_i e^{\mathrm{j}i\omega t} + \Delta k^{\omega}_{\varphi_\eta\varphi_\eta} \sum_{i=-n}^{i+n} s_i e^{\mathrm{j}i\omega t} \right) \end{Bmatrix} \tag{5.7}$$

The type and level of misalignment is reflected in the magnitudes of ACS coefficients. A parametric study by varying both these parameters can be made in experimental work.

5.3.4 Global Equation of Motion

The complex form of global EOMs of the TG system in the presence of unbalance force, AMB force and ACS force is given by

$$\left(\mathbf{M}_{sh} + \mathbf{M}_d\right)\ddot{\mathbf{u}} + \left[\mathbf{C}_b(\omega) + \mathbf{C}_c + \mathbf{C}_{sh} - \mathrm{j}\omega(\mathbf{G}_{sh} + \mathbf{G}_d)\right]\dot{\mathbf{u}} + \left(\mathbf{K}_b(\omega) + \mathbf{K}_{scs} + \mathbf{K}_{sh}\right)\mathbf{u} = \mathbf{f}_{unb} + \mathbf{f}_{AMB}(\omega) - \mathbf{f}_{ACS}(\omega) \tag{5.8}$$

The elemental matrices of shaft and disc used in Eqn. (5.8) are given in **Appendix D**. The assumed solution to Eqn. (5.8) is of following form

$$\mathbf{u}_m = \sum_{i=-\infty}^{i=+\infty} \bar{\mathbf{u}}_m e^{\mathrm{j}i\omega t} \tag{5.9}$$

The complex current vector $\mathbf{i}_c$ of AMB in Eqn. (5.5) too will have the same multi-harmonic nature as rotor displacement, as

$$\mathbf{i}_c = \sum_{i=-\infty}^{i=+\infty} \bar{\mathbf{i}}_c e^{\mathrm{j}i\omega t} \tag{5.10}$$

The force vectors, on the right side of Eqn. (5.8) are given by $\mathbf{f}_{unb} = \bar{\mathbf{f}}_{unb} e^{i\omega t}$; $\mathbf{f}_{AMB}(\omega) = \bar{\mathbf{f}}_{AMB}(\omega) e^{\mathrm{j}i\omega t}$; $\mathbf{f}_{ACS} = \bar{\mathbf{f}}_{ACS}(\omega) e^{\mathrm{j}i\omega t}$

Substituting Eqns. (5.9) and (5.10) in Eqn. (5.8) converts global EOM in time domain to frequency domain, as

$$\left(-\mathbf{M}(i\omega)^2 + \mathrm{j}(i\omega)(\mathbf{C} - \mathrm{j}\omega\mathbf{G}) + \mathbf{K}\right)\bar{\mathbf{u}} = \bar{\mathbf{f}}_{unb} + \bar{\mathbf{f}}_{AMB}(\omega) - \bar{\mathbf{f}}_{ACS}(\omega) \tag{5.11}$$

with

$$\mathbf{M} = \mathbf{M}_{sh} + \mathbf{M}_d; \quad \mathbf{C} = \mathbf{C}_b(\omega) + \mathbf{C}_c + \mathbf{C}_{sh}; \quad \mathbf{G} = \mathbf{G}_{sh} + \mathbf{G}_d; \quad \mathbf{K} = \mathbf{K}_b(\omega) + \mathbf{K}_{scs} + \mathbf{K}_{sh}$$

The development of global EOMs of TG in time domain and conversion to frequency domain is discussed in the present section. The next section discusses the condensation of EOMs, which is required for the development of identification algorithm.

5.3.5 Application of Condensation Schemes

The nodes where the external forces act on the rotor system are usually chosen as master DOFs. In the present case, the master DOFs correspond to the nodal locations of *all identifiable parameters.* They include the translational DOFs at the nodal locations of TJBs, discs, coupling, AMBs and rotational DOFs at coupling nodes. Rest of the DOFs are grouped as slave DOFs, as

$$\begin{aligned}\mathbf{u}_m = \{ & u_{AMB_1} \quad u_{d_1} \quad u_{d_2} \quad u_{TPJB_1} \quad u_{c_1} \quad \varphi_{c_1} \quad u_{c_2} \quad \varphi_{c_2} \quad u_{TPJB_2} \quad u_{d_3} \quad u_{d_4} \quad u_{AMB_2} \\ & \ldots \quad u_{AMB_{n-1}} \quad u_{d_{n-1}} \quad \ldots \quad u_{c_{n-1}} \quad \varphi_{c_{n-1}} \quad u_{c_n} \quad \varphi_{c_n} \quad \ldots \quad u_{TPJB_n} \quad u_{d_n} \; u_{AMB_n} \}^T\end{aligned} \tag{5.12}$$

The derivation of the transformation matrix $\mathbf{T}^d$, which links master DOFs to the total DOFs, is given in Kuppa and Lal (2020) and is expressed as

$$\mathbf{u} = \begin{Bmatrix} \mathbf{u}_m \\ \mathbf{u}_s \end{Bmatrix} = \mathbf{T}^d \mathbf{u}_m \tag{5.13}$$

where

$$\mathbf{T}^d = \begin{Bmatrix} \mathbf{I} \\ -[\mathbf{K}_{ss} - \omega_0^2 \mathbf{M}_{ss} - \mathrm{j}\omega_0^2 \mathbf{G}_{ss}]^{-1}[\mathbf{K}_{sm} - \omega_0^2 \mathbf{M}_{sm} - \mathrm{j}\mathbf{G}_{sm}] \end{Bmatrix} \tag{5.14}$$

In Eqn. (5.14) ω_0 is the discrete speed at which dynamic condensation is performed. EOMs in terms of reduced coordinates is given by

$$\left(-\mathbf{M}^d (i\omega)^2 + \mathrm{j}(i\omega)\left(\mathbf{C}^d - \mathrm{j}\omega\mathbf{G}^d\right) + \mathbf{K}^d\right)\bar{\mathbf{u}}_m = \bar{\mathbf{f}}_{unb}^d + \bar{\mathbf{f}}_{AMB}^d(\omega) - \bar{\mathbf{f}}_{ACS}^d(\omega) \tag{5.15}$$

with

$$\mathbf{M}^d = \left(\mathbf{T}^d\right)^T \mathbf{M}\mathbf{T}^d; \quad \mathbf{K}^d = \left(\mathbf{T}^d\right)^T \mathbf{K}\mathbf{T}^d; \quad \mathbf{C}^d = \left(\mathbf{T}^d\right)^T \mathbf{C}\mathbf{T}^d; \quad \mathbf{G}^d = \left(\mathbf{T}^d\right)^T \mathbf{G}\mathbf{T}^d$$

$$\mathbf{f}_{unb}^d = \left(\mathbf{T}^d\right)^T \mathbf{f}_{unb}; \quad \mathbf{f}_{AMB}^d(\omega) = \left(\mathbf{T}^d\right)^T \mathbf{f}_{AMB}(\omega); \quad \mathbf{f}_{ACS}^d(\omega) = \left(\mathbf{T}^d\right)^T \mathbf{f}_{ACS}(\omega);$$

The superscript d refers to the dynamically reduced form of matrices and vectors. Among all the master DOFs given by Eqn. (5.12), the rotational DOFs of coupling $\varphi_{c_1}, \varphi_{c_2}, \ldots, \varphi_{c_n}$, which are linked to k_{ang}, $\Delta k_{R\xi}$ and $\Delta k_{R\eta}$ are difficult to measure experimentally. Hence, another stage of reduction called *hybrid* condensation (Lal and Tiwari, 2012) is performed by grouping these DOFs as slave DOFs. The condensation procedure is similar to the one followed for dynamic condensation, as

$$\mathbf{u}_d = \begin{Bmatrix} \mathbf{u}_h \\ \mathbf{u}_{hs} \end{Bmatrix} = \mathbf{T}^h \mathbf{u}_h \tag{5.16}$$

The transformation matrix used to perform the reduction is given by

$$\mathbf{T}^h = \begin{Bmatrix} \mathbf{I} \\ -[\mathbf{K}_{ss}^d - \omega_0^2 \mathbf{M}_{ss}^d - \mathrm{j}\omega_0^2 \mathbf{G}_{ss}^d]^{-1}[\mathbf{K}_{sm}^d - \omega_0^2 \mathbf{M}_{sm}^d - \mathrm{j}\mathbf{G}_{sm}^d] \end{Bmatrix} \tag{5.17}$$

The global EOMs written in terms of hybrid DOFs is of the form

$$\left(-\mathbf{M}^h (i\omega)^2 + \mathrm{j}(i\omega)\left(\mathbf{C}^h - \mathrm{j}\omega\mathbf{G}^h\right) + \mathbf{K}^h\right)\bar{\mathbf{u}}_h = \mathbf{f}_{unb}^h + \mathbf{f}_{AMB}^h(\omega) - \mathbf{f}_{ACS}^h(\omega) \tag{5.18}$$

where

$$\mathbf{M}^h = \left(\mathbf{T}^h\right)^T \mathbf{M}^d \mathbf{T}^h; \quad \mathbf{K}^h = \left(\mathbf{T}^h\right)^T \mathbf{K}^d \mathbf{T}^h; \quad \mathbf{C}^h = \left(\mathbf{T}^h\right)^T \mathbf{C}^d \mathbf{T}^h; \quad \mathbf{G}^h = \left(\mathbf{T}^h\right)^T \mathbf{G}^d \mathbf{T}^h$$

$$\mathbf{f}_{unb}^h = \left(\mathbf{T}^h\right)^T \mathbf{f}_{unb}^d; \quad \mathbf{f}_{AMB}^h(\omega) = \left(\mathbf{T}^h\right)^T \mathbf{f}_{AMB}^d(\omega); \quad \mathbf{f}_{ACS}^h(\omega) = \left(\mathbf{T}^h\right)^T \mathbf{f}_{ACS}^d(\omega)$$

The global EOMs is rewritten in terms of translational DOFs, which can be obtained from proximity probes on TG sets. The development of algorithm is explained in the next section.

5.3.6 Identification Algorithm for Parameter Estimation

Eqn. (5.18) can be rearranged by relocating all the unknown parameters (disc unbalance, coupling static and additive stiffness coefficients, TPJB stiffness and damping, and AMB constants) to the right side in the following form

$$\begin{aligned}\left(-\mathbf{M}^h (i\omega)^2 + \mathrm{j}(i\omega)\left(\mathbf{C}_{sh+c}^h - \mathrm{j}\omega\mathbf{G}^h\right) + \mathbf{K}_{sh}^h\right)\bar{\mathbf{u}}_h \\ = \bar{\mathbf{f}}_{unb}^h - \bar{\mathbf{f}}_{SCS}^h + \bar{\mathbf{f}}_{AMB}^h(\omega) - \mathbf{f}_{ACS}^h(\omega) - \bar{\mathbf{f}}_{brgk}^h(\omega) - \bar{\mathbf{f}}_{brgc}^h(\omega)\end{aligned} \tag{5.19}$$

At a given speed ω the above equation can be partitioned as

$$\left\{\mathbf{A}_{unb} \quad \mathbf{A}_{SCS} \quad \mathbf{A}_{ACS}(\omega) \quad \mathbf{A}_{TPJB}(\omega) \quad \mathbf{A}_{AMB}(\omega)\right\} \begin{Bmatrix} \mathbf{x}_{unb} \\ \mathbf{x}_{SCS} \\ \mathbf{x}_{ACS}(\omega) \\ \mathbf{x}_{TPJB}(\omega) \\ \mathbf{x}_{AMB}(\omega) \end{Bmatrix} = \mathbf{b}(\omega) \tag{5.20}$$

where

$$\mathbf{x}_{unb} = \left\{U_1^{re} \quad U_1^{im} \quad U_2^{re} \quad U_2^{im} \quad U_3^{re} \quad U_3^{im} \quad U_4^{re} \quad U_4^{im}\right\}^T$$

$$\mathbf{x}_{SCS} = \left\{k_{rad} \quad k_{ang}\right\}^T$$

$$\mathbf{x}_{TPJB}(\omega) = \left\{k_{TPJB_1}(\omega) \quad k_{TPJB_2}(\omega) \quad c_{TPJB_1}(\omega) \quad c_{TPJB_2}(\omega)\right\}^T$$

$$\mathbf{x}_{AMB}(\omega) = \left\{k_s(\omega) \quad k_i(\omega)\right\}^T$$

$$\mathbf{x}_{ACS}(\omega) = \left\{\Delta k_{\eta\eta}(\omega) \quad \Delta k_{\eta\eta}(\omega) \quad \Delta k_{\varphi_\eta\varphi_\eta}(\omega) \quad \Delta k_{\varphi_\xi\varphi_\xi}(\omega)\right\}^T$$

Speed dependent parameters at n different speeds can be estimated by calculating matrix $\mathbf{A}$ and vector $\mathbf{b}$ for each of the n speeds of interest, as

$$\begin{bmatrix} \mathbf{A}(\omega_1) & 0 & 0 & 0 \\ 0 & \mathbf{A}(\omega_2) & 0 & 0 \\ \vdots & \vdots & \vdots & \vdots \\ 0 & 0 & 0 & \mathbf{A}(\omega_n) \end{bmatrix} \begin{Bmatrix} \mathbf{x}(\omega_1) \\ \mathbf{x}(\omega_2) \\ \vdots \\ \mathbf{x}(\omega_n) \end{Bmatrix} = \begin{Bmatrix} \mathbf{b}(\omega_1) \\ \mathbf{b}(\omega_2) \\ \vdots \\ \mathbf{b}(\omega_n) \end{Bmatrix} \tag{5.21}$$

The inputs to Eqns. (5.19) and (5.20) are the real and imaginary parts of complex displacements at measurement locations on rotors ($\bar{\mathbf{u}}_h^{re}$, $\bar{\mathbf{u}}_h^{im}$) and complex currents at AMB locations ($\bar{\mathbf{i}}^{re}$, $\bar{\mathbf{i}}^{im}$) obtained from full spectrum plots.

$$\bar{\mathbf{u}}_h = \bar{\mathbf{u}}_h^{re} + \mathrm{j}\bar{\mathbf{u}}_h^{im}; \qquad \bar{\mathbf{i}} = \bar{\mathbf{i}}^{re} + \mathrm{j}\bar{\mathbf{i}}^{im} \tag{5.22}$$

The discussion on the application of full spectrum is given in Chapter 2.

5.4 Results and Discussion

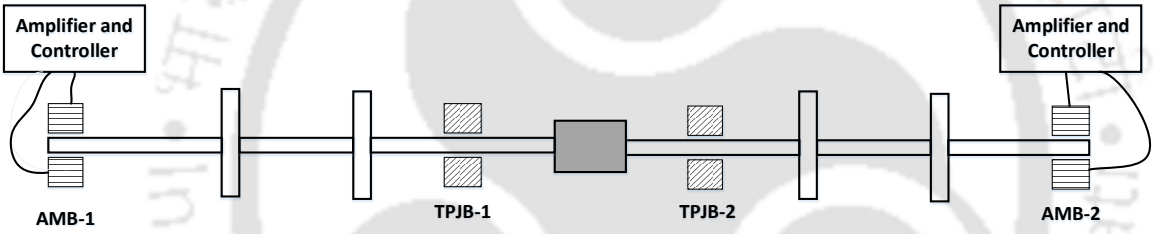

Figure 5-5 Coupled turbogenerator rotor system supported on TPJBs & AMBs

Table 5-1 Rotor and AMB specifications

Discs				
			Unbalance	
Mass, kg	Moment of inertia, kg-m^2		Amplitude, kg-m	Phase, rad
m_{d_1} = 2.25	I_{d_1} = 0.0024	I_{p_1} = 0.0048	e_1 = 4 x 10^{-5}	$\beta_1 = \pi/10$
m_{d_2} = 1.75	I_{d_2} = 0.0035	I_{p_2} = 0.007	e_2 = 3 x10^{-5}	$\beta_2 = \pi/4$
m_{d_3} = 2.5	I_{d_3} = 0.0045	I_{p_3} = 0.009	e_3 = 4 x10^{-5}	$\beta_3 = \pi/15$
m_{d_4} = 1.6	I_{d_4} = 0.004	I_{p_4} = 0.008	e_4 = 3 x10^{-5}	$\beta_4 = \pi/12$

Shaft		AMB		
d, m	l_e, m	k_p	12200	A/m
0.17	0.25	k_i	2000	A/(m-s)
		k_d	3	(A-s)/m

Table 5-2 Geometric properties of TPJB-1 and TPJB-2

Parameter	TPJB-1	TPJB-2
Length	14	20
Diameter	20	20
Clearance	100 µm	100 µm
No. of pads	4	4
Arc length	72	72
Pivot offset	0.5	0.5
Configuration	*lbp*	*lbp*

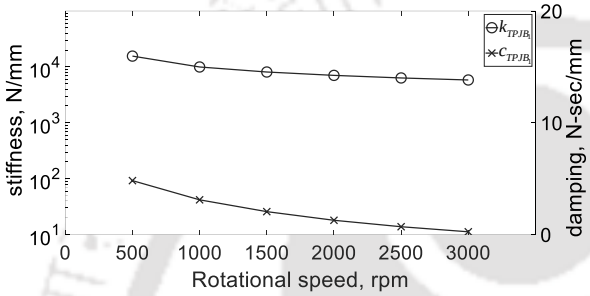

Figure 5-6 Speed-dependent k and c of TPJB-1

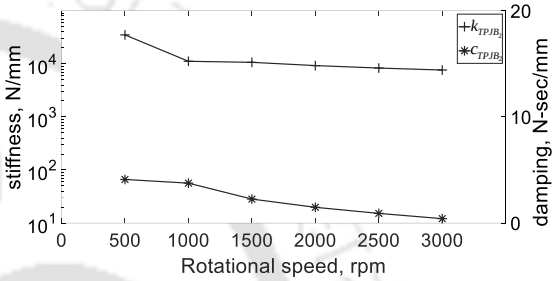

Figure 5-7 Speed-dependent k and c of TPJB-2

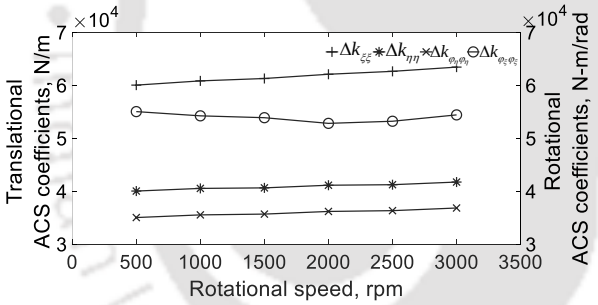

Figure 5-8 Speed-dependent ACS coefficients

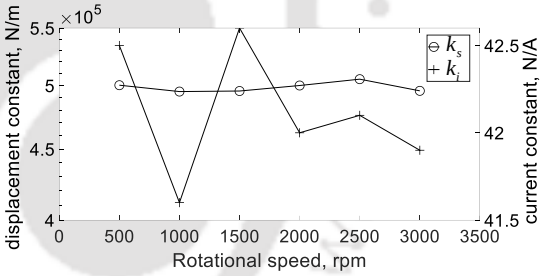

Figure 5-9 Speed-dependent AMB coefficients

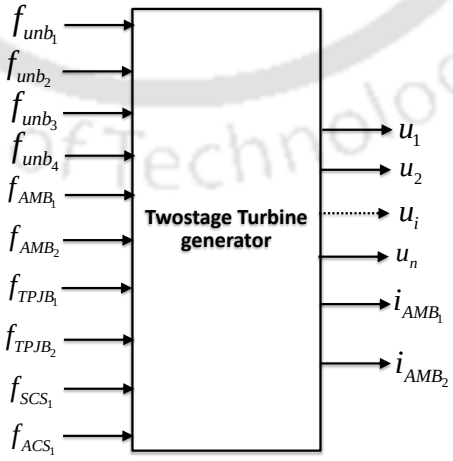

Figure 5-10 Representative Simulink model of two stage turbine generator

A representative turbogenerator running at 3000 rpm considered for numerical simulation is shown in Figure 5-5. Rotor-1 and rotor-2 each carry two rigid discs and are supported on AMBs at outboard locations and TPJBs at inboard locations. An intermediate coupling transmits the drive from rotor-1 to rotor-2. The properties of motor and drive end coupling are not included in the model. The properties of rotor, discs and AMB constants are shown in Table 5-1. The dimensions of TPJB-1 and TPJB-2 are given in Table 5-2. The stiffness and damping coefficients at six different speeds from 500 rpm to 3000 rpm generated in DyRoBeS© BePerf computer program are shown in Figure 5-6 and Figure 5-7. The assumed values of speed dependent ACS coefficients and AMB coefficients are shown in Figure 5-8 and Figure 5-9. The illustrative Simulink^{TM} model, as shown in Figure 5-10, is built using Eqn. (5.8) and it generates time domain signals of vibration of rotors and control currents in AMB coils in complex form. ODE15s which is a stiff solver is used to solve the global EOMs and the responses are logged for every $1/2^{16}$ seconds. The current orbits of AMB-1 and AMB-2 are shown in Figure 5-11. The elliptical nature of orbits are similar to those reported in the experimental results reported by Patel and Darpe (2009). Figure 5-12 shows full spectrum amplitude and phase plots of the AMB-1 and AMB-2 complex currents. The integer harmonics from -5 to +5 through 0 can be seen. This is similar to the FFT plots obtained from experimental data reported in Patel and Darpe (2009). This shows the suitability of the steering function $s(t)$ chosen for simulation.

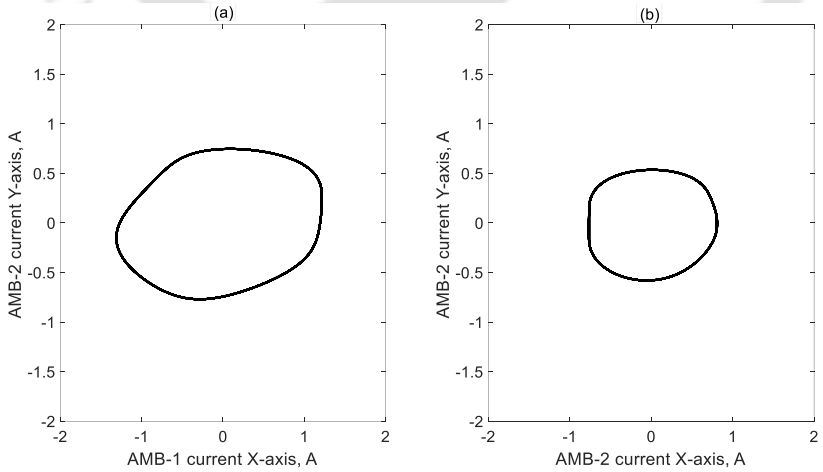

Figure 5-11 Complex current orbit of (a) AMB-1 (b) AMB-2

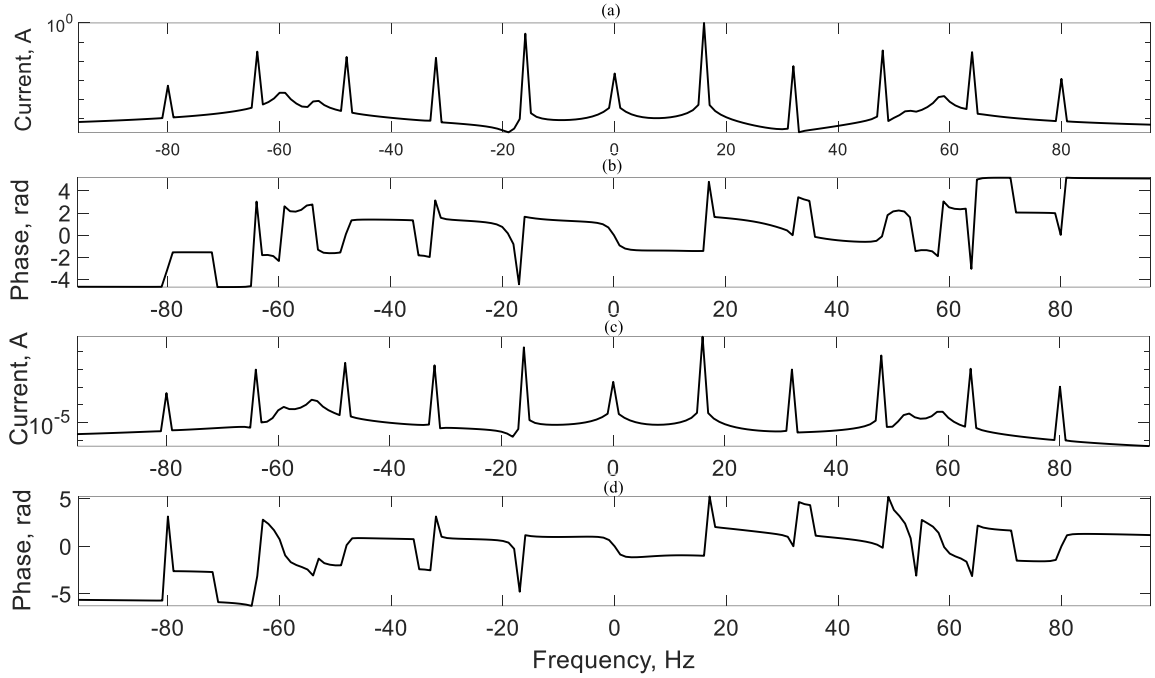

Figure 5-12 Full spectrum FFT of AMB1 (a) current amplitude (b) current phase ; AMB2 (c) current amplitude (d) current phase

The translational vibration data of rotor at two TPJBs, two AMBs, four discs and two coupling locations is acquired along with current data at the two AMBs. The real and imaginary parts of harmonics of this data is passed to the identification algorithm. At each of the six speeds (500 rpm, 1000 rpm, 1500 rpm, 2000 rpm, 250 rpm, 3000 rpm) a total of 20 parameters comprising of 8 unbalance parameters $(e_1\cos\beta_1, e_2\cos\beta_2, e_3\cos\beta_3, e_4\cos\beta_4, e_1\sin\beta_1, e_2\sin\beta_2, e_3\sin\beta_3, e_4\sin\beta_4)$, 4 TPJB parameters $(k_{TPJB_1}, c_{TPJB_1}, k_{TPJB_2}, c_{TPJB_2})$, 2 AMB parameters (k_s, k_i) and 6 coupling parameters $(k_{rad}, k_{ang}, \Delta k_{\xi\xi}, \Delta k_{\eta\eta}, \Delta k_{\varphi_\xi\varphi_\xi}, \Delta k_{\varphi_\eta\varphi_\eta})$ are estimated using linear least-squares problem from Eqn. (5.21). Figure 5-13(a) shows that the error in unbalance estimates is less than 3% with $e_3\sin\beta_3$ showing the highest deviation 2.8% at 3000 rpm. Among the bearing parameters shown in Figure 5-13(b), c_{TPJB_1} shows the highest deviation (2%) at 1500 rpm. Among coupling parameters shown in Figure 5-13(c), the maximum error is displayed by k_{ang} (-7%) at 2000 rpm. This is the result of hybrid condensation, wherein the angular displacements of coupling are made as the slave DOF. Among AMB parameters in Figure 5-13(d), k_s shows a highest deviation of 6.5% at 3000 rpm.

Table 5-3 Assumed values versus estimated values at 3000 rpm for 5% measurement noise

Parameter (units)	Assumed value	Estimated value	Error %
U_1^{re}, kg-m	1.33×10^{-4}	1.31×10^{-4}	-1.85
U_2^{re}, kg-m	8.49×10^{-5}	8.85×10^{-5}	4.27
U_3^{re}, kg-m	1.17×10^{-4}	1.17×10^{-4}	-0.44
U_4^{re}, kg-m	1.55×10^{-4}	1.56×10^{-4}	0.68
U_1^{im}, kg-m	4.33×10^{-5}	4.25×10^{-5}	-1.86
U_2^{im}, kg-m	8.49×10^{-5}	8.66×10^{-5}	2.11
U_3^{im}, kg-m	2.49×10^{-5}	2.63×10^{-5}	5.47
U_4^{im}, kg-m	4.14×10^{-5}	4.26×10^{-5}	2.96
k_{TPJB_1}, N/m	5830000	5903738	1.26
k_{TPJB_2}, N/m	7660000	7635603	-0.32
c_{TPJB_1}, N-sec/m	11200	11192	-0.07
c_{TPJB_2}, N-sec/m	12100	12131	0.25
k_s, N/m	495600	428749	-13.49
k_i, N/A	41.9	36	-12.95
k_{rad}, N/m	225000	224243	-0.34
k_{ang}, N-m/rad	200000	160492	-19.75
$\Delta k_{\xi\xi}$, N/m	63400	73409	15.79
$\Delta k_{\eta\eta}$, N/m	41700	43081	3.31
$\Delta k_{\varphi_\xi\varphi_\xi}$, N-m/rad	36800	37155	0.97
$\Delta k_{\varphi_\eta\varphi_\eta}$, N-m/rad	54380	53653	-1.34

Next a random noise of 5% is added to the vibration and current signals, and the estimation is performed again. From Figure 5-14 (a), it is seen that all the unbalance parameters show large deviation at all speeds with $e_2\cos\beta_2$ varying the highest (10% at 500 rpm). Likewise, the errors in bearing (Figure 5-14(b)), coupling (Figure 5-14 (c)) and AMB (Figure 5-14(d)) parameters due to 5% measurement noise are c_{TPJB_2} (4.5%) at 1500 rpm, k_{ang} (15%) at 1500 rpm, $\Delta k_{\xi\xi}$ (15%) at 3000 rpm and k_s (14.2%) at 3000 rpm, respectively.

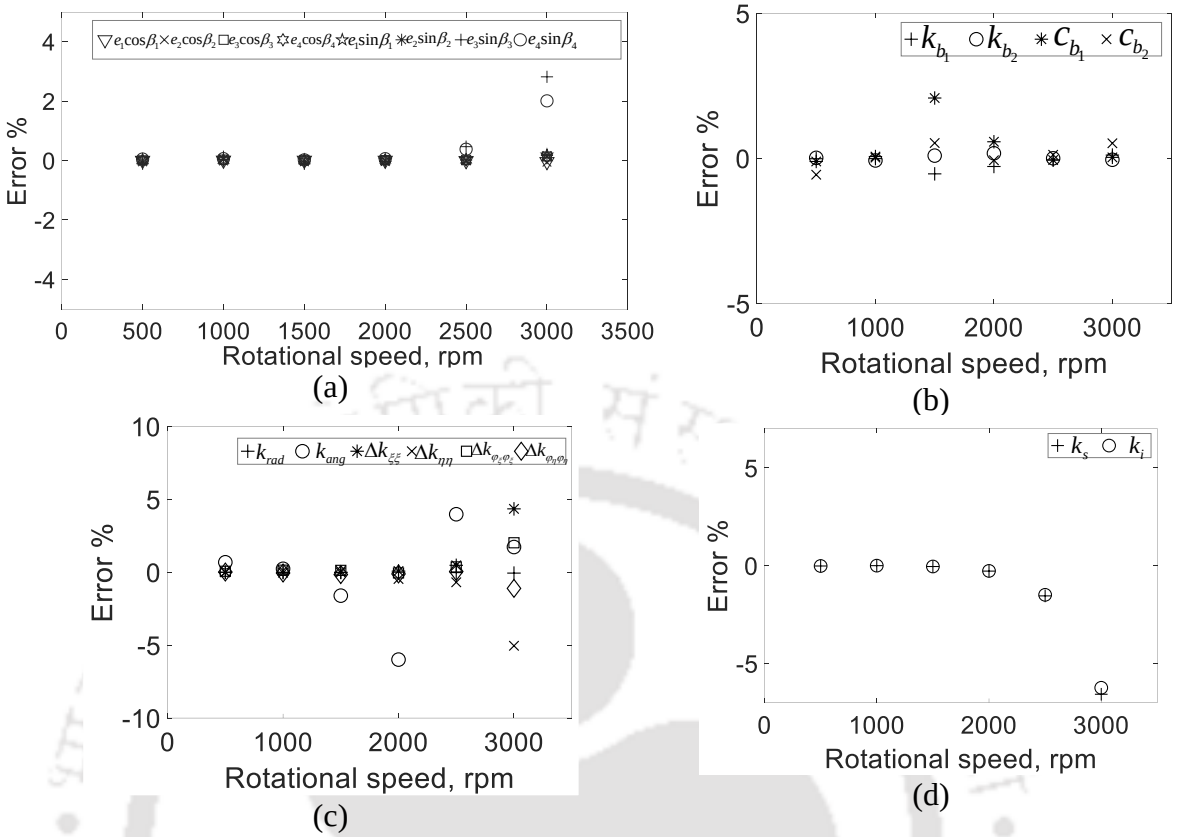

Figure 5-13 Error in estimates with 0% measurement noise in (a) unbalance of discs (b) speed dependent bearing parameters (c) speed dependent coupling parameters (d) speed dependent AMB parameters

Next the sensitivity of algorithm to modeling bias is examined. A 5% bias in $m_{d_1}, m_{d_2}, m_{d_3}, m_{d_4}$ and $\delta x_c, \delta x_{c+1}, \delta\varphi_{y_c}, \varphi_{y_{c+1}}$ is introduced. The maximum errors observed in various parameters (Figure 5-15) is $e_3 \sin\beta_3$ (2.5%) at 3000 rpm, c_{TPJB_1} (1.5%) at 1500 rpm, k_{ang} (-8%) at 2000 rpm, k_s (-6%) at 3000 rpm, respectively. The algorithm has shown more sensitivity to measurement noise than to bias in parameters. Nevertheless, the error in estimated parameters is less than 20% across all parameters which is within reasonable limits. The absolute values of estimated versus assumed parameters at 3000 rpm for the case of 5% measurement noise are shown in Table 5-3.

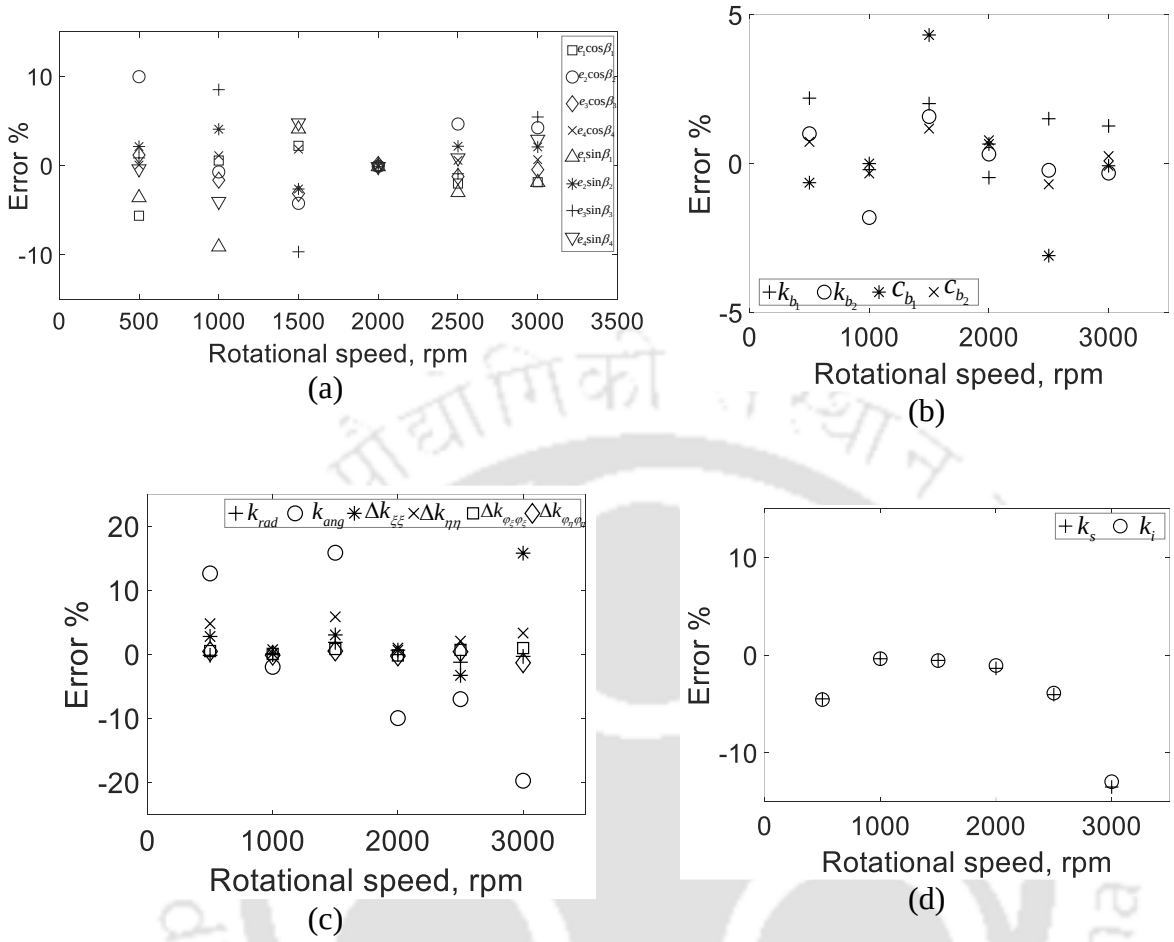

Figure 5-14 Error in estimates with 5% measurement noise in (a) unbalance of discs (b) speed dependent bearing parameters (c) speed dependent coupling parameters (d) speed dependent AMB parameters

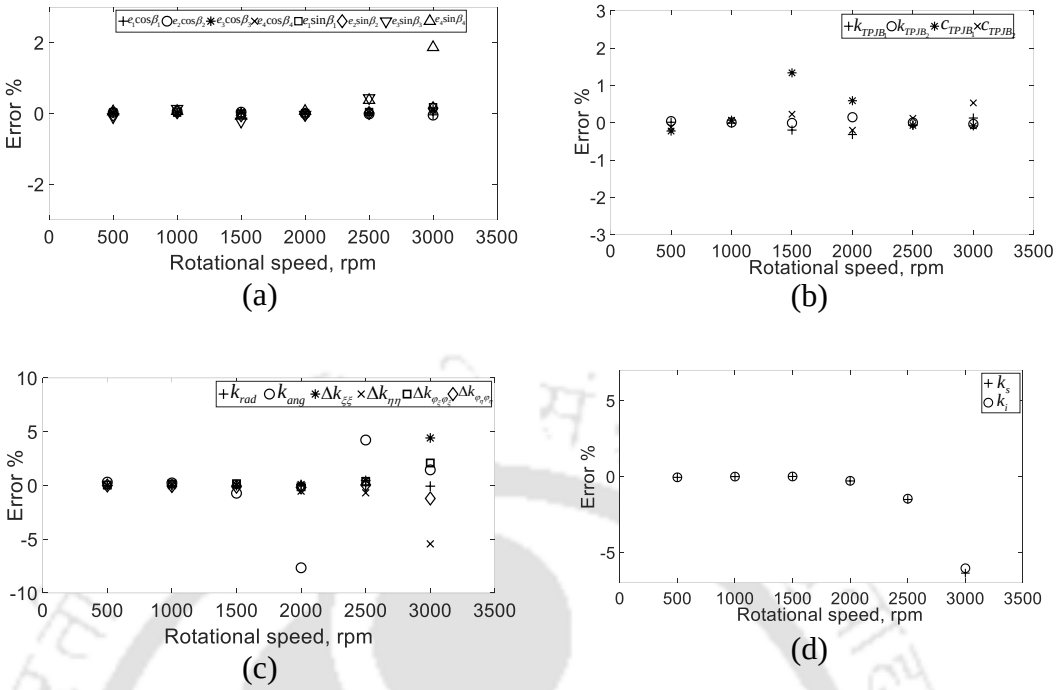

Figure 5-15 Error in estimates with 5% modelling bias (a) unbalance of discs (b) speed dependent bearing parameters (c) speed dependent coupling parameters (d) speed dependent AMB parameters

5.5 Concluding Remarks

In the present chapter, the finite element model of a TG supported on speed-dependent TPJBs and AMBs in the presence of combined misalignment is developed. The intermediate coupling stiffness has two components: an unchanging static and fluctuating additive stiffness. The mathematical model of coupling is developed based on weight dominance criteria, which is valid for heavy TG sets. A Simulink model is built to generate time domain data at various speeds. This data is used to plot the orbits and full spectrum plots, which showed behavior characteristic of misaligned rotors.

The global EOM has been first condensed using dynamic condensation and further level of hybrid condensation is performed by grouping the coupling rotational DOFs, which are difficult to experimentally measure, as slave DOFs. An identification algorithm is developed from frequency domain form of the condensed EOMs. The inputs to the algorithm are the real and imaginary components of various integer harmonics of vibration and current at the measurable locations obtained from full spectrum FFT.

The solution to the multivariate linear least-squares problem is sought at six different speeds, thereby yielding the unknown speed dependent system parameters, viz. stiffness and damping of TPJBs, static and additive stiffness of coupling, and AMB constants. Additionally, speed independent static coupling stiffness and disc unbalances are also estimated. The estimated values of the system parameters in the presence of noise and modeling bias showed reasonable level of error, thereby validating the robustness of identification algorithm.

In the next chapter the misaligned coupling model is extended to spline joints commonly used in gas turbine twin-spool rotor systems. The misalignment between bearing housings supporting compressor and turbine rotors in a gas turbine causes the spline joint to exhibit time varying stiffness. The modeling, analysis and identification of misalignment in twin spool rotors running at different speeds and mechanically connected by inter-shaft bearing is discussed in the next chapter.

CHAPTER 6

Identification of Spline Misalignment in Twin spool rotor - AMB Finite Element Systems connected by Intershaft bearing

6.1 Introduction

In Chapters 4 and 5, the mathematical model of coupling subjected to the parallel and angular mislaignments in a turbogenerator system is presented. In the present chapter, the mathematical model of an angularly misaligned spline joint in a dual rotor system (DRS) supported on rolling element bearings (REBs) and an active magnetic bearing (AMB) has been presented. Angular misalignment in spline joints has been reported to produce non-uniform pressure distribution, fretting wear and fluctuating load in the spline teeth. The DRS has two shafts, inner and outer, rotating at different speeds supported on REBs and an AMB. Additionally, there is a mechanical interconnection between the shafts by way of Intershaft bearing (ISB). Four different steering functions are used to describe the fluctuating stiffness of spline coupling in the translatory and angular directions. Since the weight of spline joint assembly is heavier than the adjacent shaft sections, *weight dominance* criteria have been assumed in the derivation of fluctuating forces and moments. The model of the coupling, AMB and twin-spool rotor are integrated to obtain the global equations of motion The Campbell diagrams of the DRS with and without AMB are generated from state space form and compared. Condensation techniques are employed to reduce the number of measurement DOFs. An identification algorithm, which uses the forward and backward harmonics of vibrations of the inner and outer rotors, and AMB current has been developed based on condensed EOMs of the system. The mean and additive stiffness of the spline coupling, rotor unbalance, bearing stiffness, bearing damping, the current and displacement stifness of AMB are numerically identified using the devloped algorithm. A comparison of parameters obtained from the regression problem using the dynamic and hybrid condensations is presented in the end.

6.2 System Configuration

A typical DRS supported on 4 bearings and an ISB is shown in Figure 6-1. The various DRS commonly used in aerospace, marine and power applications are shown in Figure 6-2 (Peduzzi, 1983).

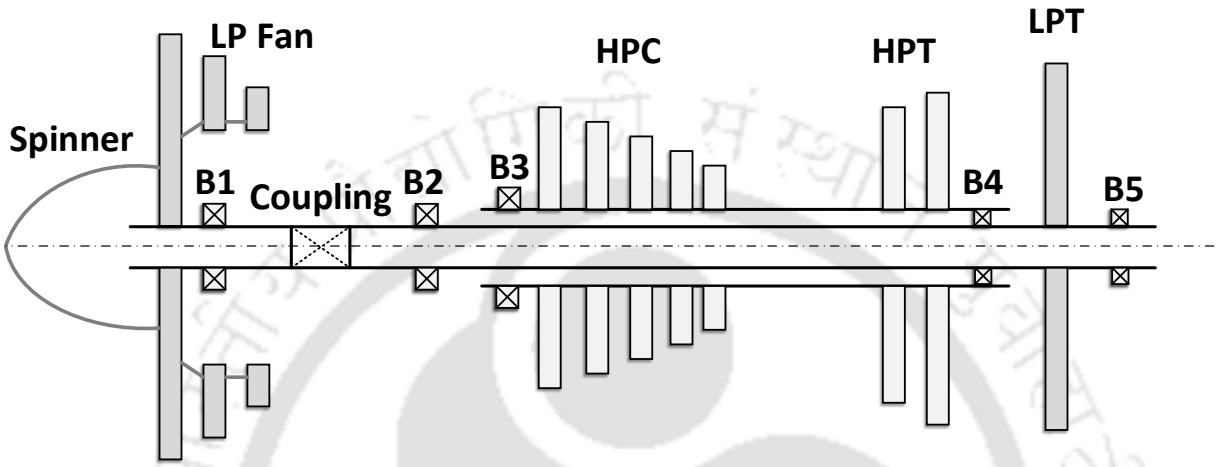

Figure 6-1 Gas turbine DRS with spline joint

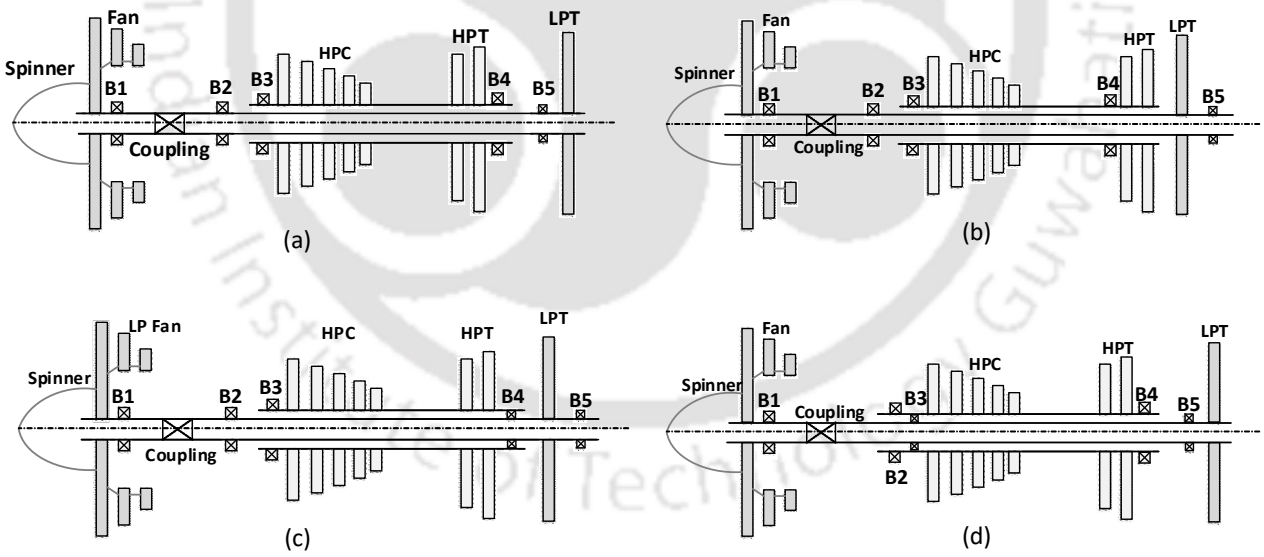

Figure 6-2 DRS configurations commonly used in Gas Turbines

Figure 6.2(a) is a twin spool rotor in which HPT is in straddle mounted arrangement. In Figure 6.2(b) HPT is in overhung arrangement. Figure 6.2(c) is a twin spool rotor with a rear Intershaft roller bearing and straddle mounted HPT. This arrangement results in weight savings and reduced turbine blade tip clearances. In Figure 6.2(d) Intershaft bearing located at the front can be a ball bearing which can take the axial load coming

from LP rotor. Due to the difference in general arrangements the placement of critical speeds is different in all the four cases. The inner rotor also called low pressure (LP) rotor consists of a multi-stage fan, fan shaft, turbine shaft and LP turbine. A spline coupling connects the turbine shaft and fan shaft. Fayong et al. (2013) discusses the various types of splines and their design features. Based on the number of the teeth, they can be divided into two categories: single pair of teeth and double pairs of teeth. Double pairs of teeth are further divided into tandem and parallel teeth configurations (Figure 6-3).

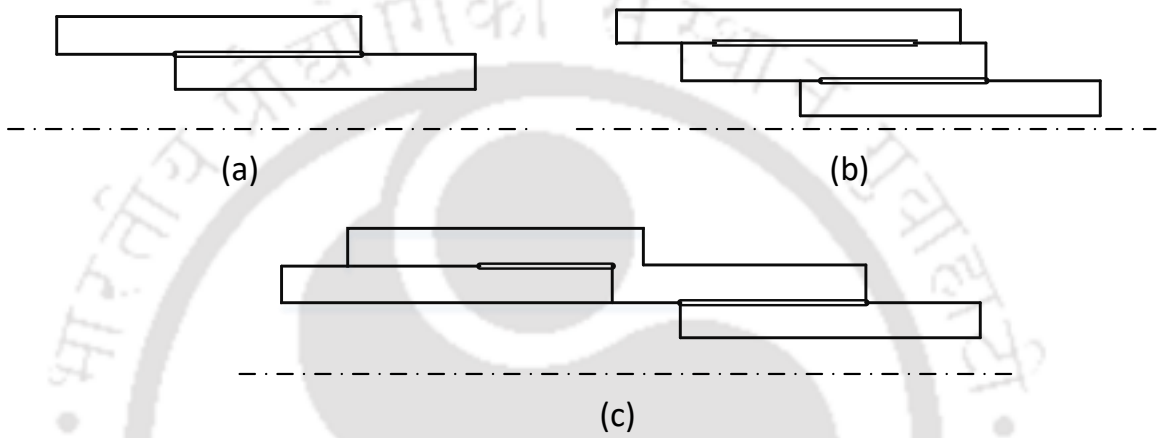

Figure 6-3 Various types of spline couplings (a) Single pair (b) Double pairs of tandem teeth (c) Double pairs of parallel teeth

The outer rotor also called the high pressure rotor (HP) has a multi-stage compressor, compressor-turbine shaft and HP turbine. The outer runs at a higher speed than the inner rotor. Both rotors are connected by Intershaft bearing (Bearing no. 4), whose races run at different speeds. All the bearings (B1 to B5) are provided with external viscous damping using conventional SFDs for vibration attenuation. The spinner located at the front of LP rotor is used for trim balancing the rotor. In the current problem bearing B2 is entirely replaced with AMB, which serves the purpose of bearing as well as a damper, however, without the need for additional lubrication. Besides functioning as a support bearing the AMB also serves the purpose for the condition monitoring.

6.3 Assumptions

i) Spline tooth in general have indexing error or spacing errors due to manufacturing tolerances (Figure 6-4). This results in non-uniform load distribution characteristics of spline coupling. It is assumed that there is some amount of indexing error present

in the spline teeth arising from imperfect manufacturing. More discussion on this topic is presented in Hong et al. (2015).

Figure 6-4 Indexing errors in spline teeth: solid - ideal profile, dotted– actual profile

ii) Spline joints are often over-dimensioned to avoid fatigue failures (Cura et al, 2017). This leads to spline joint being heavier than the adjacent shaft sections. Also the stiffness of spline joint is less than that of a continuous rotor of same dimensions due to clearance fits and structural discontinuities (Fayong et al., 2013 and Zhang et al., 2014). In such conditions the *weight dominance* criteria (Shravan and Tiwari, 2012) assumed as in the crack modelling with some difference in switching functions.

6.4 Notation

In this chapter, complex coordinates are used throughout the mathematical formulation except in some sections, where real matrices/vectors are used. In such cases superscript *re* is explicitly used to avoid confusion. Thus $\boldsymbol{\eta}$ denotes global displacement vector in *complex* coordinates, whereas $\boldsymbol{\eta}^{re}$ denotes global displacement vector in *real* coordinates. This particular notation ($\boldsymbol{\eta}^{re}$) is used in Sections 3.2, 3.3 and 3.4. In these cases, the matrices/vectors are initially written in real form and then converted to complex form. Understandably the size of $\boldsymbol{\eta}^{re}$ is twice that of $\boldsymbol{\eta}$.

6.5 Mathematical Model

Complex notation given in Chen and Gunter (2007) with two complex DOFs per node is suitable for the present formulation since it enables extraction of positive and negative

harmonics of shaft vibration and AMB current from FFT algorithm. The complex displacement vector $\boldsymbol{\eta}_i$ for i^{th} finite element with 2 nodes is given by

$$\boldsymbol{\eta}_{i_{(2\times1)}} = \begin{pmatrix} u_i & \varphi_i \end{pmatrix}^T \tag{6.1}$$

where u and φ are the complex translational and rotational displacements and are given by

$$u = x_i + \mathrm{j}y_i; \qquad \varphi = \varphi_{y_i} + \mathrm{j}\varphi_{x_i} \tag{6.2}$$

The same convention that is followed in the previous chapters for the stationary and rotating frames of reference is adopted in this chapter. The modeling of shafts, discs, coupling, bearings and AMB is described in this section.

6.5.1 Shaft and Disc Model

Timoshenko beam finite elements with 2 nodes per element are used to discretize the rotor system. The elemental matrices of shaft and disc used in this chapter are given in **Appendix D**.

6.5.2 Coupling Mathematical Model

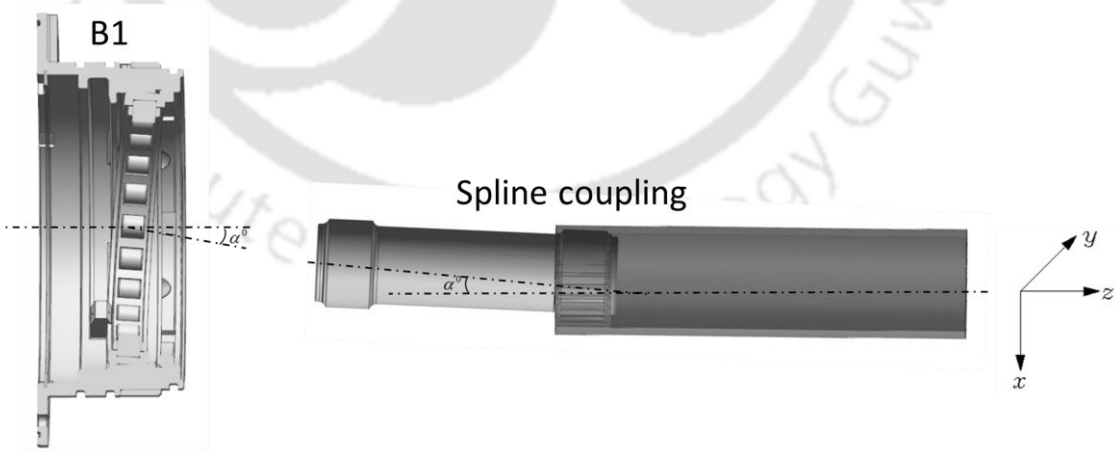

Figure 6-5 Misaligned spline coupling

The misalignment condition of the spline coupling is shown in Figure 6-5. When bearing B1 is properly seated in its bearing housing, the teeth of the spline coupling are perfectly aligned and there is only static stiffness component. When there is tilt of bearing B1 in the

housing, the teeth of mating spline coupling are angularly misaligned, as shown in Figure 6-5. This results in the generation of time-dependent fluctuating stiffness (Hong et al., 2015). Similar behaviour is also reported in misaligned rigid couplings (Lees, 2007). For a given amount of misalignment and indexing error the spline stiffness matrix can be written as sum of the static and fluctuating matrices, as

$$\mathbf{K}_{sp\_rot}^{re} = \left(\mathbf{K}_{sp\_rot}^{mean}\right)^{re} + \left(\mathbf{\Delta K}_{sp\_rot}^{fluc}(t)\right)^{re} \tag{6.3}$$

where in suffix, *sp* denotes the spline and *rot* denotes rotating frame of reference, and super scripts *mean* and *fluc* denote the mean and fluctuating components of spline stiffness, respectively.

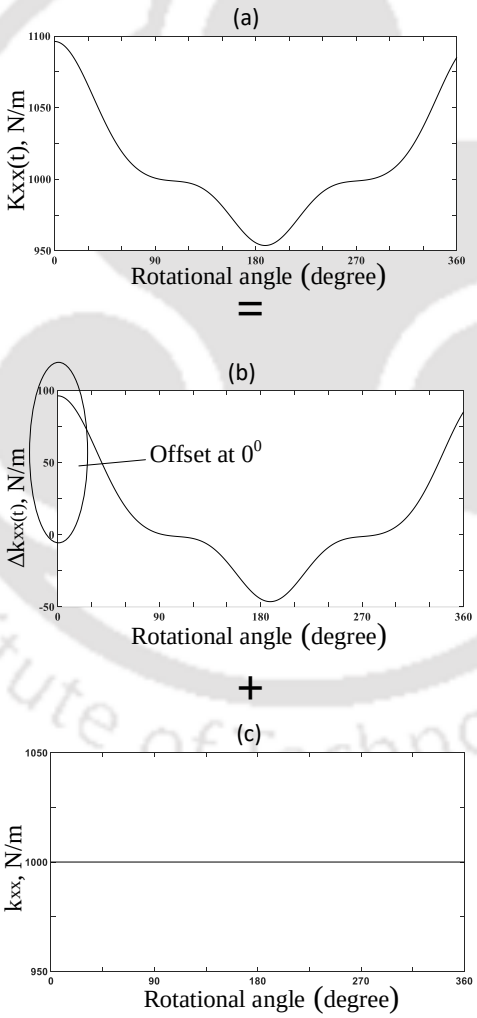

Figure 6-6 Spline coupling's stiffness over one rotation (360 degree): (a) k_{sp_rot} : Total stiffness (b) k^{fluc} : Fluctuating stiffness (c) k^{mean} : Static

Figure 6-6(a-c), which is the pictorial representation of Eqn. (6.3) depicts the total, fluctuating and mean stiffness of the spline coupling, respectively. When there is *no* misalignment and indexing error, the total stiffness of spline coupling comprises of only the static component as in Figure 6-6(c). In the presence of misalignment and indexing error, the fluctuating component arises as in Figure 6-6(b) along with the static component of Figure 6-6(c). Lal and Tiwari (2018) showed that static stiffness of coupling is more in the direction of misalignment. In the present problem that is accounted for by the stiffness offset present at time t = 0 sec at 0^0 phase position in the fluctuating component as shown in Figure 6-6(b). When the spline teeth are perfectly aligned then

$$\mathbf{f}_{sp}^{re} = \mathbf{K}_{sp}^{re}(t)\left\{\boldsymbol{\eta}_{sp_0}^{re} + \boldsymbol{\eta}_{sp}^{re}(t)\right\} \tag{6.4}$$

In the presence of faults in spline joint, the fluctuating component comes into play. In such case, we have

$$\mathbf{f}_{sp}^{re}(t) = \left[\left(\mathbf{K}_{sp\_rot}^{mean}\right)^{re} + \left(\Delta\mathbf{K}_{sp\_rot}^{fluc}(t)\right)^{re}\right]\left\{\boldsymbol{\eta}_{sp_0}^{re} + \boldsymbol{\eta}_{sp}^{re}(t)\right\} = \left(\mathbf{f}_{sp\_rot}^{mean}(t)\right)^{re} + \left(\mathbf{f}_{sp\_rot}^{fluc}(t)\right)^{re} \tag{6.5}$$

with

$$\left(\mathbf{f}_{sp\_rot}^{mean}(t)\right)^{re} = \left(\mathbf{K}_{sp\_rot}^{mean}\right)^{re}\boldsymbol{\eta}_{sp}^{re}(t) \tag{6.6}$$

$$\left(\mathbf{f}_{sp\_rot}^{fluc}(t)\right)^{re} = \left(\Delta\mathbf{K}_{sp\_rot}^{fluc}(t)\right)^{re}\boldsymbol{\eta}_{sp_0}^{re} + \left(\Delta\mathbf{K}_{sp\_rot}^{fluc}(t)\right)^{re}\boldsymbol{\eta}_{sp}^{re}(t) \tag{6.7}$$

$$\boldsymbol{\eta}_{sp_0}^{re} = \left\{\delta\xi_{sp} \quad \delta\eta_{sp} \quad \delta\varphi_{\eta_{sp}} \quad \delta\varphi_{\xi_{sp}} \quad \delta\xi_{sp+1} \quad \delta\eta_{sp+1} \quad \delta\varphi_{\eta_{sp+1}} \quad \delta\varphi_{\xi_{sp+1}}\right\}^T \tag{6.8}$$

$$\boldsymbol{\eta}_{sp}^{re} = \left\{\xi_{sp} \quad \eta_{sp} \quad \varphi_{\eta_{sp}} \quad \varphi_{\xi_{sp}} \quad \xi_{sp+1} \quad \eta_{sp+1} \quad \varphi_{\eta_{sp+1}} \quad \varphi_{\xi_{sp+1}}\right\}^T \tag{6.9}$$

It can be seen that Eqn. (6.3) has two parts: the force due to mean stiffness and the force due to fluctuating stiffness arising from coupling faults.

6.5.2.1 Static coupling stiffness force

The 5×5 stiffness matrix of the spline joint considering DOFs $x, y, \varphi_x, \varphi_y$ and φ_z is given in Hong et al. (2015). If the spline joint is assumed to connect one node on external spline

and another node on internal spline, then the stiffness matrix considering only lateral DOFs can be written as

$$\left(\mathbf{K}_{sp\_rot}^{mean}\right)^{re}=\begin{bmatrix} k_{xx} & k_{xy} & k_{x\varphi_y} & k_{x\varphi_x} & -k_{xx} & -k_{xy} & -k_{x\varphi_y} & -k_{x\varphi_x} \\ k_{xy} & k_{yy} & k_{y\varphi_y} & k_{y\varphi_x} & -k_{xy} & -k_{yy} & -k_{y\varphi_y} & -k_{y\varphi_x} \\ k_{x\varphi_y} & k_{y\varphi_y} & k_{\varphi_y\varphi_y} & k_{\varphi_y\varphi_x} & -k_{x\varphi_y} & -k_{y\varphi_y} & -k_{\varphi_y\varphi_y} & -k_{\varphi_y\varphi_x} \\ k_{x\varphi_x} & k_{y\varphi_x} & k_{\varphi_y\varphi_x} & k_{\varphi_x\varphi_x} & -k_{x\varphi_x} & -k_{y\varphi_x} & -k_{\varphi_y\varphi_x} & -k_{\varphi_x\varphi_x} \\ -k_{xx} & -k_{xy} & -k_{x\varphi_y} & -k_{x\varphi_x} & k_{xx} & k_{xy} & k_{x\varphi_y} & k_{x\varphi_x} \\ -k_{xy} & -k_{yy} & -k_{y\varphi_y} & -k_{y\varphi_x} & k_{xy} & k_{yy} & k_{y\varphi_y} & k_{y\varphi_x} \\ -k_{x\varphi_y} & -k_{y\varphi_y} & -k_{\varphi_y\varphi_y} & -k_{\varphi_y\varphi_x} & k_{x\varphi_y} & k_{y\varphi_y} & k_{\varphi_y\varphi_y} & k_{\varphi_y\varphi_x} \\ -k_{x\varphi_x} & -k_{y\varphi_x} & -k_{\varphi_y\varphi_x} & -k_{\varphi_x\varphi_x} & k_{x\varphi_x} & k_{y\varphi_x} & k_{\varphi_y\varphi_x} & k_{\varphi_x\varphi_x} \end{bmatrix} \quad (6.10)$$

Hong et al. (2015) showed that some of the off-diagonal stiffness coefficients are numerically many orders less the diagonal terms. Especially, cross-coupled terms between translational and rotational DOFs are insignificant. In such case, the first part of Eqn. (6.3) can be written as

$$\left(\mathbf{K}_{sp\_rot}^{mean}\right)^{re}=\begin{bmatrix} k_{xx} & 0 & k_{x\varphi_y} & 0 & -k_{xx} & 0 & -k_{x\varphi_y} & 0 \\ 0 & k_{yy} & 0 & k_{y\varphi_x} & 0 & -k_{yy} & 0 & -k_{y\varphi_x} \\ k_{x\varphi_y} & 0 & k_{\varphi_y\varphi_y} & 0 & -k_{x\varphi_y} & 0 & -k_{\varphi_y\varphi_y} & 0 \\ 0 & k_{y\varphi_x} & 0 & k_{\varphi_x\varphi_x} & 0 & -k_{y\varphi_x} & 0 & -k_{\varphi_x\varphi_x} \\ -k_{xx} & 0 & -k_{x\varphi_y} & 0 & k_{xx} & 0 & k_{x\varphi_y} & 0 \\ 0 & -k_{yy} & 0 & -k_{y\varphi_x} & 0 & k_{yy} & 0 & k_{y\varphi_x} \\ -k_{x\varphi_y} & 0 & -k_{\varphi_y\varphi_y} & 0 & k_{x\varphi_y} & 0 & k_{\varphi_y\varphi_y} & 0 \\ 0 & -k_{y\varphi_x} & 0 & -k_{\varphi_x\varphi_x} & 0 & k_{y\varphi_x} & 0 & k_{\varphi_x\varphi_x} \end{bmatrix} \quad (6.11)$$

Coordinate transformation is performed to convert Eqn. (6.6) into stationary frame, as

$$\left(\mathbf{f}_{sp\_stat}^{mean}(t)\right)^{re}=\mathbf{T}^{T}\left(\mathbf{K}_{sp\_rot}^{mean}\right)^{re}\mathbf{T}\boldsymbol{\eta}_{sp}^{re}(t) \quad (6.12)$$

with

$$\mathbf{T}_{8\times 8}=\begin{bmatrix} R & 0 & 0 & 0 \\ 0 & R & 0 & 0 \\ 0 & 0 & R & 0 \\ 0 & 0 & 0 & R \end{bmatrix} \text{ where } \mathbf{R}=\begin{bmatrix} \cos\omega t & \sin\omega t \\ -\sin\omega t & \cos\omega t \end{bmatrix} \quad (6.13)$$

If sp and $sp+1$ are the spline coupling node numbers then the force due to the spline coupling's mean stiffness in stationary frame of reference in complex form is given by

$$\left(\mathbf{f}_{sp\_stat}^{mean}\right)^{re} = \begin{bmatrix} k_{rad} & k_{radang} & -k_{rad} & -k_{radang} \\ k_{angrad} & k_{ang} & -k_{angrad} & -k_{ang} \\ -k_{rad} & -k_{radang} & k_{rad} & k_{radang} \\ -k_{angrad} & -k_{ang} & k_{angrad} & k_{ang} \end{bmatrix} \begin{Bmatrix} u_{sp} \\ \varphi_{sp} \\ u_{sp+1} \\ \varphi_{sp+1} \end{Bmatrix} \tag{6.14}$$

with $k_{rad} = k_{xx} = k_{yy}$; $k_{ang} = k_{\varphi_y\varphi_y} = k_{\varphi_x\varphi_x}$; $k_{radang} = k_{x\varphi_y} = k_{y\varphi_x}$; $k_{angrad} = k_{\varphi_y x} = k_{\varphi_x y}$.

Complex displacements of spline coupling ($u_{sp}, \varphi_{sp}, u_{sp+1}, \varphi_{sp+1}$) are defined in Eqn. (6.2).

6.5.2.2 Fluctuating coupling stiffness force

The force due to fluctuating stiffness of spline joint is defined thus

$$\left(\mathbf{f}_{sp\_rot}^{fluc}(t)\right)^{re} = \left(\mathbf{\Delta K}_{sp\_rot}^{fluc}(t)\right)^{re} \boldsymbol{\eta}_{sp_0}^{re} + \left(\mathbf{\Delta K}_{sp\_rot}^{fluc}(t)\right)^{re} \boldsymbol{\eta}_{sp}^{re}(t) \tag{6.15}$$

Since the spline joint assembly is heavier than a uniform shaft, the *weight dominance* criterion is assumed at the location of spline coupling (Cura et al., 2017), which gives

$$\boldsymbol{\eta}_{sp}^{re} << \boldsymbol{\eta}_{sp_0}^{re} \tag{6.16}$$

Hence, Eqn. (6.15) takes the following form

$$\left(\mathbf{f}_{sp\_rot}^{fluc}(t)\right)^{re} = \left(\mathbf{\Delta K}_{sp\_rot}^{fluc}(t)\right)^{re} \boldsymbol{\eta}_{sp_0}^{re} \tag{6.17}$$

with

$$\left(\mathbf{\Delta K}_{sp\_rot}^{fluc}(t)\right)^{re} = \begin{bmatrix} \mathbf{B}(t) & -\mathbf{B}(t) \\ -\mathbf{B}(t) & \mathbf{B}(t) \end{bmatrix}; \mathbf{B}(t) = \begin{bmatrix} \Delta k_{\xi\xi}(t) & \Delta k_{\xi\eta}(t) & \Delta k_{\xi\varphi_\eta}(t) & \Delta k_{\xi\varphi_\xi}(t) \\ \Delta k_{\eta\xi}(t) & \Delta k_{\eta\eta}(t) & \Delta k_{\eta\varphi_\eta}(t) & \Delta k_{\eta\varphi_\xi}(t) \\ \Delta k_{\varphi_\eta\xi}(t) & \Delta k_{\varphi_\eta\eta}(t) & \Delta k_{\varphi_\eta\varphi_\eta}(t) & \Delta k_{\varphi_\eta\varphi_\xi}(t) \\ \Delta k_{\varphi_\xi\xi}(t) & \Delta k_{\varphi_\xi\eta}(t) & \Delta k_{\varphi_\xi\varphi_\eta}(t) & \Delta k_{\varphi_\xi\varphi_\xi}(t) \end{bmatrix} \tag{6.18}$$

In Hong et al. (2015), it is shown that the stiffness of spline joint due to misalignment shows different patterns of fluctuation in ξ, η, φ_η and φ_ξ directions. In the present formulation, this is accounted for by choosing four different arbitrary steering

functions $s_1(t), s_2(t), s_3(t)$ and $s_4(t)$. If diagonal stiffness terms are considered Eqn. (6.18) can be written as

$$\left(\Delta\mathbf{K}_{sp\_rot}^{fluc}(t)\right)^{re} = \begin{bmatrix} \mathbf{B}_1(t) & -\mathbf{B}_1(t) \\ -\mathbf{B}_1(t) & \mathbf{B}_1(t) \end{bmatrix}; \mathbf{B}_1(t) = \begin{bmatrix} s_1(t)\Delta k_{\xi\xi} & 0 & 0 & 0 \\ 0 & s_2(t)\Delta k_{\eta\eta} & 0 & 0 \\ 0 & 0 & s_3(t)\Delta k_{\varphi_\xi\varphi_\xi} & 0 \\ 0 & 0 & 0 & s_4(t)\Delta k_{\varphi_\eta\varphi_\eta} \end{bmatrix} \tag{6.19}$$

A coordinate transformation is performed to rewrite Eqn. (6.17) in inertial coordinate system, as

$$\left(\mathbf{f}_{sp\_stat}^{fluc}(t)\right)^{re} = \mathbf{T}^T \left(\Delta\mathbf{K}_{sp\_rot}^{fluc}\right)^{re}(t)\mathbf{T}\boldsymbol{\eta}_{sp_0}^{re} \tag{6.20}$$

Where $\boldsymbol{\eta}_{sp_o}^{re}$ is the vector of static deflections at spline coupling nodes, which can be obtained as

$$\left\{\boldsymbol{\eta}_{sp_o}^{re}\right\}_{4n\times 1} = -\left(\mathbf{K}_{4n\times 4n}^{re}\right)^{-1}\left(\mathbf{M}_{4n\times 4n}^{re}\right)\left\{\mathbf{g}_{4n\times 1}^{re}\right\} \tag{6.21}$$

with

$$\mathbf{g}^{re} = \begin{Bmatrix} 0 & g & 0 & 0 & 0 & g & 0 & 0 \end{Bmatrix}^T$$

Superscript *re* refers to the matrices used in Friswell et al. (2010). The matrices are provided in **Appendix E**. The physical interpretation of Eqn. (6.19) is: With *weight-dominance* assumption, fluctuating forces and moments are a function of fluctuating/additive stiffness coefficients, an appropriate steering function and the static deflection at the coupling nodes. Eqn. (6.19) has the following form in complex coordinates

$$\mathbf{f}_{sp\_stat}^{fluc} = 0.5\begin{Bmatrix} \left(\delta x_c - \delta x_{c+1}\right)\left\{\Delta k_{T\xi} s_1(t)(1+e^{j2\omega t}) + \Delta k_{T\eta} s_2(t)(1-e^{j2\omega t})\right\} \\ \left(\delta\varphi_{y_c} - \delta\varphi_{y_{c+1}}\right)\left\{\Delta k_{R\eta} s_3(t)(1+e^{j2\omega t}) + \Delta k_{R\xi} s_4(t)(1-e^{j2\omega t})\right\} \\ \left(\delta x_{c+1} - \delta x_c\right)\left\{\Delta k_{T\xi} s_1(t)(1+e^{j2\omega t}) + \Delta k_{T\eta} s_2(t)(1-e^{j2\omega t})\right\} \\ \left(\delta\varphi_{y_{c+1}} - \delta\varphi_{y_c}\right)\left\{\Delta k_{R\eta} s_3(t)(1+e^{j2\omega t}) + \Delta k_{R\xi} s_4(t)(1-e^{j2\omega t})\right\} \end{Bmatrix} \tag{6.22}$$

6.5.3 AMB Force

The lateral force exerted by the AMB on the rotor at its nodal location has two components: the one which is proportional to the rotor vibration u_{AMB} at the AMB location and the other proportional to the current in the AMB actuator, as

$$\mathbf{f}_{AMB} = \begin{Bmatrix} k_s u_{AMB} - k_i i_c \\ 0 \end{Bmatrix} \tag{6.23}$$

where k_s and k_i are the displacement and current stiffness of AMB. In the present work, the complex current i_c is obtained as per the PID control law (Bordoloi and Tiwari, 2013).

6.5.4 Unbalance Force

The unbalance force vector due to the eccentricity of the i^{th} disc on the inner and outer rotors, respectively, are

$$\mathbf{f}_{unb\_in_i} = \begin{Bmatrix} m_i e_i \Omega_{in}^2 e^{\mathrm{j}\Omega_{in}t} e^{\mathrm{j}\beta_i} \\ 0 \end{Bmatrix} \tag{6.24}$$

$$\mathbf{f}_{unb\_ou_i} = \begin{Bmatrix} m_i e_i \Omega_{ou}^2 e^{\mathrm{j}\Omega_{ou}t} e^{\mathrm{j}\beta_i} \\ 0 \end{Bmatrix} \tag{6.25}$$

6.5.5 Bearing Force

The stiffness of REBs and their housings used in gas turbines are in series and their effective stiffness is isotropic. Also the cross-coupled coefficients are zero for a REB. The bearing force vector due to translational stiffness and damping of the i^{th} bearing on the inner and outer rotors, respectively, are

$$\mathbf{f}_{b_{k_i}} = \begin{Bmatrix} 0.5\left(k_{rad}(u_{b_i} + \bar{u}_{b_i}) + k_{rad}(u_{b_i} - \bar{u}_{b_i})\right) \\ 0 \end{Bmatrix} \tag{6.26}$$

$$\mathbf{f}_{b_{c_i}} = \begin{Bmatrix} 0.5\left(c_{rad}(\dot{u}_{b_i} + \dot{\bar{u}}_{b_i}) + c_{rad}(\dot{u}_{b_i} - \dot{\bar{u}}_{b_i})\right) \\ 0 \end{Bmatrix} \tag{6.27}$$

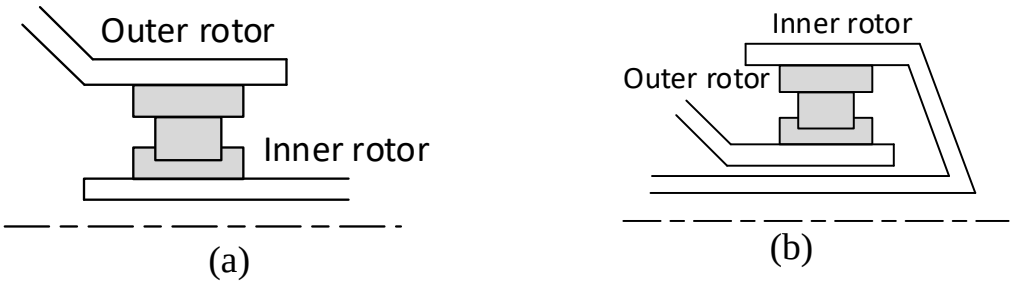

Figure 6-7 Intershaft bearing (b) Inner race on inner rotor (c) Inner race on outer rotor

The stiffness force of the inter-shaft bearing, as shown in Figure 6-7 between the nodes on the inner and outer rotors, is modelled as

$$\mathbf{f}_{isb_c} = \begin{bmatrix} c_{rad\_isb} & 0 & -c_{rad\_isb} & 0 \\ 0 & 0 & 0 & 0 \\ -c_{rad\_isb} & 0 & c_{rad\_isb} & 0 \\ 0 & 0 & 0 & 0 \end{bmatrix} \begin{Bmatrix} \dot{u}_{isb_{in}} \\ \dot{\varphi}_{isb_{in}} \\ \dot{u}_{isb_{ou}} \\ \dot{\varphi}_{isb_{ou}} \end{Bmatrix} \tag{6.28}$$

The damping force due to the inter-shaft bearing is

$$\mathbf{f}_{isb_c} = \begin{bmatrix} c_{rad\_isb} & 0 & -c_{rad\_isb} & 0 \\ 0 & 0 & 0 & 0 \\ -c_{rad\_isb} & 0 & c_{rad\_isb} & 0 \\ 0 & 0 & 0 & 0 \end{bmatrix} \begin{Bmatrix} \dot{u}_{isb_{in}} \\ \dot{\varphi}_{isb_{in}} \\ \dot{u}_{isb_{ou}} \\ \dot{\varphi}_{isb_{ou}} \end{Bmatrix} \tag{6.29}$$

6.5.6 Global EOM of Dual Rotor System

The global EOMs of the dual rotor system is obtained by assembling the sub-system matrices of the inner and outer rotors, as

$$\begin{aligned} \left(\mathbf{M}_{in} + \mathbf{M}_{ou}\right)\ddot{\boldsymbol{\eta}} + \left[\mathbf{C}_{in} + \mathbf{C}_{ou} - \mathrm{j}\Omega_{in}\mathbf{G}_{in} - \mathrm{j}\Omega_{ou}\mathbf{G}_{ou}\right]\dot{\boldsymbol{\eta}} \\ + \left(\mathbf{K}_{in} + \mathbf{K}_{ou} + \mathbf{K}_{isb}\right)\boldsymbol{\eta} = \mathbf{f}_{unb\_in} + \mathbf{f}_{unb\_ou} + \mathbf{f}_{AMB} - \mathbf{f}_{sp\_stat}^{fluc} - \mathbf{f}_{sp\_stat}^{mean} \end{aligned} \tag{6.30}$$

Eq. (6.30) can be either rewritten as

$$\mathbf{M}\ddot{\boldsymbol{\eta}} + \left[\mathbf{C} - \mathrm{j}\Omega_{in}\mathbf{G}\right]\dot{\boldsymbol{\eta}} + \mathbf{K}\boldsymbol{\eta} = \mathbf{f}_{unb\_in} + \mathbf{f}_{unb\_ou} + \mathbf{f}_{AMB} - \mathbf{f}_{sp\_stat}^{fluc} - \mathbf{f}_{sp\_stat}^{mean} \tag{6.31}$$

with

$$\mathbf{G} = \mathbf{G}_{in} + \lambda\mathbf{G}_{ou}$$

or

$$\mathbf{M}\ddot{\boldsymbol{\eta}}+\left[\mathbf{C}-\mathrm{j}\Omega_{ou}\mathbf{G}\right]\dot{\boldsymbol{\eta}}+\mathbf{K}\boldsymbol{\eta}=\mathbf{f}_{unb\_in}+\mathbf{f}_{unb\_ou}+\mathbf{f}_{AMB}-\mathbf{f}_{sp\_stat}^{fluc}-\mathbf{f}_{sp\_stat}^{mean} \tag{6.32}$$

with

$$\mathbf{G}=\left(1/\lambda\right)\mathbf{G}_{in}+\mathbf{G}_{ou}$$

Herein, either Eqn. (6.31) or Eqn. (6-32) could be used to solve numerically to obtain the vibration of inner and outer rotors and AMB current. The complex global displacement vector $\boldsymbol{\eta}$ with *m* nodes on inner rotor (suffix *in*) and *n* nodes on outer rotor (suffix *ou*) is given by

$$\boldsymbol{\eta}_{((m+n)\times 2\times 1)}=\left\{ u_{in_1} \quad \varphi_{in_1} \quad \cdots \quad u_{in_{isb}} \quad \cdots \quad u_{in_m} \quad \cdots \quad u_{ou_1} \quad \cdots \quad u_{ou_{isb}} \quad \cdots \quad \varphi_{ou_n} \right\} \tag{6.33}$$

Each global elemental matrix is a square matrix of size $\left(m+n\right)\times 2$. The two rotors are connected at the nodes with suffix '*isb*'.

6.5.7 Eigenvalues and Campbell Diagram

To determine eigenvalues, either Eqn. (6.31) or Eqn. (6.32) is rearranged in state space form as

$$\mathbf{A}\dot{\mathbf{x}}+\mathbf{B}\mathbf{x}=\mathbf{0} \tag{6.34}$$

with

$$\mathbf{A}=\begin{bmatrix}\mathbf{C}+\Omega\mathbf{G} & \mathbf{M}\\ \mathbf{M} & 0\end{bmatrix};\quad \mathbf{B}=\begin{bmatrix}\mathbf{K} & 0\\ 0 & -\mathbf{M}\end{bmatrix};\quad \mathbf{x}=\begin{Bmatrix}\boldsymbol{\eta}\\ \dot{\boldsymbol{\eta}}\end{Bmatrix} \tag{6.35}$$

Eqn. (6.34) can be thus be solved for a range of speeds to produce eigenvectors and eigenvalues. Thus we have two Campbell diagrams one each for Ω_{in} and Ω_{ou} as reference speed (Chiang and Hsu, 2004). Generally, the eigenvalues calculated with respect to Ω_{in} are more than those calculated with respect to Ω_{ou}, since the gyroscopic moments of the inner rotor are more than that of the outer rotor.

6.5.8 Global EOMs in Frequency Domain

If the inter-shaft bearing were not present, the rotors would be running independently and the vibration response is mutually exclusive assuming that the bearings do not share the common housing .Since the inner and outer rotors are mechanically coupled by inter-shaft bearing, both rotors excite each other during operation with the result that any fault such as rubbing or looseness or unbalance or misalignment or crack present on one rotor influences the vibration response of the other rotor and vice versa (Yang et al., 2016) .The solution to Eqn. (6.31) is then given by

$$\boldsymbol{\eta} = \bar{\boldsymbol{\eta}}_{in} \sum_{i=-n}^{+n} e^{\mathrm{j}i\omega t} + \bar{\boldsymbol{\eta}}_{ou} \sum_{i=-n}^{+n} e^{\mathrm{j}i\omega t} \tag{6.36}$$

Likewise, the AMB current has harmonics that are present in the vibration signal at the AMB location

$$\mathbf{i} = \bar{\mathbf{i}}_{in} \sum_{i=-n}^{+n} e^{\mathrm{j}i\omega t} \tag{6.37}$$

Herein, i denotes the harmonics present in the *global* vibration response, (a) $i = 1$ corresponds to the unbalance on inner rotor, (b) $i = -n$ through $+n$ correspond to faults in the spline joint, and (c) $i = \lambda$ corresponds to the unbalance on the outer rotor. The global EOM in frequency domain is obtained by substituting Eqn. (6.36) and Eqn. (6.37) into Eqn. (6.31), as

$$\left[-\mathbf{M}(i\omega)^2 + \mathrm{j}i\omega(\mathbf{C} - \mathrm{j}\Omega_{in}\mathbf{G}) + \mathbf{K}\right](\bar{\boldsymbol{\eta}}_{in} + \bar{\boldsymbol{\eta}}_{ou})e^{ij\omega t} = \mathbf{f}_{unb\_in} + \mathbf{f}_{unb\_ou} + \mathbf{f}_{AMB} - \mathbf{f}_{sp\_stat}^{fluc} - \mathbf{f}_{sp\_stat}^{mean} \tag{6.38}$$

The unknown parameters of the rotor system, which are on the right of Eqn. (6.38) can be arranged in the form of linear least-squares regression for their estimation. However, there are some practical difficulties in the execution of the identification algorithm, which are discussed in the next section.

6.5.9 Condensation of Global EOM

The total number of equations and DOFs of dual rotor system modelled by Eqn. (6.38) is $(m+n) \times 2$. Since these are complex DOFs, to acquire vibration data of the full rotor

system would require twice the number of sensors, i.e. $(m+n) \times 4$. To avoid having to use these impracticably large number of sensors Eqn. (6.38) is redefined in terms of master DOFs. These correspond to locations, where external forces act, i.e. discs, grounded bearings, inter-shaft bearing, AMB and spline coupling. The rest of the DOFs are slaves. The transformation matrix that links master DOFs and total DOFs is

$$\mathbf{T}^d = \begin{Bmatrix} \mathbf{I} \\ -[\mathbf{K}_{ss} - \omega_0^2 \mathbf{M}_{ss} - j\omega_0^2 \mathbf{G}_{ss}]^{-1}[\mathbf{K}_{sm} - \omega_0^2 \mathbf{M}_{sm} - j\mathbf{G}_{sm}] \end{Bmatrix} \tag{6.39}$$

The derivation of $\mathbf{T}^d$ is given in Prasad and Tiwari (2018). Eqn. (6.31) in terms of reduced coordinates is given by

$$\left[-\mathbf{M}^d (i\omega)^2 + ji\omega\left(\mathbf{C}^d - j\Omega_{in}\mathbf{G}^d\right) + \mathbf{K}^d\right]\bar{\boldsymbol{\eta}}^d e^{ij\omega t} = \left(\mathbf{f}_{unb\_in}\right)^d + \left(\mathbf{f}_{unb\_ou}\right)^d + \mathbf{f}_{AMB}^d - \left(\mathbf{f}_{sp\_stat}^{fluc}\right)^d - \left(\mathbf{f}_{sp\_stat}^{mean}\right)^d \tag{6.40}$$

with

$$\mathbf{M}^d = \left(\mathbf{T}^d\right)^T \mathbf{M}\mathbf{T}^d; \quad \mathbf{K}^d = \left(\mathbf{T}^d\right)^T \mathbf{K}\mathbf{T}^d; \quad \mathbf{C}^d = \left(\mathbf{T}^d\right)^T \mathbf{C}\mathbf{T}^d; \quad \mathbf{G}^d = \left(\mathbf{T}^d\right)^T \mathbf{G}\mathbf{T}^d$$

$$\mathbf{f}_{unb\_in}^d = \left(\mathbf{T}^d\right)^T \mathbf{f}_{unb\_in}; \quad \mathbf{f}_{unb\_ou}^d = \left(\mathbf{T}^d\right)^T \mathbf{f}_{unb\_ou}; \quad \mathbf{f}_{AMB}^d = \left(\mathbf{T}^d\right)^T \mathbf{f}_{AMB}; \quad \left(\mathbf{f}_{sp\_stat}^{fluc}\right)^d = \left(\mathbf{T}^d\right)^T \mathbf{f}_{sp\_stat}^{fluc}$$

$$\left(\mathbf{f}_{sp\_stat}^{mean}\right)^d = \left(\mathbf{T}^d\right)^T \mathbf{f}_{sp\_stat}^{mean}$$

$$\bar{\boldsymbol{\eta}}^d = \left\{u_{b_1} \quad \ldots \quad u_{b_n} \quad u_{d_1} \quad \ldots \quad u_{d_n} \quad u_{isb_1} \quad u_{isb_2} \quad u_{AMB} \quad u_{sp_1} \quad \varphi_{sp_1} \quad u_{sp_2} \quad \varphi_{sp_2}\right\}^T \tag{6.41}$$

The superscript *d* refers to the dynamically reduced form of matrices and vectors. The vibration data of the DOFs shown in Eqn. (6.41) is linked to the characteristic parameters of bearings, discs, coupling, ISB, and AMB. The next section discusses the feasibility of the measurement of this data on a a test rig. It is to be noted that φ_{sp_1} and φ_{sp_2} (rotational DOFs of the spline joint), u_{isb_1} and u_{isb_2} (translational DOFs of the inter-shaft bearing) in Eqn. (6.41) are linked to k_{ang} : angular stiffness of coupling, (k_{isb} and c_{isb}): ISB stiffness and damping, respectively. Measurement of rotational DOFs of coupling is possible but is difficult to realize. The ISB is not seated in a bearing support, but runs between two shafts, thus making the measurement of translational displacement of ISB not possible.

To get round this difficulty another step of coordinate reduction is performed. The $\varphi_{sp_1}, \varphi_{sp_2}, u_{isb_1}$ and u_{isb_2}, which are the difficult to measure DOFs, are again grouped as *hybrid* slave DOFs keeping the rest of measurable DOFs in Eqn. (6.41) as *hybrid* master DOFs. Elemental matrices **M**, (**M** and **G**) were considered by Lal and Tiwari (2013) and Sampath and Lal (2020), respectively, in the derivation of $\mathbf{T}^h$ matrix. **K** matrix is ignored in both the previous cases since the contribution of stiffness force at high speeds is not significant as compared to inertia. However, in this work **K** is also considered in the derivation of $\mathbf{T}^h$. The method of linking hybrid master DOFs and hybrid slave DOFs is given in detail in Lal and Tiwari (2013) and Sampath and Lal (2020). The new transformation matrix $\mathbf{T}^h$ is given by

$$\mathbf{T}^h = \begin{Bmatrix} \mathbf{I} \\ -[\mathbf{K}_{ss}^d - \omega_0^2 \mathbf{M}_{ss}^d - \mathrm{j}\omega_0^2 \mathbf{G}_{ss}^d]^{-1}[\mathbf{K}_{sm}^d - \omega_0^2 \mathbf{M}_{sm}^d - \mathrm{j}\mathbf{G}_{sm}^d] \end{Bmatrix} \tag{6.42}$$

The final EOM in frequency domain that utilizes only the data from hybrid master DOFs is given by

$$\left[-\mathbf{M}^h (i\omega)^2 + ji\omega\left(\mathbf{C}^h - j\Omega_{in}\mathbf{G}^h\right) + \mathbf{K}^h\right]\bar{\boldsymbol{\eta}}^h e^{ij\omega t} = \mathbf{f}_{unb\_in}^h + \mathbf{f}_{unb\_ou}^h + \mathbf{f}_{amb}^h - \left(\mathbf{f}_{sp\_stat}^{fluc}\right)^h - \left(\mathbf{f}_{sp\_stat}^{mean}\right)^h \tag{6.43}$$

where

$$\mathbf{M}^h = \left(\mathbf{T}^h\right)^T \mathbf{M}^d \mathbf{T}^h; \quad \mathbf{K}^h = \left(\mathbf{T}^h\right)^T \mathbf{K}^d \mathbf{T}^h; \quad \mathbf{C}^h = \left(\mathbf{T}^h\right)^T \mathbf{C}^d \mathbf{T}^h; \quad \mathbf{G}^h = \left(\mathbf{T}^h\right)^T \mathbf{G}^d \mathbf{T}^h$$

$$\mathbf{f}_{unb\_in}^h = \left(\mathbf{T}^h\right)^T \mathbf{f}_{unb\_in}^d; \quad \mathbf{f}_{unb\_ou}^h = \left(\mathbf{T}^h\right)^T \mathbf{f}_{unb\_ou}^d; \quad \mathbf{f}_{AMB}^h = \left(\mathbf{T}^h\right)^T \mathbf{f}_{AMB}^d; \quad \left(\mathbf{f}_{sp\_stat}^{fluc}\right)^h = \left(\mathbf{T}^h\right)^T \mathbf{f}_{sp\_stat}^{fluc}$$

$$\left(\mathbf{f}_{sp\_stat}^{mean}\right)^h = \left(\mathbf{T}^h\right)^T \mathbf{f}_{sp\_stat}^{mean}$$

$$\bar{\boldsymbol{\eta}}^h = \left\{u_{b_1} \quad \ldots \quad u_{b_n} \quad u_{d_1} \quad \ldots \quad u_{d_n} \quad u_{AMB} \quad u_{sp_1} \quad u_{sp_2}\right\}^T \tag{6.44}$$

The superscript *h* refers to the reduced form of matrices and vectors derived using $\mathbf{T}^h$ matrix. The vibration data of the DOFs shown in Eqn. (6.44) does not include $\varphi_{sp_1}, \varphi_{sp_2}, u_{isb_1}$ and u_{isb_2}, which were the problematic DOFs. The next section discusses the derivation of identification algorithm used for estimating the parameters of DRS from measurable responses.

6.5.10 Identification Algorithm for Parameter Estimation

Eqn. (6.43) is rearranged in such a way such that unknown parameters are grouped on the right side and known system parameters are grouped on left of equality sign.

$$\left(\mathbf{A}^{re} + \mathrm{j}\mathbf{A}^{im}\right)\left(\mathbf{x}^{re} + \mathrm{j}\mathbf{x}^{im}\right) = \left(\mathbf{b}^{re} + \mathrm{j}\mathbf{b}^{im}\right) \tag{6.45}$$

Upon arranging on the left side and right side, the final form of Eqn. (6.45) is

$$\mathbf{Ax} = \mathbf{b} \tag{6.46}$$

The vector **x** of the parameters to be identified and is given by

$$\mathbf{x} = \left\{ e_1^{re} \quad e_2^{re} \quad e_3^{re} \quad e_4^{re} \quad e_5^{re} \quad e_6^{re} \quad e_1^{im} \quad e_2^{im} \quad e_3^{im} \quad e_4^{im} \quad e_5^{im} \quad e_6^{im} \quad k_{b_1} \quad k_{b_2} \right.$$
$$\left. k_{b_3} \quad k_{isb} \quad c_{b_1} \quad c_{b_2} \quad c_{b_3} \quad c_{isb} \quad k_s \quad k_i \quad k_{rad}^{sp} \quad k_{ang}^{sp} \quad \Delta k_{\xi\xi} \quad \Delta k_{\eta\eta} \quad \Delta k_{\varphi_\eta\varphi_\eta} \quad \Delta k_{\varphi_\xi\varphi_\xi} \right\} \tag{6.47}$$

Solution to Eqn. (6.46) is of the form

$$\mathbf{x} = \left(\mathbf{A}(\omega)^{\mathrm{T}}\mathbf{A}(\omega)\right)^{-1}\mathbf{A}(\omega)^{\mathrm{T}}\mathbf{b}(\omega) \tag{6.48}$$

The inputs to Eqn. (6.45) are the real and imaginary parts of the harmonics (–*n* to +*n*) of all hybrid DOFs as shown in Eqn. (6.44). These can be obtained by collecting time domain data from the sensors mounted in the test rig and processing through FFT algorithm. The estimation the real and imaginary parts of the harmonics of rotor vibration and AMB current essential for solving Eqn. (6.48) is described in Chapter 2 in detail.

6.6 Results and Discussions

This section deals with the selection of suitable steering functions, numerical analysis of dual rotor system and parameter identification are discussed.

6.6.1 Selection of Steering Functions

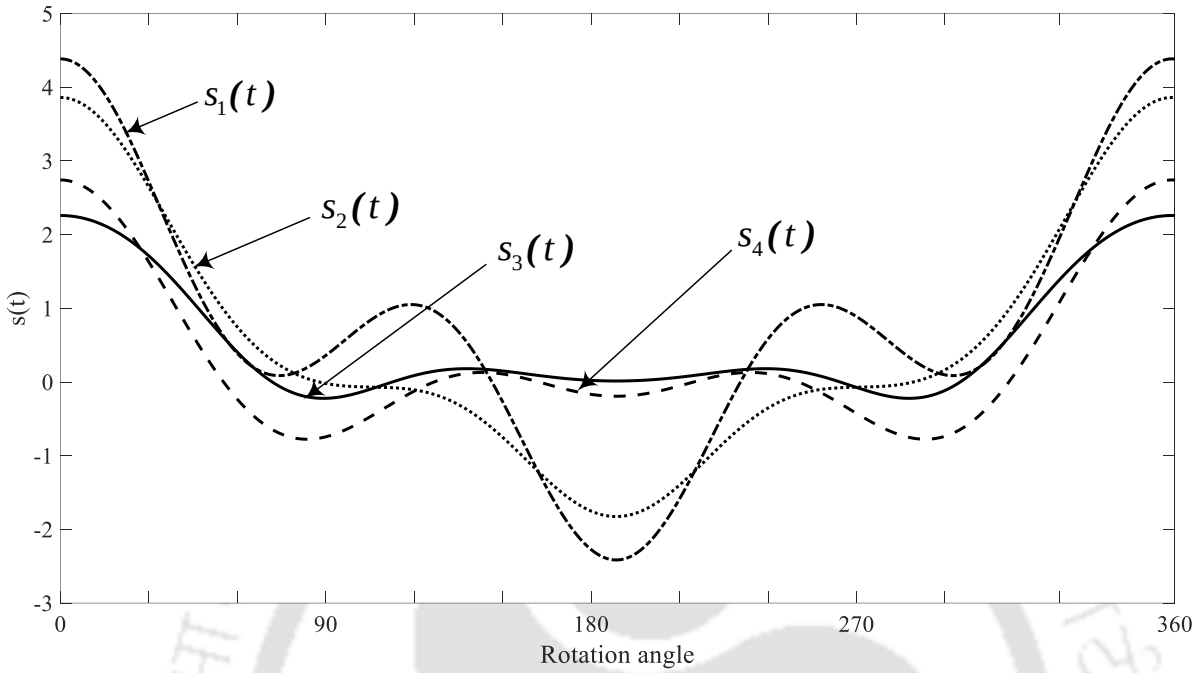

Figure 6-8 Steering functions for fluctuating stiffness of spline joint in $\xi, \eta, \varphi_\eta, \varphi_\xi$ directions

Four arbitrary steering functions: $s_1(t), s_2(t), s_3(t)$ and $s_4(t)$ are chosen to define the fluctuations of spline coupling stiffness $\Delta k_{\xi\xi}(t), \Delta k_{\eta\eta}(t), \Delta k_{\varphi_\eta\varphi_\eta}(t)$, and $\Delta k_{\varphi_\xi\varphi_\xi}(t)$, respectively. In Hong et al. (2015) there are two points that are relevant to the present problem (a) the pattern of stiffness fluctuation of spline coupling over one rotation (0^0- 360^0) is unique in all 4 directions: ξ, η, φ_η and φ_ξ . (b) The stiffness offset at 0^0 generated due to misalignment is unequal in all 4 directions. This physically means that a given amount of bearing tilt causes the spline coupling to generate forces and moments, which are distinct both in amplitude and nature. In the present problem, this requirement is fulfilled by choosing steering functions $s_1(t), s_2(t), s_3(t)$ and $s_4(t)$ whose Fourier expansions are given by (refer Figure 6-8)

$$s_1(t) = 0.75 + 0.8e^{1\mathrm{j}\omega t} + 0.22e^{2\mathrm{j}\omega t} + 1.4e^{3\mathrm{j}\omega t} + 0.05e^{4\mathrm{j}\omega t} - 0.06e^{5\mathrm{j}\omega t}$$
$$+1.2e^{-1\mathrm{j}\omega t} + 0.025e^{-2\mathrm{j}\omega t} - 0.03e^{-3\mathrm{j}\omega t} - 0.06e^{-4\mathrm{j}\omega t} + 0.09e^{-5\mathrm{j}\omega t}$$

$$s_2(t) = 0.4936 + 1.416e^{1\mathrm{j}\omega t} + 0.4936e^{2\mathrm{j}\omega t} + 0.6907e^{3\mathrm{j}\omega t} + 0.0178e^{4\mathrm{j}\omega t} - 0.0041e^{5\mathrm{j}\omega t}$$
$$+0.6907e^{-1\mathrm{j}\omega t} + 0.0378e^{-2\mathrm{j}\omega t} - 0.0011e^{-3\mathrm{j}\omega t} - 0.0252e^{-4\mathrm{j}\omega t} + 0.0512e^{-5\mathrm{j}\omega t}$$

$$s_3(t) = 0.5225 + 0.6054e^{1\mathrm{j}\omega t} + 0.5936e^{2\mathrm{j}\omega t} + 0.2604e^{3\mathrm{j}\omega t} + 0.0278e^{4\mathrm{j}\omega t} - 0.0723e^{5\mathrm{j}\omega t}$$
$$+0.2404e^{-1\mathrm{j}\omega t} + 0.0778e^{-2\mathrm{j}\omega t} + 0.0623e^{-3\mathrm{j}\omega t} - 0.0852e^{-4\mathrm{j}\omega t} + 0.0267e^{-5\mathrm{j}\omega t}$$

$$s_4(t) = 0.3 + 0.42e^{1\mathrm{j}\omega t} + 0.4036e^{2\mathrm{j}\omega t} + 0.4404e^{3\mathrm{j}\omega t} + 0.0378e^{4\mathrm{j}\omega t} - 0.0523e^{5\mathrm{j}\omega t}$$
$$+0.4404e^{-1\mathrm{j}\omega t} + 0.578e^{-2\mathrm{j}\omega t} + 0.1623e^{-3\mathrm{j}\omega t} - 0.0452e^{-4\mathrm{j}\omega t} + 0.067e^{-5\mathrm{j}\omega t} \quad (6.49)$$

It can be seen that these four steering functions have exponential terms with coefficients from (-5 to +5), which are unequal. There is no restriction on the phase of the steering functions. As such shifted steering function also works in Eq. (6.8). Upon substituting Eqn. (6.48) in Eqn. (6.22) the multi-harmonic force due to fluctuating spline stiffness in complex form is given by

$$\mathbf{f}_{sp\_stat}^{fluc} = 0.5\left\{\begin{array}{l}\left(\delta x_c - \delta x_{c+1}\right)\left(\Delta k_{T\xi}\sum_{i=-n}^{i+n} p_i e^{\mathrm{j}i\omega t} + \Delta k_{T\eta}\sum_{i=-n}^{i+n} q_i e^{\mathrm{j}i\omega t}\right) \\ \left(\delta\varphi_{y_c} - \delta\varphi_{y_{c+1}}\right)\left(\Delta k_{R\eta}\sum_{i=-n}^{i+n} r_i e^{\mathrm{j}i\omega t} + \Delta k_{R\xi}\sum_{i=-n}^{i+n} s_i e^{\mathrm{j}i\omega t}\right) \\ \left(\delta x_{c+1} - \delta x_c\right)\left(\Delta k_{T\xi}\sum_{i=-n}^{i+n} p_i e^{\mathrm{j}i\omega t} + \Delta k_{T\eta}\sum_{i=-n}^{i+n} q_i e^{\mathrm{j}i\omega t}\right) \\ \left(\delta\varphi_{y_{c+1}} - \delta\varphi_{y_c}\right)\left(\Delta k_{R\eta}\sum_{i=-n}^{i+n} r_i e^{\mathrm{j}i\omega t} + \Delta k_{R\xi}\sum_{i=-n}^{i+n} s_i e^{\mathrm{j}i\omega t}\right)\end{array}\right\} \quad (6.50)$$

wherein

$$\sum_{i=-n}^{i+n} p_i e^{\mathrm{j}i\omega t} = s_1(t)(1+e^{\mathrm{j}2\omega t}),\ \sum_{i=-n}^{i+n} q_i e^{\mathrm{j}i\omega t} = s_2(t)(1-e^{\mathrm{j}2\omega t})$$
$$\sum_{i=-n}^{i+n} r_i e^{\mathrm{j}i\omega t} = s_3(t)(1+e^{\mathrm{j}2\omega t}),\ \sum_{i=-n}^{i+n} s_i e^{\mathrm{j}i\omega t} = s_4(t)(1-e^{\mathrm{j}2\omega t})$$

In experiments, the values of p_i, q_i, r_i and s_i which denote the participation factors of harmonics of fluctuating forces and moments can be obtained from linear regression (Shravan and Tiwari, 2012).

6.6.2 Representative DRS System and Specifications

Table 6-1 Geometric properties of shafts

Element	l_e, mm	d_i, mm	d_i, mm	Element	l_e, mm	d_o, mm	d_i, mm
Inner				8–9	52	70	75
1–2	76	70	75	9–10	51	70	75
2–3	51	70	75	10–11	53	70	75
3–4	51	70	75	Outer			
4–5	51	70	75	12–13	53	80	85
5–6	83	70	75	13–14	25	80	85
6–7	55	70	75	14–15	25	80	85
7–8	50	70	75	15–16	54	80	85

Table 6-2 Geometric properties of discs

	Disc-1	Disc-2	Disc-3	Disc-4	Inner rotor	Outer rotor
m, kg	1.25	1.5	1.75	1.25	5	1.72
I_d, kg-m2	0.043	0.021	0.013	0.034		
I_p, kg-m2	0.086	0.042	0.026	0.068		
e,kg-m	$7.5e \times 10^{-5}$	6.5×10^{-5}	5.5×10^{-5}	5×10^{-5}	1×10^{-5}	1×10^{-5}
β,rad	$\pi/6$	$\pi/5$	$\pi/10$	$\pi/12$	$\pi/8$	$\pi/10$

Table 6-3 Bearing properties

	Brg-1	Brg-3	Brg-4	Brg-5
k, N/m	10×10^6	11×10^6	16×10^6	8×10^6
c, N-s/m	5500	5400	5100	3000

Table 6-4 Static and fluctuating stiffness coefficients of spline joint

K_{rad}, N/m	K_{ang}, N-m/rad	$\Delta k_{\xi\xi}$, N / m	$\Delta k_{\eta\eta}$, N / m	$\Delta k_{\varphi_\eta \varphi_\eta}$, N - m / rad	$\Delta k_{\varphi_\xi \varphi_\xi}$, N - m / rad
1.5×10^8	4×10^5	225×10^5	232.5×10^5	54×10^3	60×10^3

Table 6-5 AMB characteristics

k_s, N/m	k_i, N/A	k_P, A/m	k_I, A/(m-s)	k_D, (A-s)/m
5×10^5	40	25000	2000	5

The dual rotor system considered for numerical simulation is shown in Figure 6-9. Two cases were considered for discretization (i) 32 nodes on inner rotor and 8 nodes on outer rotor and (ii) 10 nodes on inner rotor and 4 nodes on outer rotor. Eigenvalues obtained in both cases are close to each other. Case (ii) is then chosen for further analysis since the solution time would be lesser owing to lesser number of nodes.

Node 9 on the inner rotor and node 16 on the outer rotor are joined by inter-shaft bearing. The speed ratio λ is taken as 1.5. The properties of rotors, bearings, and spline joint are listed in Table 6-1 through Table 6-4. In present problem, titanium metal matrix composite is used as material for rotors supported on AMBs due to their higher (E / ρ) compared to nickel and steel alloys: E: 172×10^3 MPa, ρ: 4010 (Storace et al., 1995).

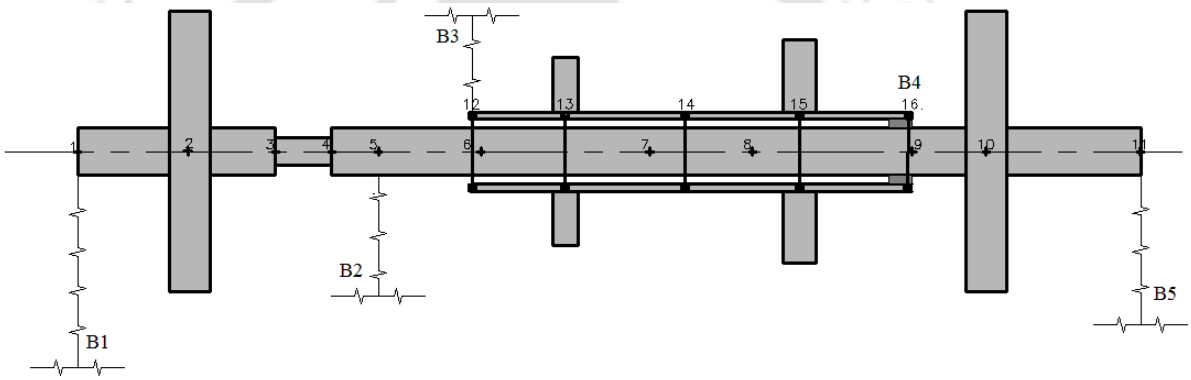

Figure 6-9 Dual rotor system with AMB (B2)

6.6.3 Campbell Diagram and Mode Shapes

The Campbell diagram of the dual rotor bearing system (inner rotor reference speed) with support AMB, with an open loop stiffness, k_s, generated from Eqn. (6.34), is shown in Figure 6-10 (dashed lines). Overlapped on the figure is the Campbell diagram of the rotor supported on all REBs (solid lines). The stiffness of bearing B2 that replaces AMB is taken as 18×10^6 N/m. The crossings of 1X line with forward whirl speeds represent critical speeds of the rotor system. The effect of introduction of AMB in the place of B2 can be seen from Figure 6-10. The crossing of 1X line with forward whirl lines has decreased from 20700 rpm to 19000 rpm. Likewise, the crossings of 1.5X line, which is the excitation of outer rotor unbalance, has reduced from 14000 rpm to 12000 rpm. The Campbell diagram of the dual rotor bearing system (outer rotor reference speed) is shown in Figure 6-11. The crossings of solid and dashed lines with 1X speed line are at 20400

rpm and 18400 rpm, respectively. It can be seen that inner rotor critical speeds are more than outer rotor critical speeds.

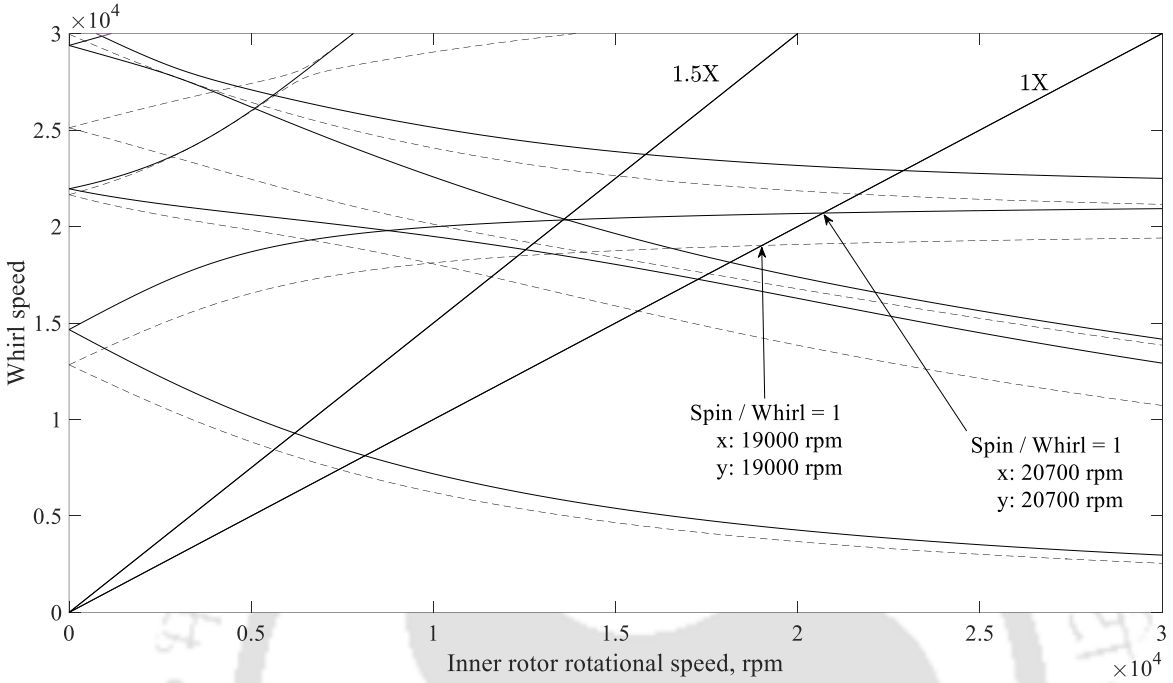

Figure 6-10 Campbell diagram (a) without AMB (solid line) (b) with AMB (dashed line)

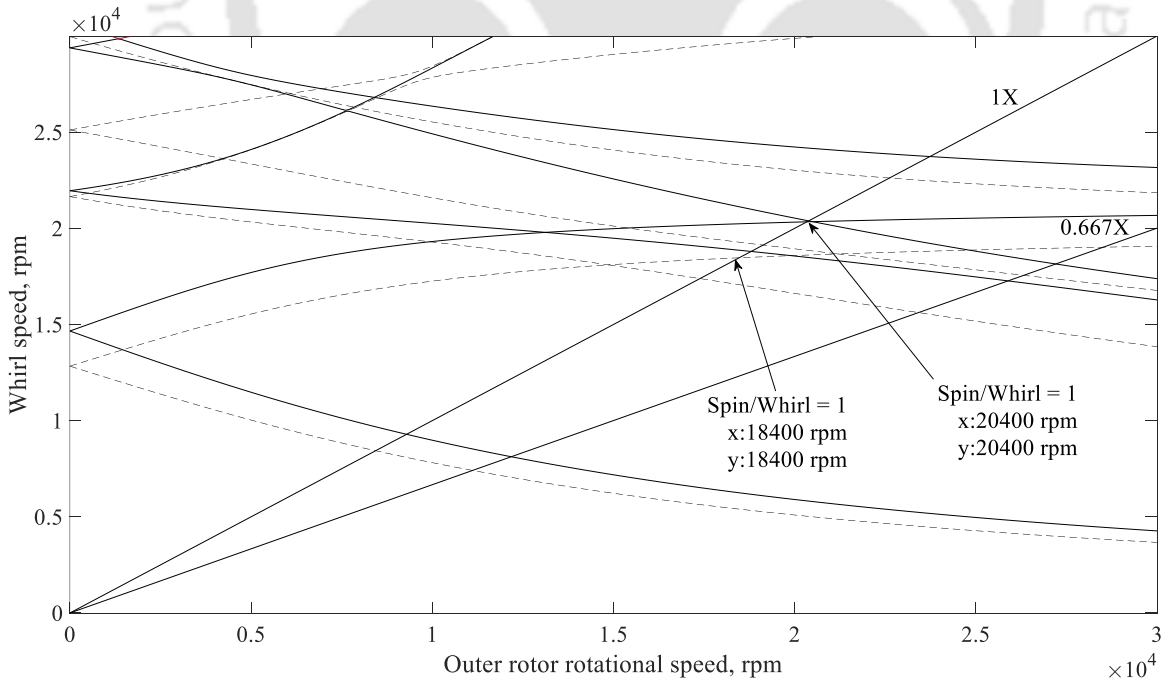

Figure 6-11 Campbell diagram (a) without AMB (solid line) (b) with AMB (dashed line)

6.6.4 Simulink Model and Numerical Analysis

The representative Simulink model constructed from Eqn. (6.31) that generates time domain responses at all the stations of dual rotor is shown in Figure 6-12. A variable-step variable-order (VSVO) solver **ODE15s**, which is based on Gear's method of numerical integration is used for solving stiff problems and is used to solve the global EOM given by Eqn. (6.31). The vibration and current responses at each node on the outer and inner spool are logged for every 1×10^{-5} sec.

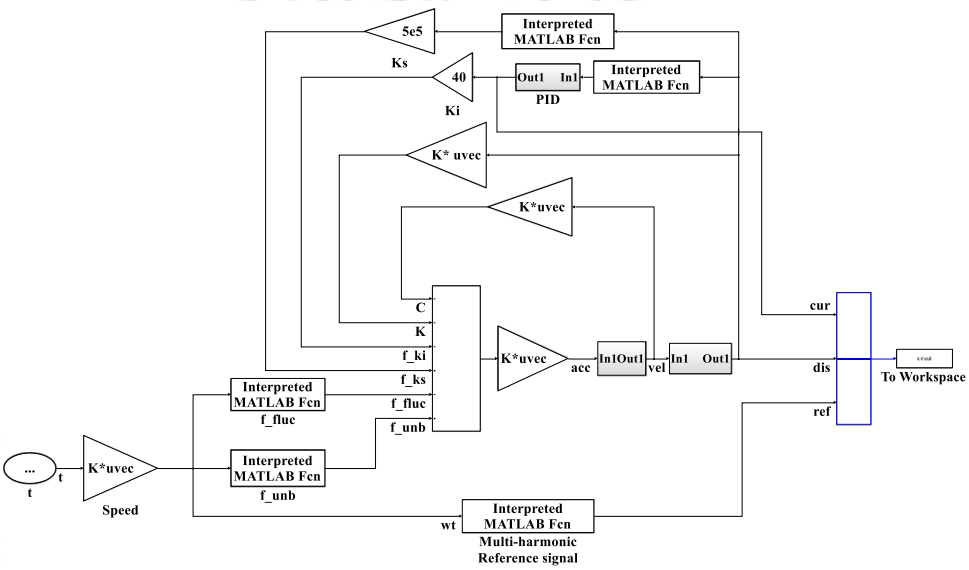

Figure 6-12 Simulink model of dual rotor system

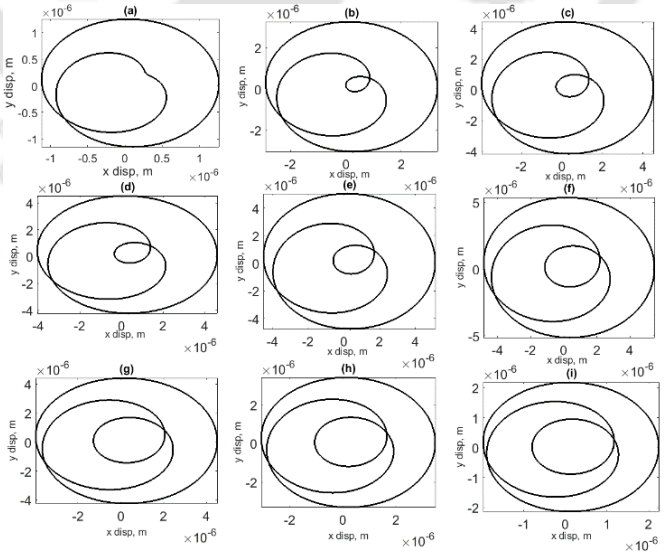

Figure 6-13 Orbits of inner rotor (a) B1 (b) D1 (c) Sp1 (d) Sp2 (e) AMB (f) mid-shaft (g) ISB (h) D4 (i) B4 at 70 Hz b (unbalances on inner and outer rotors)

It can be seen in Figure 6-13 and Figure 6-15 that when only unbalance is present in both inner and outer rotors, which are running at different speeds, the orbits display loops due to the mutual interaction happening through inter-shaft bearing. If the ISB were not present, then the rotors run independently without exciting each other thereby producing circular orbits (for the case of isotropic bearings). Figure 6-17 and Figure 6-19, which are the full spectrum plots of the inner and outer rotors, respectively, show 1X and 1.5X harmonics due to the two-way transmission of vibration through ISB. In Figure 6-14 and Figure 6-16 the loops become more complex due to the presence of spline coupling misalignment.

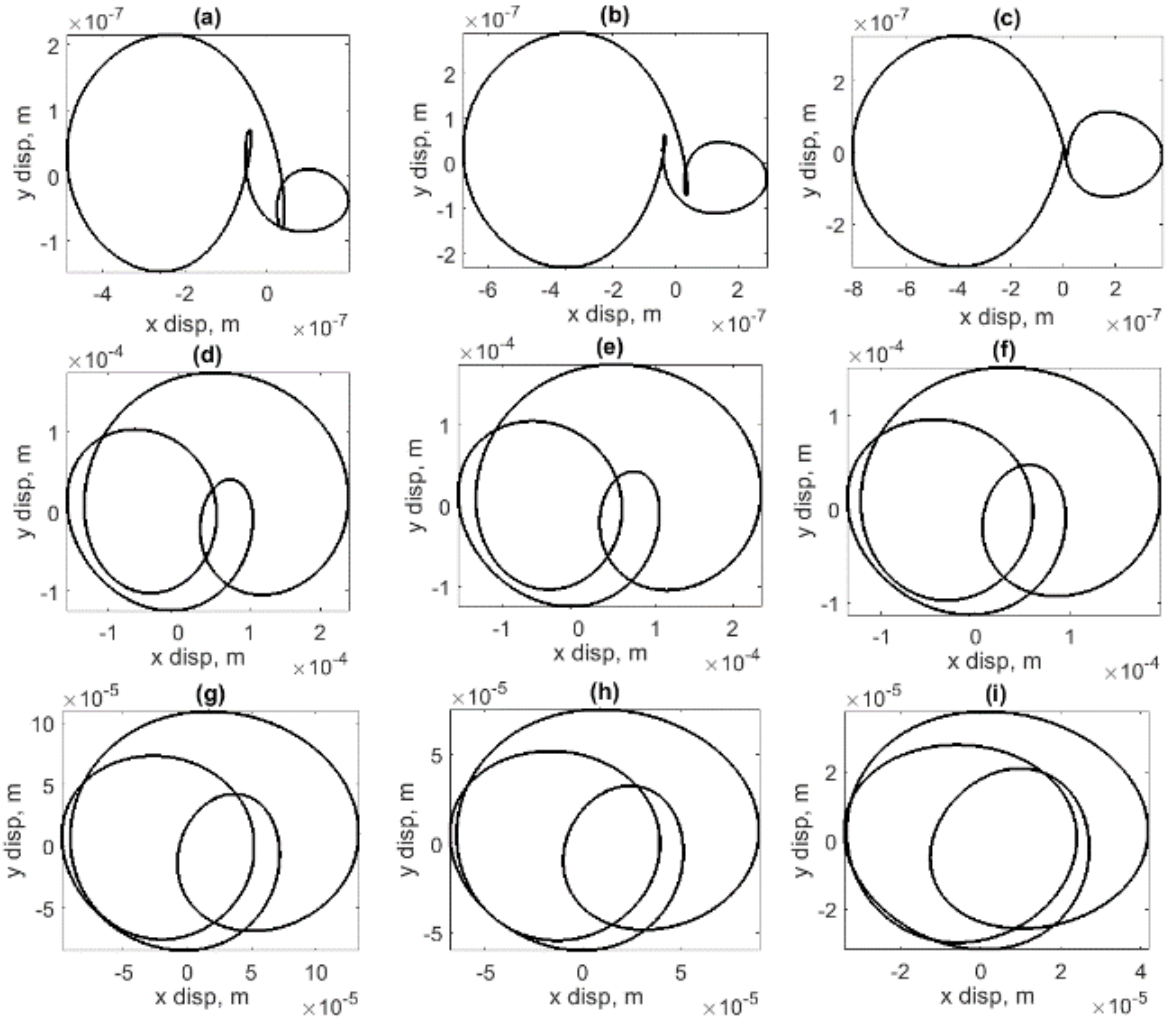

Figure 6-14 Orbits of inner rotor (a) B1 (b) D1 (c) Sp1 (d) Sp2 (e) AMB (f) mid-shaft (g) ISB (h) D4 (i) B4 at 70 Hz (both unbalances & coupling misalignment)

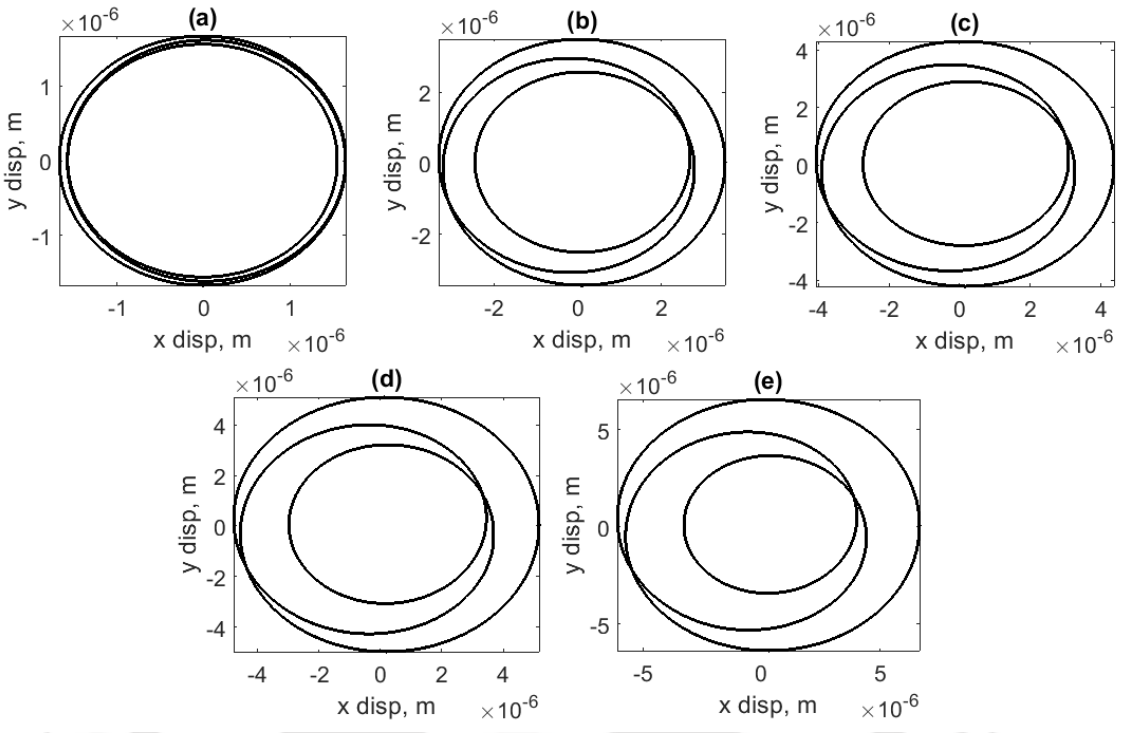

Figure 6-15 Orbits of outer rotor (a) B3 (b) D2 (c) mid-shaft (d) D3 (e) ISB at 70 Hz (unbalances on inner & outer rotors)

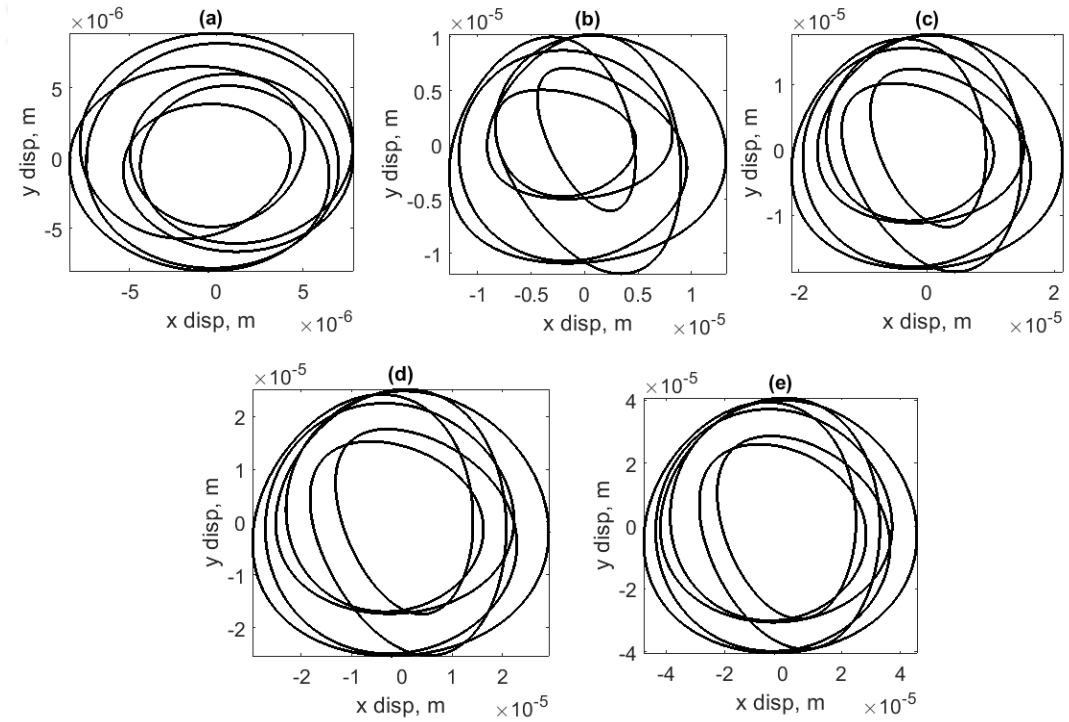

Figure 6-16 Orbits of outer rotor (a) B3 (b) D2 (c) mid-shaft (d) D3 (e) ISB at 70 Hz (Unbalances on inner & outer rotors)

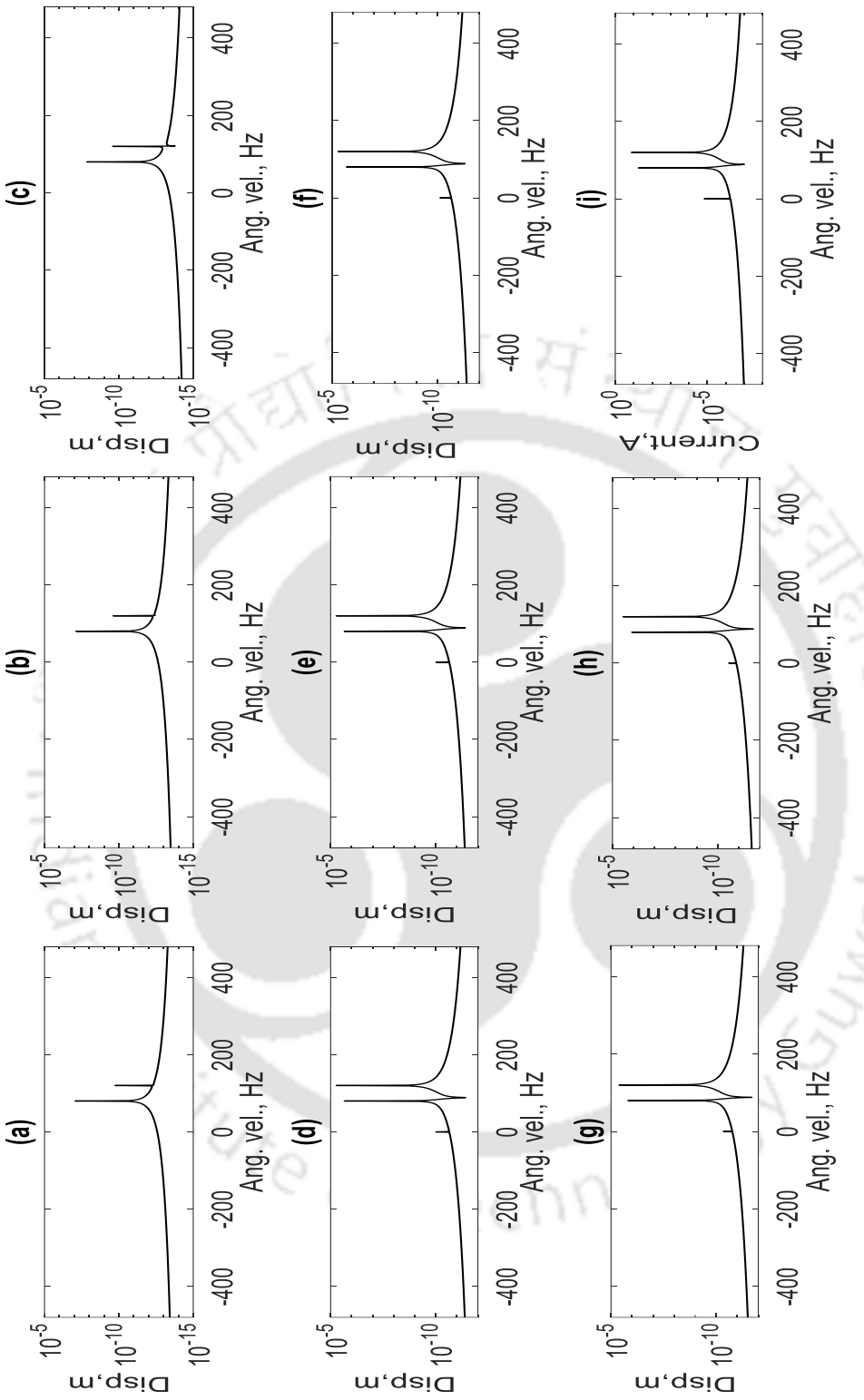

Figure 6-17 FFT of inner rotor (a) B1 (b) D1 (c) Sp1 (d) Sp2 (e) AMB (f) mid-shaft (g)ISB (h) D4 (i) B4 (Unbalances on inner & outer rotors)

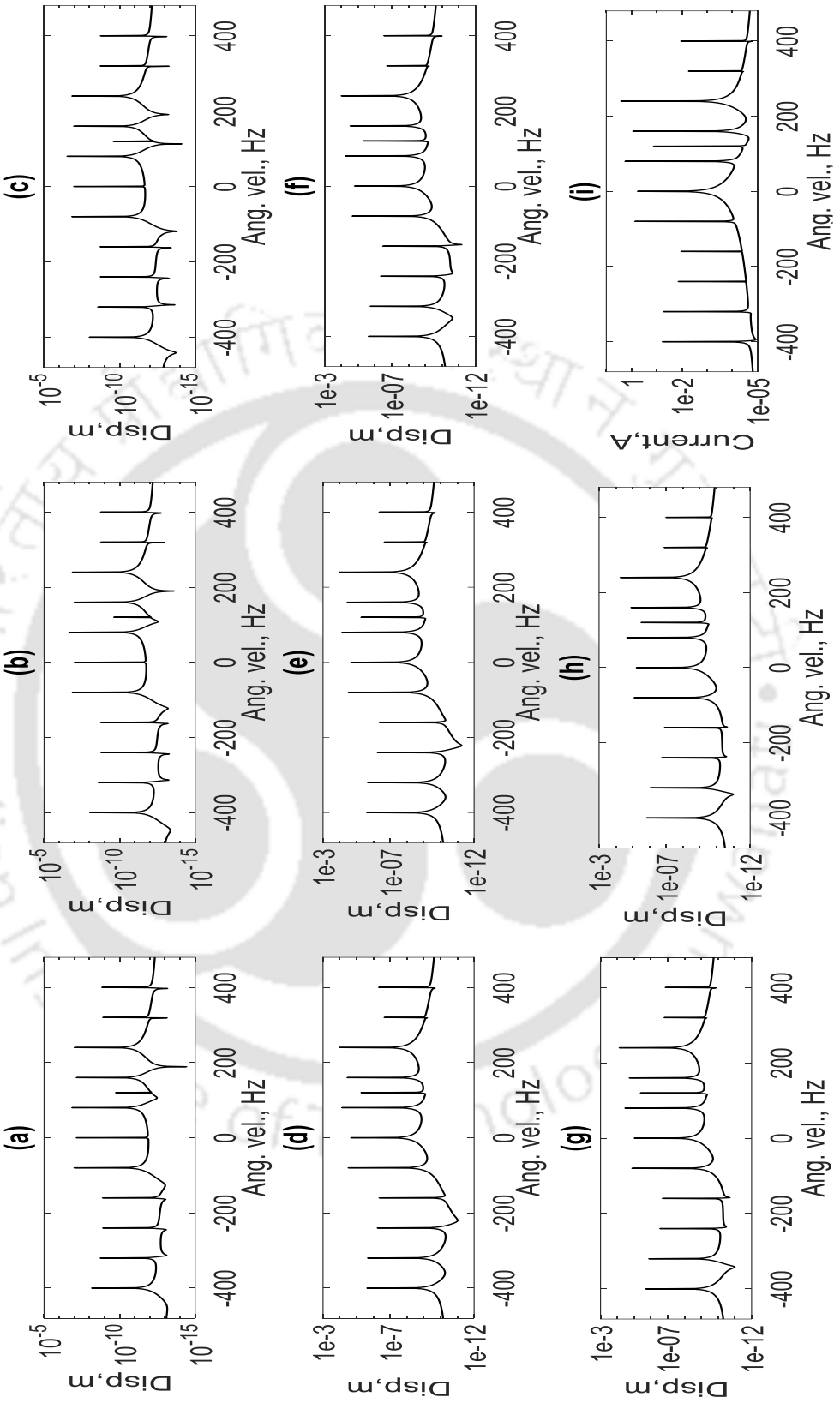

Figure 6-18 FFT of inner rotor (a) B1 (b) D1 (c) Sp1 (d) Sp2 (e) AMB (f) mid-shaft (g)ISB (h) D4 (i) B4 (both unbalances & coupling misalignment)

Figure 6-19 FFT of outer rotor: (a) B3 (b) D2 (c) mid-shaft (d) D3 (e) ISB (unbalances on inner and outer rotors)

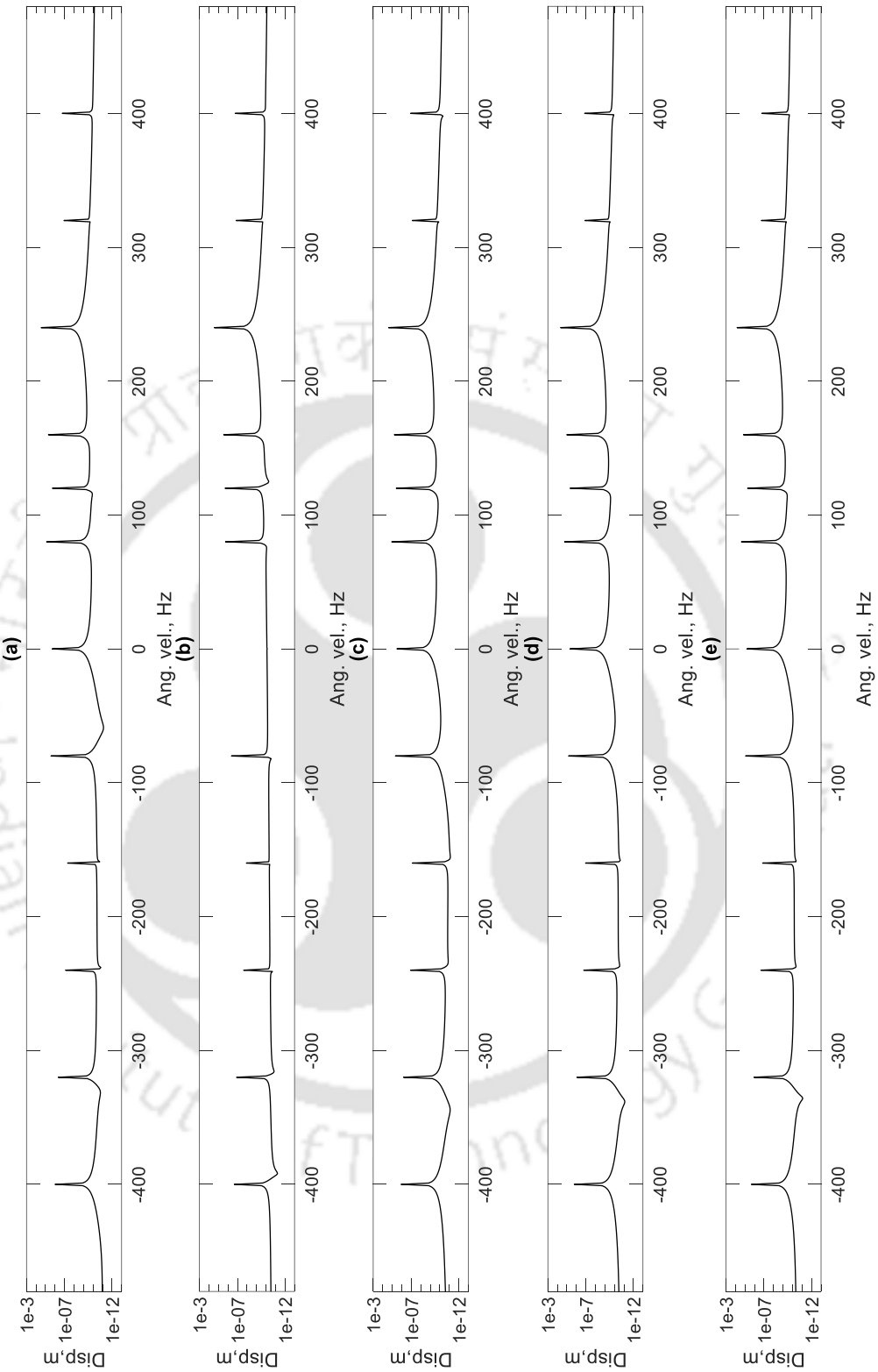

Figure 6-20 FFT of outer rotor (a) B3 (b) D2 (c) mid-shaft (d) D3 (e) ISB

This is similar to the behavior reported in existing literature (Wan et al, 2012). Likewise, Figure 6-18 and Figure 6-20 show multiple harmonics of vibration (-5, -1, 0, 1 …+5) in their full spectrum plots of vibration, which is the characteristic of misalignment as observed in experiments. Figure 6-15(i) and Figure 6-17(i) show the full spectrum of AMB current, which also exhibits multi-harmonic behavior similar to rotor vibration.

6.6.5 Identification of System Parameters

Table 6-6 (case of dynamic condensation) lists the parameters estimated from Eqn. (6.43), which is rearranged in the form of Eqn. (6.46), i.e. the linear least-squares regression form. The maximum error percentages noticed in various parameters even in the presence of measurement noise are: rotor unbalance (-1.38% @ 5% noise), bearing stiffness (-5.93% @ 5% noise), bearing damping (17.09% @ 5% noise), k_s (10.12% @ 5% noise), k_i (7.65% @ 5% noise), spline mean stiffness: k_{rad} (2.7% @2% noise), k_{ang} (-2.21% @ 2% noise), spline additive stiffness: $\Delta k_{\xi\xi}$ (1.% @ 2% noise), $\Delta k_{\eta\eta}$ (1.88% @ 2% noise), $\Delta k_{\varphi_\eta\varphi_\eta}$ (-7.08% @ 2% noise), $\Delta k_{\varphi_\xi\varphi_\xi}$ (-7.08% @ 0% noise), and $\Delta k_{\varphi_\xi\varphi_\xi}$ (0.69% @ 0% noise). It can be seen that all parameters except c_{b_1} are estimated within 10% error.

Similar trend is noticed in Table 6-7, where the bias in the mass and polar moment of inertia parameters is assumed. The high deviation of damping parameter can be attributed to the ignoring the damping matrix, **C**, in the derivation of $\mathbf{T}^d$. To study the influence of considering **G** matrix in the hybrid condensation on the estimated parameters four cases have been studied and compared in Table 6-8. Case (a) ignores **G** in the derivation of both $\mathbf{T}^d$ and $\mathbf{T}^h$. In case (b) **G** is ignored in the derivation of $\mathbf{T}^d$ and considered in $\mathbf{T}^h$ derivation, Case (c) considers **G** in $\mathbf{T}^d$ derivation and ignored in the derivation of $\mathbf{T}^h$ and Case (d) considers **G** in the derivation of both $\mathbf{T}^d$ and $\mathbf{T}^h$.

The values of three highest errors displayed and the corresponding parameters for the four cases are as follows: Case (a): k_s (79.13%), c_{b1} (28.34%), k_i (24.62%); Case (b): c_{b1} (27.79%), $\Delta k_{\xi\xi}$ (20.16%), c_{b3} (-17.15%); Case (c): c_{b1} (33.33%), c_{b3} (-24.49%), k_i (-19.61%); Case (d): c_{b1} (32.97%), k_s (-81.12%), k_i (-53.69%).

Table 6-6 Sensitivity of parameters to measurement noise at 74 Hz (Dynamic condensation)

Parameter	Assumed value	0% noise		2% noise		5% noise	
		Estimated value	Error %	Estimated value	Error %	Estimated value	Error %
e_1^{re}	6.5×10^{-5}	6.45×10^{-5}	-0.73	6.43×10^{-5}	-0.62	6.41×10^{-5}	-1.38
e_2^{re}	5.26×10^{-5}	5.21×10^{-5}	-0.88	5.21×10^{-5}	-0.03	5.26×10^{-5}	-0.03
e_3^{re}	5.23×10^{-5}	5.19×10^{-5}	-0.84	5.19×10^{-5}	0.05	5.23×10^{-5}	0.05
e_4^{re}	4.83×10^{-5}	4.79×10^{-5}	-0.80	4.79×10^{-5}	-0.01	4.83×10^{-5}	-0.01
e_5^{re}	9.2×10^{-6}	9.20×10^{-6}	-0.80	9.20×10^{-6}	-0.02	9.20×10^{-6}	-0.12
e_6^{re}	9.5×10^{-6}	9.40×10^{-6}	-0.70	9.40×10^{-6}	0.15	9.50×10^{-6}	0.15
e_1^{im}	3.75×10^{-5}	3.72×10^{-5}	-0.83	3.72×10^{-5}	0.07	3.76×10^{-5}	0.38
e_2^{im}	3.82×10^{-5}	3.79×10^{-5}	-0.84	3.79×10^{-5}	-0.01	3.82×10^{-5}	-0.01
e_3^{im}	1.7×10^{-5}	1.69×10^{-5}	-0.85	1.69×10^{-5}	0.04	1.70×10^{-5}	0.04
e_4^{im}	1.29×10^{-5}	1.28×10^{-5}	-0.85	1.28×10^{-5}	0.01	1.29×10^{-5}	0.01
e_5^{im}	3.8×10^{-6}	3.80×10^{-6}	-0.82	3.80×10^{-6}	0.01	3.80×10^{-6}	0.06
e_6^{im}	3.1×10^{-6}	3.10×10^{-6}	-0.71	3.10×10^{-6}	0.14	3.10×10^{-6}	0.14
k_{b1}	10×10^{6}	10.25×10^{6}	2.52	10.49×10^{6}	4.98	10.52×10^{6}	5.21
k_{b4}	16×10^{6}	15.81×10^{6}	-1.16	15.82×10^{6}	-1.12	15.82×10^{6}	-1.12
k_{b5}	8×10^{6}	8.09×10^{6}	1.17	8.11×10^{6}	1.45	8.11×10^{6}	1.45
k_{b3}	11×10^{6}	10.38×10^{6}	-5.57	10.34×10^{6}	-5.93	10.34×10^{6}	-5.93
c_{b1}	5.50×10^{3}	6.24×10^{3}	13.38	6.34×10^{3}	16.58	6.44×10^{3}	17.09
c_{b4}	3.00×10^{3}	3.02×10^{3}	0.68	3.03×10^{3}	0.63	3.02×10^{3}	0.63
c_{b5}	5.10×10^{3}	5.27×10^{3}	3.38	5.33×10^{3}	3.38	5.27×10^{3}	3.38
c_{b3}	5.40×10^{3}	5.01×10^{3}	-7.31	4.91×10^{3}	-7.61	4.99×10^{3}	-7.61
k_s	5.00×10^{5}	5.23×10^{5}	4.65	5.26×10^{5}	4.57	5.51×10^{5}	10.12
k_i	40	40.9	2.15	41	2.11	43.1	7.65
k_{rad}	1.5×10^{8}	1.52×10^{8}	1.15	1.50×10^{8}	2.11	1.52×10^{8}	1.04
k_{ang}	4.00×10^{5}	3.92×10^{5}	-2.07	3.89×10^{5}	-2.26	3.91×10^{5}	-2.23
$\Delta k_{\xi\xi}$	2.25×10^{7}	2.26×10^{7}	0.43	2.22×10^{7}	2.61	2.28×10^{7}	1.44
$\Delta k_{\eta\eta}$	2.325×10^{7}	2.33×10^{7}	0.33	2.30×10^{7}	1.88	2.34×10^{7}	0.77
$\Delta k_{\varphi_\eta\varphi_\eta}$	5.40×10^{4}	5.02×10^{4}	-7.08	4.97×10^{4}	-6.14	5.07×10^{4}	-6.12
$\Delta k_{\varphi_\xi\varphi_\xi}$	6.00×10^{4}	6.04×10^{4}	0.69	6.01×10^{4}	0.57	6.04×10^{4}	0.59

Table 6-7 Sensitivity of parameter estimation to modelling bias at 74 Hz (Dynamic condensation)

Parameter	Assumed value	0% noise		2% noise		5% noise	
		Estimated value	Error %	Estimated value	Error %	Estimated value	Error %
e_1^{re}	6.5×10^{-5}	6.45×10^{-5}	-0.73	6.49×10^{-5}	-0.15	6.41×10^{-5}	-1.33
e_2^{re}	5.26×10^{-5}	5.21×10^{-5}	-0.88	5.26×10^{-5}	-0.04	5.17×10^{-5}	-1.63
e_3^{re}	5.23×10^{-5}	5.19×10^{-5}	-0.84	5.23×10^{-5}	0.06	5.14×10^{-5}	-1.66
e_4^{re}	4.83×10^{-5}	4.79×10^{-5}	-0.80	4.83×10^{-5}	-0.01	4.76×10^{-5}	-1.52
e_5^{re}	9.2×10^{-6}	9.20×10^{-6}	-0.80	9.20×10^{-6}	-0.02	9.10×10^{-6}	-1.50
e_6^{re}	9.5×10^{-6}	9.40×10^{-6}	-0.70	9.50×10^{-6}	0.20	9.40×10^{-6}	-1.50
e_1^{im}	3.75×10^{-5}	3.72×10^{-5}	-0.83	3.75×10^{-5}	-0.05	3.69×10^{-5}	-1.59
e_2^{im}	3.82×10^{-5}	3.79×10^{-5}	-0.84	3.82×10^{-5}	-0.02	3.76×10^{-5}	-1.59
e_3^{im}	1.7×10^{-5}	1.69×10^{-5}	-0.85	1.70×10^{-5}	0.06	1.67×10^{-5}	-1.67
e_4^{im}	1.29×10^{-5}	1.28×10^{-5}	-0.85	1.29×10^{-5}	0.01	1.27×10^{-5}	-1.62
e_5^{im}	3.8×10^{-6}	3.80×10^{-6}	-0.82	3.80×10^{-6}	0.02	3.80×10^{-6}	-1.57
e_6^{im}	3.1×10^{-6}	3.10×10^{-6}	-0.71	3.10×10^{-6}	0.18	3.00×10^{-6}	-1.52
k_{b1}	10×10^6	10.25×10^6	2.52	10.29×10^6	2.98	10.2×10^6	2.06
k_{b4}	16×10^6	16.81×10^6	-1.16	15.78×10^6	-1.34	15.84×10^6	-1.00
k_{b5}	8×10^6	8.09×10^6	1.17	8.11×10^6	1.41	8.07×10^7	0.95
k_{b3}	11×10^6	10.38×10^6	-5.57	10.29×10^6	-6.43	10.47×10^6	-4.77
c_{b1}	5.50×10^3	6.24×10^3	13.38	6.37×10^3	15.80	6.11×10^3	11.15
c_{b4}	3.00×10^3	3.02×10^3	0.68	3.02×10^3	0.78	3.02×10^3	0.60
c_{b5}	5.10×10^3	5.27×10^3	3.38	5.30×10^3	3.99	5.24×10^3	2.81
c_{b3}	5.40×10^3	5.01×10^3	-7.31	4.95×10^3	-8.39	5.06×10^3	-6.30
k_s	5.00×10^5	5.23×10^5	4.65	5.28×10^5	5.54	5.19×10^5	3.84
k_i	40	40.9	2.15	41	2.56	40.7	1.77
k_{rad}	1.5×10^8	1.52×10^8	1.15	1.52×10^8	1.51	1.51×10^8	0.86
k_{ang}	4.00×10^5	3.92×10^5	-2.07	3.91×10^5	-2.18	3.92×10^5	-1.96
$\Delta k_{\xi\xi}$	2.25×10^7	2.26×10^7	0.43	2.29×10^7	1.61	2.24×10^7	-0.60
$\Delta k_{\eta\eta}$	2.325×10^7	2.33×10^7	0.33	2.36×10^7	1.53	2.31×10^7	-0.71
$\Delta k_{\varphi_\eta\varphi_\eta}$	5.40×10^4	5.02×10^4	-7.08	5.05×10^4	-6.42	4.99×10^4	-7.67
$\Delta k_{\varphi_\xi\varphi_\xi}$	6.00×10^4	6.04×10^4	0.69	6.08×10^4	1.40	6.00×10^4	0.04

Table 6-8: Effect of *K* and *G* in parameter estimation at 98 Hz (Hybrid condensation)

Parameter	(a) No *G* in (T^d, T^h)	(b) No *G* in T^d *G* in T^h	(c) *G* in T^d No *G* in T^h	(d) *G* in (T^d, T^h)
e_1^{re}	-2.52	-2.51	-2.48	-2.47
e_2^{re}	0.74	0.82	0.82	0.90
e_3^{re}	-9.71	-10.10	-9.63	-9.98
e_4^{re}	5.20	4.51	2.91	2.26
e_5^{re}	-5.84	-5.13	-2.74	-2.04
e_6^{re}	8.28	8.57	7.63	7.91
e_1^{im}	-1.34	0.02	-1.16	0.19
e_2^{im}	0.07	-0.10	-0.20	-0.37
e_3^{im}	-0.13	-0.85	-0.38	-1.03
e_4^{im}	6.37	13.71	8.06	15.55
e_5^{im}	-6.89	-9.61	-9.43	-12.19
e_6^{im}	2.02	2.27	6.31	6.53
k_{b1}	1.76	0.36	-0.73	-2.11
k_{b4}	-5.07	-5.38	-4.87	-5.18
k_{b5}	3.67	3.38	2.90	2.65
k_{b3}	-9.48	-8.91	-7.71	-7.22
c_{b1}	28.34	27.79	33.33	32.97
c_{b4}	13.84	7.26	2.16	-4.30
c_{b5}	7.45	9.71	11.90	14.22
c_{b3}	-12.43	-17.15	-24.49	-29.33
k_s	79.13	10.78	-10.56	-81.12
k_i	24.62	-8.09	-19.61	-53.69
k_{rad}	16.49	15.00	13.51	12.04
k_{ang}	1.80	2.12	2.06	2.38
$\Delta k_{\xi\xi}$	21.97	20.16	18.33	16.54
$\Delta k_{\eta\eta}$	15.49	14.28	13.25	12.08
$\Delta k_{\varphi_\eta\varphi_\eta}$	-1.86	-1.75	-1.84	-1.73
$\Delta k_{\varphi_\xi\varphi_\xi}$	6.35	6.60	6.64	6.89

It can be seen that Case (b) fares well compared to other cases. This is in line with the results obtained in Kuppa and Lal (2020), where both **M** and **G** matrices were considered in the derivation of $\mathbf{T}^h$. However, in the present work all three matrices **M**, **K**, **G** were considered in the derivation of $\mathbf{T}^h$. This shows that considering both **K**, **G** in the derivation of $\mathbf{T}^h$ gives better results than other cases.

6.7 Concluding Remarks

In this chapter, the mathematical model of angularly misaligned spline coupling that is commonly found in gas turbine DRS is developed. The spline model, consisting of both mean and fluctuating stiffness components, is integrated with dual rotor-bearing-AMB system. Four different steering functions are chosen to simulate the time varying behavior of spline coupling in translational and rotational directions. Campbell diagrams with references of the inner and outer rotor speeds are plotted. The critcal speeds with inner rotor excitation are found to be more than those of outer rotor due to gyroscopic effect. Two-way interaction of vibration responses between the inner and outer rotors through ISB is evident in orbits and full spectrum plots. The effect of incorporating AMB is observed by the reduction in the critical speeds of the DRS compared to a rotor system supported on all REBs. The identification algorithms utilizing dynamic and hybrid condensations performed reasonably well in the presence of measurement error and modelling bias. A comparative study of the influence of gyroscopic matrix in the derivation of transformation matrix of dynamic and hybrid condensation procedures was carried out by examining four different cases. It has been found that considering gyroscopic matrix in hybrid condensation alone yielded the best results compared to other cases.

CHAPTER 7

Summary and Conclusion

7.1 Introduction

This chapter summarizes, compares and contrasts the mathematical models and simulation results presented in Chapters 2 through Chapter 6. The method of application of the identification algorithm for condition monitoring of misalignment is explained. The advantages and drawbacks of the proposed method are explained. Lastly a discussion on the scope for future work is given.

7.2 Summary

In the present work the principal focus is laid on the development of mathematical model of an intermediate coupling connecting two rotors subjected to misalignment and identification of misalignment. The stiffness of coupling is modelled as the sum of static stiffness and time-dependent additive stiffness. Static stiffness is the value of coupling listed in the catalogue and essentially remains unchanged with or without misalignment. Additive stiffness is a time-varying stiffness component which displays multi-harmonic behaviour and exists only in the presence of misalignment. The magnitude of additive coupling stiffness (ACS) is proportional to the amount of misalignment in a specific direction. In other words, its magnitude in a given direction indicates the severity of misalignment in that direction. Due to unequal ACS coefficients the coupling's stiffness is asymmetric during operation. To numerically simulate the multi-harmonic nature of coupling forces/moments as observed in experiments, a pulse wave is used as the steering function in the mathematical model of the additive coupling stiffness (ACS). The active magnetic bearing (AMB) which acts as an auxiliary/main support on the rotor train attenuates the multi harmonic vibration produced by misalignment. The identification algorithm is a linear least squares problem used to estimate the static and additive stiffness of coupling, equivalent viscous damping of shafts, unbalance of discs, stiffness and damping of bearings and AMB displacement and current constants. The amplitude and phase of positive and negative harmonics of rotor vibration and AMB current obtained from full spectrum fft are the inputs to the identification algorithm.

In Chapter 2 a simple model consisting of coupled Jeffcott rotors with central discs and auxiliary AMB is presented. Only angular misalignment of coupling is considered in this chapter. A helical torsion spring is used to model the coupling. Weight-dominance criteria is assumed to develop a linear relationship between the slopes at coupling locations and the translational displacements at disc locations. The expressions for potential energy, kinetic energy of rotor- coupling system are written in terms of generalized coordinates of the rotor i.e. the two translational displacements at the discs. Lagrange's equation is used to write the EOM of the coupled rotor system. The stiffness of the coupling subjected to misalignment is written as the sum of direct stiffness and additive coupling stiffness (ACS). A steering function is used to model the multiharmonic nature of misalignment force. The EOM of rotor-coupling-AMB system is converted into frequency domain and rearranged in the form of a linear least squares problem. The amplitude and phase of rotor vibration and AMB current are used to estimate the unknown parameters. The identification procedure is performed using the data at discrete speeds and cumulative data from a range of speeds. The latter case yields better estimates. The estimates compare well with the assumed values even in the presence of measurement noise.

In Chapter 3 a more complex model of coupled Jeffcott rotors with offset discs is considered. The generalized coordinates of the rotor system now consist of both translational and rotational DOF i.e. displacement and tilt at disc locations. The EOM are obtained by applying Lagrange's equations on the expressions of potential and kinetic energies. Dynamic condensation procedure is performed on the EOM to eliminate rotational DOFs of the discs. The presence of offset discs has caused a slight increase in the critical speeds of the rotor system. The estimates show more deviation compared to the case of central discs due to the fact that regression equations used in least squares problem are obtained from condensed EOM.

In Chapter 5 the problem is extended to TG sets supported on tilting pad bearings and AMBs. The coefficients of bearings, AMBs and coupling are assumed to be speed-dependent. To get round the difficulty of measuring angular DOFs hybrid condensation is performed subsequent to dynamic condensation. The estimation procedure is performed at six discrete speeds within the operating range of the TG. The identification algorithm showed robustness against measurement noise and modelling bias.

Chapter	Rotor type	Bearing type	Coupling type	AMB purpose	Misalignment type	EOM obtained from	Condensation type
2	Jeffcott with central disc	Rigid	Flexible	Auxiliary support	Angular	Lagrange's eqn.	-
3	Jeffcott with offset disc	Rigid	Flexible	Auxiliary support	Angular	Lagrange's eqn.	Dynamic
4	TG	Flexible (REB)	Rigid/ Flexible	Auxiliary support	Angular and Parallel	FEM	Dynamic
5	TG	Flexible (JB & TPJB)	Rigid/ Flexible	Main support	Angular and Parallel	FEM	Hybrid
6	Gas Turbine	Flexible (REB)	Spline	Main support	Angular	FEM	Hybrid

In Chapter 6 modelling and analysis of twin spool gas turbine rotor supported on rolling element bearings and AMBs is presented. The inner and outer rotors run at different speeds and are connected mechanically by an Inter-shaft bearing. The model of spline coupling with angular misalignment on inner rotor is considered in this chapter. It has been observed that there is a two-way transmission of unbalance forces from inner rotor to the outer rotor through the Inter-shaft bearing. Likewise, misalignment forces transmit from inner to outer rotor. Due to the lesser stiffness of AMB compared to a typical rolling element bearing the critical speeds on the Campbell diagrams are found to be lower. The estimates of unknown parameters are found to be close to the assumed values against measurement noise.

7.3 Conclusions from the Present Work

The present work advances the state-of-the-art in model-based identification of misalignment in rotor-AMB systems. The following are the conclusions

- The principal contribution of the present work is the use of AMB as a condition monitoring tool apart from it being used as an auxiliary bearing or support bearing.
- The model of angularly misaligned coupling present in simple rotors with central discs is based on the linear relationship between coupling slopes and disc translational displacements. This relationship is developed from the assumptions of weight dominance criteria and flexible coupling. The time-varying nature of coupling misalignment force is simulated using a periodic function which is selected to produce the multiharmonic behavior as observed in experiments. Lagranges's equation have been used to derive the EOMs from the expressions of kinetic energy, potential energy and dissipative energy.The time domain response of disc vibration and AMB current is obtained from Simulink^{TM} model built from the global EOM. Full spectrum FFT is used to extract the amplitude and phase of harmonics of rotor vibration and AMB current. The unknown parameters of rotor-AMB-coupling system are estimated from linear least-squares identification algorithm built from the EOM in frequency domain. The values of coupling's static stiffness, additive stiffness, Disc's unbalance and AMB constants were estimated using data obtained at a single speed and from a range of speeds away from the resonant frequency of the coupled rotor system. In both cases the maximum error noticed was within 4% even when the data is corrupted with 5%

Gaussian noise levels. The identification algorithm developed helps in quantitatively assessing the ACS coefficient generated due to angular misalignment.

- For the case of simple rotors with offset discs dynamic condensation has been performed to eliminate the rotational DOFs before converting the global EOMs into frequency domain. Increasing the value of proportional constant has resulted in an increase in the critical speed of rotor system thereby providing wider operating range. The estimates of shaft damping and AMB displacement stiffness have shown high error values when data from single speed is used. This problem has been overcome by considering data from multiple speeds. The maximum deviation of the estimates from the assumed values is less than 10% even for the case of 5% measurement noise and modelling bias. Nonetheless these margins are more than those obtained for the case of central discs. This comparatively more deviation can be attributed to dynamic condensation procedure.
- For the case of turbine-generators with auxiliary AMBs mathematical model of rotor system is developed using Timoshenko beam finite elements. Both parallel and angular misalignments have been considered in the mathematical model of coupling which is developed from the vector of static deflections at coupling's nodal locations. Unlike the previous cases this model is applicable for both rigid and flexible couplings. Dynamic condensation has been performed to eliminate the DOFs where there is no external forcing. The error percentage in parameters with up to 2% Gaussian noise levels is less than 15%. For 5% measurement noise levels ACS coefficients showed high deviation. The algorithm is found to be more sensitive to measurement noise than to modelling bias. This identification algorithm considers data from translational DOFs and rotational DOFs at both ends of coupling. The data acquisition of rotational DOFs poses more difficulty than that of translational DOFs. It would be advantageous to eliminate coupling's rotational DOF before identification algorithm is developed.
- For the case of rotors supported on speed-dependent tilting pad journal bearings and speed-dependent AMBs, the additive stiffness of coupling has been modeled as a speed-dependent parameter. In the present case rotational DOF of coupling are eliminated from the global EOM by hybrid condensation. The identification of speed dependent parameters is performed at six different speeds and the estimates obtained

are found to be within 20% of the assumed values even in the presence of 5% Gaussian noise.

- The numerical analysis of dual rotor systems where angular misalignment is present only on inner rotor spline coupling has been performed. The responses of both inner and outer rotors are found to exhibit multi-harmonic behavior due to the presence of inter-shaft bearing. Studies by earlier researchers revealed that spline couplings exhibit different periodic behavior in transverse and rotational directional in the presence of angular misalignment. To account for that four different steering functions have been used in the coupling model. Four different cases of hybrid condensation have been tested for their effectiveness in parameter estimation. The case where gyroscopic matrix was considered in addition to mass and stiffness matrices yielded the closest estimates.

7.4 General Recommendations from the Thesis

- The development of the misaligned coupling model using additive stiffness component is a new deviation from the earlier works. The coupling model can be used for parallel, angular and combined misalignment conditions.
- The severity of misalignment has been quantified by estimating the amplitude of positive and negative harmonics of ACS coefficients. This is a novel approach which has not been explored hitherto. Since misalignment produces *both* forward and backward harmonics of vibration full spectrum data is mandatorily required to estimate the coefficients correctly. Since the data pertaining to backward whirl is missing in one-directional FFT it may not yield accurate estimates of parameters.
- Misalignment fault which exhibits multi-harmonic behavior can be identified using model based approach in frequency domain.
- The coupling model can be integrated with the models of simple laboratory test rotors, multi-stage turbo-generators and industrial gas turbines as well.

7.5 Method of Application

- The hardware set up required to implement the identification algorithms developed in chapters 2 through 6 on the respective misaligned coupled rotor test rigs is shown in **Appendix H**.
- The field engineer should begin by noting initial alignment readings in all directions before the run is made.
- The rotor vibration data from proximity probes and AMB current data obtained from a single run or multiple runs of an aligned rotor are recorded
- This data is passed through full spectrum FFT to obtain the real and imaginary parts of integer harmonics of vibration and current
- These coefficients are input to the identification algorithm to estimate the ACS coefficients
- The ACS coefficients obtained are mapped against the alignment readings of the aligned rotor.
- As the machine is put into operation ACS coefficients are estimated periodically.
- When higher stiffness coefficients are observed, the machine is stopped and again checked for alignment.
- These higher stiffness coefficients are then mapped to the values of the misaligned condition
- A look up table/graph prepared from the readings collected over the duration of many runs will aid the engineer to directly estimate the misalignment when the machine is in operation.

7.6 Limitations

- This mathematical model and identification algorithm assumes that the only faults present in the rotor trains are unbalance and misalignment.Other faults such as cracks, rubs have not been considered.
- The coupling model is based on weight-dominance criterion which relies on the static deflections at the coupling nodes. These values can be obtained from catenary curve or

static deflection curve. This however requires the geometric and material properties of rotors along with the support stiffness values of all the mainline bearings. In the absence of these values development of identification algorithm for a given rotor system becomes challenging

- The identification algorithm necessarily uses data from full spectrum plots. As full spectrum is the spectrum of an orbit two probes are required at each measurement location. In large TG sets the number of probes required for data acquisition will be twice the number of necessary measurement locations which can become a large number.
- Due to the restrictions posed by the general arrangement of rotors all the required locations may not be accessible for measurement and data acquisition.
- When AMB is used as main support its comparatively lesser load carrying capacity may pose a restriction on the weight of the rotor it can support.

7.7 Scope for Future Work

- The methodology can be validated experimentally on a laboratory test rig using shims to induce misalignment. For a given type of coupling the values of ACS coefficients for various amounts of misalignment can throw light on the dynamic behavior of the misaligned coupling. Theoretically the same amount of misalignment should produce different ACS coefficients in rigid and flexible couplings.
- The coupling model can be further improved by considering the vibration at coupling locations along with the static deflections. This discards the assumption of weight dominance and makes the coupling model more complete. The misalignment of drive end coupling too can be considered in the model
- Uncertainty analysis to study the discrepancies between analytical model and actual system can be performed.
- The number of measurement locations can be reduced by hybrid condensation to make the methodology more relevant to industrial rotors. However this leads to a very high condition number of the regression matrix. Various regularization techniques can be employed to improve the condition number.

- Obtaining the data of harmonics of vibration and current at multiple speeds to improve the condition number of the regression matrix requires running the rotor at many different speeds which is time consuming. The possibility of extracting the harmonics of all integer speeds by ramping up or ramping down the rotor can be explored as it saves lot of time and effort.
- The effect of rotor acceleration on the coupling forces and moments in misaligned rotor systems could be researched.
- Identifying and distinguishing crack and misalignment, when they are simultaneously present in the rotor system, could be explored.

Appendix A: Deflection of Simply Supported Beam

Deflection at any section of simply supported beam with an offset disc (Gere and Timoshenko)

$$y = \frac{Pbx}{6lEI}(l^2 - x^2 - b^2) \text{ for } 0 < x < a$$
$$y = \frac{Pb}{6lEI}\left[\frac{l}{b}(x-a)^3 + (l^2 - b^2)x - x^3\right] \text{ for } a < x < l \quad \text{(A-1)}$$

The slopes at the left and right supports which correspond to bearings/coupling locations

$$\varphi_{c_1} = -\frac{Pb(l^2 - b^2)}{6lEI}; \qquad \varphi_{c_2} = \frac{Pa(l^2 - a^2)}{6lEI} \quad \text{(A-2)}$$

where, l is the shaft length, a and b are the distances of the disc from left and right supports respectively, x is the distance of a given section from left support, P is point load, E is young's modulus and I is the polar mass moment of inertia of disc.

Appendix B: Coupled Rotor with Central Discs: Matrices and Vectors in Real Coordinates

$$\mathbf{M}_1 = \begin{pmatrix} m_1 & 0 \\ 0 & m_1 \end{pmatrix}; \mathbf{M}_2 = \begin{pmatrix} m_2 & 0 \\ 0 & m_2 \end{pmatrix};$$
$$\mathbf{K}_1 = \begin{pmatrix} k_{1xx} & 0 \\ 0 & k_{1xx} \end{pmatrix}; \mathbf{K}_2 = \begin{pmatrix} k_{2xx} & 0 \\ 0 & k_{2xx} \end{pmatrix}$$
$$\mathbf{K}_{\varphi_c} = \begin{pmatrix} k_{\varphi_c} & 0 \\ 0 & k_{\varphi_c} \end{pmatrix}; \mathbf{C}_1 = \begin{pmatrix} c_{1xx} & 0 \\ 0 & c_{1xx} \end{pmatrix}; \mathbf{C}_2 = \begin{pmatrix} c_{2xx} & 0 \\ 0 & c_{2xx} \end{pmatrix}$$
$$\mathbf{f}_{unb_1} = \begin{pmatrix} m_1 e_1 \omega^2 \cos(\omega t + \beta_1) \\ m_1 e_1 \omega^2 \sin(\omega t + \beta_1) \end{pmatrix}; \mathbf{f}_{unb_2} = \begin{pmatrix} m_2 e_2 \omega^2 \cos(\omega t + \beta_2) \\ m_2 e_2 \omega^2 \sin(\omega t + \beta_2) \end{pmatrix}$$

Appendix C: Coupled Rotor with Offset Discs: Matrices and Vectors in Real Coordinates

$$\mathbf{M}_1 = \begin{Bmatrix} m_1 & 0 & 0 & 0 \\ 0 & m_1 & 0 & 0 \\ 0 & 0 & I_{d_1} & 0 \\ 0 & 0 & 0 & I_{d_1} \end{Bmatrix}; \mathbf{M}_2 = \begin{Bmatrix} m_2 & 0 & 0 & 0 \\ 0 & m_2 & 0 & 0 \\ 0 & 0 & I_{d_2} & 0 \\ 0 & 0 & 0 & I_{d_2} \end{Bmatrix}$$

$$\mathbf{K}_1=\begin{bmatrix} k_{1xx} & 0 & k_{1x\varphi_y} & 0 \\ 0 & k_{1xx} & 0 & k_{1x\varphi_y} \\ k_{1\varphi_y x} & 0 & k_{1\varphi_y\varphi_y} & 0 \\ 0 & k_{1\varphi_y x} & 0 & k_{1\varphi_y\varphi_y} \end{bmatrix};\mathbf{K}_2=\begin{bmatrix} k_{2xx} & 0 & k_{2x\varphi_y} & 0 \\ 0 & k_{2xx} & 0 & k_{2x\varphi_y} \\ k_{2\varphi_y x} & 0 & k_{2\varphi_y\varphi_y} & 0 \\ 0 & k_{2\varphi_y x} & 0 & k_{2\varphi_y\varphi_y} \end{bmatrix}$$

$$\mathbf{G}_1=\begin{bmatrix} 0 & 0 & 0 & 0 \\ 0 & 0 & 0 & 0 \\ 0 & 0 & 0 & I_{p_1} \\ 0 & 0 & -I_{p_1} & 0 \end{bmatrix};\mathbf{G}_2=\begin{bmatrix} 0 & 0 & 0 & 0 \\ 0 & 0 & 0 & 0 \\ 0 & 0 & 0 & I_{p_2} \\ 0 & 0 & -I_{p_2} & 0 \end{bmatrix}$$

$$\mathbf{C}_1=\begin{bmatrix} c_{1xx} & 0 & c_{1x\varphi_y} & 0 \\ 0 & c_{1xx} & 0 & c_{1x\varphi_y} \\ c_{1\varphi_y x} & 0 & c_{1\varphi_y\varphi_y} & 0 \\ 0 & c_{1\varphi_y x} & 0 & c_{1\varphi_y\varphi_y} \end{bmatrix};\mathbf{C}_2=\begin{bmatrix} c_{2xx} & 0 & c_{2x\varphi_y} & 0 \\ 0 & c_{2xx} & 0 & c_{2x\varphi_y} \\ c_{2\varphi_y x} & 0 & c_{2\varphi_y\varphi_y} & 0 \\ 0 & c_{2\varphi_y x} & 0 & c_{2\varphi_y\varphi_y} \end{bmatrix}$$

$$\mathbf{K}_{\varphi_c}=\begin{bmatrix} k_{\varphi_c} & 0 & 0 & 0 \\ 0 & k_{\varphi_c} & 0 & 0 \\ 0 & 0 & 0 & 0 \\ 0 & 0 & 0 & 0 \end{bmatrix}$$

Appendix D: Elemental Matrices for Assembling Global Matrices

Translational mass matrix

$$\mathbf{M}_T=\frac{\rho A_r l_e}{420(1+\Phi)^2}\begin{bmatrix} m_1 & m_2 & m_3 & m_4 \\ m_2 & m_5 & -m_4 & m_6 \\ m_3 & -m_4 & m_1 & -m_2 \\ m_4 & m_6 & -m_2 & m_5 \end{bmatrix} \quad \text{(D-1)}$$

$m_1=\left(156+294\Phi+140\Phi^2\right)$ $m_2=l_e\left(22+38.5\Phi+17.5\Phi^2\right)$

$m_3=\left(54+126\Phi+70\Phi^2\right)$ $m_4=l_e\left(-13-31.5\Phi-17.5\Phi^2\right)$

$m_5=l_e^2\left(4+7\Phi+3.5\Phi^2\right)$ $m_6=l_e^2\left(-3-7\Phi-3.5\Phi^2\right)$

Rotational mass matrix

$$\mathbf{M}_R=\frac{\rho I_e}{30l_e(1+\Phi)^2}\begin{bmatrix} n_1 & n_2 & -n_1 & n_2 \\ n_2 & n_3 & -n_2 & n_4 \\ -n_1 & -n_2 & n_1 & -n_2 \\ n_2 & n_4 & -n_2 & n_3 \end{bmatrix} \quad \text{(D-2)}$$

$n_1 = 36 \quad n_2 = l_e\left(3-15\Phi\right)$

$n_3 = l_e^2\left(4+5\Phi+10\Phi^2\right) \quad n_4 = l_e^2\left(-1-5\Phi+5\Phi^2\right)$

Stiffness matrix

$$\mathbf{K}_s = \frac{EI_e}{l_e^3\left(1+\Phi\right)}\begin{bmatrix} k_1 & k_2 & -k_1 & k_2 \\ k_2 & k_3 & -k_2 & k_4 \\ -k_1 & -k_2 & k_1 & -k_2 \\ k_2 & k_4 & -k_2 & k_3 \end{bmatrix} \tag{D-3}$$

$k_1 = 12 \quad k_2 = 6le \quad k_3 = \left(4+\Phi\right)l_e^2 \quad k_4 = \left(2-\Phi\right)l_e^2$

Gyroscopic matrix

$$\mathbf{G}_s = \frac{\rho I_e}{15l_e\left(1+\Phi\right)^2}\begin{bmatrix} n_1 & n_2 & -n_1 & n_2 \\ n_2 & n_3 & -n_2 & n_4 \\ -n_1 & -n_2 & n_1 & -n_2 \\ n_2 & n_4 & -n_2 & n_3 \end{bmatrix} \tag{D-4}$$

$n_1 = 36 \quad n_2 = l_e\left(2\text{-}\,15\Phi\right) \quad n_3 = l_e^2\left(4+5\Phi+10\Phi^2\right) \quad n_4 = l_e^2\left(-1-5\Phi+5\Phi^2\right)$

l_e is the shaft length, E is young's modulus and I_e is the polar inertia of shaft. $\Phi = 12EI_e / \left(0.886A_r Gl_e^2\right)$

Disc mass matrix

$$\mathbf{M}_d = \begin{bmatrix} m_{d_1} & 0 \\ 0 & I_{d_1} \end{bmatrix} \tag{D-5}$$

Disc gyroscopic matrix

$$\mathbf{G}_d = \begin{bmatrix} 0 & 0 \\ 0 & -I_{p_1} \end{bmatrix} \tag{D-6}$$

m_{d_1} is the shaft length, I_e is the polar inertia of shaft.

Appendix E: Elemental Matrices for Plotting Catenary Curve

Shaft stiffness matrix

$$\mathbf{K}^{re} = \frac{EI_e}{l_e^3(1+\Phi)}\begin{bmatrix} k_{11} & 0 & 0 & k_{41} & k_{51} & 0 & 0 & k_{81} \\ 0 & k_{22} & k_{32} & 0 & 0 & k_{62} & k_{72} & 0 \\ 0 & k_{32} & k_{33} & 0 & 0 & k_{63} & k_{73} & 0 \\ k_{41} & 0 & 0 & k_{44} & k_{54} & 0 & 0 & k_{84} \\ k_{51} & 0 & 0 & k_{54} & k_{55} & 0 & 0 & k_{85} \\ 0 & k_{62} & k_{63} & 0 & 0 & k_{66} & k_{76} & 0 \\ 0 & k_{72} & k_{73} & 0 & 0 & k_{76} & k_{77} & 0 \\ k_{81} & 0 & 0 & k_{84} & k_{85} & 0 & 0 & k_{88} \end{bmatrix} \quad \text{(E-1)}$$

$k_{22} = k_{11}; k_{33} = k_{44}; k_{66} = k_{55}; k_{77} = k_{88}; k_{32} = -k_{41}$

$k_{62} = k_{51}; k_{72} = -k_{81}; k_{63} = -k_{54}; k_{73} = k_{84}; k_{76} = -k_{85}$

$k_{11} = 12; k_{41} = 6l_e; k_{51} = -12; k_{81} = 6l_e; k_{44} = (4+\Phi)l_e^2$

$k_{54} = -6l_e; k_{84} = (2-\Phi)l_e^2; k_{55} = 12; k_{85} = -6l_e; k_{88} = (4+\Phi)l_e^2$

Shaft translational mass matrix

$$\mathbf{M}^{re} = \frac{\rho A_r l_e}{420(1+\Phi)^2}\begin{bmatrix} m_{11} & 0 & 0 & m_{41} & m_{51} & 0 & 0 & m_{81} \\ 0 & m_{22} & m_{32} & 0 & 0 & m_{62} & m_{72} & 0 \\ 0 & m_{32} & m_{33} & 0 & 0 & m_{63} & m_{73} & 0 \\ m_{41} & 0 & 0 & m_{44} & m_{54} & 0 & 0 & m_{84} \\ m_{51} & 0 & 0 & m_{54} & m_{55} & 0 & 0 & m_{85} \\ 0 & m_{62} & m_{63} & 0 & 0 & m_{66} & m_{76} & 0 \\ 0 & m_{72} & m_{73} & 0 & 0 & m_{76} & m_{77} & 0 \\ m_{81} & 0 & 0 & m_{84} & m_{85} & 0 & 0 & m_{88} \end{bmatrix} \quad \text{(E-2)}$$

$m_{54} = -m_{81}; m_{55} = m_{11}; m_{85} = -m_{41}; m_{88} = m_{44}$

$m_{11} = (156 + 294\Phi + 140\Phi^2); m_{41} = l_e(22 + 38.5\Phi + 17.5\Phi^2)$

$m_{51} = (54 + 126\Phi + 70\Phi^2); m_{81} = l_e(-13 - 31.5\Phi - 17.5\Phi^2)$

$m_{44} = l_e^2(4 + 7\Phi + 3.5\Phi^2) \quad m_{84} = l_e^2(-3 - 7\Phi - 3.5\Phi^2)$

Shaft rotational mass matrix

$$\mathbf{M}^{re}=\frac{\rho I_e}{30l_e\left(1+\Phi\right)^2}\begin{bmatrix} n_{11} & 0 & 0 & n_{41} & n_{51} & 0 & 0 & n_{81} \\ 0 & n_{22} & n_{32} & 0 & 0 & n_{62} & n_{72} & 0 \\ 0 & n_{32} & n_{33} & 0 & 0 & n_{63} & n_{73} & 0 \\ n_{41} & 0 & 0 & n_{44} & n_{54} & 0 & 0 & n_{84} \\ n_{51} & 0 & 0 & n_{54} & n_{55} & 0 & 0 & n_{85} \\ 0 & n_{62} & n_{63} & 0 & 0 & n_{66} & n_{76} & 0 \\ 0 & n_{72} & n_{73} & 0 & 0 & n_{76} & n_{77} & 0 \\ n_{81} & 0 & 0 & n_{84} & n_{85} & 0 & 0 & n_{88} \end{bmatrix} \tag{E-3}$$

$n_{11} = 36 \quad n_{41} = l_e\left(3 - 15\Phi\right)$

$n_{44}=l_e^2\left(4+5\Phi+10\Phi^2\right) \quad n_{84}=l_e^2\left(-1-5\Phi+5\Phi^2\right)$

$n_{51}=-n_{11};\ n_{81}=n_{41};\ n_{54}=-n_{81};\ n_{55}=n_{11}$

$n_{85}=-n_{41};\ n_{88}=n_{44};\ n_{22}=n_{11};\ n_{33}=n_{44}$

$n_{66}=n_{55};\ n_{77}=n_{88};\ n_{32}=-n_{41};\ n_{62}=n_{51};$

$n_{72}=-n_{81};\ n_{63}=-n_{54};\ n_{73}=n_{84};\ n_{76}=-n_{85}$

$\Phi=12EI_e/\left(0.886A_rGl_e^2\right)$

Appendix F: Elements of $\tilde{\mathbf{K}}$ matrix

$$\tilde{\mathbf{K}}=\mathbf{T}^T\mathbf{K}\mathbf{T}=\begin{bmatrix} \tilde{k}_{xx} & \tilde{k}_{xy} & 0 & 0 & -\tilde{k}_{xx} & -\tilde{k}_{xy} & 0 & 0 \\ \tilde{k}_{yx} & \tilde{k}_{yy} & 0 & 0 & -\tilde{k}_{yx} & -\tilde{k}_{yy} & 0 & 0 \\ 0 & 0 & \tilde{k}_{\varphi_y\varphi_y} & \tilde{k}_{\varphi_y\varphi_x} & 0 & 0 & -\tilde{k}_{\varphi_y\varphi_y} & -\tilde{k}_{\varphi_y\varphi_x} \\ 0 & 0 & \tilde{k}_{\varphi_x\varphi_y} & \tilde{k}_{\varphi_x\varphi_x} & 0 & 0 & -\tilde{k}_{\varphi_x\varphi_y} & -\tilde{k}_{\varphi_x\varphi_x} \\ -\tilde{k}_{xx} & -\tilde{k}_{xy} & 0 & 0 & \tilde{k}_{xx} & \bar{k}_{xy} & 0 & 0 \\ -\tilde{k}_{yx} & -\tilde{k}_{yy} & 0 & 0 & \tilde{k}_{yx} & \tilde{k}_{yy} & 0 & 0 \\ 0 & 0 & -\tilde{k}_{\varphi_y\varphi_y} & \tilde{k}_{\varphi_y\varphi_x} & 0 & 0 & \tilde{k}_{\varphi_y\varphi_y} & \tilde{k}_{\varphi_y\varphi_x} \\ 0 & 0 & -\tilde{k}_{\varphi_x\varphi_y} & -\tilde{k}_{\varphi_x\varphi_x} & 0 & 0 & \tilde{k}_{\varphi_x\varphi_y} & \tilde{k}_{\varphi_x\varphi_x} \end{bmatrix} \tag{F-1}$$

where

$$\tilde{k}_{xx} = \cos^2\omega t(k_{xx}) + \sin^2\omega t(k_{yy}) - \cos\omega t + \sin\omega t\left(k_{xy} + k_{yx}\right)$$
$$\tilde{k}_{xy} = \cos^2\omega t(k_{xy}) - \sin^2\omega t(k_{yx}) + \cos\omega t + \sin\omega t(k_{\xi\xi} - k_{\eta\eta})$$
$$\tilde{k}_{yx} = \cos^2\omega t(k_{yx}) - \sin^2\omega t(k_{xy}) + \cos\omega t + \sin\omega t(k_{\xi\xi} - k_{\eta\eta})$$
$$\tilde{k}_{yy} = \cos^2\omega t(k_{yy}) + \sin^2\omega t(k_{xx}) + \cos\omega t + \sin\omega t\left(k_{xy} + k_{yx}\right)$$
$$\tilde{k}_{\varphi_x\varphi_x} = \cos^2\omega t\left(\Delta k_{\varphi_x\varphi_x}\right) + \sin^2\omega t\left(\Delta k_{\varphi_y\varphi_y}\right)$$
$$\tilde{k}_{\varphi_x\varphi_y} = \cos\omega t\sin\omega t\left(k_{\varphi_x\varphi_x}\right) - \cos\omega t\sin\omega t\left(k_{\varphi_y\varphi_y}\right)$$
$$\tilde{k}_{\varphi_y\varphi_x} = \cos\omega t\sin\omega t\left(k_{\varphi_x\varphi_x}\right) - \cos\omega t\sin\omega t\left(k_{\varphi_y\varphi_y}\right)$$
$$\tilde{k}_{\varphi_y\varphi_y} = \cos^2\omega t\left(\Delta k_{\varphi_y\varphi_y}\right) + \sin^2\omega t\left(\Delta k_{\varphi_x\varphi_x}\right)$$

Appendix G: Elements of A Matrix

Elements in various columns of $\mathbf{A}$ correspond to various system parameters in the rows of vector $\mathbf{x}$. The harmonic index i runs from –5 to 5 through 0. To separate real and imaginary parts of complex nodal displacements, *re* and *im* are used as superscripts. For example u_{1i}^{re} ,u_{1i}^{im} correspond to node 1's real and imaginary parts.

D.1 Disc unbalance and phase

$$\mathbf{A}(24,1) = m_{d_1}\omega^2;\quad \mathbf{A}(35,2) = m_{d_1}\omega^2;\quad \mathbf{A}(68,3) = m_{d_2}\omega^2;\quad \mathbf{A}(79,4) = m_{d_2}\omega^2$$
$$\mathbf{A}(222,5) = m_{d_3}\omega^2;\ \mathbf{A}(233,6) = m_{d_3}\omega^2;\ \mathbf{A}(266,7) = m_{d_4}\omega^2;\ \mathbf{A}(277,8) = m_{d_4}\omega^2 \qquad \text{(G-1)}$$

D.2 Bearing stiffness in x and y directions

$$\mathbf{A}(1+i,9) = -u_{1i}^{re};\qquad \mathbf{A}(89+i,10) = -u_{5i}^{re}$$
$$\mathbf{A}(199+i,11) = -u_{10i}^{re};\quad \mathbf{A}(287+i,12) = -u_{14i}^{re}$$
$$\mathbf{A}(12+i,13) = -u_{1i}^{im};\quad \mathbf{A}(100+i,14) = -u_{5i}^{im} \qquad \text{(G-2)}$$
$$\mathbf{A}(210+i,15) = -u_{10i}^{im};\ \mathbf{A}(298+i,16) = -u_{14i}^{im}$$

D.3 AMB displacement and current constants

$$\mathbf{A}(45+i,17) = u_{3i}^{re};\quad \mathbf{A}(56+i,17) = u_{3i}^{im}$$
$$\mathbf{A}(243+i,17) = u_{12i}^{re};\ \mathbf{A}(254+i,17) = u_{12i}^{im}$$
$$\mathbf{A}(45+i,18) = i_{amb1i}^{re};\quad \mathbf{A}(56+i,18) = i_{amb1i}^{im} \qquad \text{(G-3)}$$
$$\mathbf{A}(243+i,18) = i_{amb2i}^{re};\ \mathbf{A}(254+i,18) = i_{amb2i}^{im}$$

D.4 Coupling's static stiffness coefficients

$$\mathbf{A}(111+i,19) = -(u_{6i}^{re} - u_{8i}^{re});\ \mathbf{A}(122+i,19) = -(u_{6i}^{im} - u_{8i}^{im})$$
$$\mathbf{A}(133+i,20) = -(\varphi_{7i}^{re} - \varphi_{9i}^{re});\ \mathbf{A}(144+i,20) = -(\varphi_{7i}^{im} - \varphi_{9i}^{im})$$
$$\mathbf{A}(155+i,19) = -(u_{8i}^{re} - u_{6i}^{re});\ \mathbf{A}(166+i,19) = -(u_{8i}^{im} - u_{6i}^{im})$$
$$\mathbf{A}(177+i,20) = -(\varphi_{9i}^{re} - \varphi_{7i}^{re});\ \mathbf{A}(188+i,20) = -(\varphi_{9i}^{im} - \varphi_{7i}^{im}) \quad \text{(G-4)}$$

D.5 ACS coefficients

$$\mathbf{A}(111+i,21) = -0.5\left(\delta x_c - \delta x_{c+1}\right) p(i);\quad \mathbf{A}(111+i,22) = -0.5\left(\delta x_c - \delta x_{c+1}\right) q(i)$$
$$\mathbf{A}(133+i,23) = -0.5\left(\delta \varphi_{y_c} - \delta \varphi_{y_{c+1}}\right) p(i);\ \mathbf{A}(133+i,24) = -0.5\left(\delta \varphi_{y_c} - \delta \varphi_{y_{c+1}}\right) q(i)$$
$$\mathbf{A}(155+i,21) = 0.5\left(\delta x_c - \delta x_{c+1}\right) p(i);\quad \mathbf{A}(155+i,22) = 0.5\left(\delta x_c - \delta x_{c+1}\right) q(i)$$
$$\mathbf{A}(177+i,23) = 0.5\left(\delta \varphi_{y_c} - \delta \varphi_{y_{c+1}}\right) p(i);\ \mathbf{A}(177+i,24) = 0.5\left(\delta \varphi_{y_c} - \delta \varphi_{y_{c+1}}\right) q(i) \quad \text{(G-5)}$$

Appendix H: Hardware Set-up for Experimental Validation

The following set up has been made in Advanced Vibrations Lab at IIT Guwahati

Coupled Rotor-Bearing Test rig

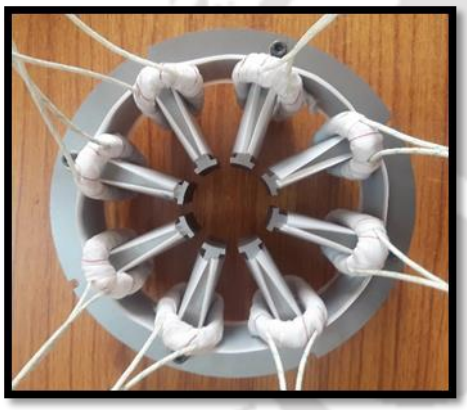

8 pole AMB actuator

DSP controller

Amplifier

Current probe

References

- Aenis, M., Knopf, E., Nordmann, R., 2002, "Active magnetic bearings for the identification and fault diagnosis in turbo machinery", Mechatronics, Volume 12, Issue 8, October 2002, 1011–1021
- Ahmad, A.M., El-Shefai. A., 2006, "Effect of Misalignment on the Characteristics of Journal Bearings", ASME Turbo Expo 2006: Power for Land, Sea and Air, May 8-11, Barcelona, Spain, 5, pp. 1295 – 1302.
- Ahn, H.J., Han, D.C., Maslen, E.H., 2003, "Frequency domain identification of a MIMO AMB rigid rotor system based on measured open-loop frequency responses", Proceedings of ASME/IGTI Turbo Expo 2003, Power for Land, Sea & Air, June 16-19, 2003, Atlanta, Georgia, USA
- Alguindigue, I., Uhrig, R.E., 1991, "Vibration Monitoring with Artificial Neural Networks", Proceedings of the Smorn VI Symposium on Nuclear Reactor Surveillance and Diagnostics, Gatlinburg, Tennessee, 19-24
- Al-Hussain, K.M., Redmond, I., 2002, "Dynamic Response of Two Rotors Connected by Rigid Mechanical Coupling with Parallel Misalignment", Journal of Sound and Vibration, 249, 3, pp. 483-498.
- Al-Hussain, K.M., 2003, "Dynamic Stability of Two Rigid Rotors Connected by a Flexible Coupling with Angular Misalignment", Journal of Sound and Vibration, 266, pp. 217-234.
- Allaire, P. E., Lewis, D. W., Knight, J.D., 1983, "Active vibration control of a single a mass rotor on flexible supports", Journal of the Franklin Institute, Volume 315, Issue 3, 211 – 222
- Allaire, P.E., Kasarda, M. E. F., Humphris, R. R., Lewis, D. W., 1989, "Vibration reduction in a multi-mass flexible rotor using a mid-span magnetic damper", Proceedings of the First International Symposium, ETH Zurich, Switzerland, 149-158
- Allaire, P.E., Kasarda, M.E.F., Maslen, E.H., Gillis, G., 1996, "Rotor Power Loss Measurements for Heteropolar and Homopolar Magnetic Bearings", 5th International Symposium on Magnetic Bearings, Virginia.
- Amer, Y. A., Eissa, M. H., Hegazy, U. H., Sabbah, A. S., 2006, "Dynamic Behaviour of an AMB/Supported Rotor Subject to Parametric Excitation", ASME Journal of Vibration and Acoustics, 128(5), 646 – 652

- Anegawa, N., Fujiwara, H., Matsushita. O., 2008, "Blade-Shaft Coupled Resonance Vibration by Using Active Magnetic Bearing Excitation", Proceedings of ASME Turbo Expo 2008: Power for Land, Sea and Air, GT2008, Berlin, Germany
- Arredondo, I., Jugo, J., Etxebarria, V., 2008, "Modelling and control of a flexible rotor system with AMB-based sustentation", ISA Transactions, Volume 47, Issue 1, 101–112
- Arredondo, I., Jugo, J., 2012, "2-DOF Controller Design for Precise Positioning a Spindle Levitated with Active Magnetic Bearings", European Journal of Control, Volume 8, Issue 2, 194–206
- Avendano, R.D., Childs, D.W., 2012, "One Explanation for 2N Response due to Misalignment in Rotors Connected by Flexible Couplings", Proceedings of ASME Turbo Expo 2012, GT2012, June 11-15, Copenhagen, Denmark, pp. 563-573.
- Bouaziz, S., Messaoud, N. B., Mataar, M., Fakhfakh, T., Haddar, M., 2011, "A Theoretical Model for Analyzing the Dynamic Behavior of a Misaligned Rotor with Active Magnetic Bearings", Mechatronics, 21, pp. 899 – 907.
- Bouaziz, S., Messaoud, N.B., Cholley, J.Y., Maatar, M., Haddar, M., Transient response of a rotor-AMBs system connected by a flexible mechanical coupling, Mechatronics, 23(6), 573-580, 2013
- Bouaziz, A., Bouaziz, S.,Hentati, T., Choley, J.Y., Haddar, M., Vibrations monitoring of high speed spindle with active magnetic bearings in presence of defects, International Journal of Applied Electromagnetics and Mechanics, 49(2), pp. 207-221, 2015
- Bordoloi, D.J., Tiwari, R., Optimization of controller parameters of Active Magnetic Bearings in Rotor Bearing Systems, Advances in Vibration Engineering, 12, pp 319 – 327, 2013
- Bachschmid, N., Pennacchi, P., Tanzi, E., 2010, "Cracked Rotors: A Survey on Static and Dynamic Behaviour Including Modelling and Diagnosis", Springer, 399 pages
- Barbaraci, G., 2016, "Axial active magnetic bearing design", Journal of Vibration and Control, Volume 22, Issue 5, 1190–1197
- Basaran, S., Sivrioglu, S., Okur, B., and Zergeroglu, E., 2011, "Robust H∞ control of Flexible Rotor Active Magnetic Bearing System", 6th International Advanced Technologies Symposium, Elazig, Turkey, 39 – 43

- Bash, T.J., 2005, “Active Magnetic Bearings used as an Actuator for Rotor Health Monitoring in Conjunction with Conventional Support Bearings”, Thesis, Master of Science in Mechanical Engineering, Virginia Polytechnic Institute and State University
- Baun, D. O., and Flack, R. D, 1997, “A Plexiglas Research Pump with Calibrated Magnetic Bearings/Load Cells For Radial and Axial Hydraulic Force Measurement” , ASME Fluids Engineering Division Summer Meeting
- Betchson, F., 2000, “Design Principles of Integrated Magnetic Bearings”, Thesis, Doctor of Technical Sciences, Swiss Federal Institute of Technology, Zurich
- Bishop, R. E. D., and Gladwell, G. M. L., 1959, “The Vibration and Balancing of an Unbalanced Flexible Rotor,” Proceedings of Institution of Mechanical Engineers, IMechE Conference., Volume 1, Issue 1, 66–77
- Bornstein, K.R., 1991, “Dynamic Load Capabilities of Active Electromagnetic Bearings”, Joint ASME/STLE Tribology Conference, Toronto, Canada, Volume 113, 598 – 603
- Bouaziz, S., Messaoud, N.B., Mataar, M., Fakhfakh, T., Haddar, M., 2011, “A theoretical model for analysing the dynamic behaviour of a misaligned rotor with active magnetic bearings”, Mechatronics, Volume 21, Issue 6, 899–907
- Bouaziz, S., Messaoud, N.B., Choley, J.Y., Maatar, M., Haddar M., 2013, “Transient response of a rotor-AMBs system connected by a flexible mechanical coupling”, Mechatronics, Volume 23, Issue 6, 573–580
- Bouaziz, A., Bouaziz S., Hentati, T., Cholley, J.Y, Haddar, M., 2015, “Vibrations monitoring of high speed spindle with active forcing and base motion disturbances” Proceedings of Institution of Mechanical Engineers, Volume 212, Part C,535 – 546
- Brown, D. L., Randall, J. A., Phillips, A.W., 2015, “Forty Years of Use And Abuse of Impact Testing: A Practical Guide To Making Good FRF Measurements”, Experimental Techniques, Rotating Machinery, and Acoustics, Volume 8, Proceedings of the 33rd IMAC, A Conference and Exposition on Structural Dynamics, 221 – 242
- Brusa, E., 2014, “Semi-Active and Active Magnetic Stabilization of Supercritical Rotor Dynamics by Contra-Rotating Damping”, Mechatronics, Volume 24, Issue 5, 500–510
- Cade, I.S.,Keogh, P.S.,Sahinkaya, M.N., Fault identification in rotor/magnetic bearing systems using discrete time wavelet coefficients, IEEE/ASME Transactions on Mechatronics,10(6), 648-657, 2005

- Chacon, J.L.F., Andicoberry, E.A., Kappatos, V., Asfis, G., 2014, "Shaft Angular Misalignment Detection Using Acoustic Emission", Applied Acoustics, 85, pp.12–22.
- Chandra, N. H., Sekhar, A, S., Fault detection in rotor bearing systems using time frequency techniques, Mechanical Systems and Signal Processing, pp 72-73, pp 105-133, May, 2016
- Chasalevris, A.C., Dohnal, F., Markert, R., 2011, "Symptoms of Misaligned Worn Journal Bearings in Rotor Response under External Excitation by A Magnetic Bearing", Proceedings of the ASME 2011 International Design Engineering Technical Conferences & Computers and Information in Engineering Conference, IDETC/CIE 2011, August 28-31, Washington, DC, USA
- Chasalevris, A.C., Dohnal, F., Chatzisavvas, I., 2014, "Experimental detection of additional harmonics due to wear in journal bearings using excitation from a magnetic bearing", Tribology International, Volume 71, 158–167
- Chasalevris, A.C., Papadopoulos C.A., 2015, "Experimental detection of an early developed crack in rotor-bearing systems using an AMB", International Journal of Structural Integrity, Volume 6, Issue 2, 194 – 213
- Chen, G., Hao, T.F., Wang, H.F., Zhao, B., Wang, J., Cheng, X.Y., 2014, "Sensitivity Analysis and Experimental Research on Ball Bearing Early Fault Diagnosis Based on Testing Signal From Casing", Journal of Dynamic Systems, Measurement, and Control, Volume 136, 061009-1 – 061009-10
- Chen, H.M., 1988, "Active Magnetic Bearing Design Methodology - A Conventional Rotordynamics Approach", Tribological Design of Machine Elements, Tribology Series 14, Proceedings of the 15th Leeds-Lyon Symposium on Tribology, The University of Leeds, UK
- Chen, W.J., Gunter, E.J, 2007, "Introduction to Dynamics of Rotor-Bearing Systems", Trafford Publishing, Charlottesville, Virginia, 469 pages.
- Chen, W. J., A Note on Computational Rotor Dynamics, Journal of Vibration and Acoustics, 120, pp 228 – 233, January, 1998
- Chiang, C.C., "Scaling Algorithms for Matrices", Thesis, Doctor of Philosophy, Oklahoma State University, USA, 2007
- Chiang, H, D., Hsu, C, "Rotor-Bearing Analysis for Turbomachinery Single and Dual-Rotor Systems", Journal of Propulsion and Power, 20, 6, 1096-1104, 2004

- Clark, D.J., Jansen, M.J., Montague, G.T., “An Overview of Magnetic Bearing Technology for Gas Turbine Engines”, NASA Glenn Research Centre; Cleveland, OH, United States, 14 pages, 2004
- Clements, J.R., 2000, “The Experimental Testing of an Active Magnetic Bearing/Rotor System Undergoing Base Excitation”, Thesis, Masters of Science in Mechanical Engineering, Virginia Polytechnic Institute and State University, Blacksburg, Virginia
- Cole,M.O.T., Keogh,P.S., Burrows, C.R., 1998, “ Vibration control of a flexible rotor/magnetic bearing system subject to direct forcing and base motion disturbances” , Proceedings of the Institution of Mechanical Engineers, Part C: Journal of Mechanical Engineering Science,: 212(7), 535-546
- Cole, M.O.T., Chamroon, C., Ngamprapasom P., 2012, “Force Feedback Control for Active Stabilization of Synchronous Whirl Orbits in Rotor Systems With Nonlinear Stiffness Elements”, J. Vib. Acoust, 134(2), 10 pages,
- Cole, M.O.T., Keogh, P.S., Burrows, C.R., Control of multi-frequency rotor vibration components, Proceedings of the Institution of Mechanical Engineers, Part C: Journal of Mechanical Engineering Science, 216(2), 165-177, 2002
- Cura, F., Mura, A., “Analysis of a Load Application Point in Spline Coupling Teeth”, Journal of Zhejiang University science A , 15, 302-308, 2014
- Cura, F, Mura, A, Adamo, F., “Fatigue Damage in Spline Couplings: Numerical Simulations and Experimental Validation”, Procedia Structural Integrity, 5, 1326-1333, 2017
- Cuffaro, V., Cura, F., Mura, A., “Test Rig for Spline Couplings Working in Misaligned Conditions”, Journal of Tribology, 136, 011104-1 - 011104-7, 2014
- Darlow, M.S., 1987, “Balancing of High-Speed Machinery: Theory, Methods and Experimental Results”, Mechanical Systems and Signal Processing, Volume l, Issue 1, 105-134
- Darlow, M.S., 1989, “Balancing of High-Speed Machinery”, Mechanical Engineering Series, Springer, New York, 158 pages
- Das, A.S., Nighil, M.C., Dutt, J.K., Irretier, H., 2008, “Vibration control and stability analysis of rotor-shaft system with electromagnetic exciters”, Mechanism and Machine Theory, Volume 43, Issue 10, 1295–1316

- Das, A.S., Dutt, J.K., Ray, K., 2010, "Active vibration control of unbalanced flexible rotor–shaft systems parametrically excited due to base motion", Applied Mathematical Modelling, Volume 34, Issue 9, 2353–2369
- Das, A.S., Dutt, J.K., 2010, "Control of Flexible Rotor Vibration using Electromagnetic Actuator Based on Active Disturbance Rejection Technique", Proceedings of ISMA, 1559 - 1571
- Das, A.S., Dutt, J.K., Ray, K., 2011, "Active control of coupled flexural-torsional vibration in a flexible rotor–bearing system using electromagnetic actuator", International Journal of Non-Linear Mechanics, Volume 46, Issue 9, 1093–1109
- Das, A.S., Nighil, M.C., Dutt, J.K., Irretier, H., 2008, "Vibration control and stability analysis of rotor-shaft system with electromagnetic exciters", Mechanism and Machine Theory, 43(10), 1295-1316,
- Davies, A., 1998, "Handbook of Condition Monitoring Techniques and Methodology", Springer-Science + Business Media, Dordrecht, 565 pages
- Defoy, B, Alban, T, Jarir M., 2014, "Experimental Assessment of a New Fuzzy Controller Applied to a Flexible Rotor Supported by Active Magnetic Bearing", ASME Journal of Vibration and Acoustics, Volume 136, 051006-1 - 051006-8
- De Moraes, D. C., Nicoletti, R., 2010, "Hydrodynamic Bearing with Electromagnetic Actuators: Rotor Vibration Control and Limitations", Proceedings of ISMA, 3715 - 3721
- DeSmidt,H.A., Wang, K.W., Smith, E.C., Multiharmonic Adaptive Vibration Control of Misaligned Driveline via Active Magnetic Bearings, Journal of Dynamic Systems, Measurement and Control, 130(4), 13 pages, 2008
- DeSmidt, H. A., Wang, K. W., Smith, E. C., 2004, "Multi-Harmonic Adaptive Vibration Control of Magnetic Bearing-Driveline with Auxiliary Feedback: Theory and Experiment", ASME Journal of Dynamic Systems, Measurement, and Control, Volume 130, 041006-1 - 041006-13
- DeSmidt, H. A., Wang, K. W., Smith, E. C., 2004, "Multi-Harmonic Adaptive Vibration Control of Magnetic Bearing-Driveline with Auxiliary Feedback: Theory and Experiment", 45th AIAA/ASME/ASCE/AHS/ASC Structures, Structural Dynamics & Materials Conference, Palm Springs, California

- DeSmidt, H. A., 2007, “Structural Damage Identification of Bladed-Disk Systems via Active Magnetic Bearings”, 48th AIAA/ASME/ASCE/AHS/ASC Structures, Structural Dynamics, and Materials Conference, Honolulu, Hawaii
- Dhar, D., Barrett, L. E., 1993, “Design of Magnetic Bearings for Rotor Systems with Harmonic Excitations”, ASME Journal of Vibration and Acoustics, Volume 115, 359 – 366
- Di, L., Lin, Z., 2014, “Control of a flexible rotor active magnetic bearing test rig: a characteristic model based all-coefficient adaptive control approach”, Control Theory Tech, Volume 12, No. 1, 1–12
- Dimitri, A.S., Mahfoud, J., El-Shafei, A., 2016, “Oil Whip Elimination Using Fuzzy Logic Controller”, ASME Journal of Engineering for Gas Turbines and Power, Volume 138, 062502-1 - 062502-8
- Ding, W., Zhu, C., Ming, T., Bin, Z., 2010, “The Effect of Controllers on the Dynamic Behaviour of a Rotor Supported on Active Magnetic Bearings”, International Conference on Electrical and Control Engineering, 2336 – 2339
- Ehrich, F.F., 1990, “Pseudo-High-Speed Balancing”, Journal of Vibration and Acoustics, Volume 112, 418 – 426
- Ehrich, F.F., 2001, “Handbook of Rotordynamics”, Krieger Publishing Company, 3rd edition, Malabar, Florida, USA, 480 pages
- Eissa, M.H., Hegazy, U.H., Amer, Y.A., 2008, “Dynamic behaviour of an AMB supported rotor subject to harmonic excitation”, Applied Mathematical Modelling, Volume 32, 1370–1380
- El-Shafei, A., Dimitri, A.S., 2010, “Controlling Journal Bearing Instability Using Active Magnetic Bearings”, Journal of Engineering for Gas Turbines and Power, 132, 9 pages, 2010
- El-Shafei, A., Dimitri, A.S., 2010, “Controlling Journal Bearing Instability Using Active Magnetic Bearings”, ASME Journal of Engineering for Gas Turbines and Power, Volume 132(1), 012502-1 – 012502 – 9
- Enemark, S., Santos, I.F., 2016, “Feed forward compensation control of rotor imbalance for high-speed magnetically suspended centrifugal compressors using a novel adaptive notch filter”, Journal of Sound and Vibration, Volume 366, 1 – 14

- Ertas, B.H., Vance, J.M., 2004, “Effect of Static and Dynamic Misalignment on Ball Bearing Radial Stiffness”, Journal of Propulsion and Power, 20, 4, pp. 634 – 647.
- Ewins, D.J., Modal Testing: Theory, Practice and Application, Wiley-Blackwell, 2nd edition, Hoboken, New Jersey, USA, 2000
- Fan, C.C., Pan, M.C., 2009, “Active Self-Excited Vibration Elimination of Rotating Machine with an Electromagnetic Exciter”, Proceedings of the ASME 2009 International Design Engineering Technical Conferences &Computers and Information in Engineering Conference, IDETC/CIE 2009, San Diego, California, USA
- Fan, C.C., Pan, M.C., 2010, “Fluid-induced instability elimination of rotor-bearing system with an electromagnetic exciter”, International Journal of Mechanical Sciences, Volume 52, Issue 4, 581–589
- Fan, C.C., Pan, M.C., 2011, “Active Self-Excited Vibration Elimination of Rotating Machine with an Electromagnetic Exciter”, Mechanism and Machine Theory, 46,290–304
- Fan, C.C., Pan, M.C., 2011, “Experimental study on the whip elimination of rotor-bearing systems with electromagnetic exciters”, Mechanism and Machine Theory, Volume 46, Issue 3, 290–304
- Fan, C.C., Pan, M.C., 2011, “Active elimination of oil and dry whips in a rotating machine with an electromagnetic actuator”, International Journal of Mechanical Sciences, Volume 53, Issue 2, 126–134
- Fang, J., Xu, X., Xie, J., 2015, “Active vibration control of rotor imbalance in active magnetic bearing systems”, Journal of Vibration and Control, Volume 21, Issue 4, 684–700
- Fang, J., Tang, E., Zheng, S., 2015, “Optimum Damping Control of the Flexible Rotor in High Energy Density Magnetically Suspended Motor”, Volume 137, 082505-1 - 082505-9
- Fayong, W., Zhichao, L., Yanghong, Ma., Dayi, Z., “Bending Stiffness and Dynamic Characteristics of a Rotor with Spline Joints”, Proceedings of the ASME 2013 International Mechanical Engineering Congress and Exposition, IMECE2013, November 15-21, 2013, San Diego, USA, 2013
- Fei, Z., Tong, S., Wei, C., “Investigation of the Dynamic Characteristics of a Dual Rotor System and its Start-Up Simulation Based on Finite Element Method”, Journal

Of Zhejiang University-science A (Applied Physics & Engineering), 14, 4, 268-280, 2013

- Ferraris, G., Maisonneuve, V., Lalanne, M., "Prediction of the Dynamic Behaviour of Non-Symmetric Coaxial Co- or Counter-Rotating Rotors", Journal of Sound and Vibration, 195, 4, 649-666, 1996
- Fittro,R.L., C. R. Knospe, C.R., The μ Approach to Control of Active Magnetic Bearings, Journal of Engineering for Gas Turbines and Power, 124(3): 566-570, 2002
- Fittro, R. L., Knospe, C. R., 2002, " The μ Approach to Control of Active Magnetic Bearings", ASME Journal of Engineering For Gas Turbines And Power, Volume 124, 566 – 570
- Friswell M.I., Penny, J.E.T., Garvey, S.D., Lees, A.W., Dynamics of Rotating Machines, Cambridge University Press, 1st Edition, March, 2010, New York, USA
- Friswell M.I., Penny, J.E.T., Garvey, S.D., Lees, A.W., Dynamics of Rotating Machines, Cambridge University Press, 1st Edition, March, New York, USA, 2010
- Friswell, M.I., Litak, G., Sawicki, J.T., 2010, "Crack identification in rotating machines with active bearings", Proceedings of ISMA, 2843 – 2855
- Funakoshi, D., Okada, S., Watanabe, T., Seto, K., 2012, "Levitation And Vibration Suppression Of An Elastic Rotor By Using Active Magnetic Bearings", ASME 2012 5th Annual Dynamic Systems And Control Conference Joint With The JSME 2012 11th Motion And Vibration Conference , Fort Lauderdale, Florida, USA
- Ganesan, S., Padmanabhan, C., 2011, "Modelling of parametric excitation of a flexible coupling–rotor system due to misalignment", Proceedings of IMechE, Vol. 225, Part C: Journal of Mechanical Engineering Science, 2907 - 2918
- Gamble, W.L., Valori, R, "Development of Counter-Rotating Intershaft Support Bearing Technology for Aircraft Gas Turbine Engines", AIAA/SAE/ASME 19th Joint Propulsion Conference, Cleveland, Ohio, USA, June 21-23, 1982
- Gere and Timoshenko, 2006, "Mechanics of Materials", Second edition, CBS Publications, 762 pages.
- Gibbons, C.B., 1976, "Coupling Misalignment Forces", Proceedings of the fifth turbo machinery symposium, Gas Turbine Laboratories, Texas A&M University, pp.111-116.

- Gnielka, P., 1983, “Modal Balancing Of Flexible Rotors without Test Runs: An Experimental Investigation”, Journal of Sound and Vibration, Volume 90, Issue 2, 157-172
- Goodwin, M.J., 1989, “Dynamics of Rotor-bearing Systems”, Kluwer Academic, 320 pages
- Gosiewski, Z., 1985, “Automatic Balancing of Flexible Rotors, Part I: Theoretical Background”, Journal of Sound and Vibration, Volume 100, Issue 4, 551-567
- Gosiewski, Z., 1987, “Automatic Balancing of Flexible Rotors, Part II: Theoretical Background”, Journal of Sound and Vibration, Volume 114, Issue 1, 103-119
- Goldman, P., Muszynska, A, 1999, “Application of Full Spectrum to Rotating Machinery Diagnostics”, Orbit, First Quarter, pp. 17 – 21.
- Gunter, E.J., “Dynamic Analysis and Balancing of an Aircraft Gas Turbine”, Dyrobes, 33 pages 2001
- Guskov, M., Sinou, J.J., Thouverez, F., Naraikin, O.S., “Experimental and Numerical Investigations of a Dual-Shaft Test Rig with Intershaft Bearing”, International Journal of Rotating Machinery, 12 pages, 2007
- Guinzburg, A., Buse, F.W., 1995, “Magnetic Bearings an Impeller force measurement technique”, Proceedings of the Twelfth International Pump Users Symposium, 69 – 76
- Halminen, O., Aceituno, J.F., Escalona, J.L., Sopanen, J., Mikkola, A.,2017, Models for dynamic analysis of backup ball bearings of an AMB-system” ,Mechanical Systems and Signal Processing, 95, 324–344
- Hou, L, Chen, Y., Fu, Y., Chen, H., Lu, Z., Liu, Z., “Application of The HB–AFT Method to the Primary Resonance Analysis of a Dual-Rotor System”, Nonlinear Dynamics, 88, 2531-2551, 2017
- Hong, J., Talbot, D., Kahraman, A., “ Effects of Tooth Indexing Errors on Load Distribution and Tooth Load Sharing of Splines Under Combined Loading Conditions”, ASME, Journal Of Mechanical Design, 137, 032601-1 – 032601-10, 2015
- Haberman, H., Liard, G., 1980,” An Active Magnetic Bearing System”, Tribology International, Volume 2, Issue 3, April, 85 - 89
- Haberman, H., Brunet, M., 1984, “The Active Magnetic Bearing enables Optimum Damping of Flexible Rotor”, ASME Paper No. 84-GT- 117, ASME Gas Turbine Conf., Amsterdam, June.

- Habib, M.K., Hussain, J.I.I, 2004, “Fuzzy Logic Based Control of Rotor Motion in Active Magnetic Bearings”, Proceedings of the 2004 IEEE Conference on Cybernetics and Intelligent Systems, Singapore, 1219 – 1225
- Hongwei, L., Yang, X., Huidong, G., Lei, Z., 2007, “Field Dynamic Balance Method Study for the AMB - Flexible Rotor System”, Transactions, SMiRT 19, Toronto, 1 – 7
- Hu, W., Miah, H., Feng, N.S., Hahn, E.J., 2000, “A Rig for Testing Lateral Misalignment Effects in a Flexible Rotor Supported on Three or More Hydrodynamic Journal Bearings”, Tribology international, 33, pp. 197-204.
- Huang, J., Wang, Y., “Transient Analysis for a Twin Spool Rotor with Squeeze‑Film Dampers Considering Blade Loss”, Journal of vibration engineering and technologies, 8, 95 – 104, 2018
- Huang, T., Chen, Z., Zhang, H.T., Ding, H., 2015, “Active Control of an Active Magnetic Bearings Supported Spindle for Chatter Suppression in Milling Process”, ASME Journal of Dynamic Systems, Measurement, and Control, Volume 137, 111003-1 - 111003-11
- Hussain, J. I. I., 2007, “Nonlinear Dynamics of a Flexible Rotor in Active Magnetic Bearings”, 2007 International Symposium on Nonlinear Theory and it Applications, NOLTA'07, Vancouver, Canada
- Hussain, K. M., Redmond, I., 2007, “Dynamic Response of two Rotors Connected by Rigid Mechanical Coupling with Parallel Misalignment”, Journal of Sound and Vibration, 249 (3), 483–498, 2002
- Hussain, J. I. I., 2009, “Geometric coupling effects on the bifurcations of a flexible rotor response in active magnetic bearings”, Chaos, Solitons and Fractals, Volume 41, Issue 5, 2664–2671
- Hussain, J. I. I., 2010, “Non-linear dynamics of a statically misaligned flexible rotor in active magnetic bearings”, Commun Nonlinear SciNumer Simulat, Volume 15, Issue 3, 764–777
- Hui, G., Xu, L., Yili, Z., 2013, “Unbalance Vibratory Displacement Compensation for Active Magnetic Bearings”, Chinese Journal of Mechanical Engineering, Volume 26, No. 1, 95 -103
- Ichihara, M., Shida, H., Sagane, T., Tajima, H., Saigou, M., Seto, K., 2003, “A New Modelling Technique and Control System Design of A Flexible Rotor Supported By

Active Magnetic Bearings for Motion and Vibration Control", Proceedings of DETC.03, ASME 2003, Design Engineering Technical Conferences and Computers and Information in Engineering Conference Chicago, Illinois, USA

- Inagaki, T., Kanki, H., Shiraki. K., 1982, "Transverse Vibrations of a General Cracked-Rotor Bearing System", Journal of Mechanical Design, Volume 104, 345-355
- ISO 1940-1:2003, "Mechanical vibration - Balance quality requirements for rotors in a constant (rigid) state -- Part 1: Specification and verification of balance tolerances"
- ISO 11342:1998(E), "Mechanical vibration – Methods and criteria for the mechanical balancing of flexible rotors",
- ISO 14839-4:2012, "Mechanical Vibration-Vibration of rotating machinery equipped with active magnetic bearings - Part 4: Technical guidelines"
- Jalali, M., Ghayour, M., Rad, S.D., Shahriari, B., "Dynamic Analysis of a High Speed Rotor-Bearing System", Measurement, 53, 1-9, 2014
- Jalan, A.K., Mohanty, A.R., 2009, "Model Based Fault Diagnosis of a Rotor-Bearing System for Misalignment and Unbalance under Steady State Condition", Journal of Sound and Vibration, 327, pp. 604-622.
- Jun, L., Jie, H., Yanghong, M., Dayi, Z., " Modelling Of Misaligned Rotor Systems In Aero-Engines", Proceedings of the ASME 2012 International Mechanical Engineering Congress & Exposition, Houston, Texas, USA, IMECE2012 , November 9-15, 2012
- Johnson, M.E., Kasarda, M.E.F., 2002, "Active Control of Gear Noise Using Magnetic Bearings For Actuation", Proceedings of IMechE2002, ASME International Mechanical Engineering Congress & Exposition, New Orleans, Louisiana
- Johnson, M.E., Nascimento, L.P., Kasarda, M.E.F., Fuller, C.R., 2003, "The Effect of Actuator and Sensor Placement on the Active Control of Rotor Unbalance", ASME Journal of Vibration and Acoustics, Volume 125, 365 – 373
- Johnson, D., Brown, G.V., Mehmed, O., 1998, "A Magnetic Suspension and Excitation System for Spin Vibration Testing of Turbomachinery Blades", American Institute of Aeronautics and Astronautics Inc., 12 pages
- Jeon, S, Ahn, H.J., Han, D.C., 2002, "Model Validation and Controller Design for Vibration Suppression of Flexible Rotor Using AMB", KSME International Journal, Volume 16, No. 12, 1583- 1593

- Jiang, K., Zhu, C., 2011, "Multi-frequency periodic vibration suppressing in active magnetic bearing-rotor systems via response matching in frequency domain", Mechanical Systems and Signal Processing, Volume 25, Issue 4, 1417–1429
- Jiang, K., Zhu, C., Chen, L., Qiao, X, 2015, "Multi-DOF rotor model based measurement of stiffness and damping for active magnetic bearing using multi-frequency excitation" Mechanical Systems and Signal Processing, Volumes 60-61, 358–374
- Kärkkäinen, A., Helfert, M., Aeschlimann, B.,Mikkola,A., Dynamic Analysis of Rotor System With Misaligned Retainer Bearings, Journal of Tribology, 130(2), 10 pages, 2008
- Kasarda, M. E. F., Allaire, P. E., Humphris, R. R., Barrett, L. E., 1990, "A Magnetic Damper for First-mode Vibration Reduction in Multi-mass Flexible Rotors", ASME Journal of Engineering for Gas Turbines and Power, Volume 112, 463 – 469
- Kasarda, M. E. F., Allaire, P.E., Norris. P.M., Mastrangelo, C., Maslen, E.H., 1999, "Experimentally determined rotor power losses in Homopolar and Heteropolar Magnetic Bearings", Journal of Engineering for Gas Turbines and Power, Volume 121, 697 - 702
- Kasarda, M. E. F., Imlach. J., Balaji. P.A., Marshall. J., 2000, "The Concurrent Use of Magnetic Bearings for Rotor Support and Force Sensing for the Non-destructive Evaluation of Manufacturing Processes", Smart Structures and Materials: Smart Structures and Integrate systems, 352 – 363
- Kasarda, M. E. F., 2000, "An Overview of Active Magnetic Bearing Technology and Applications", The Shock and Vibration Digest, Volume 32, No. 2, 91-99.
- Kasarda, M.E.F, Mendoza, H., Kirk, R.G., Wicks, A., 2004, "Reduction of sub-synchronous vibrations in a single-disk rotor using an active magnetic damper", Mechanics Research Communications, Volume 31, Issue 6, 689–695
- Kasarda, M.E.F, Mendoza, H., Kirk, R.G., Wicks, A., 2005, "An Experimental Investigation of The Effect of an Active Magnetic Damper on Reducing Sub synchronous Vibrations In Rotating Machinery", Proceedings of GT2005, ASME Turbo Expo 2005: Power for Land, Sea and Air, Reno-Tahoe, Nevada, USA,
- Kasarda, M.E.F., Bash, T., Quinn, D., Mani, G., Inman, D., Kirk, R. G., 2007, "A New Approach for Health Monitoring and Detection of a Shaft Crack Using an Active

Magnetic Actuator during Steady-State Rotor Operation", Proceedings of GT2007, ASME Turbo Expo 2007: Power for Land, Sea and Air, Montreal, Canada

- Keith, F.J., 1990, "Switching amplifier design for magnetic bearings", Proceedings of 2nd International Symposium on Magnetic Bearings, July 12 – 14, Tokyo, Japan, 211 - 218
- Keogh, P. S., Mu, C., Burrows, C. R., 1995, "Optimised design of vibration controllers for steady and transient excitation of flexible rotors", Proceedings of Institution of Mechanical Engineers, Volume 209, 155 – 168
- Keogh, P. S., Cole, M. O. T., Burrows, C. R., 2002, "Multi-State Transient Rotor Vibration Control Using Sampled Harmonics", ASME Journal of Vibration and Acoustics, Volume 124(2), 186 – 197
- Keogh, P. S., Cole, M.O.T., Sahinkaya, N., Burrows, C., 2002, "On the Control of Synchronous Vibration in Rotor/Magnetic Bearing Systems Involving Auxiliary Bearing Contact", Proceedings of ASME Turbo Expo 2002, Amsterdam, Netherlands
- Keogh, P. S., Cole, M.O.T.,2004, "Contact Dynamic Response With Misalignment In A Flexible Rotor/Magnetic Bearing System" , Proceedings of ASME Turbo Expo 2004 Power for Land, Sea, and Air, Vienna, Austria
- Keogh, P. S., Cole, M.O.T., 2006, "Contact Dynamic Response with Misalignment in a Flexible Rotor/Magnetic Bearing System", Journal of Engineering for Gas Turbines and Power, Volume 128, 362 - 369
- Kim, S.J., Lee, C.W., 1999, "Online Identification of Current and Position Stiffness's by LMS Algorithm in Active Magnetic Bearing System Equipped With Force Transducers", Mechanical Systems and Signal Processing, 13(5), 681-690
- Kim, K.J, Lee, C.W, 2003, "Identification of Dynamic Stiffness of Squeeze Film Damper using Active Magnetic Bearing System as an Exciter", ISCORMA-2, Gdansk, Poland, 1 – 10
- Kozanecka, D., Kozanecki, Z., Lech, T., Kaczmarek, A., 2007, "Application of Active Magnetic Bearings for Identification of the Force Generated In the Labyrinth Seal", Journal of Theoretical and Applied Mechanics, 45, 1, 53-60
- Kozanecka, D., Kozanecki, Z., Lech, T., 2008, "Experimental Identification of Dynamic Parameters for Active Magnetic Bearings", Journal of Theoretical and Applied Mechanics, 46, 1, 41-50

- Kozanecka, D., Kozanecki, Z., Lagodzinski, J., 2011, "Active magnetic damper in a power transmission system", Commun Nonlinear Sci Numer Simulat, Volume 16, Issue 5, 2273–2278
- Knospe, C. R., Humphris, R.R., 1992, "Control Of Unbalance Response with Magnetic Bearings", 11th American Control Conference, Chicago, IL, Proceedings. Volume 1, 211-215
- Knospe, C.R., Hope, R.W., Fedigan, S.J., Williams, R, 1995, "Experiments in the control of unbalance response using magnetic bearings", Mechatronics, Volume 5, No. 4, 385-400,
- Knospe, C. R., Hope, R. W., Tamer, S. M., Fedigan, S. J., 1996, "Robustness of Adaptive Unbalance Control of Rotors with Magnetic Bearings", Journal of Vibration and Control, Volume 2, Issue 1, 33-52
- Knospe, C. R., Tamer, S.M., 1997, "Experiments In Robust Control Of Rotor Unbalance Response Using Magnetic Bearings", Mechatronics, Volume 7, No.3. 217 – 229
- Koroishi, E.H., Borges, A.S., Cavalini, A.A.Jr., and Steffen, V. Jr., 2014, "Numerical and Experimental Modal Control of Flexible Rotor Using Electromagnetic Actuator", Mathematical Problems in Engineering, 1 – 14
- Kreyszig, E, 2011, "Advanced Engineering Mathematics", Wiley, Tenth edition, Hoboken, New Jersey, USA, 1283 pages.
- Kudo, T., Shiohata, K., Matsushita, O., Fujiwara, H., Okabe, A., Sakurai, S., Experimental study of torsional-bending coupled vibration of a rotor system with a bladed disk, Proceedings of the ASME 2013 International Design Engineering Technical Conferences and Computers and Information in Engineering Conference. 8: 22nd Reliability, Stress Analysis, and Failure Prevention Conference; 25th Conference on Mechanical Vibration and Noise. Portland, Oregon, USA. August 4–7, 2013.
- Kumar, C., Rastogi, V., 2009, "A Brief Review on Dynamics of a Cracked Rotor", International Journal of Rotating Machinery", 6 pages
- Kumar, G., Choudhury, M.D, Natesan, S., Kalita, K., 2016, "Design and Analysis of a Radial Active Magnetic Bearing for Vibration Control", 12th International Conference on Vibration Problems, ICOVP 2015, Procedia Engineering, 144, 810 – 816

- Kumar, P., Tiwari, R., 2020, “Dynamic analysis and identification of unbalance and misalignment in a rigid rotor with two offset discs levitated by active magnetic bearings: a novel trial misalignment approach”, Propulsion and Power Research (Available online)
- Kuppa, S.K., Mohit Lal, M., Dynamic behaviour analysis of coupled rotor active magnetic bearing system in the supercritical frequency range, Mechanism and Machine Theory, 152, 19 pages, 2020
- Lal, M. and R. Tiwari, R., 2012, “Multi-Fault Identification in Simple Rotor-Bearing-Coupling Systems based on Forced Response Measurements”, Mechanism and Machine Theory, 51, pp. 87-109.
- Lal, M. and R. Tiwari, R., 2013, “Quantification of Multiple Fault Parameters in Flexible Turbo-Generator Systems with Incomplete Rundown Vibration Data”, Mechanical Systems and Signal Processing, 41, 1, pp. 546 – 563.
- Lal, M. and R. Tiwari, R., 2015, “Experimental Estimation of Misalignment Effects in Rotor-Bearing-Coupling Systems”, Proceedings of the 9th IFToMM International conference on Rotor Dynamics, Springer, Sep 22-25, Milan, pp. 779 – 789.
- Lal, M., Tiwari, R., 2018, Experimental Identification of Shaft Misalignment in a Turbo-Generator System, Sadhana, 43, pp 1-20
- Lang, O., Wasserman, J., Springer, H., 1995, “Adaptive Vibration Control of a Rigid Rotor Supported by Active Magnetic Bearings”, ASME Journal of Engineering for Gas Turbines and Power, Volume 118, 825 – 829
- Larsonneur, R., 1990, “Design and Control of Active Magnetic Bearing Systems for High Speed Rotation”, Thesis, Doctor of Technical Sciences, Swiss Federal Institute of Technology, Zurich
- Larsonneur, R., Richard, P., 2008, Smart Turbo machines Using Active Magnetic Bearings, Proceedings of ASME Turbo Expo 2008: Power for Land, Sea and Air, GT2008, Berlin, Germany
- Lu,Z., Hou, L., Chen,Y., Sun, C., “Nonlinear Response Analysis for a Dual-rotor System With a Breathing Transverse Crack in the Hollow Shaft”, Nonlinear Dynamics, 83, 169–185, 2016
- Lee, Y.S., Lee, A.W., 1999, “Modeling and Vibration Analysis of Misaligned Rotor-Ball Bearing Systems”, Journal of Sound and Vibration, 224, 1, pp. 17-32.

- Lees, A.W., 2007, “Misalignment in Rigidly Coupled Rotors”, Journal of Sound and Vibration, 305, pp. 261 – 271.
- Lee, Y.K., 2008, “Mech300G Mechanical Vibrations”, Spring 2008”, The University of California, Los Angeles
- Lee, C.W., Kim, J.S., 1992, “Modal Testing and Suboptimal Vibration Control of Flexible Rotor Bearing System by Using a Magnetic Bearing”, ASME Journal of Dynamic Systems, Measurement, and Control, Volume 114, 244 - 252
- Lei, S., Palazzolo, A., 2008, “Control of flexible rotor systems with active magnetic bearings”, Journal of Sound and Vibration, Volume 314, Issues 1-2, 19–38
- Li, G., Lin, Z., Allaire, P.E., Luo, J., 2006, “Modelling of a High Speed Rotor Test Rig with Active Magnetic Bearings”, ASME Journal of Vibration and Acoustics, Volume 128, 269 – 281
- Li, H., Wang, C., Chen, C., Yan, G., 2011, “Review of Vibration Signals Trend Forecasting Methods”, 3rd International Conference on Environmental Science and Information Application Technology ESIAT 2011, Procedia Environmental Sciences, Volume 10, Part A, 837-842
- Lijesh, K.P., and Hirani, H., 2015, “Optimization of Eight Pole Radial Active Magnetic Bearing”, Journal of Tribology, Volume 137, 024502-1 - 024502-7
- Lijesh, K.P., and Hirani, H., 2016, “Failure Mode and Effect Analysis of Active Magnetic Bearings”, Tribology in Industry, Volume 38, No. 1, 90-101
- Litak, G., Sawicki, J.T., Kasperek, R., 2009, “Cracked rotor detection by recurrence plots”, Non-destructive Testing and Evaluation, Volume 24, No. 4, 347–351
- Lum, K.Y., Coppola, V.T., Bernstein, D.S., 1996, “ Adaptive Auto centring Control for an Active Magnetic Bearing Supporting a Rotor with Unknown Mass Imbalance”, IEEE Transactions On Control Systems Technology, Volume 4, No. 5, 587 – 597
- Lusty, C., Sahinkaya, N., Keogh, P., 2014, “A Novel Twin-Shaft Rotor with Active Magnetic Couplings for Vibration Control”, ISMB14, 14th International Symposium on Magnetic Bearings, Linz, Austria, 655 - 660
- Lusty, C., Sahinkaya, N., Keogh, P., 2016, “A novel twin-shaft rotor layout with active magnetic couplings for vibration control”, Proceedings of Institute of Mechanical Engineers, Part I: Journal of Systems and Control Engineering, Volume 230, Issue 3, 266–276

- Lyu, X., Di, L., Yoon, S.Y., Lin, Z., Hu, Y., 2016, "A platform for analysis and control design: Emulation of energy storage flywheels on a rotor-AMB test rig", Mechatronics, Volume 33, 146–160
- Lyu, M., Wang, Z, Liu, T, Jia, X, Wang, Y, 2016, "Frequency Analysis of the Orbit Responses of Active Magnetic Bearings in Touchdown Using Hilbert Transform", International Journal of Structural Stability and Dynamics, Volume 17, No. 8, 1750086-1 - 1750086-31
- Lyu, M., Liu, T, Wang, Z., Yan, S., Jia, X., Wang, Y., 2018, "A control method of the rotor re-levitation for different orbit responses during touchdowns in active magnetic bearings", Mechanical Systems and Signal Processing, 105, 241–260
- Ma, L., Zhang, J., Lin, J., Wang, J., Lu, X., 2016, "Dynamic Characteristics Analysis of a Misaligned Rotor-Bearing System with Squeeze Film Dampers", Journal of Zhejiang University-Science A (Applied Physics & Engineering), 17, 8, pp. 614 – 631.
- Macmillan, R, B., 2003, "Rotating machinery: Practical solutions to unbalance and misalignment", Fairmont Press, 1st edition, December, Georgia, USA
- Mani,G., Quinn, D.D.,Kasarda, M., Active health monitoring in a rotating cracked shaft using active magnetic bearings as force actuators, Journal of Sound and Vibration, 294(3),454-465, 2006
- Mayes, I.W., Davies, W.G.R., A method of calculating the vibrational behaviour of coupled rotating shafts containing a transverse crack, 2nd International Conference, Vibrations in Rotating Machinery, 17-28, September, Cambridge, UK, 1980
- Madden, R.J., Sawicki, J.T., 2012, "Rotor Model Validation for an Active Magnetic Bearing Machining Spindle Using Mu-Synthesis Approach", Journal of Engineering for Gas Turbines and Power, Volume 134, 092501-1 - 092501-6
- Mani, G., Quinn, D.D., Kasarda, M.E.F., 2006, "Active health monitoring in a rotating cracked shaft using active magnetic bearings as force actuators", Journal of Sound and Vibration, Volume 294, Issue 3, 454–465
- Marshall, J.T., Kasarda, M.E.F., and Imlach, J., 2002, "A Multipoint Measurement Technique for the Enhancement of Force Measurement with Active Magnetic Bearings", Journal of Engineering for Gas Turbines and Power, Volume 125, Issue 1, 90-94

- Marshall, J.T., Kasarda, M.E.F., Joe, I., 2001, "A Multi-point measurement technique for the enhancement of force measurement with Active Magnetic Bearings", Proceedings of ASME Turboexpo 2001, June 4-7, 2001, New Orleans, Louisiana, USA
- Marx, S., Nataraj, C., 2007, "Suppression of Base Excitation of Rotors on Magnetic Bearings", International Journal of Rotating Machinery, 1 – 10
- Maslen, E.H., Allaire, P.E., Allaire, P.E., Noh, M.D., Sortere, C.K., 1996, "Magnetic Bearing Design for Reduced Power Consumption", Journal of Tribology, Volume 118, 839 – 846
- Maslen, E.H., Sawicki, J.T., 2007, "Mu-synthesis for Magnetic Bearings: Why use such a Complicated Tool?", Proceedings of IMECE2007 ASME International Mechanical Engineering Congress and Exposition, November 11-15, Seattle, Washington, USA
- Matras, A.L., Flowers, G.T., Fuentes, R., Balas, M., Fausz, J., 2006, "Suppression of Persistent Rotor Vibrations Using Adaptive Techniques", ASME Journal of Vibration and Acoustics, Volume 128(6), 682 - 689
- Matsushita, O., Imashima, T., Hisanaga, Y., Okubo, H., 2002, "Aseismic Vibration Control of Flexible Rotors Using Active Magnetic Bearing", ASME Journal of Vibration and Acoustics, Volume 124, 49 – 57
- McMullen, P.T., Huynh, C.S., Hayes, R.J., 2000, "Combination radial - axial magnetic bearing", Seventh International Symposium on Magnetic Bearings, August 23-25, ETH Zurich
- Medina, S., Olver, A.V., "An Analysis of Misaligned Spline Coupling", Proceedings of the Institution of Mechanical Engineers, Part J: Journal of Engineering Tribology, 216, 269-278, 2002
- Meireles, M.R., Magali R. G., Almeida, P.E.M., Simoes, M.G., 2003, "A Comprehensive Review for Industrial Applicability of Artificial Neural Networks", IEEE Transactions on Industrial Electronics, Volume 50, No. 3, 585 - 601
- Morais T S., Steffen, V. Jr., Mahfoud, J., 2012, "Control of the breathing mechanism of a cracked rotor by using electro-magnetic actuator: numerical study", Latin American Journal of Solids and Structures, Volume 9, No. 5, 581 – 596
- Monte, M., Verbelen, F., Vervisch, B., Detection of Coupling Misalignment by Extended orbits, Experimental Techniques, Rotating Machinery, and Acoustics, 8, In:

Proceedings of the Society for Experimental Mechanics Series, pp 243 – 250, February, 2015

- Monte M, Verbelen, F, Vervisch, B., The use of orbitals and full spectra to identify misalignment, Structural Health Monitoring, 5, pp 215–222, February, 2014
- Moradi, M., "Solving Ill-Conditioned Linear Equations Using Simulated Annealing Method", Journal of Hyperstructures, 7, pp 60-66, 2018.
- Mura, A., Cura, C., Molfetta, A.D., "Investigation of Bearings Overloads due to Misaligned Splined Shafts", Procedia Structural Integrity, 12, 52–57, 2018
- Mushi, S.E., Lin, Z., Allaire, P.E., 2010, "Stability analysis of a flexible rotor on active magnetic bearings subject to aerodynamic loads", Proceedings of 12th International Symposium on Magnetic Bearings, Wuhan, China, 22-25
- Mushi, S.E., Lin, Z., Allaire, P.E., 2012, "Design, Construction, and Modelling of a Flexible Rotor Active Magnetic Bearing Test Rig", IEEE/ASME Transactions on Mechatronics, Volume 17, No. 6, 1170 – 1182
- Mushi, S.E., Lin, Z., Allaire, P.E., Evans, S., "Aerodynamic cross-coupling in a flexible rotor: control design and implementation", 11th International symposium on Magnetic bearings, Nara, Japan, 12 – 17
- Muszynska, A., 2005, "Rotordynamics", CRC Press, , Taylor and Francis Group, Boca Raton, Florida, USA, 1128 pages
- Myburgh, S., Schoor, G.V, Ranft, E.O., 2010, "A Non-linear Simulation Model of an Active Magnetic Bearings Supported Rotor System", XIX International Conference on Electrical Machines - ICEM 2010, Rome
- Mykhaylyshyn, V., 2001, "Application of Active Magnetic Force Actuator for Control of Flexible Rotor System Vibrations", Thesis, Master of Science in Mechanical Engineering, Cleveland State University
- Mystkowski, A., 2010, "μ-synthesis Control of Flexible Modes of AMB Rotor", Acta Mechanica et Automatica, Volume 4, No.4, 83 – 90
- Nakajima, Y., Sagane, T., Watanabe, T., Seto, K., 2005, "Modelling, Motion And Vibration Control For Flexible Rotor Supported By Active Magnetic Bearings", Proceedings of IDETC/CIE 2005, ASME 2005, International Design Engineering Technical Conferences & Computers and Information in Engineering Conference, Long Beach, California, USA

- Nandi, S., Toliyat, H, A., Li, X., 2005, "Condition Monitoring and Fault Diagnosis of Electrical Motors—A Review", IEEE Transactions on Energy Conversion, Volume 20, No. 4, 719 – 729
- Nelson, H. D., McVaugh, J, M., The dynamics of rotor bearing systems using finite elements, Journal of Engineering for Industry, pp 593 – 600, May, 1976
- Nelson H. D., Rotor Dynamics Equations in Complex Form, Journal of Vibration, Acoustics, Stress and Reliability in Design, Technical brief, 107, pp 460-461, October, 1985
- Nikolajsen, J. L., Holmes, R., Gondhalekar, V., 1979, "Investigation of an Electromagnetic Damper for Vibration Control of A Transmission Shaft", Institution of Mechanical Engineers
- Nivas, D.S.K., 2012, "Rotordynamic Analysis of RM12 Jet Engine Rotor Using ANSYS", MS Thesis, Blekinge Institute of Technology, Karlskona, Sweden
- Nikolajsen, J.L., 1996, "The Effect of Misalignment on Rotor Vibrations", ASME International Gas Turbine and Aero Engine Congress & Exhibition, June 10-13, Birmingham, UK, 120, 3, pp. 635 – 640.
- Nonami K, 1988, "Vibration and Control of Flexible Rotor Supported by Magnetic Bearings", First International Conference on Magnetic Bearings cosponsored by the Swiss Federal Institute of Technology (ETH) and the Swiss Society of Microtechnics (SGMT), Zurich, Switzerland
- Nonami K, Ito T, 1996, "Mu-Synthesis of Flexible Rotor-Magnetic Bearing Systems", IEEE Transactions on Control Systems Technology, Volume 4, No. 5, 503-512
- Nordmann, R., Aenis, M., 2004, "Fault Diagnosis in a Centrifugal Pump Using Active Magnetic Bearings", International Journal of Rotating Machinery, 10(3), 183–191
- Okada, Y., Saitoh, T., Shinoda, Y., 1999, "Vibration Control of Flexible Rotor Supported by Inclination Control Magnetic Bearings", Proceedings of the 1999 IEEE/ ASME International Conference on Advanced Intelligent Mechatronics, 788 – 793
- Patel, T.H., Darpe, A.K., 2009, "Experimental Investigations on Vibration Response of Misaligned Rotors", Mechanical Systems and Signal Processing, 23, 7, pp. 2236-2252.
- Peduzzi, A., "Simulation of Advanced Engine Lubrication and Rotor Dynamics Systems – Rig Design and Fabrication", AIAA/SAE/ASME 19th Joint Propulsion Conference, Seattle, Washington, USA, June 27 – 29, 1983

- Pennachhi, P., Vania, A., Chatterton, S., 2012, "Nonlinear Effects Caused by Coupling Misalignment in Rotors Equipped with Journal Bearings", Mechanical Systems and Signal Processing, 30, 2012, pp. 306 – 322.
- Pesch, A.H., Sawicki, J.T., Stabilizing Hydrodynamic Bearing Oil Whip with μ-Synthesis Control of an Active Magnetic Bearing, Proceedings of ASME Turbo Expo 2015: Turbine Technical Conference and Exposition GT2015, June 15 – 19, Montréal, Canada, 12 pages, 2015
- Penny, J.E.T., Friswell, M.I., Zhou, C., 2006, "Condition Monitoring of Rotating Machinery using Active Magnetic Bearings", Proceedings of ISMA, 3497 – 3506
- Pesch, A.H., 2008, "Damage Detection of Rotors Using Magnetic Force Actuator: Analysis and Experimental Verification", Master of Science in Mechanical Engineering, Cleveland State University
- Pesch, A.H., Sawicki, J.T., 2015, "Stabilizing Hydrodynamic Bearing Oil Whip with μ-synthesis Control of an Active Magnetic Bearing", Proceedings of ASME Turbo Expo 2015: Turbine Technical Conference and Exposition, GT2015, Montreal, Canada
- Pilat, A., 2010, "Analytical modelling of active magnetic bearing geometry", Applied Mathematical Modelling, Volume 34, Issue 12, 3805–3816
- Pilotto, R., Nordmann, R., Atzrodt, H.,Herold, S., 2017, "Use of Magnetic Bearings in Vibration Control of a Steam Turbine with Oil Film Bearings", 24th International Congress on Sound and Vibration, 23 – 27 July, London, UK, 2017
- Piotrowski, S., 2006, "Shaft Alignment Handbook", CRC Press, 3rd edition, November, Boca Raton, USA, 2006
- Parkinson, A.G., Darlow, M.S., Smalley, A.J., 1980, "Theoretical Introduction to the Development of a Unified Approach to Flexible Rotor Balancing", Journal of Sound and Vibration, Volume 68, Issue 4, 489-506
- Prabhu, B.S., 1997, "An Experimental Investigation on the Misalignment Effects in Journal Bearings", Tribology Transactions, 40, 2, pp. 235-242.
- Prasad, V., Tiwari, 2018, "Identification of Speed-Dependent Active Magnetic Bearing Parameters and Rotor Balancing in High-Speed Rotor Systems", Journal of Dynamic Systems, Measurement, and Control, 141, 4, pp 1 – 10
- Qu, Z.Q., 2004, "Model Order Reduction Techniques with Applications in Finite Element Analysis", Springer-Verlag, London, UK, 2004.

- Quinn, D. D., Mani, G., Kasarda, M.E.F., Bash, T., Inman, D.J., Kirk, R. G.,2005, “Damage Detection of a Rotating Cracked Shaft Using an Active Magnetic Bearing as a Force Actuator-Analysis and Experimental Verification”, IEEE/ASME Transactions on Mechatronics, Volume 10, No. 6, 640 – 647
- Randall, R.B., 2011, “Vibration-based Condition Monitoring: Industrial, Aerospace and Automotive Applications”, John Wiley & Sons, Ltd, 310 Pages
- Ranjan, G., Tiwari, R., 2020, “On-site high-speed balancing of flexible rotor-bearing system using virtual trial unbalances at slow run”, International Journal of Mechanical Sciences, 183, 105786
- Rao, A.S., Sekhar, A.S., 1996, “Vibration Analysis of Rotor-Coupling-Bearing System with Misaligned Shafts”, ASME International Gas Turbine and Aero Engine Congress & Exhibition, June 10-13, Birmingham, UK, 8 pages.
- Rao, J.S., Sreenivas, R., Chawla, A., 2001, “Experimental Investigation of Misaligned Rotors”, Proceedings of ASME Turbo expo, June 4-7, New Orleans, Louisiana, 4, 8 pages.
- Rao, J. S., Sreenivas, R. and Veeresh, C. V., 2002, “Solid Rotordynamics”, Fourteenth U.S. National Congress of Theoretical and Applied Mechanics, Blacksburg, VA, USA, June 23-28
- Rao, J.S., Sreenivas, R., “Dynamics of a Three Level Rotor System Using Solid Elements”, Proceedings of the ASME Turbo Expo 2003, collocated with the 2003 International Joint Power Generation Conference. Volume 4: Turbo Expo 2003. Atlanta, Georgia, USA. June 16–19, 601-606, 2003
- Rao, J. S., and Tiwari, R., 2008, "Optimum Design and Analysis of Thrust Magnetic Bearings Using Multi Objective Genetic Algorithms", International Journal for Computational Methods in Engineering Science and Mechanics, Volume 9, 223-245.
- Rybczynski, J., 2011, “The Possibility of Evaluating Turbo-Set Bearing Misalignment Defects on the Basis of Bearing Trajectory Features”, Mechanical Systems and Signal Processing, 25, pp. 521-536
- Reddy, M.C.S., Sekhar, A.S., 2015, “Detection and Monitoring of Coupling Misalignment in Rotors Using Torque Measurements”, Measurement, 61, pp. 111-122.

- Raymer, S.G., Childs, D.W., 2001, “Force Measurements in Magnetic Bearings using Fibre Optic Strain Gauges”, Proceedings of ASME Turbo Expo 2001 June 4-7, 2001, New Orleans, Louisiana
- Riemann, B., Perini, E.A., Cavalca, K. L., Castro, H. F., Rinderknecht, S., 2013, “Oil whip instability control using μ-synthesis technique on a magnetic actuator”, Journal of Sound and Vibration, Volume 332, Issue 4, 654–673
- Riemann,B., Perini, E.A., Cavalca, K.L., Castro, H.F.,Rinderknecht, S.,2013, “Oil Whip Instability Control Using μ -synthesis Technique on a Magnetic Actuator”, Journal of Sound and Vibration, 332, 654–673
- Roy, H.K., Das A.S., Dutt J.K., 2016, “An efficient rotor suspension with active magnetic bearings having viscoelastic control law”, Mechanism and Machine Theory, Volume 98, 48–63
- Saavedra, P. N., Ramirez, D. E., Vibration Analysis of Rotors for the Identification of Shaft Misalignment Part 1: Theoretical Analysis, Proceedings of Institute of Mechanical Engineers, Part C: Journal of Mechanical Engineering Science, 218 (9), pp 971–985, 2004
- Saavedra, P. N., Ramirez, D. E., Vibration Analysis of Rotors for the Identification of Shaft Misalignment Part 2: Experimental Validation, Proceedings of Institute of Mechanical Engineers, Part C: Journal of Mechanical Engineering Science, 218 (9), pp 987–999, 2004
- Sabnavis, G., Kirk, R.G, Kasarda, M.E.F., Quinn, D., 2004, “Cracked shaft detection and diagnostics: A literature review”, The Shock and Vibration Digest, Volume 36, 287–296
- Sahinkaya, M. N., Cole, M.O.T, Burrows, C.R., 2002, “On the Use of Schroeder Phased Harmonic Sequences in Multi-Frequency Vibration Control of Flexible Rotor/Magnetic Bearing Systems” 8th International Symposium on Magnetic bearings, Mito, Japan
- Sahinkaya, M. N., Abulrub, A.G., Burrows, C.R., 2011, “An Adaptive Multi-Objective Controller for Flexible Rotor and Magnetic Bearing Systems”, ASME Journal of Dynamic Systems, Measurement, and Control, Volume 133, 031003-1 - 031003-9

- Saket, F.Y., Sahinkaya, M.N., Keogh, P.S., 2019, "Measurement and calibration of rotor/touchdown bearing contact in active magnetic bearing systems", Mechanical Systems and Signal Processing, 122,1–18
- Sampath, K, K., Lal, M., 2020,"Dynamic Behaviour Analysis of Coupled Rotor Active Magnetic Bearing System in the Supercritical Frequency Range", Mechanism and Machine Theory,152
- Sanadgol, D., Maslen, E., 2005, "Back stepping For Active Control of Surge in Unshrouded Centrifugal Compressors with Magnetic Thrust Bearing Actuation", Proceedings of GT2005, ASME Turbo Expo 2005: Power for Land, Sea and Air, Reno-Tahoe, Nevada, USA
- Sarmah, N., Tiwari, R., 2018, "Model based identification of crack and bearing dynamic parameters in flexible rotor systems supported with an auxiliary active magnetic bearing", Mechanism and Machine Theory, 122, 292–307
- Sarmah, N., Tiwari, R., 2020, "Analysis and identification of the additive and multiplicative fault parameters in a cracked-bowed-unbalanced rotor system integrated with an auxiliary active magnetic bearing", Mechanism and Machine Theory 146,103744
- Sawicki, J.T., Maslen, E.H., 2007, "Rotordynamic Response and Identification of AMB Machining Spindle", Proceedings of GT2007, ASME Turbo Expo 2007: Power for Land, Sea and Air, May 14-17, 2007, Montreal, Canada
- Sawicki, J.T., 2008, "Rationale for Mu-Synthesis Control of Flexible Rotor-Magnetic Bearing Systems", Acta Mechanica et Automatica, Volume 2, No.2, 67 - 74
- Sawicki, J.T., Friswell, M.I., Pesch, A.H., Wroblewski, A., 2008, "Condition Monitoring Of Rotor Using Active Magnetic Actuator", Proceedings of ASME Turbo Expo 2008: Power for Land, Sea and Air, GT2008, Berlin, Germany
- Sawicki, J.T., 2009, "Rotor Crack Detection using Active Magnetic Bearings", Solid State Phenomena, Volume 144, 9-15
- Sawicki, J.T., Storozhev, D.L., Lekki, J.D., 2011, "Exploration of NDE Properties of AMB Supported Rotors for Structural Damage Detection", ASME Journal of Engineering for Gas Turbines and Power, Volume 133, 102501-1 – 102501-9

- Sawicki, J.T., Friswell, M.I., Kulesza, Z., Wroblewski, A., Lekki, J.D., 2011, "Detecting cracked rotors using auxiliary harmonic excitation", Journal of Sound and Vibration, 330, pp. 1365 – 1381.
- Sawicki, J.T., 2015, "Rotor Active Structural Health Monitoring", International Symposium on Transport Phenomena and Dynamics of Rotating Machinery, Keynote Lecture VI
- Schweitzer, G., Maslen, E.H., 2009, "Magnetic Bearings: Theory, Design and Application to Rotating Machinery", Springer-Verlag, Berlin, Heidelberg
- Schweitzer, G., 2009, "Applications and Research Topics for Active Magnetic Bearings", Proceedings of IUTAM-Symposium on Emerging Trends in Rotor Dynamics, March 23-26, 2009, Indian Institute of Technology, Delhi, India. Springer-Verlag
- Sekhar, A.S., Prabhu, B.S., 1995, "Effects of Coupling Misalignment on Vibrations of Rotating Machinery", Journal of Sound and Vibration, 185, 4, pp. 655-671.
- Sharp, R.S., 1980, "Flexible rotor balancing: A review of principles and practices", Tribology International, Volume 13, Issue 5, 211-217
- Shende, R.W., Sane,S.K., "Squeeze Film Damping for Aircraft Gas Turbines", Defence Science Journal, 38, 4, 439 – 456, 1988
- Sheu, G. J., Yang S. M., Yang C. D., 1997, "Design of Experiments for the Controller of Rotor Systems With a Magnetic Bearing", ASME Journal Of Vibration And Acoustics, Volume 119, 200 - 207
- Shiau, T. N., Sheu, G. J., Yang, C. D., 1997, "Vibration and Control of a Flexible Rotor in Magnetic Bearings Using Hybrid method and T Control Theory" Transactions of the ASME, 39thInternational Gas Turbine and Aero engine Congress and Exposition, The Hague, The Netherlands, Volume 119, 178 – 185
- Shravankumar, C., Tiwari,R., Identification of stiffness and periodic breathing forces of a transverse switching crack in a Laval Rotor, Fatigue and Fracture of Engineering Materials and Structures, 36, pp 254-269, 2012.
- Shravankumar,C., Tiwari, R., Mahibalan, A.,2015, Experimental Identification of Rotor Crack Forces, Proceedings of the 9th IFToMM International Conference on Rotor Dynamics, Mechanisms and Machine Science 21, pp 361-371

- Shuguo, L., Yanhong, M., Dayi, Z., Jie, H.,2012, "Studies on Dynamic Characteristics of the Joint in the Aero-Engine Rotor System", Mechanical systems and signal processing, 29, 120-136
- Shravankumar, C., Tiwari, R., 2012, "Identification of stiffness and periodic excitation forces of a transverse switching crack in a Laval rotor", Fatigue & Fracture of Engineering Materials & Structures, Blackwell Publishing Ltd., 1 - 12
- Singh, S., Tiwari, R., 2015, "Model-based fatigue crack identification in rotors integrated with active magnetic bearings", Journal of Vibration and Control, 1 – 21
- Singh, S., Tiwari R., 2016, "Model-based Switching-Crack Identification in a Jeffcott Rotor with an offset disk integrated with an Active Magnetic Bearing", ASME Journal of Dynamic Systems, Measurement, and Control, Volume 138, 031006-1 - 031006-11
- Sinha, J.K., Higher order spectra for crack and misalignment identification in the shaft of a rotating machine, Structural Health Monitoring, 6, pp 325 – 334, December, 2007
- Siva Srinivas, R., Tiwari, R., Kannababu, Ch., Application of active magnetic bearings in flexible rotordynamic systems - A state-of-the-art review, Mechanical Systems and Signal Processing, 106, pp 537 – 572, June, 2018.
- Siva Srinivas, R., Tiwari, R., Kannababu, Ch., Model based analysis and Identification of Multiple Fault Parameters in Coupled Rotor Systems with Offset Discs in the presence of misalignment and integrated with an Active Magnetic Bearing, Journal of Sound and Vibration, 450, pp 109-140, 2019.
- Someya, T., 1989, "Journal-Bearing Databook", Springer-Verlag, Berlin, 326 pages.
- Soulas, T.A., Kuzdzal, M.J., 2009, "Rotordynamic Testing and Evaluation of a Large Centrifugal Compressor Using a Magnetic Bearing Exciter", Proceedings of ASME Turbo Expo 2009: Power for Land, Sea and Air, Orlando, Florida, USA
- Spakovszky, Z.S., Paduano, J.D., Larsonneur, R., Traxler, A., Bright, M.M., 2011, Tip Clearance Actuation with Magnetic Bearings for High-Speed Compressor Stall Control, Journal of Turbomachinery, 123, 9 pages, 2011
- Spakovszky, Z. S., Paduano, J. D., Larsonneur, R., Traxler, A., Bright, M. M., 2001, " Tip Clearance Actuation With Magnetic Bearings for High-Speed Compressor Stall Control", 45th International Gas Turbine and Aero engine Congress and Exhibition, Munich, Germany, Volume 123, 464 – 472

- Spakovszky, Z. S., Paduano, J. D., Larsonneur, R., Traxler, A., Bright, M. M., 2001, "Tip Clearance Actuation with Magnetic Bearings for High-Speed Compressor Stall Control", Proceedings of ASME Turbo Expo, Munich Germany
- Sreenivasa Rao, A., Sekhar, A. S., Vibration Analysis of Rotor-Coupling-Bearing System with Misaligned Shafts, Proceedings of 41st ASME Gas Turbine and Aero engine Congress Exposition to be held in Birmingham, UK, Paper No.96-GT 012, 1996
- Stimac, G., Braut, S., Bulic, N., Zigulic, R., 2013, "Modelling and Experimental Verification of a Flexible Rotor/AMB System", COMPEL - The international journal for computation and mathematics in electrical and electronic engineering, Volume 32, Issue 4, 1244 – 1254
- Storace, A.F., Sood, D., Lyons, J.P., Preston, M.A., "Integration of Magnetic Bearings in the Design of Advanced Gas Turbine Engines", Journal of Engineering for Gas Turbines and Power, 117, 655- 665, 1995
- Storozhev, D.L., 2009, "Smart Rotating Machines for Structural Health Monitoring", Thesis, Master of Science in Mechanical Engineering, Cleveland State University
- Sudhakar, G.N.D.S., Sekhar, A.S., 2009, "Coupling misalignment in rotating machines: Modelling, Effects and Monitoring", Noise & Vibration Worldwide, Sage Journals, 40, 1, pp. 17 -39.
- Sun, G., Palazzolo, A., Provenza, A., Lawrence, C., Carney, K., " Long Duration Blade Loss Simulations including Thermal Growths for Dual-Rotor Gas Turbine Engine", Journal of Sound and Vibration, 316, 147 – 163, 2008
- Sun, Z., Zhao, J., Shi, Z., Yu, S., 2013, "Identification of Flexible Rotor Suspended By Magnetic Bearings", Proceedings of the 2013, 21st International Conference on Nuclear Engineering ICONE21, Chengdu, China
- Sun, C., Chen, Y., Hou, L., "Steady-State Response Characteristics of a Dual Rotor System Induced by Rub-Impact", Nonlinear Dynamics, 86, 91–105, 2016
- Tammi, K., 2009, "Active Control of Rotor Vibrations by Two Feed-forward Control Algorithms", ASME Journal of Dynamic Systems, Measurement, and Control, Volume 131, 051012-1 - 051012-10
- Tang, E., Fang, J., Zheng, S., Jiang, D., 2015, "Active Vibration Control of the Flexible Rotor to Pass the First Bending Critical Speed in High Energy Density Magnetically

Suspended Motor", ASME Journal of Engineering for Gas Turbines and Power, Volume 137, 112501-1 – 112501-9

- Tieu, A.K., Qiu, Z.L., 1994, "Identification of sixteen dynamic coefficients of two journal bearings from experimental unbalance responses", Wear, Volume 177, Issue 1, 63-69
- Tieu, A.K., Qiu, Z.L., 1997, "Identification of sixteen force coefficients of two journal bearings from impulse responses", Wear, Volume 212, Issue 2, 206 – 212
- Tiwari, R., 2017, "Rotor systems: Analysis and Identification", CRC press, Taylor and Francis Group, Boca Raton, Florida, USA, 1059 pages.
- Taplak, H., Parlak, M., "Evaluation of Gas Turbine Rotor Dynamic Analysis using the Finite Element Method", Measurement, 45, 1089–1097, 2012
- Tiwari, R.,2005, Conditioning of regression matrices for simultaneous estimation of the residual unbalance and bearing dynamics parameters, Mechanical System and Signal Processing, 19, 1085–1095.
- Tiwari, R., 2011, "Active Magnetic Bearings in Rotors", Chapter 18, Rotordynamics, NPTEL, Indian Institute of Technology Guwahati
- Tiwari, R., Chougale, A., 2014, "Identification of bearing dynamic parameters and unbalance states in a flexible rotor system fully levitated on active magnetic bearings", Mechatronics, Volume 24, Issue 3, 274–286
- Tiwari, R., Viswanadh, T., 2015, "Estimation of speed-dependent bearing dynamic parameters in rigid rotor systems levitated by electromagnetic bearings", Mechanism and Machine Theory, Volume 92, 100–112
- Tsou, P., Shen, M.H.H., 1994, "Structural damage detection and identification using neural networks", AIAA Journal, Volume 32, No. 1, 176-183.
- Tuckmantel, F.W.S., Schoola, C. G., Cavalca, K. L., Flexible Disc Coupling Model in Rotating Shafts, Proceedings of the 10th International Conference on Rotor Dynamics, Mechanisms and Machine Science, IFToMM 2018, 61, pp 502 – 517, 2019
- Vance, J, 1988, "Rotordynamics of Turbomachinery", Wiley-Interscience; 1st edition, 400 pages
- Vazquez, J.A., Maslen, E.H., Ahn, H.J, Han, D.C, 2001, "Model Identification of a Rotor with Magnetic Bearings", Proceedings of ASME Turbo Expo 2001, New Orleans, Louisiana

- Viveros, H.P., Nicoletti, R., 2014, “Lateral Vibration Attenuation of Shafts Supported by Tilting-Pad Journal Bearing With Embedded Electromagnetic Actuators”, ASME Journal of Engineering for Gas Turbines and Power, Volume 136, 042503-1 - 042503-12
- Voigt, A, J., Santos, I, F., 2012, “Theoretical and Experimental Investigation of Force Estimation Errors using Active Magnetic Bearings with Embedded Hall Sensors”, ASME Turbo Expo 2012: Turbine Technical Conference and Exposition, Volume 7: Structures and Dynamics, Parts A and B, Copenhagen, Denmark
- Wagner, M.B., Younan, A., Allaire, P., Cogill, R., 2010, “Model Reduction Methods for Rotor Dynamic Analysis: A Survey and Review”, International Journal of Rotating Machinery, 17 pages.
- Wang, N., Jiang, D., “Vibration Response Characteristics of a Dual-Rotor with Unbalance-Misalignment Coupling Faults: Theoretical Analysis And Experimental Study”, Mechanism and Machine Theory, 25, 207-219, 2018
- Wang, D., Wang, N., Chen, K., 2019, “Unbalance Response of a Magnetic Suspended Dual-Rotor System”, Proceedings of the Institution of Mechanical Engineers, Part G: Journal of Aerospace Engineering, 233, 15, 5758-5772
- Wang, N., Liu, C., Jiang, D., 2019, “Prediction of Transient Vibration Response of Dual-Rotor-Blade-Casing System with Blade-Off”, Proceedings of the Institution of Mechanical Engineers, Part G: Journal of Aerospace Engineering, 233, 14, 5164-5176
- Wang, N., Liu, C., Jiang, D., Behdianan, K., 2019, “Casing Vibration Response Prediction of Dual-Rotor-Blade-Casing System With Blade-Casing Rubbing”, Mechanical Systems and Signal Processing, 118, 61-77
- Wang, F., Luo, G., Yan, S., Cui, H, 2017, “ A Comparison Study on Co- and Counter rotating Dual-Rotor System with Squeeze Film Dampers and Intermediate Bearing”, Shock and Vibration, 25 pages
- Wang, M., Han, Q., Wen, B., Zhang, H., Guan, T., 2016, “Modal Characteristics and Unbalance Responses of Fan Rotor System with Flexible Support Structures in Aero-Engine”, Proceedings of the Institution of Mechanical Engineers, Part G: Journal of Aerospace Engineering, 231, 9, 1686-1705

- Wang, N., Jiang, J., Xu, H., 2017, “Dynamic Characteristics Analysis of a Dual-Rotor System with Inter-Shaft Bearing”, Proceedings of the Institution of Mechanical Engineers, Part G: Journal of Aerospace Engineering, 233: 3, 1147-1158
- Wang, N., Xu, H., Jiang, D., 2016, “Dynamic Model and Fault Feature Research of Dual-Rotor System with Bearing Pedestal Looseness”, Mathematical Problems in Engineering, 18 pages
- Wang, Y., Fang, J., Zheng, S., 2014, “A Field Balancing Technique Based on Virtual Trial-Weights Method for a Magnetically Levitated Flexible Rotor”, ASME Journal of Engineering for Gas Turbines and Power”, Volume 136, 092502-1 - 092502-7
- Wauer, J., 1990, “On the dynamics of cracked rotors: A literature survey”, Applied Mechanics Review, Volume 43, No. 1, 13 – 17
- Walker, D., “Torsional Vibration of Rotating Machinery”, McGraw-Hill Professional, 1st edition, 2003, New York, USA
- Wowk, V., Machine Vibration: Alignment, McGraw-Hill, 1st edition, New York, USA, 2000
- Wu, F., Liang, Z., Ma, Y., Zhang, D., "Bending Stiffness and Dynamic Characteristics of a Rotor With Spline Joints", Proceedings of the ASME 2013 International Mechanical Engineering Congress and Exposition. Volume 4A: Dynamics, Vibration and Control. San Diego, California, USA. November 15–21, 2013
- Wroblewski, A.C., Pesch, A.H., Sawicki, J.T., 2013, “Structural Change Quantification in Rotor Systems based on Measured Resonance and Antiresonance Frequencies”, Proceedings of ASME Turbo Expo 2013: Turbine Technical Conference and Exposition GT2013, June 3-7, 2013, San Antonio, Texas, USA
- Xu, M., Marangoni, D., 1994, “Vibration Analysis of a Motor – Flexible Coupling – Rotor system subjected to Misalignment and Unbalance, PART I: Theoretical Model”, Journal of Sound and Vibration, 176 (5), pp 663–680,
- Xu, M., Marangoni, R.D., 1994, “Vibration Analysis of a Motor-Flexible-Coupling-Rotor System Subject to Misalignment and Unbalance, Part II: Experimental Validation”, Journal of Sound and Vibration, 176, 5, pp. 681-691.
- Xu, H., Wang, N., Jiang, D., Han, T., Li, D, 2016, “Dynamic Characteristics and Experimental Research of Dual-Rotor System with Rub-Impact Fault”, Shock and Vibration, 11 pages

- Xu, Y., Zhou, J., Di, L., Zhao C., and Guo Q., 2015, "Active Magnetic Bearing Rotor Model Updating Using Resonance and MAC Error", Shock and Vibration, 1 - 9
- Xu, Y., Zhou, J., Di, L., Zhao C., 2016, "Active magnetic bearings dynamic parameters identification from experimental rotor unbalance response", Mechanical Systems and Signal Processing, Volume 83, 228 - 240
- Xu, Y., Di, L., Zhou, J., Jin, C, Guo, Q, 2016, "Active magnetic bearings used as exciters for rolling element bearing outer race defect diagnosis", ISA Transactions 61, 221–228
- Xu, Y., Zhou, J., Di, L., Zhao, C., 2017, "Active magnetic bearings dynamic parameters identification from experimental rotor unbalance response", Mechanical Systems and Signal Processing, 83, 228–240
- Xu, Y., Zhou, J., Lin, Z., Jin, C., 2018, "Identification of dynamic parameters of active magnetic bearings in a flexible rotor system considering residual unbalances", Mechatronics, 49, 46–55
- Yan hong, M., Zhichao, L., Meng, C., Jie, H., Interval analysis of rotor dynamic response with uncertain parameters, Journal of sound and vibration, 332, 3869-3880, 2013
- Yang, S. M., Sheu, G. J., Yang, C. D., 1997, "Vibration Control of Rotor Systems With Non-collocated Sensor/Actuator by Experimental Design", ASME Vibration and Acoustics, Volume 119, 420 – 427
- Yang, Y., Cao, D., Wang, D., Jiang, G., "Fixed-point Rubbing Characteristic Analysis of a Dual-Rotor System Based on the Lankarani-Nikravesh model", Mechanism and Machine Theory, 103, 202–221, 2016
- Yang, S., 2011, "Electromagnetic Actuator Implementation and Control for Resonance Vibration Reduction in Miniature Magnetically Levitated Rotating Machines", IEEE Transactions on Industrial Electronics, Volume 58, No. 2, 611 – 617
- Yoon,S.Y., Lin, Z, Jiang, W., Allaire, P.E., Flow-Rate Observers in the Suppression of Compressor Surge Using Active Magnetic Bearings, Journal of Turbomachinery, 135, 11 pages, 2013
- Yoon, S.Y., Lin, Z., Lim, K.T., Goyne, C., Allaire, P.E., 2010, "Model Validation for an Active Magnetic Bearing Based Compressor Surge Control Test Rig", ASME Journal of Vibration and Acoustics, Volume 132, 061005-1 - 061005-13

- Yoon, S.Y, Lin, Z., Jiang, W., Allaire, P.E., 2013, Flow-Rate Observers in the Suppression of Compressor Surge Using Active Magnetic Bearings, ASME Journal of Turbo machinery, Volume 135, 041015-1 - 041015-11
- Yu, P., Zhang, D., Ma, Y., Hong, J., Dynamic Modelling and Vibration Characteristics Analysis of the Aero-Engine Dual-Rotor System With Fan Blade-Out, Mechanical Systems and Signal Processing,106, 158-175, 2018.
- Yu, P., Zhang, D, Ma, Y., Hong, J., "Dynamic Modelling and Vibration Characteristics Analysis of the Aero-Engine Dual-Rotor System with Fan Blade Out", Mechanical Systems and Signal Processing, 106, 158–175, 2018
- Yu, Z., Meng, L.T., King, L.M., 1998, "Electromagnetic bearing actuator for active vibration control of a flexible rotor", Proceedings of Institution of Mechanical Engineers, Volume 212, Part C, 705 – 716
- Zhang, Z.X., Wang, L.Z., Jin, Z. J., Zhang, Q., Li, X.L., "Non-Whole Beat Correlation Method for the Identification of an Unbalance Response of a Dual-Rotor System with a Slight Rotating Speed Difference", Mechanical Systems and Signal Processing, 39, 452-460, 2013
- Zhang, Q., Li, W., Liang, Z., Hong, J., 2014, "Study on the Stiffness Loss and its Affecting Factors of the Spline Joint Used in Rotor Systems" , Proceedings of ASME Turbo Expo: Turbine Technical Conference and Exposition GT2014, June 16 – 20, Dusseldorf, Germany
- Zhang, J., 1995, "Power Amplifiers for Magnetic Bearings", Swiss Federal Institute of Technology
- Zhao, G., Liu, Z., Chen, F., "Meshing Force of Misaligned Spline Coupling and the Influence on Rotor System", International Journal of Rotating Machinery, 8 pages, 2008
- Zhao, W., Hua, C., Dong, D., Ouyang, H.,A Novel method for identifying crack and shaft misalignment in rotor systems under noisy environments based on CNN, Sensors, 19(23), pp51-58, 2019
- Zhao, J., Zhang, H.T., Fan, M.C., Wu, Y., 2015, "Control of a Constrained Flexible Rotor on Active Magnetic Bearings", International Federation of Automatic Control Papers Online, Volume 48, Issue 28, 156–161

- Zhe, S., Ying, H., Jingjing, Z., Zhengang, S., Lei, Z., Suyuan, Y., 2014, “Identification of active magnetic bearing system with a flexible rotor”, Mechanical Systems and Signal Processing, Volume 49, 302–316
- Zheng, S., Chen, Q., Ren, H., 2015, “Active Balancing Control of AMB-rotor Systems Using a Phase-Shift Notch Filter Connected in Parallel Mode”, IEEE Transactions On Industrial Electronics, 1 - 9
- Zheng, S., Feng, R., 2016, “Feed forward compensation control of rotor imbalance for high-speed magnetically suspended centrifugal compressors using a novel adaptive notch filter”, Journal of Sound and Vibration, Volume 366, 1–14
- Zhong, Z.X., Zhu, C.S., 2013, “Vibration of flexible rotor systems with two- degree-of-freedom PID controller of active magnetic bearings”, Journal of Vibroengineering, Volume 15, Issue 3, 1302 -310
- Zhong, W., Palazzolo A., 2015, “Magnetic Bearing Rotordynamic System Optimisation Using Multi-Objective Genetic Algorithms”, ASME Journal of Dynamic Systems, Measurement, and Control, Volume 137, 021012-1 - 021012-12
- Zhou, J., Di, L , Cheng , C., Xu ,Y., Lin, Z., 2016, “A rotor unbalance response based approach to the identification of the closed-loop stiffness and damping coefficients of active magnetic bearings”, Mechanical Systems and Signal Processing, Volume 66-67, 665–678
- Zhou, S., Shi, J., 2001, “Active Balancing and Vibration Control of Rotating Machinery: A Survey”, The Shock and Vibration Digest, Volume 33, No. 4, 361-371
- Zhou, C., Friswell, M.I., Li, J., 2007, “Condition Monitoring of Cracked Shaft using Active Magnetic Bearings”, International Conference on Power Engineering, Hangzhou, China, 424 - 504
- Zhu, C., Robb, D.A., Ewins, D.J., 2003, “The dynamics of a cracked rotor with an active magnetic bearing”, Journal of Sound and Vibration, Volume 265, Issue 3, 469–487
- Zutavern, Z.S., Childs, D.W., 2005, “Fibre-optic strain gage calibration and dynamic flexibility transfer function identification in magnetic bearings”, Proceedings of GT2005, ASME Turbo Expo 2005: Power for Land, Sea and Air, June 6-9, 2005, Reno-Tahoe, Nevada

- Zutavern, Z.S., Childs, D.W., 2008, “Identification of Rotordynamic Forces in a Flexible Rotor System Using Magnetic Bearings”, ASME Journal of Engineering for Gas Turbines and Power, Volume 130, 022504-1 – 022504-6

Publications from the present work

Journals

1) Srinivas, R, S., Tiwari, R., Kannababu, Ch., " Application of Active Magnetic Bearings in Flexible Rotordynamic systems- A State of the Art Review ", Mechanical Systems and Signal Processing, Volume 106, June 2018, Pages 537–572

2) Srinivas, R, S., Tiwari, R., Kannababu, Ch., "Model Based Analysis and Identification of Multiple Fault Parameters in Coupled Rotor Systems with Offset Discs in the Presence of Angular Misalignment and Integrated with an Active Magnetic Bearing ", Journal of Sound and Vibration, Volume 450, 23 June 2019, Pages 109-140

3) Srinivas, R, S., Tiwari, R., Kannababu, Ch., "Modelling, Analysis and Identification of the Parallel and Angular Misalignments in a Coupled Rotor-Bearing-AMB System", Dynamic Systems Measurement and Control (Published Online)

4) Siva Srinivas, R., Tiwari, R., Ch Kannababu, "Identification of fluctuating forces and moments of a misaligned spline joint of gas turbine dual rotor system supported on rolling element bearings and AMB". (Communicated)

5) Siva Srinivas, R., Tiwari, R., Ch Kannababu," Identification of speed-dependent parameters in turbogenerators supported on tilting pad journal bearings and active magnetic bearings in the presence of combined misalignment" (Communicated)

Conferences

1) Siva Srinivas, R., Tiwari, R., Kannababu, Ch., " Interaction between unbalance and misalignment responses in coupled rotor systems integrated with AMB", ASME GTINDIA, Bangalore, India, December 7-8, 2017

2) Siva Srinivas, R., Tiwari, R., Kannababu, Ch., " Some numerical studies on coupled Turbine Generator Rotor System models", 13th International Conference on Vibration problems, Indian Institute of Technology Guwahati, Guwahati, November 29 – December 2, 2017

3) Siva Srinivas, R., Tiwari, R., Kannababu, Ch., " Studies on Misaligned rotor – train systems integrated with Active Magnetic Bearing", Fifth National Symposium on Rotordynamics, Indian Institute of Technology Patna, Patna, December 12 -13, 2017

4) Siva Srinivas, R., Tiwari, R., Kannababu, Ch., "Identification of Coupling Parameters in Flexibly Coupled Jeffcott Rotor Systems with Angular Misalignment and Integrated

through Active Magnetic Bearing", Mechanisms and Machine Science, Proceedings of the 10th International Conference on Rotor Dynamics –IFToMM, Vol. 3, Rio de Janeiro, Brazil, September 23 -27, 2018

5) Siva Srinivas, R., Tiwari, R., Kannababu, Ch., " Finite Element Modeling and Analysis of Coupled Rotor System Integrated with AMB in the Presence of Parallel and Angular Misalignments", Sixth National Symposium on Rotordynamics, CSIR - National Aerospace Laboratories, Bangalore, July 2-3, 2019 (**Best Paper Award**)

6) Siva Srinivas, R., Tiwari, R., Kannababu, Ch., "Identification of misaligned additive forces and moments of coupling in turbo-generator system integrated with an active magnetic bearing", Vibrations in Rotating Machinery, VIRM 12, Liverpool, UK, September 8 – 10, 2020